Direct Torque Control of Permanent Magnet Synchronous Machines using Matrix Converters

Thesis submitted to the Universitat Politècnica de Catalunya
for the Degree of Doctor of Philosophy, June 2008.

Author: **Carlos Ortega**

First supervisor: **Antoni Arias**

Second supervisor: **Cedric Caruana**

June 17, 2008

To my wife Noelia,
for her love and continuous encouragement,

To my daughter Berta,

&

To my parents,
for guiding me towards higher education,

and my sister,
for her unconditional love.

Contents

List of Figures

Acknowledgements

The work presented in this thesis has been carried out at the Electronic Engineering Department at the Universitat Politècnica de Catalunya with the support of the "Ministerio de Ciencia y Tecnología de España" under the TEC 2004-00589, TEC2007-61582-MIC and ENE2007-67033-C03-01 research projects. Part of the work was realized at the Power Electronics Department at the University of Malta under a Marie Curie research training fellowship (Research Project number: MEST-CT-2004-504243), where the candidate stayed for one year. Some of the experimental test has been carried out at the Research Department at the Escola Universitària Salesiana de Sarrià, receiving private economical support.

I would like to express my most sincere gratitude to my supervisor Dr. Antoni Arias for his guidance over the course of this work. I would also like to thank Dr. Cedric Caruana, as my external supervisor, for his advice and support.

Thanks also goes for Dr. Maurice Apap for his helpful assistance, and Dr. Cyril Spiteri for his valuable comments.

I am also very grateful to Prof. Greg Asher for his intervention in the fellowship issues.

I must also thank Dr. Xavier del Toro for his collaboration and support.

Finally, I would like to thank my friends and colleagues at the Power Elec-

tronics Department at the University of Malta, Dr. Marek Stulraiter for his helpful suggestions, Mr. James Borg for his help setting up the experimental rig, and Mr. Reiko Route for holding valuable discussions with me.

Abstract

The control of AC machine drives is a continuously advancing subject satisfying increasing high performance applications demands. Induction Motor (IM) drives with cage-type machines has been the workhorses of industrial variable speed drives applications, including pumps and fans, paper and textile mills, electric vehicles, locomotive propulsion, wind generation systems, etc. In addition to performance requirements, energy saving aspects of variable speed drives is gaining attention nowadays.

Permanent Magnet Synchronous Machines (PMSM) are becoming a very attractive alternative to IM. They are generally more expensive than IM. However, among other advantages, these type of machines offer higher efficiency, high power density and very fast dynamic performance. Permanent magnet machines, in particular in the low power range, are already widely used in industry and recently, the interest in their application is growing, particularly up to 100 kW [1].

Variable speed drives fed by voltage source inverters has been traditionally employed in industrial applications. In the past few years, matrix converters have emerged to become a close competitor to the conventional inverter [2]. A matrix converter is an advanced circuit topology capable of converting AC-AC, providing generation of load voltage with arbitrary amplitude and frequency, bi-directional power flow, sinusoidal input/output waveforms [3], and operation under unity input power factor. Furthermore, since no inductive or capacitive elements are required, MC allows a very compact design [3], [4].

There are several methods to control AC machines, vector control methods being the most suitable for high performance demands. Among others, field oriented control [5], [6] and direct torque control [7] are the most widely used.

Although being one of the emerging control techniques for industrial applications, the direct torque control has some inherent drawbacks that are still being investigated by researchers.

The work reported in this thesis is devoted to the investigation of direct torque control of permanent magnet synchronous machine drives fed by matrix converters.

This work considers the replacement of the conventional voltage source inverter by a matrix converter. The features of matrix converters are exploited to reduce the inherent electromagnetic torque and stator flux ripples arising from the direct torque control driving a permanent magnet synchronous machine. A new direct torque control using small and large voltage vectors of matrix converters has been developed during the course of this work.

The undesirable effects of the common mode voltage related with the utilization of the conventional voltage source inverter, like electromagnetic interferences and the machine early failures, are other issues with which this work is also concerned. A very simple algorithm to reduce the common mode voltage in direct torque control drives using matrix converters is developed and investigated in this work.

The main limitation of all sensorless vector control schemes, based on the conventional fundamental frequency models or observers, is that they fail at very low speeds. The desirability to operate continuously at low or zero speed has led to another sensorless approaches where the saliency of the machine is tracked through some form of signal injection to obtain flux or position

information. A new algorithm to inject a rotating vector in the $\alpha - \beta$ frame when employing a direct torque control has been developed in this thesis.

Nomenclature

α	α-axis in the stationary reference frame	
β	β-axis in the stationary reference frame	
ΔL_s	variation of the stator inductance	H
$\hat{T}_e^{error}$	relative error of the torque mean value	Nm
$\hat{x}$	mean value of a generic variable x	
$\hat{\gamma}_s$	estimated value of the stator flux angle	rad
$\hat{\psi}_\alpha^s$	estimated value of the α stator flux component	Wb
$\hat{\psi}_\beta^s$	estimated value of the β stator flux component	Wb
ω_e	stator electrical or synchronous speed	rad/s
ω_i	injection pulsation	rad/s
ω_r	electrical rotor speed	rad/s
ω_s	slip speed	rad/s
ϕ_i	input angle displacement	rad
ϕ_o	output angle displacement	rad
ψ_α^m	α magnetizing flux component	Wb
ψ_α^r	α rotor flux component	Wb
ψ_β^m	β magnetizing flux component	Wb

ψ^r_β	β rotor flux component	Wb
ψ^s_a	stator flux of phase a	Wb
ψ^s_b	stator flux of phase b	Wb
ψ^s_c	stator flux of phase c	Wb
ψ^m_d	magnetizing flux d-axis component	Wb
ψ^r_d	rotor flux d-axis component	Wb
ψ^s_d	stator flux d-axis component	Wb
ψ^m_q	magnetizing flux q-axis component	Wb
ψ^r_q	rotor flux q-axis component	Wb
ψ^s_q	stator flux q-axis component	Wb
ψ^s_α	α stator flux component	Wb
ψ^s_β	β stator flux component	Wb
ψ_{PM}	permanent magnet flux	Wb
σ_x	standard deviation of a generic variable x	
τ_r	rotor time constant	s
θ_r	rotor angle (*position*)	rad
φ	voltage or current displacement angle	rad
$\vec{\psi}^m$	magnetizing flux vector	Wb
$\vec{\psi}^s$	stator flux vector	Wb
$\vec{i}^s$	stator current vector	A
$\vec{i}_i$	low frequency component of the MC input current vector	A
$\vec{i}_o$	MC output current vector	A

$\vec{v}$	stator voltage space vector	V
$\vec{v}^*$	reference voltage vector	V
$\vec{v}_i$	MC input voltage vector	V
$\vec{v}_o$	low frequency component of the MC output voltage vector	V
$s\vec{w}$	average number of switching events due to zero vectors selection	
C_f	filter capacitance	F
d	d-axis in the rotating reference frame	
f_i	injection frequency	Hz
i_A	phase A MC input current	A
i_a	phase a MC output current	A
i_a^s	stator current of phase a	A
i_B	phase B MC input current	A
i_b	phase b MC output current	A
i_b^s	stator current of phase b	A
i_C	phase C MC input current	A
i_c	phase c MC output current	A
i_c^s	stator current of phase c	A
i_d^r	rotor current d-axis component	A
i_d^s	stator current d-axis component	A
I_h	distortion component of current I	A
i_q^r	rotor current q-axis component	A
i_q^s	stator current q-axis component	A

i^s_α	α stator current component	A
i^s_β	β stator current component	A
i^s_{dn}	high frequency negative sequence current $d-axis$ component (*position signal*)	A
i^s_{dp}	high frequency positive sequence current $d-axis$ component	A
$i^s_{i\alpha}$	high frequency position current α component	A
$i^s_{i\beta}$	high frequency position current β component	A
i^s_{qn}	high frequency negative sequence current $q-axis$ component (*position signal*	A
i^s_{qp}	high frequency positive sequence current $q-axis$ component	A
J	moment of inertia	Kgm^2
k	injection voltage repetition rate	
L_a	inductance value of phase a	H
L_b	inductance value of phase b	H
L_c	inductance value of phase c	H
L^s_d	d-axis stator inductance	H
L_f	filter inductance	H
L^r_l	rotor leakage inductance	H
L^s_l	stator leakage inductance	H
L_m	magnetizing inductance	H
L^s_q	q-axis stator inductance	H
L_r	rotor inductance	H
L_s	stator inductance	H

L_{dm}	d-axis magnetizing inductance	H
M	transfer matrix of the MC	
m_c	current modulation index	
m_v	voltage modulation index	
M_{ab}	mutual inductance value between phases ab	H
M_{bc}	mutual inductance value between phases bc	H
M_{ca}	mutual inductance value between phases ca	H
$m_{ij}(t)$	duty ratio of switch S_{ij} connecting input phase i to output phase j	
p	number of pole pairs	
q	q-axis in the rotating reference frame	
R_f	filter resistance	Ω
R_r	Rotor resistance	Ω
R_s	stator resistance	Ω
sw_{event}	number of switching events per second	
T_e	electromagnetic torque	Nm
t_i	injection time	s
T_L	load torque	Nm
T_s	sampling time	s
V^i	magnitude of the injected voltage vector	V
v_A	phase A MC input voltage	V
v_a^s	stator voltage of phase a	V
v_B	phase B MC input voltage	V

v_b^s	stator voltage of phase b	V
v_C	phase C MC input voltage	V
v_c^s	stator voltage of phase c	V
v_d^r	rotor voltage d-axis component	V
v_d^s	stator voltage d-axis component	V
v_q^r	rotor voltage q-axis component	V
v_q^s	stator voltage q-axis component	V
v_α^s	α stator voltage components	V
v_β^s	β stator voltage components	V
v_{ab}	voltage between phases a and b	V
v_{aN}	voltage of phase a respect to the neutral point	V
v_{bc}	voltage between phases b and c	V
v_{bN}	voltage of phase b respect to the neutral point	V
v_{ca}	voltage between phases c and a	V
v_{cm}	common mode voltge	V
v_{cm}^a	common mode voltage for active vectors	V
v_{cm}^z	common mode voltage for null vectors	V
v_{cN}	voltage of phase c respect to the neutral point	V
v_{DC}	voltage of the DC link	V
$v_{i\alpha}^s$	high frequency injected voltage α component	V
$v_{i\beta}^s$	high frequency injected voltage β component	V
V_{pn}	fictitious DC-link voltage	V
zv_{event}	number of zero vectors events per second	

Chapter 1

Introduction

1.1 Background

Despite electric and magnetic effects appearing in the nature have been observed by human beings since antiquity, it was not until the middle of the eighteenth century, that speculations about the link between electricity and magnetism was a favorite pursuit. At the beginning of the nineteenth century many researchers attempted to establish such connection. The main breakthrough is attributed to the discovery of the magnetic effect of an electric current by Hans Christian Oersted (1777-1851). An account of this significant discovery was published in 1820 [8]. One year later, Michael Faraday (1791-1867) set up an experiment demonstrating for the first time the possibility of converting electric current into continuous mechanical motion. The experiment is considered to be the first DC motor. Faraday went on to discover the electromagnetic induction in 1831 [8], however, it was Walter Bailey who demonstrated, in 1879, the possibility of producing a magnetic field without the aid of mechanical motion. Nikola Tesla (1856-1943), patented the principles for the design and operation of AC motors on 1st May, 1888. George Westinghouse bought Tesla's patents and employed him to produce

the first practical IM in 1892 [8]. Since then, AC machines, especially the IM, have been widely used in industry [9] except for variable speed application. Before 1950s, DC machines were extensively used in variable speed applications since AC machines were not capable of varying speed smoothly [8]. In particular, DC machines with separated excitation were preferred for applications with fast response and four quadrant operation requirements, since their flux and torque could be easily controlled by the field and armature currents [1]. However, due to the existence of mechanical commutators (brushes), DC machines have several disadvantages. Concretely, they cannot be used in explosive or corrosive environments and require periodic maintenance. Moreover, the brushes in this type of machines limit the speed and current [1], [10].

These problems can be overcome by the substitution of DC machines by AC machines, which have a simple and rugged structure, do not need maintenance and are more economic than the former. Furthermore, for the same output power, AC machines can be designed with smaller dimensions, lower weight and lower rotating mass.

Recently, the awareness of environmental problems worldwide have shown great interest in developing high efficient motor technologies and their applications. Electrical energy saving programs have become a very important issue in realizing a sustainable society. At present, more than 50% of all the electrical energy produced in Japan is converted to mechanical energy by means of electrical motors. Improving the efficiency of each electrical motor by just 1%, could eliminate the need for a nuclear plant of approximately 500 MW [11].

PMSM has become, in recent years, a suitable candidate to face energy saving issues. The invention of high performance magnets like samarium cobalt and neodymium-iron-boron, have made possible to achieve motor performance that can surpass IMs. Because PMSMs do not require the use of extra current to produce magnetic power in the rotor, the conduction losses

are concentrated in the stator where they can be easily dissipated. This fact, essentially contributes to improve the efficiency compared to IMs. Moreover, eliminating cooper in the rotor allows the design of machines with smaller rotor diameters, actually resulting in smaller machine size, with higher power density and lower rotor inertia than IMs.

Controlling an AC machine is significantly more complicated than its DC counterpart, however, thanks to the rapid and continuous evolution in the power electronics field and microelectronics devices, these control complexities have been overcome and many efforts have been made towards the research and development of different variable speed drives employing AC machines.

Among all control methods for AC machines, due to its simplicity, the most widely used in industrial applications was and still is the v/f control. The v/f control is a scalar control which consists in maintaining a constant relation between the terminal voltage and its frequency. Its structure is very simple and, usually, works without speed feedback. However, the v/f control cannot achieve good dynamic performance neither in speed nor torque.

Despite the fact that v/f control is the most widespread, being in the majority of industrial applications, the industry demand of high performance drive systems increases very fast. Vector control techniques allow the control of not only the magnitude but also the phase of the voltage, current, and flux space vectors, which further significantly improves the dynamic performance in both speed and torque, even at stand still. The most important contribution in this field was the Field Oriented Control (FOC) proposed by Hasse [6] and Blaschke [5] in 1972. However, its main disadvantages are the huge computational capability required and the compulsory good identification of the machine parameters [10].

In the mid eighties, a new control method was presented by Takahashi [7], known as Direct Torque Control (DTC). Since ABB launched the first known

commercial DTC drive[1] in 1995, these type of drives are very popular due to their simple structure and robustness. The decoupling of stator flux and electromagnetic torque employing nonlinear coordinates transformation and PI controllers is replaced with hysteresis controllers yielding very fast torque response. This control method allows the direct control of both stator flux and electromagnetic torque. Further investigation is, however, required to improve the drive performance and better behavior regarding Electro Magnetic Interferences (EMI).

The main features of DTC are:

- Direct control of both stator flux linkage and electromagnetic torque by selecting the optimum power converter vectors.
- Indirect control of currents (*approximately sinusoidal*) and voltages.
- High dynamic performance even at stand still.
- The inverter switching frequency depends on the widths of both flux and torque hysteresis bands.

DTC main advantages are:

- Absence of coordinate transform.
- Absence of separated voltage modulator block.
- Absence of current PID controllers.
- Minimal torque response time.

However, some disadvantages are also present such as:

- Possible problems during starting.

[1]Although the first commercial drive was developed in Japan, it was not a success, hence, the ABB ACS600 developed in Finland is considered the first commercial application.

- Requirement of torque and flux estimators[2].
- Varying switching frequency.
- Inherent torque and stator flux ripple.

Some approaches have been recently published using 3-level converters in order to increase the number of available vectors in a DTC scheme [12], [13]. The stator flux and electromagnetic torque hysteresis comparators are modified increasing the respective error levels achieving better performance regarding the torque and flux ripple.

Another alternative to conventional Voltage Source Inverters (*VSI*) is the Matrix Converter (*MC*). The MC is an advanced circuit topology capable of directly converting AC-AC. Among different advantages, controllable input power factor and a very compact design are the most relevant advantages of such converters. In 2001 a new DTC using MC was introduced by D. Casadei [2], which gives similar performance to that obtained by a conventional VSI while is able to maintain the input power factor close to one. The authors claim that this DTC scheme gives good performance in the high speed range but no investigation have been made to determine how the limit of the voltage transfer ratio[3] is affected [14].

In recent years, great efforts have been made to introduce sensorless AC drives. Sensorless AC drives is a generic term defining AC drives operating without a speed or shaft position sensor. These type of drives are of huge commercial significance and have become a norm for industry, being introduced by almost every large manufacturer (*Control Techniques plc, Siemens, Hitachi, Yaskawa, Eurotherm, etc.*) [10]. However, sensorless AC drives are gaining popularity in all industry applications except for those requiring servo performance or sustained zero/low frequency operation. This is due to the

[2]Torque and flux estimators or observers are also required by other vector control techniques.

[3]The voltage transfer ratio corresponds to the relation between the output and input voltage V_{out}/v_{in} of the matrix converter.

main feature of almost all these industrial drives; their performance deteriorates at low and zero frequency due to the loss of information as the induced back emf becomes very small.

One method to overcome this limitation is to inject a high frequency (*hf*) test signal on the fundamental excitation. Due to asymmetries of the machine, the resulting *hf* currents are modulated by variations in the reluctance. In the case of Surface Mounted PMSM (SM-PMSM), these variations arises from the saturation of the main flux path [15]. Hence, for SM-PMSM, knowledge of the main rotor flux position yields rotor position. However, sensorless techniques based on the injection *hf* test signals seems to be limited to *FOC* schemes.

The classical DTC also lends itself easily to sensorless control through the flux model estimator [10], but as other sensorless control schemes based on conventional fundamental frequency models or observer, fulfill the demand in the higher speed range but have been shown to give poor and asymptotically failing performance as zero speed is approached.

1.2 Objectives and Scope of the Thesis

This thesis deals with the development of a new DTC for PMSM fed by MCs. The advantages of the MC are combined with those of the DTC to drive a PMSM.

The main motivation behind this work is that while a number of schemes replacing the conventional VSI by a MC to drive AC machines have been reported in the literature, the potential of the latest has not been completely exploited to improve the DTC performance. Another significant motivation arises from the fact that, although a huge amount of research publications in the field of sensorless control in the low speed region are still appearing every year, almost all of them are devoted to FOC schemes and no approach for DTC drives have been yet reported in the literature.

The principal objective of this work is to investigate the characteristics of the MC that can be exploited to improve the conventional DTC performance. In addition to the capability of controlling the input power factor, a new technique to reduce the electromagnetic torque and stator flux ripples is investigated in this thesis.
Another objective of this thesis is to investigate a very simple method to reduce the common mode voltage at the output of the MC.
Finally, this work investigates the extension of a high frequency injection technique to DTC drives in order to overcome the limitations of model based sensorless techniques normally employed in DTC sensorless drives.

1.3 Structure of the Thesis

This thesis is organized as follows:

Chapter 2 starts with a brief review of the dynamic equations of both IM and PMSM.
The most relevant control methods are briefly described giving special attention to the DTC scheme.
The remainder of the chapter gives a state of the art review of model based and non-model based sensorless techniques.

Chapter 3 describes the conventional VSI topology and the most relevant modulation techniques.
The MC topology and the related modulation techniques are then examined. The bidirectional switches commutation techniques are reviewed.

Chapter 4 is devoted to describe the conventional DTC fed by a VSI for both IM and PMSM pointing out the advantages and disadvantages of this control method. The conventional DTC driving an IM is firstly analyzed by means of simulation and experimental tests. Due to lack of permanent magnets, the use of an IM allows to study the operation principles of the

conventional DTC without danger of demagnetization. Once the DTC algorithm has been tested driving an IM, the DTC performance is analyzed driving a PMSM.

Chapter 5 describes the DTC using a MC proposed in [2] driving an IM. The same control method is then implemented and analyzed driving a PMSM. The use of small voltage vectors[4] of the MC is investigated in order to reduce the electromagnetic torque and stator flux ripples.

Chapter 6 analyzes the common mode voltage present at the output of the MC. The advantages of having three different null vectors in such converters are exploited developing a very simple algorithm to reduce the common mode voltage in DTC drives.

Chapter 7 starts examining the nature of the saliencies in a SM-PMSM which can be exploited to estimate the rotor or flux position. The $\alpha - \beta$ frame persistent high frequency rotating carrier injection technique and a demodulation scheme are then reviewed. Finally, a new high frequency injection technique, based on the $\alpha - \beta$ frame persistent high frequency rotating carrier injection one, is developed to be employed with DTC drives.

Chapter 8 concludes the thesis describing what has been achieved. Investigation of other injection techniques is also recommended to follow up the work presented in this thesis.

[4]The term *small voltage vectors* refers to vectors of MC with smaller amplitude that those normally used.

Chapter 2

Modelling and Control of AC Machines

2.1 Introduction

This chapter covers the mathematical models required for the control of AC machines. The equivalent two-phase machine and the axes transformation to the stationary ($\alpha - \beta$) and the synchronous (d-q) reference frames are first derived. Both, Induction Machine (IM) and Synchronous Machine (SM) dynamic models are presented. The equivalent circuits of the dynamic models are also reviewed.

The requirements of an electrical drive will depend on its application. To satisfy these requirements, there are several ways to control the drive. The most common control methods v/f, Field Oriented Control (FOC) and Direct Torque Control (DTC) are briefly introduced. The open loop scalar v/f control is suitable for low dynamic requirements. FOC allows precise torque control and fast dynamic performance but at the cost of a speed/position sensor and high computing demand. On the other hand, DTC has become a

good alternative providing similar performance with a simpler scheme.

Since the presence of speed/position sensors increases the cost of the drive and decreases its reliability, there has been considerable interest for the development of sensorless drives. A short review of sensorless control is presented pointing out the problems, at low speed, of methods based on the machine model.

2.2 AC Machine Modelling

In order to understand and design vector controlled drives[1], a dynamic model of the machine under control is mandatory. The dynamic model can be just a good approximation of the real plant. Moreover, the model must incorporate all important effects occurring during both steady-state and transient operation. For simplicity, the machines considered here are analyzed under the following assumptions:

- Symmetrical two-pole, three-phase windings.
- The slotting effects are neglected.
- The permeability of the iron parts is infinite.
- The flux density is radial in the air gap.
- Iron losses are neglected.
- The stator and the rotor windings are simplified as a single, multi-turn full pitch coil situated on the two sides of the air gap.

2.2.1 Induction Machine

Among all types of AC machines, the IM, particularly the cage type, is the most commonly used in industry. These type of machines are economical, rugged and reliable. Low-power machines are available in single phase, but

[1] a brief review of different control methods is given in section 2.3 of the present chapter.

three-phase machines are frequently used in variable speed drives. The fundamental principles of an IM is the creation of a rotating sinusoidal distributed magnetic field in the air gap. It can be shown that, in an idealized machine as the one shown in Fig. 2.1, a balanced sinusoidal three-phase power supply in the three-phase stator windings creates a magnetic field that rotates at the synchronous speed ω_e .

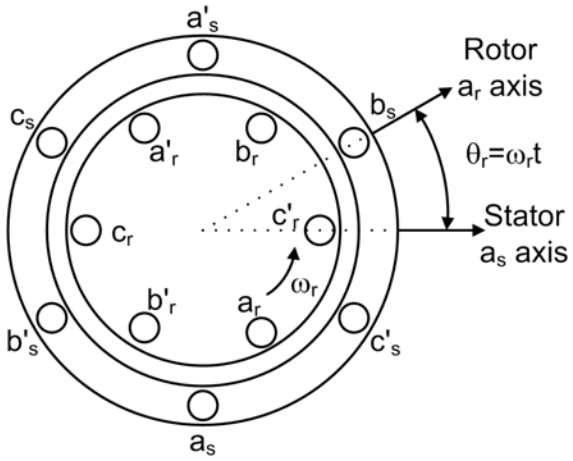

Figure 2.1: Three-phase, two-pole induction machine.

At stand still, the conductors of the rotor will be subjected to a sweeping magnetic field, inducing currents in the short-circuited rotor at the same frequency, yielding in torque production due to the interaction of the air gap flux and the rotor magnetomotive force (mmf). If the rotor rotates at the synchronous speed ω_e , no current can be induced in it, and therefore, no torque is produced. At any other speed ω_r (rotor electrical speed), and due to the difference between speeds ω_e -ω_r , called slip speed ω_s, currents are induced in the rotor and torque is then developed.

Instantaneous voltage equations of an IM

The instantaneous stator voltage equations of an IM in a stationary reference frame fixed to the stator, are written as follows:

$$v_a^s = R_s i_a^s + \frac{d}{dt}\psi_a^s \tag{2.1}$$

$$v_b^s = R_s i_b^s + \frac{d}{dt}\psi_b^s \tag{2.2}$$

$$v_c^s = R_s i_c^s + \frac{d}{dt}\psi_c^s \tag{2.3}$$

where ψ_a^s, ψ_b^s and ψ_c^s are the linkage flux of stator phase a, b and c respectively, i_a^s, i_b^s and i_c^s are the corresponding phase currents and R_s is the stator phase resistor.

In a similar way, the instantaneous rotor voltage equations in a stationary reference frame fixed to the rotor, can be expressed as:

$$v_a^r = R_r i_a^r + \frac{d}{dt}\psi_a^r \tag{2.4}$$

$$v_b^r = R_s i_b^r + \frac{d}{dt}\psi_b^r \tag{2.5}$$

$$v_c^r = R_s i_c^r + \frac{d}{dt}\psi_c^r \tag{2.6}$$

Equivalent two-phase Machine

The dynamic performance of an IM is somewhat complex because the three-phase rotor windings are in motion with respect to the three-phase stator windings. Basically, it can be looked on as a transformer with a moving secondary, where the coupling coefficients between the rotor and stator phases changes continuously as a function of the rotor position θ_r .

The model can be described by differential equations with time-varying mutual inductances, but such a model tends to be very complex. Note that a three-phase machine can be represented by an equivalent two-phase (Clarke transformation) machine as shown in Fig. 2.2 (b), where $\alpha^s - \beta^s$ corresponds to the stator direct and quadrature axes, and $\alpha^r - \beta^r$ corresponds to the rotor

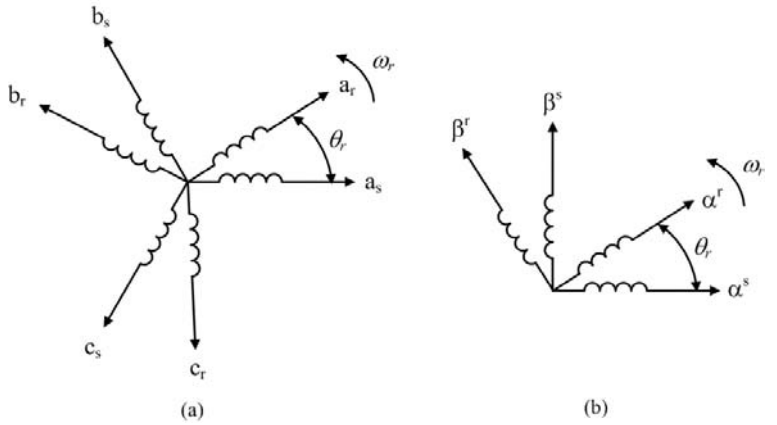

Figure 2.2: Machine transformation. (a) Three-phase machine. (b) Equivalent two-phase machine.

direct and quadrature axes. However, the problem of time-variant parameters still remains. In 1920, R. H. Park proposed a new theory of electric machine in order to solve this problem. He transformed, or referred, the stator variables to a synchronous rotating frame fixed to the rotor. With this transformation (Park's transformation), he showed that all time-varying inductances that occurs due to an electric circuit in relative motion and electric circuits with varying magnetic reluctance can be eliminated [1].

Axes Transformation

The variables of a three-phase machine can be transformed into the fictitious equivalent two-phase values by means of Clarke transformation as shown in (2.7). The inverse transformation can be written as in (2.8).

$$\begin{bmatrix} \alpha \\ \beta \\ 0 \end{bmatrix} = c \cdot \begin{bmatrix} \cos\theta & \cos(\theta - \frac{2\pi}{3}) & \cos(\theta + \frac{2\pi}{3}) \\ -\sin\theta & -\sin(\theta - \frac{2\pi}{3}) & \sin(\theta + \frac{2\pi}{3}) \\ \frac{1}{\sqrt{2}} & \frac{1}{\sqrt{2}} & \frac{1}{\sqrt{2}} \end{bmatrix} \cdot \begin{bmatrix} a \\ b \\ c \end{bmatrix} \tag{2.7}$$

$$\begin{bmatrix} a \\ b \\ c \end{bmatrix} = c \cdot \begin{bmatrix} \cos\theta & -\sin\theta & \frac{1}{\sqrt{2}} \\ \cos(\theta - \frac{2\pi}{3}) & -\sin(\theta - \frac{2\pi}{3}) & \frac{1}{\sqrt{2}} \\ \cos(\theta + \frac{2\pi}{3}) & -\sin(\theta + \frac{2\pi}{3}) & \frac{1}{\sqrt{2}} \end{bmatrix} \cdot \begin{bmatrix} \alpha \\ \beta \\ 0 \end{bmatrix} \tag{2.8}$$

Where "c" is a constant that can take either the values $\frac{2}{3}$, for the so-called non-power invariant form, or $\sqrt{\frac{2}{3}}$ for the power-invariant form. It is convenient to set $\theta = 0$, so that the α-axis is aligned with the a magnetic axis.

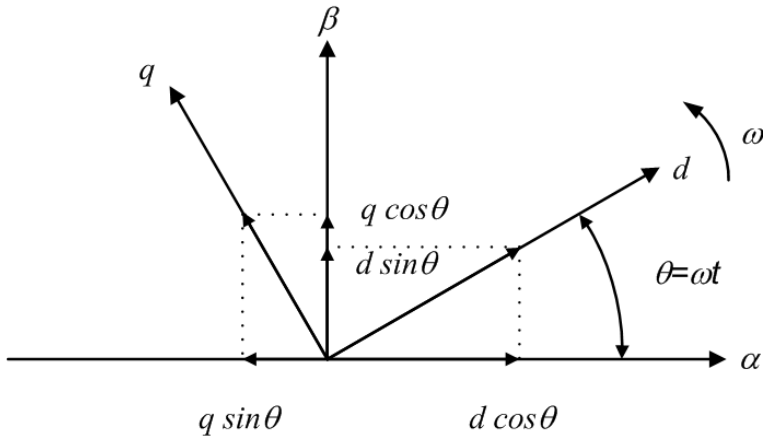

Figure 2.3: Stationary reference frame ($\alpha - \beta$) to synchronous rotating frame (d-q) transformation.

The Park's transformation from the stationary reference frame $\alpha - \beta$ to a d-q frame rotating at a generic speed ω, and its inverse can be derived from Fig. 2.3 and written in the matrix form as,

$$\begin{bmatrix} \alpha \\ \beta \end{bmatrix} = \begin{bmatrix} \cos\theta & -\sin\theta \\ \sin\theta & \cos\theta \end{bmatrix} \cdot \begin{bmatrix} d \\ q \end{bmatrix} \tag{2.9}$$

$$\begin{bmatrix} d \\ q \end{bmatrix} = \begin{bmatrix} \cos\theta & \sin\theta \\ -\sin\theta & \cos\theta \end{bmatrix} \cdot \begin{bmatrix} \alpha \\ \beta \end{bmatrix} \tag{2.10}$$

Dynamic Model in the Stationary Reference Frame

The dynamic model in the stationary reference $\alpha - \beta$ frame can be easily derived by applying the axes transformation described in (2.7) to the voltage equations (2.1), (2.2) and (2.3) for the stator and (2.4), (2.5) and (2.6) for the rotor respectively. The machine voltage equations in the stationary reference $\alpha - \beta$ frame are given as:

$$v_\alpha^s = R_s i_\alpha^s + \frac{d}{dt}\psi_\alpha^s \tag{2.11}$$

$$v_\beta^s = R_s i_\beta^s + \frac{d}{dt}\psi_\beta^s \tag{2.12}$$

$$v_\alpha^r = R_r i_\alpha^r + \frac{d}{dt}\psi_\alpha^r - \omega_r \psi_\beta^r \tag{2.24}$$

$$v_\beta^r = R_r i_\beta^r + \frac{d}{dt}\psi_\beta^r + \omega_r \psi_\alpha^r \tag{2.25}$$

where $v_\alpha^r = v_\beta^r = 0$.

The corresponding equivalent circuits in the stationary $\alpha - \beta$ frame are represented in Fig. 2.4. Note that, in steady state, the variables appear as sine waves with sinusoidal inputs.

From Fig. 2.4, the flux linkage expressions can be derived as follows:

$$\psi_\alpha^s = L_l^s i_\alpha^s + L_m(i_\alpha^s + i_\alpha^r) \tag{2.26}$$

$$\psi_\alpha^r = L_l^r i_\alpha^r + L_m(i_\alpha^s + i_\alpha^r) \tag{2.27}$$

$$\psi_\alpha^m = L_m(i_\alpha^s + i_\alpha^r) \tag{2.28}$$

$$\psi_\beta^s = L_l^s i_\beta^s + L_m(i_\beta^s + i_\beta^r) \tag{2.29}$$

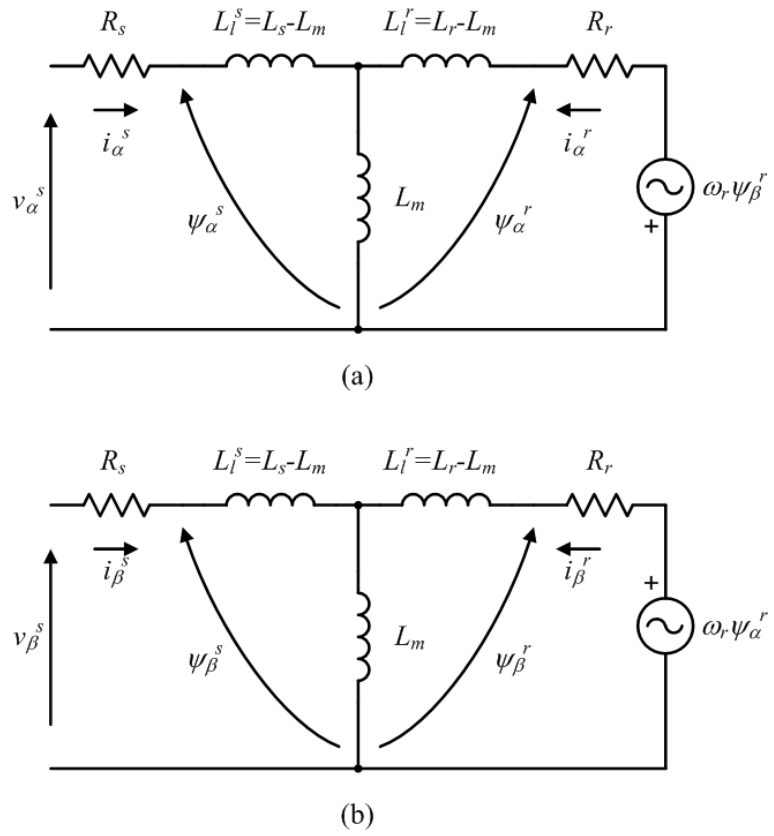

Figure 2.4: Dynamic $\alpha - \beta$ model equivalent circuit of an induction machine. (a) α-axis circuit. (b) β-axis circuit.

$$\psi_\beta^r = L_l^r i_\beta^r + L_m(i_\beta^s + i_\beta^r) \tag{2.30}$$

$$\psi_\beta^m = L_m(i_\beta^s + i_\beta^r) \tag{2.31}$$

where L_m is the magnetizing inductance and, L_l^s and L_l^r are the stator and rotor leakage inductances respectively.

Combining the above expressions with the stator and rotor voltage equations (2.1) through (2.6), the following matrix equation can be derived:

$$\begin{bmatrix} v_\alpha^s \\ v_\beta^s \\ v_\alpha^r \\ v_\beta^r \end{bmatrix} = \begin{bmatrix} R_s + sL_s & 0 & sL_m & 0 \\ 0 & R_s + sL_s & 0 & sL_m \\ sL_m & -\omega_r L_m & R_r + sL_r & -\omega_r L_r \\ \omega_r L_m & sL_m & \omega_r L_r & R_r + sL_r \end{bmatrix} \cdot \begin{bmatrix} i_\alpha^s \\ i_\beta^s \\ i_\alpha^r \\ i_\beta^r \end{bmatrix} \tag{2.32}$$

where s is the Laplace operator.

Dynamic Model in the Synchronous Rotating Frame

For the two-phase machine shown in Fig. 2.2(b), we need to represent both $\alpha^r - \beta^r$ and $\alpha^s - \beta^s$ circuits and their variables in the synchronous rotating frame *d-q* . The $\alpha - \beta$ components of the stator voltage, given in (2.11) and (2.12), can be transformed to the synchronous rotating *d-q* frame applying (2.10). The stator voltage equations in the *d-q* frame can be written as:

$$v_d^s = R_s i_d^s + \frac{d}{dt}\psi_d^s - \omega_e \psi_q^s \tag{2.33}$$

$$v_q^s = R_s i_q^s + \frac{d}{dt}\psi_q^s + \omega_e \psi_d^s \tag{2.34}$$

The last term in (2.33) and (2.34) is defined as the back Electro-Magnetic Force *emf* which depends on the speed ω_e due to the rotation of the axes, thus when $\omega_e = 0$, the equations revert to stationary form. At stand still, that is, $\omega_r = 0$, the rotor equations will be very similar to the stator equations (2.33) and (2.34):

$$v_d^r = R_r i_d^r + \frac{d}{dt}\psi_d^r - \omega_e \psi_q^r \tag{2.35}$$

$$v_q^r = R_r i_q^r + \frac{d}{dt}\psi_q^r + \omega_e \psi_d^r \tag{2.36}$$

where all the variables and parameters are referred to the stator. Since the rotor is moving at ω_r , the axes fixed to the rotor are rotating at a speed

$\omega_s = \omega_e - \omega_r$ relative to the synchronous rotating d-q frame. Therefore, in d-q frame, the rotor equations should be modified as

$$v_d^r = R_r i_d^r + \frac{d}{dt}\psi_d^r - (\omega_e - \omega_r)\psi_q^r \tag{2.37}$$

$$v_q^r = R_r i_q^r + \frac{d}{dt}\psi_q^r + (\omega_e - \omega_r)\psi_d^r \tag{2.38}$$

The dynamic d-q model equivalent circuits that satisfy equations (2.33) through (2.38) are presented in Fig. 2.5. Note that for a singly-fed machine, such as a cage-type motor, $v_d^r = v_q^r = 0$. The advantage of the dynamic d-q model is that all sinusoidal variables in the stationary $\alpha - \beta$ frame appear as constant quantities in the synchronous rotating d-q frame.

From Fig. 2.5, the flux-linkage expressions can be derived as follows:

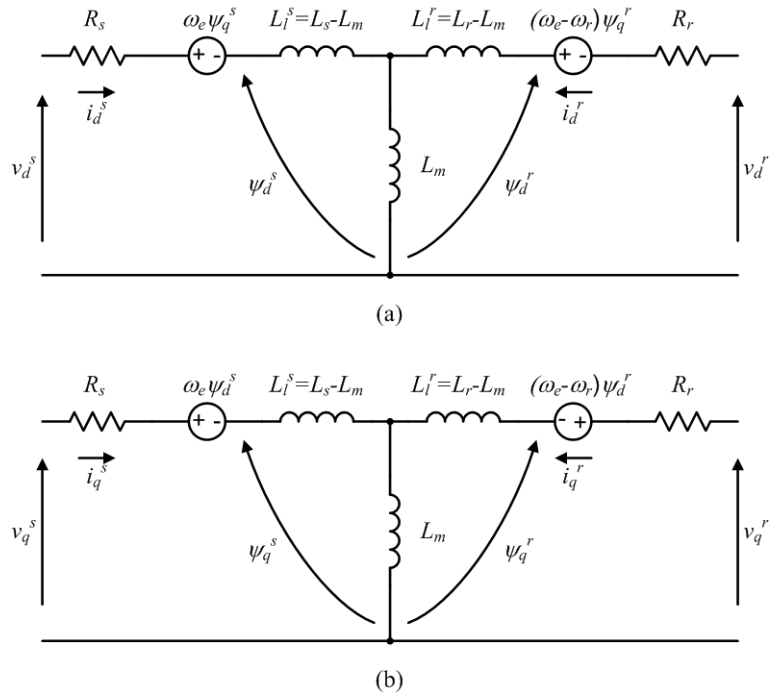

Figure 2.5: Dynamic d-q model equivalent circuit of an induction machine. (a) d-axis circuit. (b) q-axis circuit.

$$\psi_d^s = L_l^s i_d^s + L_m(i_d^s + i_d^r) \tag{2.39}$$

$$\psi_d^r = L_l^r i_d^r + L_m(i_d^s + i_d^r) \tag{2.40}$$

$$\psi_d^m = L_m(i_d^s + i_d^r) \tag{2.41}$$

$$\psi_q^s = L_l^s i_q^s + L_m(i_q^s + i_q^r) \tag{2.42}$$

$$\psi_q^r = L_l^r i_q^r + L_m(i_q^s + i_q^r) \tag{2.43}$$

$$\psi_q^m = L_m(i_q^s + i_q^r) \tag{2.44}$$

where L_m is the magnetizing inductance and, L_l^s and L_l^r are the stator and rotor leakage inductances respectively.

The above equations can be combined with the stator and rotor equations, (2.33), (2.34), (2.35) and (2.36), to obtain the following matrix equation:

$$\begin{bmatrix} v_d^s \\ v_q^s \\ v_d^r \\ v_q^r \end{bmatrix} = \begin{bmatrix} R_s + sL_s & -\omega_e L_s & -\omega_e s L_m & L_m \\ \omega_e L_s & R_s + sL_s & \omega_e L_m & sL_m \\ sL_m & -\omega_s L_m & R_r + sL_r & -\omega_s L_r \\ \omega_s L_m & sL_m & \omega_s L_r & R_r + sL_r \end{bmatrix} \cdot \begin{bmatrix} i_d^s \\ i_q^s \\ i_d^r \\ i_q^r \end{bmatrix} \tag{2.45}$$

where $\omega_s = \omega_e - \omega_r$ is the slip speed, s is the Laplace operator, $L_s = L_l^s + L_m$ and $L_r = L_l^r + L_m$ are the stator and rotor inductances respectively. Generally, the speed ω_r in (2.45) cannot be treated as a constant. Instead it can be related to the torque as

$$T_e = T_L + J\frac{d}{dt}\omega_m \tag{2.46}$$

where T_L is the load torque, J is the rotor inertia, and the rotor mechanical speed is $\omega_m = \omega_r/p$, p being the number of pole pairs of the machine.

A general form for the electromagnetic torque expression is

$$T_e = \frac{2}{3} p \vec{\psi}^s \times \vec{i}^s \tag{2.47}$$

or

$$T_e = \frac{2}{3} p \vec{\psi}^m \times \vec{i}^r \tag{2.48}$$

which resolving into the *d-q* frame components can be expressed as

$$T_e = \frac{2}{3} p (\psi_d^m i_q^r - \psi_q^m i_d^r) \tag{2.49}$$

and substituting (2.41) and (2.44) in (2.49) gives

$$\begin{aligned} T_e &= \frac{2}{3} p L_m (i_d^s i_q^r - i_q^s i_d^r) = \\ &= \frac{2}{3} p (\psi_d^r i_q^r - \psi_q^r i_d^r) \end{aligned} \tag{2.50}$$

2.2.2 Synchronous Machine

Synchronous machines drives are close competitors to IM drives in many industrial applications where variable speed is required. Generally, they are more expensive than induction machines drives, but the higher efficiency is an important advantage. Furthermore, synchronous machines show better dynamic performance in comparison to the IM. As the name indicates, a synchronous machine rotates at the synchronous speed. The stator windings are identical to that of the IM, but the rotor has a winding carrying DC current that produces the air gap flux in high power machines. For medium and low power machines the air gap flux can be created by permanent magnets. This air gap flux helps the stator rotating magnetic field to drag the rotor

along with it producing torque. In high power wound field machines, the rotor usually contains a damper winding which is similar to the short-circuited squirrel-cage bars in an IM. The cross-section of a three-phase two-pole synchronous machine is shown in Fig. 2.6.

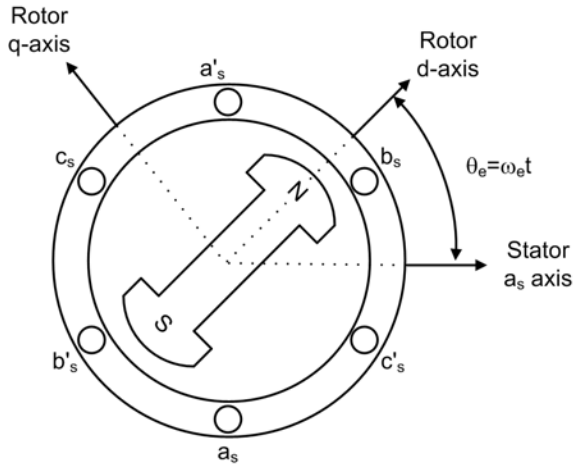

Figure 2.6: Three-phase two-pole synchronous machine.

Permanent Magnet Synchronous Machine

In a PMSM, the rotor DC field winding is replaced by permanent magnets eliminating copper losses in the rotor. Thus, conduction losses are concentrated in the stator where they can be easily dissipated. This allows the design of machines with smaller rotor diameters, resulting in smaller machine sizes, with high power density and very low rotor inertia [10].

The selection of the permanent magnets with proper materials is very important in the design of a PMSM [1]. Figure 2.7 shows the demagnetization quadrant of the $B - H$ curve in which the permanent magnet is designed to operate. Initially, if the magnet is short-circuited (no air gap), the maximum flux density B_r will be available. Once the magnet is installed in the machine, the air gap will have some demagnetization effect and the corresponding operating point at no-load will be moved to B'. A smaller slope

of the no-load line will be obtained with higher air gap. Current flowing in the stator winding will introduce further demagnetization effect, which will further reduce the air gap flux density. Once the operating point reaches D (worst-case demagnetization), which can be due to a starting, transient, or machine fault condition, and the demagnetization effect is removed, the magnet will recover along the recoil line [1]. It should be noted that the recoil line has approximately the same slope as the original $H - B$ curve near $H = 0$. The stable operating point in subsequent operation will be determined by the intersection of the load line and the recoil line. Therefore, the magnet will be permanently demagnetized under no load operation, corresponding to the vertical distance between B_r and A'. The worst-case demagnetization point is vitally important and should be always under control. However, if the material of the permanent magnet have a strait line demagnetization characteristic, the recoil line will coincide with the demagnetization line irrespective of the worse demagnetization point (i.e., permanent magnet demagnetization can be negligible) [1].

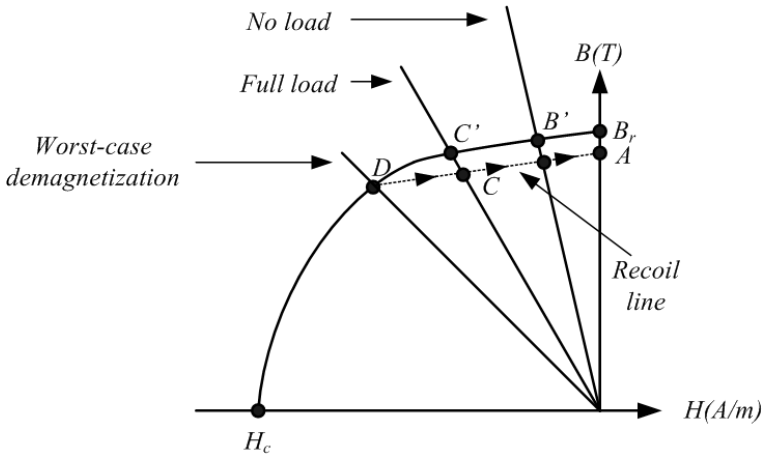

Figure 2.7: Permanent magnet operating points.

If the material of the permanent magnet is selected to have a straight-line demagnetization curve in the operating quadrant, the recoil line will coincide with that of the demagnetization. Thus, the permanent demagnetization

will be negligible. The most common magnetic materials are Alnico (Al, Ni, Co), Ferrite, and rare-earth materials such as samarium-cobalt (SmCo) and neodymium-iron-boron (NdFeB) [15]. Despite the lower service temperature NdFeB magnets are finding their way into an increasing number of applications. The characteristics of these materials are presented in Fig. 2.8.

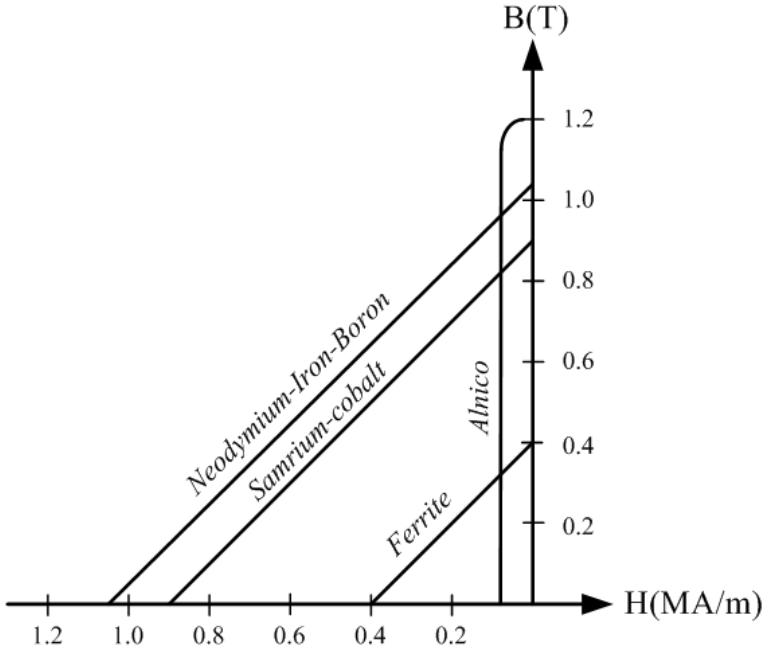

Figure 2.8: Permanent magnets characteristics.

There are two types of PMSM regarding the construction of the rotor: the SM-PMSM and the Interior Permanent Magnet Machine (I-PMSM). A cross-section of both machines is shown in Fig. 2.9.

SM-PMSMs are widely used and have a very simple rotor design consisting of a cylindrical iron core with magnets glued on its surface with epoxy adhesive. Since the rare earth magnets permeability is close to that of the air, the SM-PMSM presents a constant effective air gap ($L_{dm} = L_{qm}$) resulting in a geometrically non-salient pole machine. Unlike the SM-PMSM, in the I-PMSM, the magnets are mounted inside the rotor generating radial flux

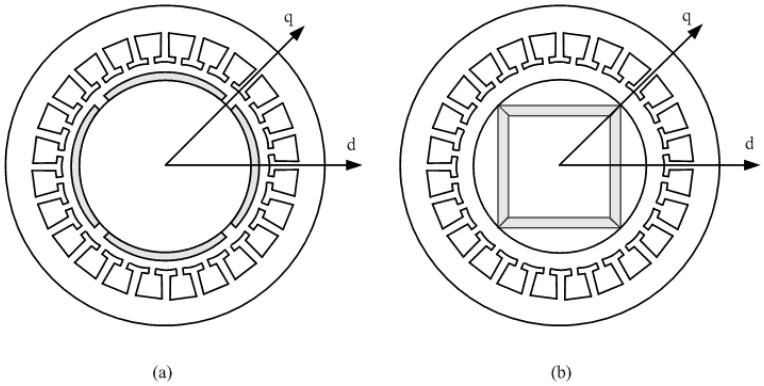

Figure 2.9: Cross section of permanent magnet machines. (a) SM-PMSM. (b) I-PMSM

in the air gap. The flux in the direction of the magnets (d-axis flux) goes through the magnets across a high reluctance path. However, the quadrature flux (q-axis flux) is closed through the steel poles across a low reluctance path. Therefore, the I-PMSM is a salient pole machine (i.e. $L_{qm} > L_{dm}$).

Dynamic Model in the Stationary Reference frame

The stator voltage equations for a PMSM are the same as those for an IM (2.1), (2.2) and (2.3) and are repeated here in its matrix form:

$$\begin{bmatrix} v_a^s \\ v_b^s \\ v_c^s \end{bmatrix} = R_s \cdot \begin{bmatrix} i_a^s \\ i_b^s \\ i_c^s \end{bmatrix} + \frac{d}{dt} \begin{bmatrix} \psi_a^s \\ \psi_b^s \\ \psi_c^s \end{bmatrix} \tag{2.51}$$

The total per phase flux-linkage in (2.51) are given by

$$\begin{bmatrix} \psi_a^s \\ \psi_b^s \\ \psi_c^s \end{bmatrix} = \begin{bmatrix} L_a & M_{ab} & M_{ac} \\ M_{ba} & L_b & M_{bc} \\ M_{ca} & M_{cb} & L_c \end{bmatrix} \cdot \begin{bmatrix} i_a^s \\ i_b^s \\ i_c^s \end{bmatrix} + \psi_{PM} \begin{bmatrix} \cos\theta_r \\ \cos\left(\theta_r - \frac{2\pi}{3}\right) \\ \cos\left(\theta_r - \frac{4\pi}{3}\right) \end{bmatrix} \tag{2.52}$$

where ψ_{PM} is the magnitude of the permanent magnet flux in each phase when it is aligned with the corresponding magnetic axis, and the reciprocal

mutual inductances are equal i.e. $M_{ab} = M_{ba}$, $M_{bc} = M_{cb}$, and $M_{ca} = M_{ac}$. As mentioned before, in a I-PMSM, the effective air gap length is larger in the direction of the permanent magnet (d-axis) than in quadrature direction (q-axis) which produces stator phase inductance variations as function of the rotor position. This in known as saliency. Considering only the fundamental inductances variation (fundamental saliency),[2] the stator phase inductance can be written as:

$$\begin{bmatrix} L_a \\ L_b \\ L_c \end{bmatrix} = L_l + L_m - \begin{bmatrix} \Delta L_m \cos 2\theta_r \\ \Delta L_m \cos\left(2\theta_r - \frac{4\pi}{3}\right) \\ \Delta L_m \cos\left(2\theta_r - \frac{2\pi}{3}\right) \end{bmatrix} \tag{2.53}$$

and the mutual inductances are given by

$$\begin{bmatrix} M_{ab} \\ M_{bc} \\ M_{ca} \end{bmatrix} = -\frac{L_m}{2} - \begin{bmatrix} \Delta L_m \cos\left(2\theta_r - \frac{2\pi}{3}\right) \\ \Delta L_m \cos 2\theta_r \\ \Delta L_m \cos\left(2\theta_r - \frac{4\pi}{3}\right) \end{bmatrix} \tag{2.54}$$

Applying the axes transformation given in (2.7) to the PMSM basic equations (2.51) and (2.52), and substituting the inductance values given in (2.53) and (2.54), the dynamic model in the stationary $\alpha - \beta$ reference frame can be written as:

$$\begin{bmatrix} v_\alpha^s \\ v_\beta^s \end{bmatrix} = R_s \cdot \begin{bmatrix} i_\alpha^s \\ i_\beta^s \end{bmatrix} + \frac{d}{dt} \begin{bmatrix} L_s - \Delta L_s \cos 2\theta_r & \Delta L_s \sin 2\theta_r \\ \Delta L_s \sin 2\theta_r & L_s + \Delta L_s \cos 2\theta_r \end{bmatrix} \cdot \begin{bmatrix} i_\alpha^s \\ i_\beta^s \end{bmatrix} + \psi_{PM} \frac{d}{dt} \begin{bmatrix} \cos\theta_r \\ \cos\left(\theta_r - \frac{\pi}{2}\right) \end{bmatrix} \tag{2.55}$$

where $L_s = L_l + \frac{3}{2} L_m$ and $\Delta L_s = \frac{3}{2} \Delta L_m$. For a SM-PMSM, since there is no saliency, there will be no inductance variation, hence $\Delta L_m = 0$.

Dynamic Model in the Synchronous Rotating frame

The PMSM model in the d-q frame can be derived following the same procedure as for an IM. Applying the axes transformation (2.10) to the $\alpha - \beta$ frame voltage equations given in (2.55) yields:

[2] It is assumed that the variation of the air gap does not affect the leakage inductance[15].

$$v_d^s = R_s i_d^s - \omega_r \psi_q^s + \frac{d}{dt}\psi_d^{'s} \tag{2.56}$$

$$v_q^s = R_s i_q^s + \omega_r \psi_d^{'s} + \omega_r \psi_{PM} + \frac{d}{dt}\psi_q^s \tag{2.57}$$

where ψ_{PM} is the permanent magnet flux and

$$\psi_d^{'s} = i_d^s(L_{ls} + L_{dm}) = i_d^s L_{ds} \tag{2.58}$$

$$\psi_d^s = \psi_{PM} + \psi_d^{'s} = \psi_{PM} + i_d^s L_{ds} \tag{2.59}$$

$$\psi_q^s = i_q^s(L_{ls} + L_{qm}) = i_q^s L_{qs} \tag{2.60}$$

The equivalent circuits in the *d-q* frame are shown in Fig. 2.10.

Substituting (2.58), (2.59) and (2.60) in (2.56) and (2.57) gives:

$$v_d^s = R_s i_d^s - \omega_r L_q^s i_q^s + L_d^s \frac{d}{dt} i_d^s \tag{2.61}$$

and

$$v_q^s = R_s i_q^s + \omega_r L_d^s + \omega_r \psi_{PM} + L_q^s \frac{d}{dt} i_q^s \tag{2.62}$$

The developed torque is given by:

$$T_e = \frac{3}{2} p[\psi_{PM} i_q^s + (L_d^s - L_q^s) i_d^s i_q^s] \tag{2.63}$$

The second term in (2.63) is called the reluctance torque and it appears due to the saliency of the machine. The theory presented above can be applied to a non-salient PMSM by considering $L_d^s = L_q^s$. The reluctance term in the torque equation disappears for a non-salient machine.

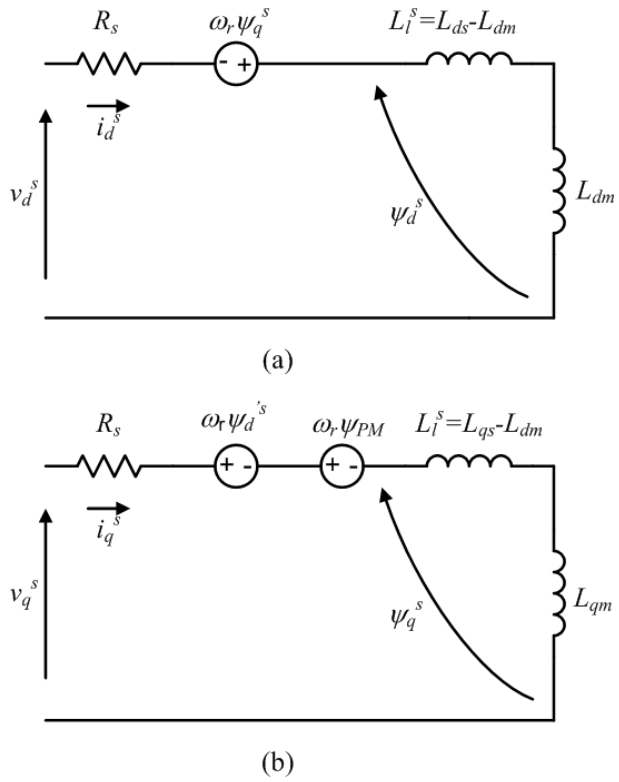

Figure 2.10: Dynamic d-q model equivalent circuit of a PMSM. (a) d-axis circuit. (b) q-axis circuit.

2.3 Control Methods of AC Machines

Depending on whether the controller has the ability to control, not only the magnitude, but also the position of the voltage, current, and flux space vectors the control methods for ac machines can be divided into scalar and vector control [14]. A possible classification of variable frequency control methods is presented in Fig. 2.11.

2.3.1 Scalar Control

In many industrial applications, specially in those where no fast speed changes are required, the dynamics requirement of the drive control is not of much importance. For these cases, the most common method of controlling an AC

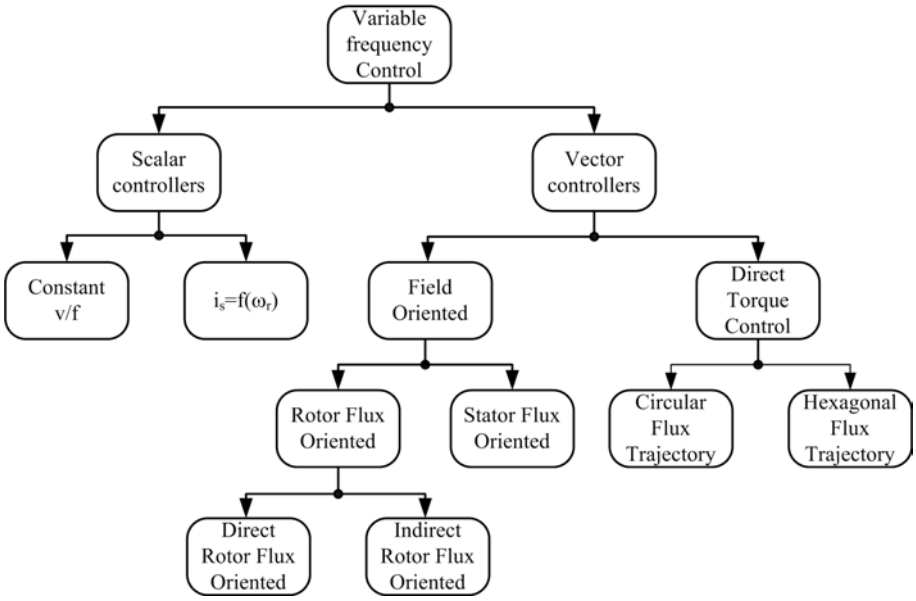

Figure 2.11: Classification of AC machines control methods

machine is the open loop v/f control. It is based on the steady state model of the machine and, as mentioned before, it controls only the amplitude of the voltage vector.

Representing (2.33) and (2.34) in its vector form we obtain

$$\vec{v}^s_{dq} = R_s \vec{i}^s_{dq} + \frac{d}{dt}\vec{\psi}^s_{dq} + j\omega_e \vec{\psi}^s_{dq} \tag{2.64}$$

Under steady state conditions and neglecting the stator resistive voltage drop, (2.64) simplifies to:

$$\vec{v}^s_{dq} = j\omega_e \vec{\psi}^s_{dq} \tag{2.65}$$

In order to maintain the stator flux at its nominal value the ratio v/f is kept constant, hence the name v/f control. A typical scheme for v/f control is shown in Fig. 2.12.

To justify the assumption of steady state conditions, the slope of the stator frequency command signal is limited reducing its bandwidth. Since

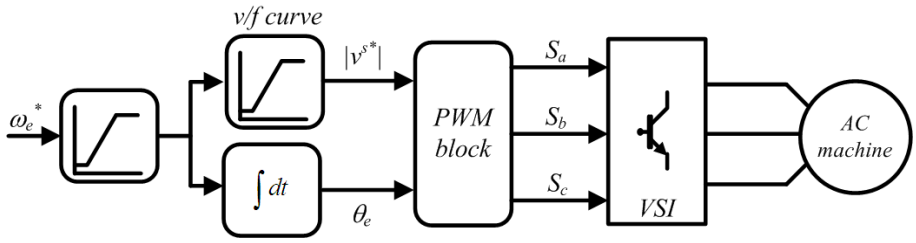

Figure 2.12: v/f scalar control. Block diagram.

the resistive voltage drop has been neglected, a preset minimum value of the stator voltage (known as *boost voltage*) is used, at low stator frequency, to compensate for the resistive voltage drop. Despite the reduced dynamic performance, v/f ensures robustness and is suitable for a wide range of low-cost drives. Typical applications are pumps and fan drives [1].

2.3.2 Field Oriented Control

Field Oriented Control (FOC) is based on the decomposition of the stator currents into a flux-producing current and torque-producing current. It allows, then, a separate control of torque and flux with a similar control structure of that of a separately excited DC machine. There are different flux linkage vectors to which the orientation can be done, however, the orientation with the rotor flux linkage is the most popular [10]. In a synchronous rotating frame the time-varying currents appear as constant values at steady state. Zero steady state error can then be achieved.

Field Oriented Control of Induction Machines

In a cage-type induction motor, the rotor equations given in (2.37) and (2.38) can be rewritten as:

$$0 = R_r i_d^r + \frac{d}{dt}\psi_d^r - (\omega_e - \omega_r)\psi_q^r \tag{2.66}$$

$$0 = R_r i_q^r + \frac{d}{dt}\psi_q^r + (\omega_e - \omega_r)\psi_d^r \tag{2.67}$$

Taking into account that $L_r = L_{lr} + L_m$, the rotor flux equations (2.40) and (2.43) can be expressed as follows:

$$\psi_d^r = L_r i_d^r + L_m i_d^s \tag{2.68}$$

$$\psi_q^r = L_r i_q^r + L_m i_q^s \tag{2.69}$$

and resolving for i_d^r and i_q^r we get

$$i_d^r = \frac{1}{L_r}\psi_d^r - \frac{L_m}{L_r} i_d^s \tag{2.70}$$

$$i_d^r = \frac{1}{L_r}\psi_d^r - \frac{L_m}{L_r} i_d^s \tag{2.71}$$

Since the rotor currents are not accessible, they can be eliminated from (2.66) and (2.67) by substituting (2.70) and (2.71).

$$0 = \frac{R_r}{L_r}\psi_d^r + \frac{d}{dt}\psi_d^r - \frac{L_m}{L_r} R_r i_d^s - (\omega_e - \omega_r)\psi_q^r \tag{2.72}$$

$$0 = \frac{R_r}{L_r}\psi_q^r + \frac{d}{dt}\psi_q^r - \frac{L_m}{L_r} R_r i_q^s + (\omega_e - \omega_r)\psi_d^r \tag{2.73}$$

If the synchronous d-q frame is rotor flux orientated, then $\psi_q^r \triangleq 0$. Furthermore, if the rotor flux ψ^r is constant, which is usually the case, it can be written as:

$$\psi^r = L_m i_d^s \tag{2.74}$$

Under rotor flux orientation, the torque expression given in (2.50) simplifies to:

$$T_e = \frac{3}{2} p \frac{L_m}{L_r} \psi^r i_q^s \tag{2.75}$$

Equations (2.74) and (2.75) show that the flux and torque of an IM can be independently controlled through the stator currents components i_d^s and i_q^s respectively. From (2.7) and (2.8), given in section 2.2.1, it should be noted that the rotor flux position γ_r is needed for the axes transformation. This

angle can be measured but requires further sensors i.e. search coils inserted into the machine. However, computing the slip frequency as:

$$\omega_s = \frac{L_m}{\tau_r \psi^r} i_q^s \tag{2.76}$$

where τ_r is the rotor time constant defined by $\tau_r = L_r/R_r$, rotor flux orientation can be established. This approach is more commonly used and is known as Indirect Rotor Flux Orientation (IRFO). The block diagram for IRFO is shown in Fig. 2.13.

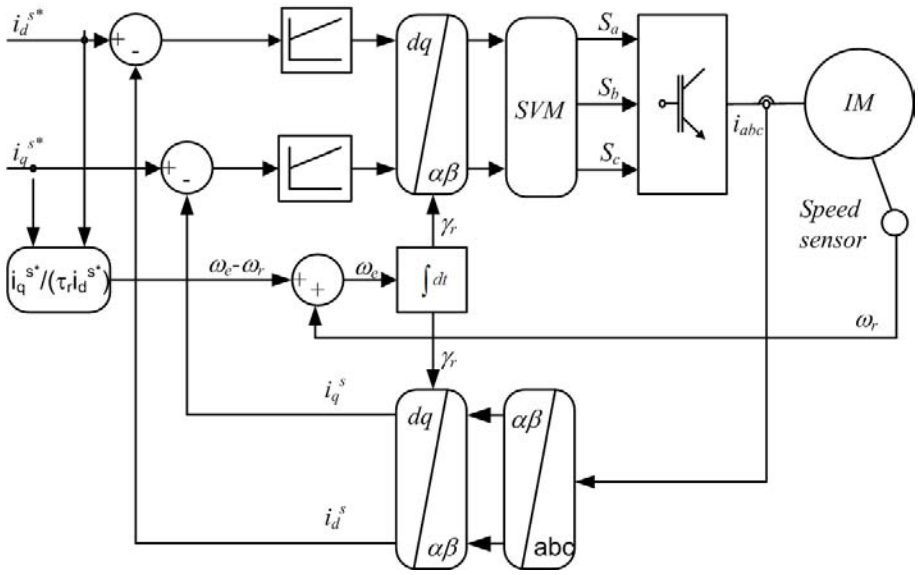

Figure 2.13: Indirect Rotor Flux Orientation (IRFO). Block diagram.

Field Oriented Control of Surface Mounted PMSM

The vector control for PMSM with surface mounted magnets is somewhat simpler. As it was mentioned in section 2.2.2, the SM-PMSM is a non-salient pole machine with large effective air gap, thus the synchronous inductance L_s and consequently the corresponding armature flux are very small i.e. $\psi^s = \psi_m = \psi_{PM}$ [10]. For maximum torque per ampere (i.e. maximum efficiency)

the direct stator current can be set to zero, $i_d^s = 0$. This implies the stator current modulus to be $i^s = i_q^s$. The torque expression for the developed torque can be derived from (2.63), giving:

$$T_e = \frac{3}{2} p \psi_{PM} i_q^s \tag{2.77}$$

Figure 2.14 shows the block diagram for FOC of a PMSM.

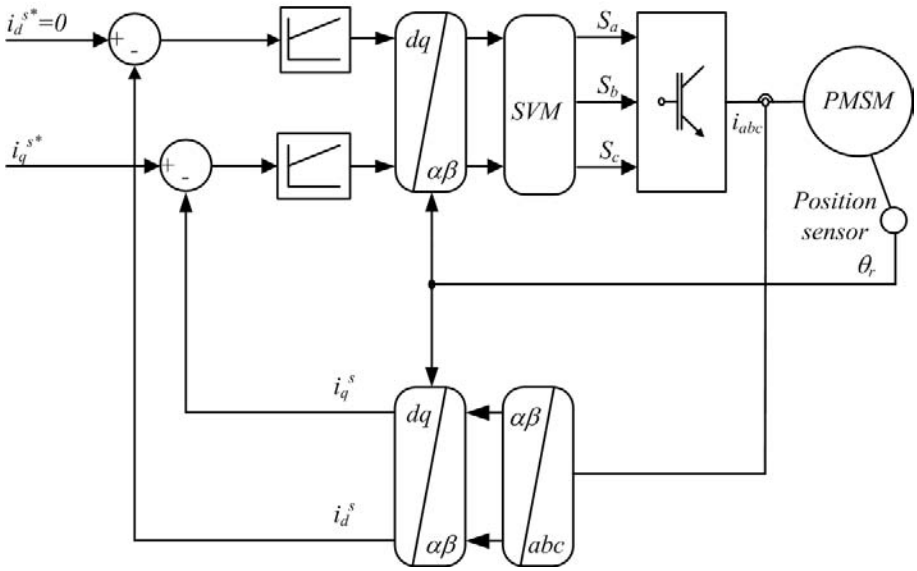

Figure 2.14: Indirect Rotor Flux Orientation (IRFO). Block diagram.

Vector control for PMSM is very similar to that of the IM except for the following:

- The slip frequency $\omega_s = 0$ because the PMSM runs at the synchronous speed.
- The magnetizing current $i_d^s = 0$ because the rotor flux is supplied by the permanent magnets.
- Unlike the slipping pole of an IM, in a PMSM the poles are fixed to the rotor, thus the rotor flux angle is directly generated from a position sensor.

2.3.3 Direct Torque Control

In the mid 1980's, a new advanced control technique, known as Direct Torque Control (DTC) [7] or Direct Self-Control (DSC) [16], was introduced for voltage-fed PWM inverter drives. Since then, DTC has gained popularity and nowadays is becoming one of the most popular control methods for AC machines and has been shown to be a worthy alternative to other vector control drives.

The basic principle of DTC is to directly select stator voltage vectors by means of a hysteresis stator flux and torque control loops [10].

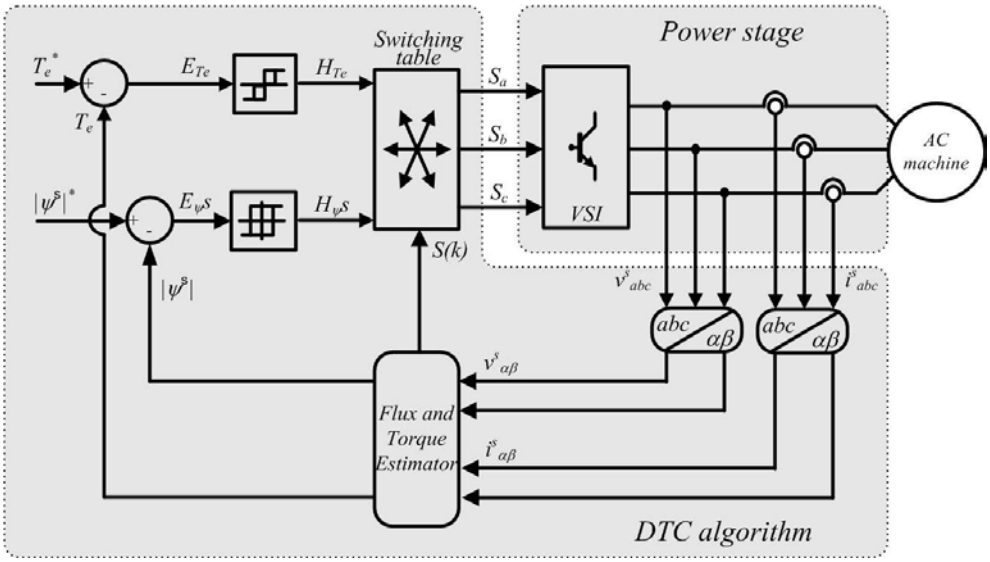

Figure 2.15: Direct Torque Control. Block diagram.

As it is shown in Fig. 2.15, stator flux $|\psi^{s^*}|$ and torque T_e^* references are compared with the corresponding estimated values. Both stator flux and torque errors, E_ψ and E_{T_e}, are processed by means of hysteresis band comparators. In particular, stator flux is controlled by a two-level hysteresis comparator, whereas the torque is controlled by a three-level comparator. On the basis of the hysteresis comparators and stator flux sector $S(k)$, a proper

VSI voltage vector is selected by means of the look-up table[3].

The fundamentals of DTC are the same irrespective of the type of machine under control (IM or PSMS). However, the stator flux and electromagnetic torque estimators will depend on the particular machine to be controlled. Usually, stator flux estimators based on the machine model are employed. From these estimators, the stator flux angle can be easily derived and determine the sector $S(k)$ in which is lying. Since the model based flux estimators employ only terminal quantities as voltage and currents, it can be said that DTC is, intrinsically, a sensorless drive. However, as other sensorless control schemes based on conventional fundamental-frequency models or observer based methods, fulfill the demand in the higher speed range but have been shown to give poor and asymptotically failing performance as zero speed is approached due to the loss of information[4].

2.3.4 Sensorless Control of AC Machines

Performing the control tasks of an AC drive without a speed/position sensor is usually referred to as sensorless control. The term sensorless is normally referred to the lack of a speed/position sensor rather than the complete lack of sensors since, at least, current transducers are needed for any vector controlled drive. Since the lack of a speed/position sensor reduces the total drive cost (specially significant in small drives), facilitates the installation because of cabling reduction, and eliminates the housing of the sensor at the end of the machine shaft yielding to a reduction of the drive volume, sensorless control drives interest is growing up in the recent years. Despite several methods have been proposed in the literature, the basic idea behind all these methods is the estimate of flux or rotor position from the terminal quantities of the machine. According to the position estimate technique employed, sensorless control can be classified as Model-Based and Non-Model-Based.

[3]A deep review of direct torque control is given in chapter 4.

[4]Model based sensorless control is briefly discussed in next section.

Model based Sensorless Control

When the estimate of flux or rotor position is derived from a model, the method is referred to as Model-Based sensorless control. A comparative analysis of three different observers is carried out in [17].

The simplest Model-Based method, voltage model, consist in estimating the stator flux $\hat{\psi}^s$ in the $\alpha - \beta$ stationary reference frame by integrating the stator voltage corrected by the resistance drop.

$$\hat{\psi}^s_{\alpha\beta} = \int (v^s_{\alpha\beta} - R_s i^s_{\alpha\beta}) dt \tag{2.78}$$

From the $\alpha - \beta$ components in (2.78), the stator flux angle can be derived as follows:

$$\hat{\gamma}_s = \tan^{-1} \frac{\hat{\psi}^s_\beta}{\hat{\psi}^s_\alpha} \tag{2.79}$$

It is important to note that the performance of a PMSM drive using equation (2.79) is highly dependent on the accuracy of the stator flux-linkage estimator which also depends on the accuracy of the voltage and current measurements and the integration technique. Moreover, estimators based on the voltage model are very sensitive to variations of the stator resistance R_s, which varies as a function of the winding temperature. At low speed, the stator voltage drop becomes dominant, degrading the flux estimator performance. Several algorithms, including artificial neural networks [18] has been proposed in order to estimate R_s.

In the voltage model, also state observer [19], [20], [21] or Kalman filters [22], [23], [24] have been used in order to reduce the parameter variation effect. However, the common problem of the above-mentioned methods is that the performance of the rotor position estimate is critically dependent on the magnitude of the back-*emf* voltage which is proportional to the rotor

speed. In the low-speed region, where the magnitude of back-*emf* voltage is very small, the performance is significantly degraded.

Non-Model based Sensorless Control

As discussed in the previous section, Model-Based sensorless methods fails at low and zero speeds due to the lack of back-*emf*. Consequently, alternative methods which do not rely upon the fundamental quantities are gaining attention. The derivation of the machine model for fundamental operation is done under several assumptions. The model, then, represents the ideal machine. The Non-Model-Based sensorless schemes exploit the non-ideal machine characteristics to obtain flux or rotor position information. Tracking the variations of the impedance with rotor position (saliency) has been proposed as a mechanism for rotor position detection of salient AC machines as the interior permanent magnet machine [25], [26], [27], [28] and synchronous reluctance machines [29], [30].

Saliency position detection is carried out by means of a test high frequency (*hf*) signal injection into the machine. According to the type of the injected signal, these techniques can be classified as persistent *hf* voltage injection [28], [31], [32], [33] or *hf* current injection [34], and discrete voltage test pulses injection [27], [35], [36], [37]. Different PMSM structures and sensorless techniques are compared in [38].

2.4 Conclusions

Induction machine and permanent magnet synchronous machine mathematical models have been presented.

Different control methods for AC machines drives have been briefly reviewed. The most popular scalar control, v/f, is suitable for many industrial applications where the dynamic performance is not of much importance. FOC allows for separate control of flux and torque yielding in a very high performance drive but at the cost of a complicated structure and a position sensor.

Due to its simplicity and robustness, DTC seems to be a convenient choice in many applications.

The classical DTC leads itself easily to sensorless control through the flux model estimator, but as other sensorless control schemes based on the fundamental frequency models have been shown to give poor and asymptotically failing performance as zero speed is approached.

Tracking the variation of the inductances with rotor position has been shown to be a good alternative to the model-based sensorless methods.

Chapter 3

Power Converters for Motor Drives

3.1 Introduction

Electric power for industrial applications is supplied in a three-phase form with fixed frequency and fixed voltage. Some AC motors, like IM and PMSM with damper windings[1], can be operated directly from the mains, however, variable speed and often better energy efficiency are achieved by means of a frequency converter between the mains and the motor [14].

The most commonly used power converter for AC motor control applications is the well-known Voltage Source Inverter (VSI). In recent years Matrix Converters (MC) are gaining interest due to its advantages over the VSI. This chapter explains the basic principles of both VSI and MC. The classical VSI is first briefly reviewed and then a deep explanation of the MC main concepts is given.

[1]Damper windings are used in some line-start PMSM to allow them to start asynchronously from the mains.

3.2 Voltage Sources Inverters

VSIs receive DC voltage at the input side and convert it to AC voltage on the output side. Usually, the DC input voltage is constant and may be obtained, after rectifying and filtering, from the utility line or a rotating AC machine. It can also be obtained from a battery or a solar photovoltaic array [1]. Depending on the application the AC output voltage and frequency can be constant or variable. Some of its main applications are motor drives, Uninterruptable Power Supplies, power supply from battery or photovoltaic array, and Active Harmonic filter.

3.2.1 Topology

In general, a VSI for motor drives must satisfy the following basic requirements:

- Adjust the frequency according to the motor speed.
- Adjust the output voltage as to maintain the air gap flux at a desired value.
- Supply the rated current on a continuous basis at any frequency.

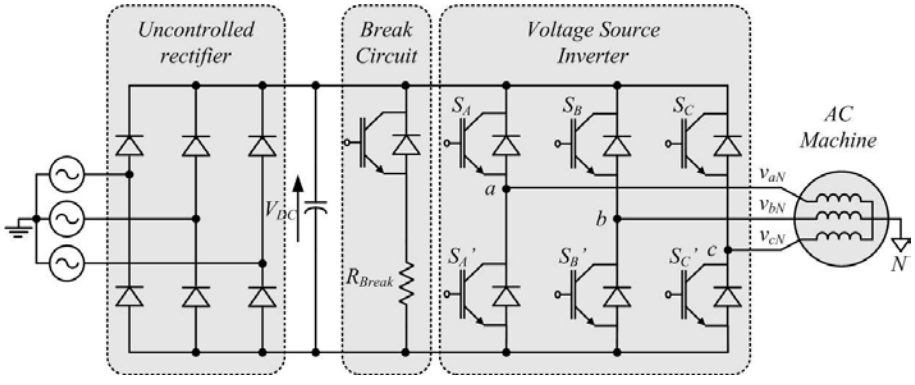

Figure 3.1: Voltage Source Inverter schematic.

Being precise, a VSI is a converter through which the power flow can be reversible. However, since most of the time the power will flow from the

DC side to the AC side, an uncontrolled diode rectifier is normally used at the input side. However, to slow down the motor, the kinetic energy associated with the inertia of the system (*motor+load*), will revert. Since the current direction through the uncontrolled diode rectifier cannot reverse, a power resistor in parallel with the DC bus will provide the VSI with braking capabilities. The resistor will be switched on if the capacitor voltage exceeds a preset level, hence dissipating the stored power.

3.2.2 Output Voltage Vectors

As it can be seen in Fig 3.1, in order to avoid any short circuit at the input power supply, the two switches in one leg may not be on simultaneously. On the other hand, there is no danger in turning both switches off. However, the output voltage in one leg when both switches are turned off will depend on the conducting diode and could not be determined without sensing the current. Therefore, only two states are allowed for each leg of the inverter. A single function can be assigned to each leg as follows [14]:

$$x = \begin{cases} 0 & \text{if } S_y = on \text{ and } S'_y = off \\ 1 & \text{if } S_y = off \text{ and } S'_y = on \end{cases} \tag{3.1}$$

where $x = a, b, c$ are the functions assigned to legs a, b and c and $y = A, B, C$ are the corresponding switches. Thus, the three phase inverter shown in Fig. 3.1 has $2^3 = 8$ permissible switching states.

From (3.1) the line-to-line and the line-to-neutral voltages can be derived as

$$\begin{bmatrix} v_{ab} \\ v_{bc} \\ v_{ca} \end{bmatrix} = V_{DC} \begin{bmatrix} 1 & -1 & 0 \\ 0 & 1 & -1 \\ -1 & 0 & 1 \end{bmatrix} \begin{bmatrix} a \\ b \\ c \end{bmatrix} \tag{3.2}$$

$$\begin{bmatrix} v_{aN} \\ v_{bN} \\ v_{cN} \end{bmatrix} = \frac{V_{DC}}{3} \begin{bmatrix} 2 & -1 & -1 \\ -1 & 2 & -1 \\ -1 & -1 & 2 \end{bmatrix} \begin{bmatrix} a \\ b \\ c \end{bmatrix} \tag{3.3}$$

where V_{DC} is the DC link voltage.

The space vectors theory introduced in chapter 2, is also a very useful tool for analysis and control of power converters [14]. Denoting the output voltages of an inverter, as the one shown in Fig. 3.1, by v_a, v_b and v_c, and considering that they can be line-to-line (v_{ab}, v_{bc}, v_{ca}), line-to-ground (v_{an}, v_{bn}, v_{cn}) or line-to-neutral (v_{aN}, v_{bN}, v_{cN}) voltages, the voltage space vector $\vec{v}$ is defined as

$$\vec{v} = v_\alpha + jv_\beta \tag{3.4}$$

where v_α and v_β can be found making $\theta = 0$ and $c = 1$ in (2.7), hence

$$\begin{bmatrix} v_\alpha \\ v_\beta \end{bmatrix} = \begin{bmatrix} 1 & -\frac{1}{2} & -\frac{1}{2} \\ 0 & \frac{\sqrt{3}}{2} & -\frac{\sqrt{3}}{2} \end{bmatrix} \cdot \begin{bmatrix} v_a \\ v_b \\ v_c \end{bmatrix} \tag{3.5}$$

Note that the reduction from three phase v_a, v_b and v_c, to two phase v_α and v_β is only possible in balanced systems, that is when $v_a + v_b + v_c = 0$. Under this condition, one of these voltage is dependent on the other two, thus the information contained in v_a, v_b and v_c is the same as that contained in v_α and v_β. Assuming a three phase voltages balanced system as

$$\begin{bmatrix} v_a \\ v_b \\ v_c \end{bmatrix} = V \cdot \begin{bmatrix} \cos(\omega t + \varphi) \\ \cos(\omega t + \varphi - \frac{2}{3}\pi) \\ \cos(\omega t + \varphi - \frac{4}{3}\pi) \end{bmatrix} \tag{3.6}$$

where V is the per phase voltage magnitude, then the $\alpha - \beta$ components of these voltages are

$$\begin{bmatrix} v_\alpha \\ v_\beta \end{bmatrix} = \frac{3}{2} V \cdot \begin{bmatrix} \cos(\omega t + \varphi) \\ \sin(\omega t + \varphi) \end{bmatrix} \tag{3.7}$$

hence, the voltage space vector is

$$\vec{v} = \frac{3}{2} V e^{j(\omega t + \varphi)} \tag{3.8}$$

Table 3.1: Switching states of a VSI

	Switch Functions			On Devices			line-to-neutral Voltages			line-to-line Voltages		
	a	b	c	A	B	C	V_{aN}	V_{bN}	V_{cN}	V_{ab}	V_{bc}	V_{ca}
V_0	0	0	0	S'_A	S'_B	S'_C	0	0	0	0	0	0
V_1	1	0	0	S_A	S'_B	S'_C	$2V_{DC}/3$	$-V_{DC}/3$	$-V_{DC}/3$	V_{DC}	0	$-V_{DC}$
V_2	1	1	0	S_A	S_B	S'_C	$V_{DC}/3$	$V_{DC}/3$	$-2V_{DC}/3$	0	V_{DC}	$-V_{DC}$
V_3	0	1	0	S'_A	S_B	S'_C	$-V_{DC}/3$	$2V_{DC}/3$	$-V_{DC}/3$	$-V_{DC}$	V_{DC}	0
V_4	0	1	1	S'_A	S_B	S_C	$-2V_{DC}/3$	$V_{DC}/3$	$V_{DC}/3$	$-V_{DC}$	0	V_{DC}
V_5	0	0	1	S'_A	S'_B	S_C	$-V_{DC}/3$	$-V_{DC}/3$	$2V_{DC}/3$	0	$-V_{DC}$	V_{DC}
V_6	1	0	1	S_A	S'_B	S_C	$V_{DC}/3$	$-2V_{DC}/3$	$V_{DC}/3$	V_{DC}	$-V_{DC}$	0
V_7	1	1	1	S_A	S_B	S_C	0	0	0	0	0	0

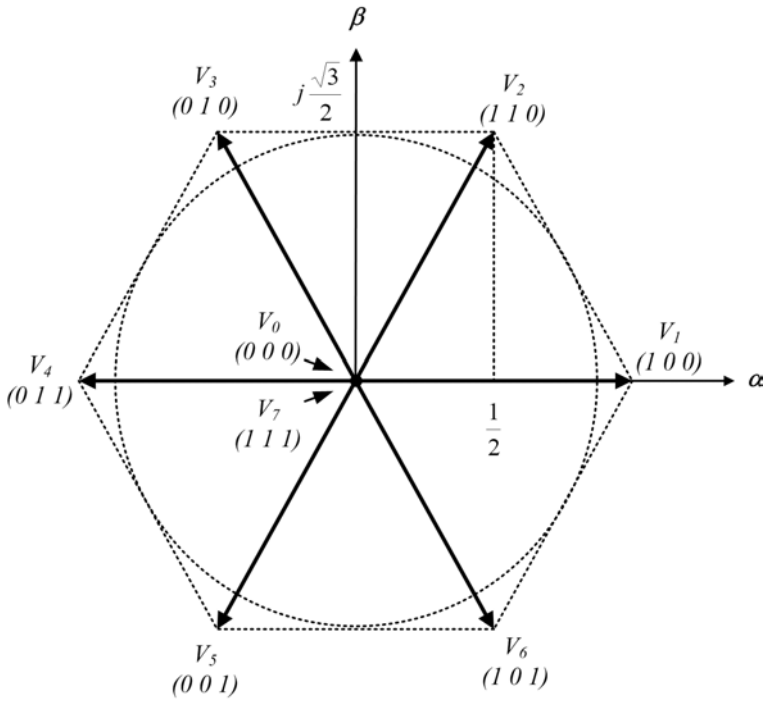

Figure 3.2: Line-to-line voltage vectors of a three phase VSI.

As it can be noted from (3.8), the voltage space vector rotates with an angular speed ω in a plane defined by the orthogonal coordinates α and β.

Applied to a VSI, the rotating voltage vector describes the fundamental output voltages. Since the VSI can only produce a specific number of stationary voltage space vectors, summarized in Table 3.1, the rotating vector $\vec{v}$ can be synthesized by means of an averaging process of the stationary space vectors. The output line-to-line voltage space vectors of a VSI like the one in Fig. 3.1 are shown in Fig. 3.2.

3.2.3 Modulation Techniques

Prior to the microprocessor development, the triangular Carrier-Based (CB) sinusoidal Pulse Width Modulation (PWM) was the most commonly used modulation method for three-phase static converters control [39]. However, with high performance microprocessors, the Space Vector Modulation (SVM) has become a basic processing technique in three-phase PWM converters.

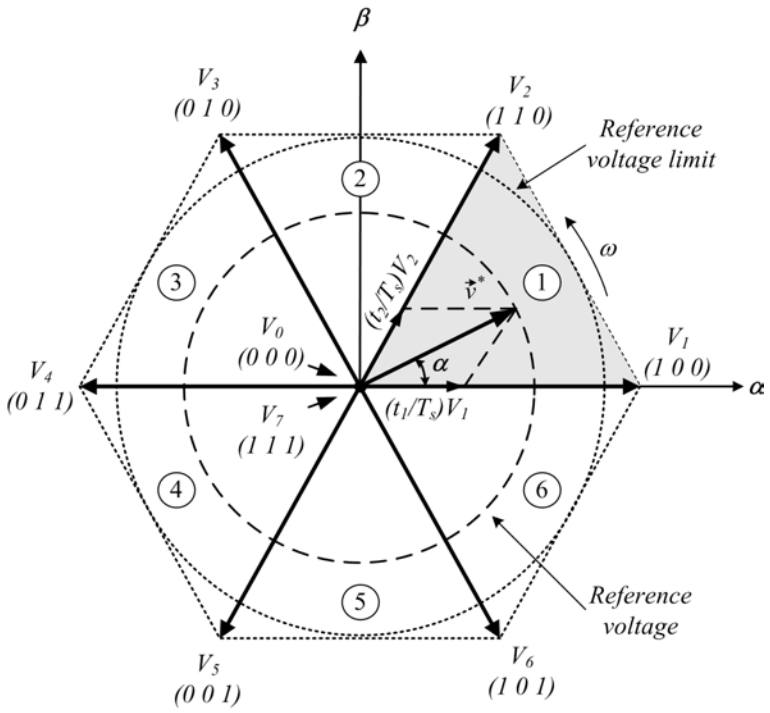

Figure 3.3: SVM. Synthesization of the reference voltage vector.

The SVM is an advanced, computation-intensive method and is possibly the best among all the modulation techniques for variable-frequency drive applications [1]. It is based on the representation of the converter output side voltage vectors shown in Fig. 3.3. As shown in table 3.1, a two-level inverter provides eight possible switching states, six active vectors ($V_1 - V_6$), which divide the plane into six sectors, and two null (or zero) vectors (V_0 and V_7) at the origin. The reference voltage vector $\vec{v}^*$, which is located in sector 1 in Fig. 3.3, can be synthesized using the adjacent vectors V_1 and V_2 in a part-time basis to satisfy the average output voltage demand. The time intervals t_1 and t_2 corresponding to vectors V_1 and V_2 can be derived with the help of a simple trigonometrical relationship from Fig. 3.3 as follows:

$$v^* \sin(\frac{\pi}{3} - \alpha) = V_1 \frac{t_1}{T_s} \sin\frac{\pi}{3} \tag{3.9}$$

$$v^* \sin\alpha = V_2 \frac{t_2}{T_s} \sin\frac{\pi}{3} \tag{3.10}$$

resolving for t_1 and t_2,

$$t_1 = \frac{2}{\sqrt{3}} \frac{v^*}{V_1} T_s \sin(\frac{\pi}{3} - \alpha) \tag{3.11}$$

$$t_2 = \frac{2}{\sqrt{3}} \frac{v^*}{V_2} T_s \sin\alpha \tag{3.12}$$

where Ts is the sampling time.

The residual sampling time, $t_0 + t_7$, is reserved for zero vectors V_0 and V_7 with the condition that $t_1 + t_2 + t_0 + t_7 = T_s$.

$$t_0 + t_7 = T_S - (t_1 + t_2) \tag{3.13}$$

Note that times t_1, t_2, t_0 and t_7 can be recalculated for any sector. Equations (3.11) to (3.13) are identical for all SVM methods, which only differ in the placement of the zero vectors. The most popular SVM method is the one with symmetrical placement of zero vectors. The construction of the symmetrical pulse pattern for three-phase inverters is shown in Fig. 3.4.

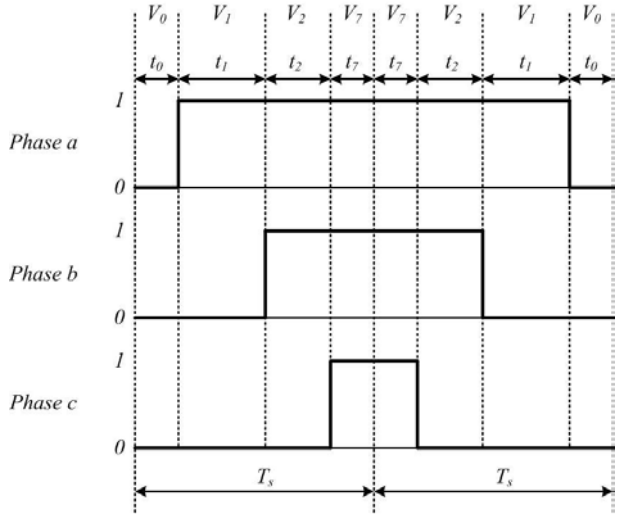

Figure 3.4: Construction of symmetrical pulse pattern for three-pase inverters.

3.3 Matrix Converters

In the last years, MCs have emerged to become a good alternative to the well-known Voltage Source Inverter (VSI) [2]. The MC is an advanced circuit topology capable of converting AC-AC, providing generation of load voltage with arbitrary amplitude and frequency, bi-directional power flow, sinusoidal input/output waveforms [3], and operation with unity input power factor. Furthermore, since no inductive or capacitive elements are required, MC allows a very compact design [3], [4]. Various methods to control MCs have been proposed [2], [40], the indirect space vector modulation being the most widely used.

3.3.1 Topology

A MC is an AC-AC converter, with $m \times n$ bi-directional switches, which connects an m-phase voltage source to an n-phase load. From a practical point of view, the three-phase, 3×3 switches MC shown in Fig. 3.5 is the most interesting as it connects a three-phase load into a three-phase power supply. It consists of nine bi-directional switches, arranged in three groups of three.

Each of these groups (S_{Aj}, S_{Bj}, S_{Cj}) is associated with an output phase j. In the MC shown in Fig. 3.5, v_{Si}, with $i = A, B, C$ are the source voltages, i_{Si}, with $i = A, B, C$ are the source currents, v_{jN}, with $j = a, b, c$ are the load voltages, i_j, with $j = a, b, c$ are the load currents, v_i, with $i = A, B, C$ are the MC input voltages and i_i , with $i = A, B, C$ are the input currents. A switch, S_{ij}, with $i = A, B, C$ and $j = a, b, c$ can connect the input phase i to the load phase j.

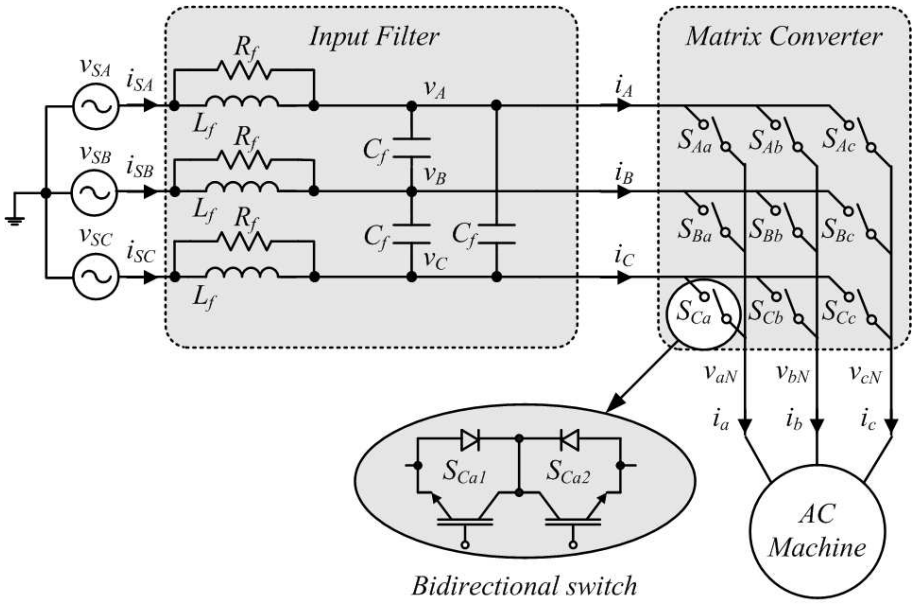

Figure 3.5: 3×3 Matrix Converter.

3.3.2 Output Voltage Vectors

The switches states are characterized by the following function

$$S_{ij} = \begin{cases} 0 & \text{if switch } S_{ij} \text{ is open} \\ 1 & \text{if switch } S_{ij} \text{ is closed} \end{cases} \tag{3.14}$$

There are 512 possible combinations of switches in a 3×3 MC. However, when operating with bi-directional switches, two basic rules must be followed:

Table 3.2: Voltage and Current Vectors of a 3×3 MC

MC State	On Devices	v_o	α_o	i_i	β_i
$+1$	$S_{Aa}\ S_{Bb}\ S_{Bc}$	$2/3v_{AB}$	0	$2/\sqrt{3}i_a$	$-\pi/6$
-1	$S_{Ba}\ S_{Ab}\ S_{Ac}$	$-2/3v_{AB}$	0	$-2/\sqrt{3}i_a$	$-\pi/6$
$+2$	$S_{Ba}\ S_{Cb}\ S_{Cc}$	$2/3v_{BC}$	0	$2/\sqrt{3}i_a$	$\pi/2$
-2	$S_{Ca}\ S_{Bb}\ S_{Bc}$	$-2/3v_{BC}$	0	$-2/\sqrt{3}i_a$	$\pi/2$
$+3$	$S_{Ca}\ S_{Ab}\ S_{Ac}$	$2/3v_{CA}$	0	$2/\sqrt{3}i_a$	$7\pi/6$
-3	$S_{Aa}\ S_{Cb}\ S_{Cc}$	$-2/3v_{CA}$	0	$-2/\sqrt{3}i_a$	$7\pi/6$
$+4$	$S_{Ba}\ S_{Ab}\ S_{Bc}$	$2/3v_{AB}$	$2\pi/3$	$2/\sqrt{3}i_b$	$-\pi/6$
-4	$S_{Aa}\ S_{Bb}\ S_{Ac}$	$-2/3v_{AB}$	$2\pi/3$	$-2/\sqrt{3}i_b$	$-\pi/6$
$+5$	$S_{Ca}\ S_{Bb}\ S_{Cc}$	$2/3v_{BC}$	$2\pi/3$	$2/\sqrt{3}i_b$	$\pi/2$
-5	$S_{Ba}\ S_{Cb}\ S_{Bc}$	$-2/3v_{BC}$	$2\pi/3$	$-2/\sqrt{3}i_b$	$\pi/2$
$+6$	$S_{Aa}\ S_{Cb}\ S_{Ac}$	$2/3v_{CA}$	$2\pi/3$	$2/\sqrt{3}i_b$	$7\pi/6$
-6	$S_{Ca}\ S_{Ab}\ S_{Cc}$	$-2/3v_{CA}$	$2\pi/3$	$-2/\sqrt{3}i_b$	$7\pi/6$
$+7$	$S_{Ba}\ S_{Bb}\ S_{Ac}$	$2/3v_{AB}$	$4\pi/3$	$2/\sqrt{3}i_c$	$-\pi/6$
-7	$S_{Aa}\ S_{Ab}\ S_{Bc}$	$-2/3v_{AB}$	$4\pi/3$	$-2/\sqrt{3}i_c$	$-\pi/6$
$+8$	$S_{Ca}\ S_{Cb}\ S_{Bc}$	$2/3v_{BC}$	$4\pi/3$	$2/\sqrt{3}i_c$	$\pi/2$
-8	$S_{Ba}\ S_{Bb}\ S_{Cc}$	$-2/3v_{BC}$	$4\pi/3$	$-2/\sqrt{3}i_c$	$\pi/2$
$+9$	$S_{Aa}\ S_{Ab}\ S_{Cc}$	$2/3v_{CA}$	$4\pi/3$	$2/\sqrt{3}i_c$	$7\pi/6$
-9	$S_{Ca}\ S_{Cb}\ S_{Ac}$	$-2/3v_{CA}$	$4\pi/3$	$-2/\sqrt{3}i_c$	$7\pi/6$
0_a	$S_{Aa}\ S_{Ab}\ S_{Ac}$	0	$\ldots$	0	$\ldots$
0_b	$S_{Ba}\ S_{Bb}\ S_{Bc}$	0	$\ldots$	0	$\ldots$
0_c	$S_{Ca}\ S_{Cb}\ S_{Cc}$	0	$\ldots$	0	$\ldots$
$+10$	$S_{Aa}\ S_{Bb}\ S_{Cc}$	v_{imax}	α_i	i_{omax}	β_i
-10	$S_{Aa}\ S_{Cb}\ S_{Bc}$	v_{imax}	$-\alpha_i$	i_{omax}	$-\beta_i$
$+11$	$S_{Ca}\ S_{Ab}\ S_{Bc}$	v_{imax}	$\alpha_i + 2\pi/3$	i_{omax}	$\beta_i + 2\pi/3$
-11	$S_{Ba}\ S_{Ab}\ S_{Cc}$	v_{imax}	$-\alpha_i - 2\pi/3$	i_{omax}	$-\beta_i - 2\pi/3$
$+12$	$S_{Ba}\ S_{Cb}\ S_{Ac}$	v_{imax}	$\alpha_i + 4\pi/3$	i_{omax}	$\beta_i + 4\pi/3$
-12	$S_{Ca}\ S_{Bb}\ S_{Ac}$	v_{imax}	$-\alpha_i - 4\pi/3$	i_{omax}	$-\beta_i - 4\pi/3$

- Avoid connecting two different input lines to the same output line, since it would lead into a short-circuit of the mains.

- Avoid disconnecting the output line circuits, since interrupting inductive currents, will cause overvoltages.

When these two basic rules are taken into consideration, the number of possible switching states is reduced to 27. The permitted switching states of a 3×3 MC are shown in table 3.2, and have been classified in groups. The first three groups containing the states (±1, ±2, ±3), (±4, ±5, ±6), and(±7, ±8, ±9), produces active vectors of variable amplitude, depending on the input voltages, but at stationary position (*pulsating vectors*). Sates 0_a, 0_b

and 0_c, corresponding to group 4, connecting all the output lines to the same input line, are the corresponding zero vectors. And the last six states (*group 5*), providing a direct connection of each output line to a different input line, are the rotating vectors.

The state of the converter switches can be represented by means of the so-called transfer matrix T which has the following form:

$$T = \begin{bmatrix} S_{Aa}(t) & S_{Ba}(t) & S_{Ca}(t) \\ S_{Ab}(t) & S_{Bb}(t) & S_{Cb}(t) \\ S_{Ac}(t) & S_{Bc}(t) & S_{Cc}(t) \end{bmatrix} \tag{3.15}$$

Each row shows the state of the switches connected to the same output line while each column shows the state of the switches connected to the same input line. Due to the instantaneous power transfer of MC, voltages and currents in one side may be reconstructed, at any instant, by means of the corresponding voltages and currents in the other side [41]. Because the MC is connected to the grid, the input line-to-neutral voltages are known, therefore, applying Kirchhoff's voltage law in Fig. 3.5, the output line-to-neutral output voltages are found as follows:

$$\begin{bmatrix} v_{aN}(t) \\ v_{bN}(t) \\ v_{cN}(t) \end{bmatrix} = \begin{bmatrix} S_{Aa}(t) & S_{Ba}(t) & S_{Ca}(t) \\ S_{Ab}(t) & S_{Bb}(t) & S_{Cb}(t) \\ S_{Ac}(t) & S_{Bc}(t) & S_{Cc}(t) \end{bmatrix} \begin{bmatrix} v_A(t) \\ v_B(t) \\ v_C(t) \end{bmatrix} \tag{3.16}$$

The output currents results from applying these output voltages to a given load. Measuring the output currents and applying Kirchhoff's current law, the input currents can be easily found:

$$\begin{bmatrix} i_A(t) \\ i_B(t) \\ i_C(t) \end{bmatrix} = \begin{bmatrix} S_{Aa}(t) & S_{Ab}(t) & S_{Ac}(t) \\ S_{Ba}(t) & S_{Bb}(t) & S_{Bc}(t) \\ S_{Ca}(t) & S_{Cb}(t) & S_{Cc}(t) \end{bmatrix} \begin{bmatrix} i_a(t) \\ i_b(t) \\ i_c(t) \end{bmatrix} \tag{3.17}$$

As it can be seen in (3.17), in order to find the input currents the transpose transfer matrix T^T is applied.

$$T^T = \begin{bmatrix} S_{Aa}(t) & S_{Ab}(t) & S_{Ac}(t) \\ S_{Ba}(t) & S_{Bb}(t) & S_{Bc}(t) \\ S_{Ca}(t) & S_{Cb}(t) & S_{Cc}(t) \end{bmatrix} \tag{3.18}$$

It can be noted, from (3.16), that with a suitable switching strategy, arbitrary voltages v_{jN} at an arbitrary frequency can be synthesized.

3.3.3 Modulation Techniques

The output waveforms of a MC are formed by selecting each of the input phases in sequence for specific periods of time. The output voltage consist of segments made up from the three input voltages. On the other hand, the input currents consist of segments of the output currents plus blank periods during which the output currents freewheels through the converter switches.

A modulation method for MC was first proposed by Venturini [42], who used a complicated scalar model with a maximum voltage transfer ratio of 0.5 [43]. In [44] the injection of a third harmonic method, which allows a maximum transfer ratio of 0.86, is proposed. In order to make possible the implementation of classical PWM strategies with MC, a new approach, known as indirect modulation, is proposed in [45], [46] and [47].

Scalar Modulation

Scalar modulation, also known as Venturini modulation, establishes independent relations for each output by considering time windows in which the instantaneous values of the desired output voltages are sampled and the instantaneous input voltages are used in order to synthesize a signal whose low frequency component follows the reference output phase voltages.

If t_{ij} is defined as the time during which switch S_{ij} is on and T_S as the sampling period, the output voltage vector can be expressed as

$$\vec{v}_{jN} = \frac{t_{Aj}v_A(t) + t_{Bj}v_B(t) + t_{Cj}v_C(t)}{T_S} \tag{3.19}$$

Since $T_S = t_{Aj} + t_{Bj} + t_{Cj}$, the following duty ratios can be defined

$$m_{Aj} = \frac{t_{Aj}}{T_S} \qquad m_{Bj} = \frac{t_{Bj}}{T_S} \qquad m_{Cj} = \frac{t_{Cj}}{T_S} \tag{3.20}$$

Substituting the switching states by the duty ratios in (3.16) and (3.17), the following equations for the output voltages and input currents can be derived

$$\begin{bmatrix} v_{aN}(t) \\ v_{bN}(t) \\ v_{cN}(t) \end{bmatrix} = \begin{bmatrix} m_{Aa}(t) & m_{Ba}(t) & m_{Ca}(t) \\ m_{Ab}(t) & m_{Bb}(t) & m_{Cb}(t) \\ m_{Ac}(t) & m_{Bc}(t) & m_{Cc}(t) \end{bmatrix} \begin{bmatrix} v_A(t) \\ v_B(t) \\ v_C(t) \end{bmatrix} \tag{3.21}$$

$$\vec{v}_o(t) = M(t)\vec{v}_i(t) \tag{3.22}$$

$$\begin{bmatrix} i_A(t) \\ i_B(t) \\ i_C(t) \end{bmatrix} = \begin{bmatrix} m_{Aa}(t) & m_{Ab}(t) & m_{Ac}(t) \\ m_{Ba}(t) & m_{Bb}(t) & m_{Bc}(t) \\ m_{Ca}(t) & m_{Cb}(t) & m_{Cc}(t) \end{bmatrix} \begin{bmatrix} i_a(t) \\ i_b(t) \\ i_c(t) \end{bmatrix} \tag{3.23}$$

$$\vec{i}_i(t) = M^T(t)\vec{i}_o(t) \tag{3.24}$$

Where $\vec{v}_o(t)$ and $\vec{i}_i(t)$ are the low frequency components[2] of the output voltage and input current vectors respectively. On the other hand, $\vec{i}_o(t)$ and $\vec{v}_i(t)$ are the instantaneous output current and input voltage vectors respectively. $M(t)$ is the low frequency transfer matrix, also known as modulation matrix. From (3.21) and (3.23), it can be concluded that firstly the output voltages are synthesized with the instantaneous values of the input voltages and secondly the input currents are synthesized with the instantaneous values of output currents. The derivation of the modulation matrix is carried out under the assumption that the required output voltages and input currents are sinusoidal.

Given the input voltages and output currents as,

[2]The low frequency component refers to the mean value calculated over one sampling interval.

$$\left[v_i(t)\right] = V_i \begin{bmatrix} \cos\omega_i t + \phi_i \\ \cos\omega_i t + \frac{2\pi}{3} + \phi_i \\ \cos\omega_i t + \frac{4\pi}{3} + \phi_i \end{bmatrix} \qquad \left[i_o(t)\right] = I_o \begin{bmatrix} \cos\omega_o t + \phi_o \\ \cos\omega_o t + \frac{2\pi}{3} + \phi_o \\ \cos\omega_o t + \frac{4\pi}{3} + \phi_o \end{bmatrix} \tag{3.25}$$

where V_i and I_o are the voltage and current amplitudes respectively, the objective is to find a modulation matrix $M(t)$ that satisfies the following equations

$$\left[v_o(t)\right] = qV_i \begin{bmatrix} \cos\omega_o t + \phi_o \\ \cos\omega_o t + \frac{2\pi}{3} + \phi_o \\ \cos\omega_o t + \frac{4\pi}{3} + \phi_o \end{bmatrix} \qquad \left[i_i(t)\right] = qI_o \begin{bmatrix} \cos\omega_i t + \phi_i \\ \cos\omega_i t + \frac{2\pi}{3} + \phi_i \\ \cos\omega_i t + \frac{4\pi}{3} + \phi_i \end{bmatrix} \tag{3.26}$$

where q is the input to output voltage ratio. There are two possible solutions to this problem derived by Venturini [48]:

$$\left[M_1(t)\right] = \frac{1}{3} \begin{bmatrix} 1 + 2q\cos\omega_m t & 1 + 2q\cos\omega_m t - \frac{2\pi}{3} & 1 + 2q\cos\omega_m t - \frac{4\pi}{3} \\ 1 + 2q\cos\omega_m t - \frac{4\pi}{3} & 1 + 2q\cos\omega_m t & 1 + 2q\cos\omega_m t - \frac{2\pi}{3} \\ 1 + 2q\cos\omega_m t - \frac{2\pi}{3} & 1 + 2q\cos\omega_m t - \frac{4\pi}{3} & 1 + 2q\cos\omega_m t \end{bmatrix} \tag{3.27}$$

with $\omega_m = \omega_o - \omega_i$.

$$\left[M_2(t)\right] = \frac{1}{3} \begin{bmatrix} 1 + 2q\cos\omega_m t & 1 + 2q\cos\omega_m t - \frac{2\pi}{3} & 1 + 2q\cos\omega_m t - \frac{4\pi}{3} \\ 1 + 2q\cos\omega_m t - \frac{2\pi}{3} & 1 + 2q\cos\omega_m t - \frac{4\pi}{3} & 1 + 2q\cos\omega_m t \\ 1 + 2q\cos\omega_m t - \frac{4\pi}{3} & 1 + 2q\cos\omega_m t & 1 + 2q\cos\omega_m t - \frac{2\pi}{3} \end{bmatrix} \tag{3.28}$$

with $\omega_m = -(\omega_o - \omega_i)$.

The solution in (3.27) yields $\phi_i = \phi_o$, giving the same phase displacement at the input and output of the MC whereas the solution in (3.28) yields

$\phi_i = -\phi_o$ giving reversed phase displacement at the input. A combination of both solutions provides the method for input angle displacement control.

$$\left[M(t)\right] = \alpha_1 \left[M_1(t)\right] + \alpha_2 \left[M_2(t)\right] \tag{3.29}$$

where $\alpha_1 + \alpha_2 = 1$. Setting $\alpha_1 = \alpha_2$ gives unity input Power Factor (PF) regardless of the load angle. Setting α_1 and α_2 to different values, leading PF (capacitive) at the input and lagging (inductive) at the output and vice versa can be achieved. For $\alpha_1 + \alpha_2 = 1$ the modulation duty ratios can be expressed in a compact expression as

$$m_{ij}(t) = \frac{1}{3}\left[1 + 2\frac{v_{iN}(t)v_{jN}(t)}{V_i^2}\right] \tag{3.30}$$

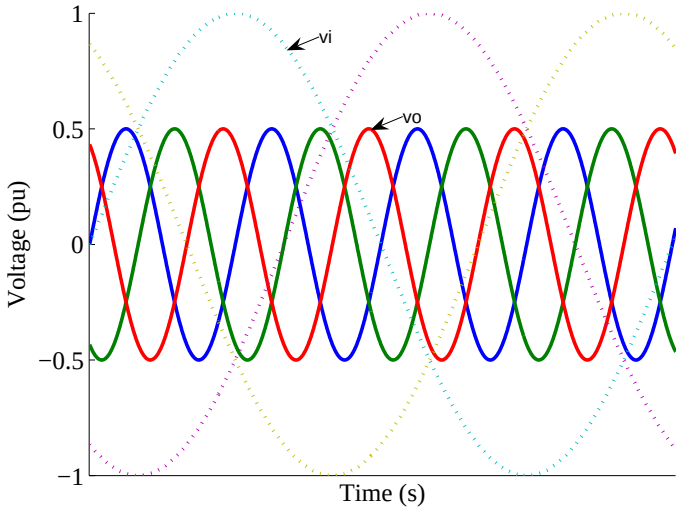

Figure 3.6: Output voltage target to input voltage ratio, q=0.5.

Using this solution the maximum input to output voltage ratio q that can be achieved is 50%. The waveforms of the target output voltages and the input voltages are shown in Fig. 3.6.

In order to increase the input to output voltage ratio q, a modification in the modulation matrix, including the injection of the third harmonic of the

input and output frequencies is proposed in [44].

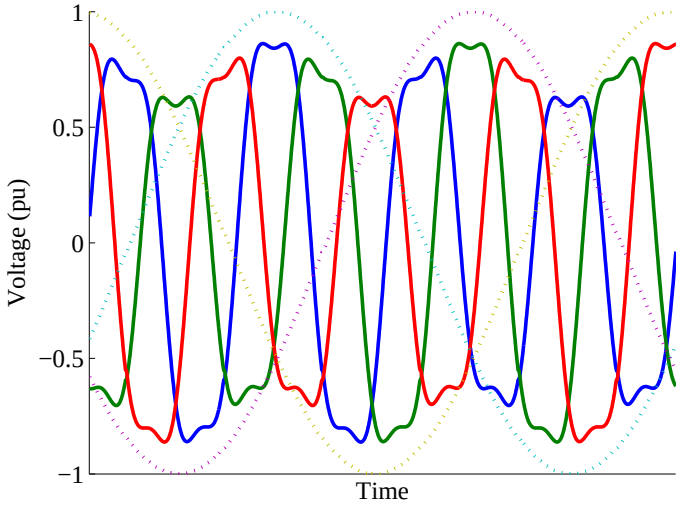

Figure 3.7: Injection of the third harmonics, q=0.86.

Using third harmonic injection, the maximum voltage transfer ratio can be improved up to $q = 0.86$, and the equation given in (3.30) becomes

$$m_{ij}(t) = \frac{1}{3}\left[1 + 2\frac{v_{iN}(t)v_{jN}(t)}{V_i^2} + \frac{2}{3}\sin(\omega_i t + \beta_i)\sin(3\omega_i t)\right] \tag{3.31}$$

where $\beta_i = 0, \frac{2\pi}{3}, \frac{4\pi}{3}$ for $i = A, B, C$ respectively. As it is shown in Fig. 3.7, the target output voltage now uses fully the input voltage envelope.

Indirect Modulation

The main idea of the indirect modulation is to consider the matrix converter as a two-stage converter; a rectification stage followed by an inversion stage. As shown in Fig. 3.8, the rectification stage will provide a virtual DC-link voltage V_{pn}, while producing sinusoidal input currents. The inversion stage will produce the three output voltages [49]. The decoupling between input currents and output voltages is reached dividing the transfer matrix T in

(3.15) in two new transfer matrices, one for the rectification stage R and other for the inversion stage I.

$$T = I \cdot R \tag{3.32}$$

$$\begin{bmatrix} S_{Aa}(t) & S_{Ba}(t) & S_{Ca}(t) \\ S_{Ab}(t) & S_{Bb}(t) & S_{Cb}(t) \\ S_{Ac}(t) & S_{Bc}(t) & S_{Cc}(t) \end{bmatrix} = \begin{bmatrix} S_7 & S_8 \\ S_9 & S_{10} \\ S_{11} & S_{12} \end{bmatrix} \begin{bmatrix} S_1 & S_3 & S_5 \\ S_2 & S_4 & S_6 \end{bmatrix} \tag{3.33}$$

This method allows to consider the MC as a back-to-back converter without energy storage devices [50]. Thus, common SVM strategies can be used with MC.

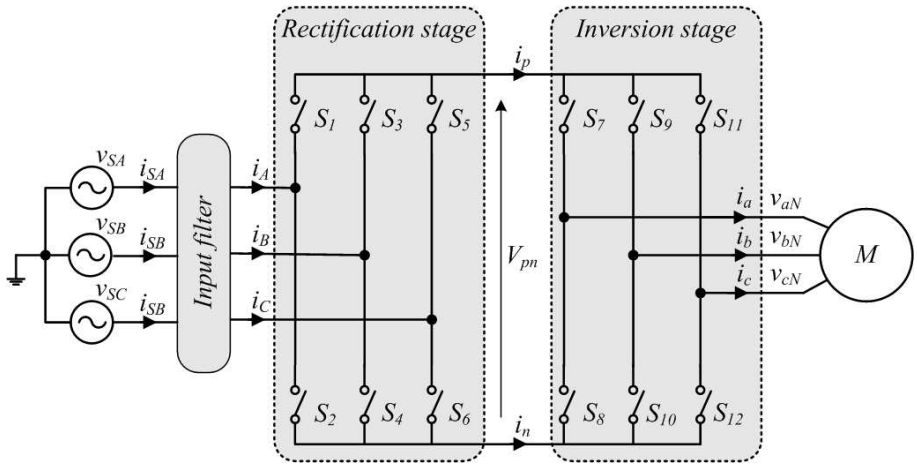

Figure 3.8: MC model for indirect modulation.

Using the new transfer matrices I and R, (3.16) can be expressed as follows:

$$\begin{bmatrix} v_{aN}(t) \\ v_{bN}(t) \\ v_{cN}(t) \end{bmatrix} = \begin{bmatrix} S_7 & S_8 \\ S_9 & S_{10} \\ S_{11} & S_{12} \end{bmatrix} \begin{bmatrix} S_1 & S_3 & S_5 \\ S_2 & S_4 & S_6 \end{bmatrix} \begin{bmatrix} v_A(t) \\ v_B(t) \\ v_C(t) \end{bmatrix} \tag{3.34}$$

and rearranging (3.34)

$$\begin{bmatrix} v_{aN}(t) \\ v_{bN}(t) \\ v_{cN}(t) \end{bmatrix} = \begin{bmatrix} S_7S_1 + S_8S_2 & S_7S_3 + S_8S_4 & S_7S_5 + S_8S_6 \\ S_9S_1 + S_{10}S_2 & S_9S_3 + S_{10}S_4 & S_9S_5 + S_{10}S_6 \\ S_{11}S_1 + S_{12}S_2 & S_{11}S_3 + S_{12}S_4 & S_{11}S_5 + S_{12}S_6 \end{bmatrix} \begin{bmatrix} v_A(t) \\ v_B(t) \\ v_C(t) \end{bmatrix} \tag{3.35}$$

The expression in (3.35) reveals that the output voltages are a composition of products and sums of the input voltages by means of the rectification stage switches, $S_7 - S_{12}$ and those of the inversion stage, $S_1 - S_6$.

Space Vector Modulation. Inversion stage.

Considering the inversion stage of Fig. 3.8 as a common VSI supplied by a DC-Link voltage, V_{pn}, the output voltages can be derived by the DC-Link voltage and the inversion stage switching states, in other words, the inversion stage transfer matrix, I. In the same way the current through the DC-Link, I_{pn}, can obtained by means of the transposed matrix I^T as it is shown in (3.36) and (3.37).

$$\begin{bmatrix} v_{aN}(t) \\ v_{bN}(t) \\ v_{cN}(t) \end{bmatrix} = \begin{bmatrix} S_7 & S_8 \\ S_9 & S_{10} \\ S_{11} & S_{12} \end{bmatrix} \begin{bmatrix} V_p \\ V_n \end{bmatrix} \tag{3.36}$$

$$\begin{bmatrix} I_p \\ I_n \end{bmatrix} = \begin{bmatrix} S_1 & S_3 & S_5 \\ S_2 & S_4 & S_6 \end{bmatrix} \begin{bmatrix} i_a(t) \\ i_b(t) \\ i_c(t) \end{bmatrix} \tag{3.37}$$

As in a common VSI, there are only eight possible combination that avoids short-circuit between the inverter's legs. These eight combinations are di-

vided into six active vectors $V_1 - V_6$ and two zero vectors V_0 and V_7. Vector V_1 indicates that output phase v_{aN} is connected to the positive side of the DC-Link, V_p, and the other two phases v_{bN} and v_{cN} are connected to the negative side V_n. The magnitude of this vector can be obtained applying Clark's transformation as in (3.8), resulting

$$V_1 = \frac{2}{3}(v_{aN} + v_{bN}e^{j\frac{2\pi}{3}} + v_{cN}e^{j\frac{4\pi}{3}}) = \frac{2}{3}V_{pn}e^{j\frac{\pi}{6}} \tag{3.38}$$

Applying the same transformation to the other vectors, all eight vectors can be represented in the $\alpha - \beta$ plane as in Fig. 3.2.

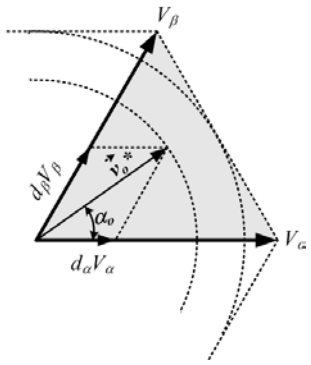

Figure 3.9: Voltage reference vector generation.

As for the VSI, any vector inside the hexagon can be synthesized by adding two adjacent vectors and a null vector. The active vectors and their duty cycles will determine the direction of the desired vector $\vec{v}_o^*$ while the null vector will determine its magnitude. The duty cycles for the active vectors can be obtained by dividing the time intervals in (3.11) and (3.12) by the sampling period T_s. As shown in Fig. 3.9, for any sector inside the hexagon, the time intervals for the adjacent vectors can take the following form

$$d_\alpha = \frac{t_\alpha}{T_s} = m_v \sin(\frac{\pi}{3} - \alpha_0) \tag{3.39}$$

$$d_\beta = \frac{t_\beta}{T_s} = m_v \sin \alpha_0 \tag{3.40}$$

As the sum of all three duty cycles must be $d_\alpha + d_\beta + d_0 = 1$, the duty cycle for the null vector can be expressed as

$$d_0 = \frac{t_0}{T_s} = 1 - d_\alpha - d_\beta \tag{3.41}$$

The voltage modulation index m_v, determines the voltage transfer ratio as

$$m_v = \sqrt{3}\frac{v_o^*}{V_{pn}} \qquad 0 < m_v < 1 \tag{3.42}$$

The virtual DC-Link voltage V_{pn} depends on the input voltages, the current modulation index m_c and the displacement angle between the input voltage and current ϕ_i. In the case of balanced and sinusoidal input voltages, with $m_c = 1$ and $\phi_i = 0$, the virtual DC-Link voltage becomes

$$V_{pn} = \frac{2}{3}V_i \tag{3.43}$$

where V_i is peak value of the input voltage.

Space Vector Modulation. Rectification stage.

In the same way as for the inversion stage, the rectification stage can be considered as a common Current Source Rectifier (CSR) loaded with a DC current supply I_{pn}. The input currents can derived by means of the virtual DC current supply and the rectification stage switching state, in other words,

the transfer matrix R. The virtual DC-Link voltage can be also derived by means of transposed transfer matrix R^T.

$$\begin{bmatrix} i_A(t) \\ i_B(t) \\ i_C(t) \end{bmatrix} = \begin{bmatrix} S_1 & S_2 \\ S_3 & S_4 \\ S_5 & S_6 \end{bmatrix} \begin{bmatrix} I_p \\ I_n \end{bmatrix} \tag{3.44}$$

$$\begin{bmatrix} V_p \\ V_n \end{bmatrix} = \begin{bmatrix} S_1 & S_3 & S_5 \\ S_2 & S_4 & S_6 \end{bmatrix} \begin{bmatrix} v_A(t) \\ v_B(t) \\ v_C(t) \end{bmatrix} \tag{3.45}$$

Only nine combinations of the rectification stage switches, which avoids disconnecting the DC-Link bus, are available. These nine switching states yields in six active current vectors $I_1 - I_6$ and three null vectors. Vector $I_1(AB)$ means that phase A is connected to the DC-Link positive potential V_p, and phase B is connected to the negative side V_n. Again, applying Clark's transformation, this vector can be expressed as follows:

$$I_1 = \frac{2}{3}(i_A + i_B e^{j\frac{2\pi}{3}} + i_C e^{j\frac{4\pi}{3}}) = \frac{2}{3} I_{pn} e^{j\frac{-\pi}{6}} \tag{3.46}$$

Applying the same transformation to the other vectors, all nine vectors can be represented in the $\alpha - \beta$ plane as in Fig. 3.10.

As in the case of the inversion stage, any vector $\vec{i}_i^*$ inside the hexagon can be synthesize by means of two adjacent vectors and a zero vector. From Fig. 3.11, the duty cycles can be derived as follows:

$$d_\gamma = \frac{t_\alpha}{T_s} = m_c \sin(\frac{\pi}{3} - \alpha_i) \tag{3.47}$$

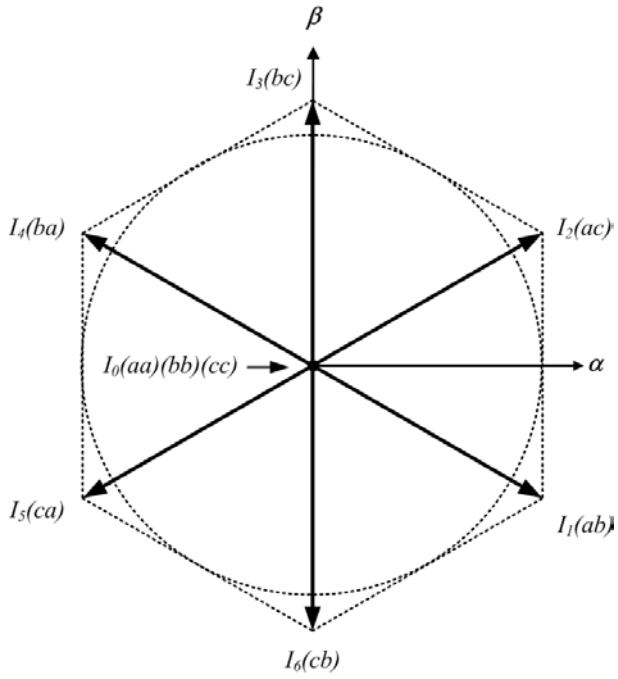

Figure 3.10: Rectification stage input current vectors.

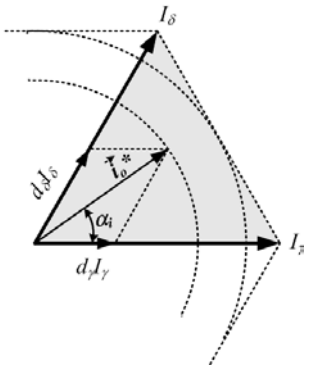

Figure 3.11: Current reference vector generation.

$$d_\delta = \frac{t_\delta}{T_s} = m_c \sin \alpha_i \tag{3.48}$$

As the sum of all three duty cycles must be $d_\gamma + d_\delta + d_0 = 1$, the duty

cycle for the null vector can be expressed as

$$d_0 = \frac{t_0}{T_s} = 1 - d_\gamma - d_\delta \tag{3.49}$$

The current modulation index m_c, determines the current transfer ratio as

$$0 < m_c < 1 \qquad m_c = \frac{i_i^*}{I_{pn}} \tag{3.50}$$

Space Vector Modulation. Entire Matrix Converter.

In the above sections, both rectification and inversion stages duty cycles have been obtained by means of the MC equivalent circuit when indirect modulation is used. In order to obtain a correct balance of the input currents and the output voltages, the entire MC modulation pattern must be a combination of both the rectification and inversion stage. The duty cycle of each sequence is determined as the product of the corresponding duty cycles [14]:

$$\begin{aligned} d_{\alpha\gamma} &= d_\alpha d_\gamma \qquad d_{\alpha\delta} = d_\alpha d_\delta \\ d_{\beta\gamma} &= d_\beta d_\gamma \qquad d_{\beta\delta} = d_\beta d_\delta \end{aligned} \tag{3.51}$$

The duration of each sequence $\alpha\gamma$, $\alpha\delta$, $\beta\gamma$, $\beta\delta$, is obtained multiplying the sample period T_s by the corresponding duty cycle. To obtain the desired values of the current $\vec{i}_i^*$ and voltage $\vec{v}_o^*$, while minimizing the number of commutation during one sample period, a change of sequences is proposed in [51], so that only one switch commutation per sequence is achieved. As it is shown in table 3.3, the sequence pattern varies depending on the parity of the sum of actual sectors in both input and output hexagons.

Table 3.3: Commutation sequence for indirect modulation of MC.

Sum of sectors	Commutation sequence								
Even	$\beta\gamma$	$\alpha\gamma$	$\alpha\delta$	$\beta\gamma$	0	$\beta\gamma$	$\alpha\delta$	$\alpha\gamma$	$\beta\gamma$
Odd	$\alpha\gamma$	$\beta\gamma$	$\beta\delta$	$\alpha\gamma$	0	$\alpha\gamma$	$\beta\delta$	$\beta\gamma$	$\alpha\gamma$

3.3.4 Bidirectional Switches

Bi-directional switches, capable of blocking voltage and conducting current in both directions are indispensable in MC. The lack of such devices has reduced industrial development of MC. A bi-directional switch can be built using unidirectional switches available on the market. Basically, there are three different structures to obtain a bi-directional switch cell as shown in Fig. 3.12. The diode bridge, the common emitter back-to-back and the common collector back-to-back structures.

Since in the diode bridge there is only one transistor witch handles the current in both directions, only one gate driver is needed per switch cell. However, conduction losses are high since there are three devices conducting at the same time. Moreover, the direction of current through the cell can not be controlled, being a disadvantage in advanced commutation methods.

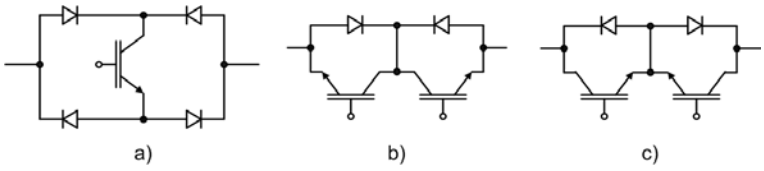

Figure 3.12: Switch cell. (a) Diode bridge. (b) Common collector back-to-back. (c) Common emitter back-toback.

The common collector and common emitter switch cells, shown in Fig. 3.12(b) and Fig. 3.12(c) respectively, allow for lower conduction losses because there are only two devices conducting at the same time. Although the advantage of common collector switch cell is that only six isolated power supplies are needed to supply the gate drive signals, as highlighted in [52],

the common emitter topology is preferred in practice because minimizes the stray inductance [41].

Bi-Directional switches Commutation Techniques

Since in MC there are no natural freewheeling paths, the current commutation is more difficult than in conventional VSIs. The commutation has to be controlled according to the basic rules explained in section 3.3.2. There are two possibilities for performing the commutation in the case of ideal true four-quadrant switches [14]:

- *Dead-time current commutation*: In order to avoid short-circuit of the inputs, the off-going switch is turned off while the on-coming is still disconnected. Using this method implies overvoltage on the output side and therefore a clamp circuit is necessary at the output to avoid load currents discontinuities.

- *Overlap current commutation*: The main goal of this method is to avoid disconnection of the output line circuit. This is achieved turning on the on-coming switch while the off-going is still conducting. Obviously, this will imply short-circuit of the inputs, thus causing high currents circulation between inputs, which has to be eliminated by means of additional chokes to decrease di/dt.

The need of extra reactive components and the high losses involved when employing these methods, makes them unpractical. Since bi-directional switches uses independent controllable unidirectional switches, the current direction can be controlled. Therefore, other commutation strategies have been proposed [53], [54] providing safe commutation based on two or four-step commutation techniques.

Basically, There are two strategies to perform safe commutation. The first is based on the direction of the current [53], [54] while the other is based on the sign of the line-to-line voltage between the two switches involved in the commutation process [53]. However, since the load is usually inductive, the current sign detection is considered to offer safer operation [14].

Current sign four-step semi-soft commutation technique

In order to implement this technique the switch cell must be designed in such a way to allow the current direction to be controllable. The four steps in which the commutation takes place are as follows:

- Step 1: Turn off the off-going non-conducting switch.
- Step 2: Turn on the on-coming conducting switch.
- Step 3: Turn off the off-going conducting switch.
- Step 4: Turn on the on-coming non-conducting switch.

A schematic representation of a two-phase to single phase MC is shown in Fig. 3.13 (a), in which switch cells S_{Aa} and S_{Ba} represents the first two switches in the converter of Fig. 3.5.

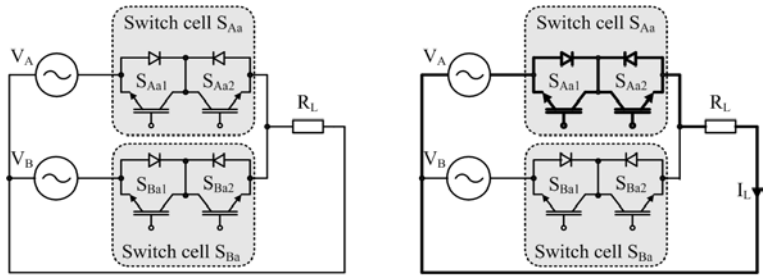

(a) Two phase to single single phase MC (b) Initial condition. S_{Aa} on and $I_L>0$.

Figure 3.13: (a) Two-phase to single phase MC. (b) Initial conditions with SAa on and $I_L > 0$

In the following explanation it is assumed that S_{Aa} is on, and the current direction is positive as indicated in Fig. 3.13(b).

As explained above, when a commutation to switch S_{Ba} is required, the first step is to turn off the off-going non-conducting switch. In order to determine which device in the active switch cell is not conducting, the current

direction has to be known. In this case, as $I_L > 0$, S_{Aa1} is turned off. According to step 2, the on-coming conducting switch must be turned on. Because $I_L > 0$, the conducting device in the on-coming switch cell will be S_{Ba2}. Step 3 implies turning off the off-going conducting switch, in this case, according to the current direction in Fig. 3.13(b), S_{Aa2} will be turned off. Finally, in order to re-establish the four-quadrant characteristic of the AC switch, the on-coming non-conducting switch, S_{Ba2}, is turned on allowing currents to change its direction naturally.

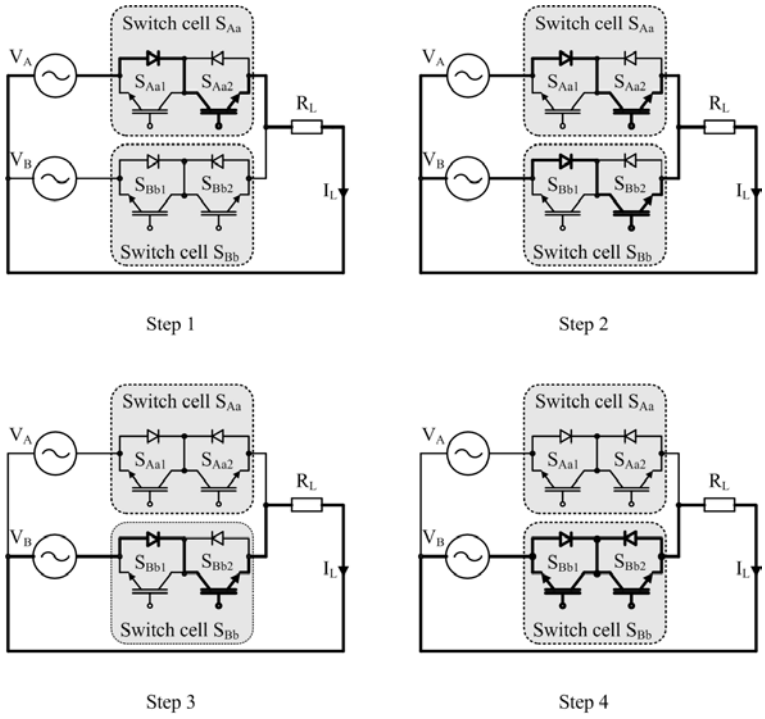

Figure 3.14: Current path during four-step commutation process.

Since steps one and four are passive and non-critical, their states can be changed faster. On the contrary, the duration of steps two and three is critical and must agree with the switch characteristics.

The current path during the four-step commutation process when $I_L > 0$ is illustrated in Fig. 3.14. A similar explanation holds for the commutation

process when $I_L < 0$.

This technique allows the commutation process without causing input line-to-line short-circuit or disconnecting the output lines. Furthermore, the switching losses are reduced by 50% because half of the commutation process is soft-switching [55].

3.3.5 The input filter

A low-pass filter is used at the input side of the MC to reduce the switching frequency harmonics. The filter requirements are as follows [14]:

- To have a cutoff frequency lower than the switching frequency:

$$\omega_o = \frac{1}{\sqrt{C_f L_f}} \tag{3.52}$$

  where L_f and C_f are the inductance and capacitance and $\omega_o = 2\pi f_o$ is the resonance pulsation of the input filter.

- Minimize its reactive power at the power grid frequency.
- Minimize the volume and weight for capacitor and chokes.
- Minimize the inductance voltage drop at the rated current in order to avoid a reduction in the voltage transfer ratio.

Firstly, the cutoff frequency of the LC filter is chosen to provide the desired attenuation at the switching frequency. The value of the capacitor or the inductance is calculated based on one of the above criteria.

3.3.6 Over-voltage protection

In the previous section a four-step commutation technique which avoids both overvoltage and overcurrent has been presented. However, there are another sources of overvoltage when operating with a MC, as grid perturbations and fault states in the load. When the output of MC is disconnected, thus suddenly interrupting the load current, the energy stored in the load

inductance has to be discharged without generating high overvoltages. The most common solution is the use of a clamp circuit as shown in Fig. 3.15, where the capacitor is charged at the desired clamp level. This circuit uses twelve fast recovery diodes connecting the capacitor to the input and output terminals.

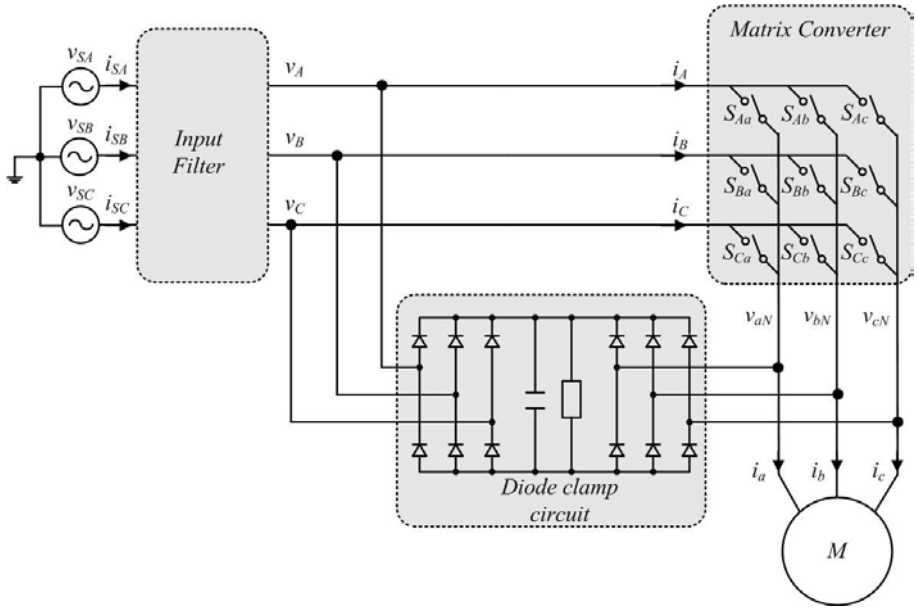

Figure 3.15: Matrix converter with clamp circuit.

When overvoltages occurs, the diodes conducts and the RC circuit maintains the voltage level at a safe value. In normal conditions, the diodes are not conducting and the clamp circuit has no effect in the MC operation. A new configuration which uses six diodes from the bi-directional switches is proposed in [56]. Another strategy is proposed in [57], replacing the clamp circuit by varistors at the input an output, plus an extra protection circuit for each IGBT. Controlled shutdown without a clamp circuit is proposed in [58] using controlled freewheeling states in order to reduce the motor current to zero.

3.4 Conclusions

Two different converters, the most commonly used in AC motor applications (VSI) and an advanced AC-AC topology (MC), has been examined. MCs have several advantages over the conventional VSI as bi-directional power flow with input power factor correction capability. Moreover, since there is no DC-link in a MC no large energy storage elements are needed, allowing for a very compact design. However, the need of bi-directional switches makes the control of the MC more complex when compared to the VSI. Similar to the standard diode bridge VSI, the MC has to be protected against over-voltage and overcurrent. Due to the lack of energy storage elements in the DC-link, the MC topology is more sensitive to disturbances. A solution to solve these problems consist on connecting a clamp circuit on the output which is one of the main drawbacks of this topology.

Among the known advantages of MCs over VSIs, as the capability to control the input power factor, no need for energy storage elements and bi-directional power flow, MCs can generate more voltages vectors than VSIs which can be exploited to reduce the inherent torque and flux ripples present when DTC schemes are employed. Taking into consideration the advantages and disadvantages of both converters, the author has considered the use of the MC throughout this work.

Chapter 4

Direct Torque Control

4.1 Introduction

Traditionally, AC machines, especially the IM connected to a constant frequency sinusoidal power supply have been used in constant speed applications, whereas DC machines were used for variable speed drives. The converter and control of a DC drive are simple. Moreover, DC machines have a very fast torque response. However, the commutators and brushes of DC machines, not only limit the speed and current, but also are a source of EMI, and do not allow this type of machine to operate in explosive or corrosive environments. In contrast, as mentioned in chapter 2, AC machines do not have these disadvantages, however, their control complexity has been a challenge to use them in variable speed applications. Thanks to the rapid development in the field of power electronics and fast microprocessors (*such as DSPs*) in the last decades, high performance applications using IM and PMSM drives are now possible. Furthermore, it is expected that, even in applications where high dynamics performance are not required, speed and torque control of various types of AC machines will become a commonly used technique due to the improvements achieved in terms of efficiency.

Various types of control techniques have been briefly discussed in section 2.3 of chapter 2, DTC being one of the most popular nowadays. This chapter is devoted to describe the classical DTC technique for both IM and PMSM pointing out the advantages and disadvantages of this control method. Simulation and experimental tests have been carried out to analyze the DTC working principle and its dynamic performance when fed by a VSI.

4.2 Direct Torque Control for Induction Machines

In a DTC-IM drive it is possible to control directly the electromagnetic torque and stator flux linkage magnitudes by selecting the appropriate inverter output voltage vectors. The selection of these vectors must restrict both magnitude errors within their respective flux and torque hysteresis bands. In order to select the proper voltage vectors, understanding of both flux and torque variation as a function of the applied voltages is mandatory.

In section 2.2.1 of chapter 2, various equations for the electromagnetic torque were presented, a general form being

$$T_e = \frac{2}{3} p \vec{\psi}^s \times \vec{i}^s \tag{4.1}$$

Both, stator and rotor fluxes can be expressed in terms of stator and rotor currents as follows:

$$\vec{\psi}^s = L_s \vec{i}^s + L_m \vec{i}^r \tag{4.2}$$

$$\vec{\psi}^r = L_r \vec{i}^r + L_m \vec{i}^s \tag{4.3}$$

Eliminating $\vec{i}^r$ from (4.2), the following equation can be derived

$$\vec{\psi}^s = \frac{L_m}{L_r} \vec{\psi}^r + L'_s \vec{i}^s \tag{4.4}$$

where $L'_s = L_s L_r - L_m^2$. Thus, the stator current can be expressed as follows:

$$\vec{i}^s = \frac{1}{L'_s}(\vec{\psi}^s - \frac{L_m}{L_r}\vec{\psi}^r) \tag{4.5}$$

Replacing (4.5) into (4.1), the following expression for the electromagnetic torque can be written as follows:

$$T_e = \frac{3}{2}p\frac{L_m}{L_r L'_s}\vec{\psi}^r \times \vec{\psi}^s \tag{4.6}$$

or

$$T_e = \frac{3}{2}p\frac{L_m}{L_r L'_s}|\psi^r||\psi^s|\sin\gamma \tag{4.7}$$

where $\gamma = \gamma_s - \gamma_r$ is the angle between stator and rotor fluxes. The phase diagram corresponding to (4.6) is shown in Fig. 4.1.

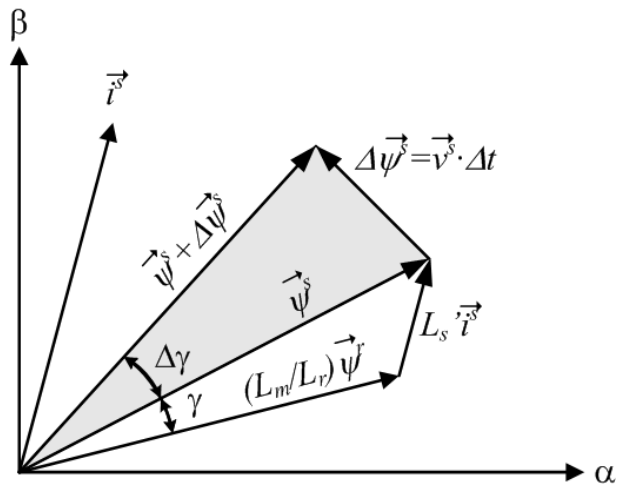

Figure 4.1: Phase diagram in the stationary reference frame.

In an IM, the rotor time constant can be considered larger than the stator one, therefore, the rotor flux linkage varies slower than the stator flux linkage. Thus, during a short transient (*sampling period*), the rotor flux linkage will remain almost unchanged. If the rotor flux linkage remains constant and

the stator one is changed incrementally by means of the stator voltage $\vec{v}^s$, and the corresponding change of γ is $\Delta\gamma$, the incremental torque ΔT_e can be expressed as follows:

$$\Delta T_e = \frac{3}{2} p \frac{L_m}{L_r L'_s} |\psi^r| |\psi^s + \Delta\psi^s| \sin \Delta\gamma \tag{4.8}$$

If for simplicity it is assumed that the stator resistance can be neglected, then

$$\vec{v}^s \approx \frac{d}{dt} \vec{\psi}^s \tag{4.9}$$

It follows from (4.9), that in a short Δt time (*sampling period*), the stator flux linkage variation can be approximated by

$$\Delta\vec{\psi}^s \approx \vec{v}^s \Delta t \tag{4.10}$$

Thus, the stator flux linkage varies $\Delta\vec{\psi}^s \approx \vec{v}^s \Delta t$ in the same direction of the applied stator voltage vector and proportionally to the voltage vector magnitude and sampling time. Selecting the appropriate voltage vector in every sampling period $T_s = \Delta t$, the stator flux linkage vector can be changed in the desired manner. By acting on the tangential and radial flux components, decoupled control of the electromagnetic torque and stator flux linkage can be achieved. Since these two components are proportional to the applied voltage vector components lying on the same directions, they can be controlled selecting appropriate inverter switching states. The tangential component of the voltage vector will force the stator flux vector to move away from the rotor flux one, thus increasing the angle γ between them. Since the angle γ is increased, according to (4.8) the electromagnetic torque will be increased. The stator flux linkage vector magnitude will depend on the radial component of the voltage vector.

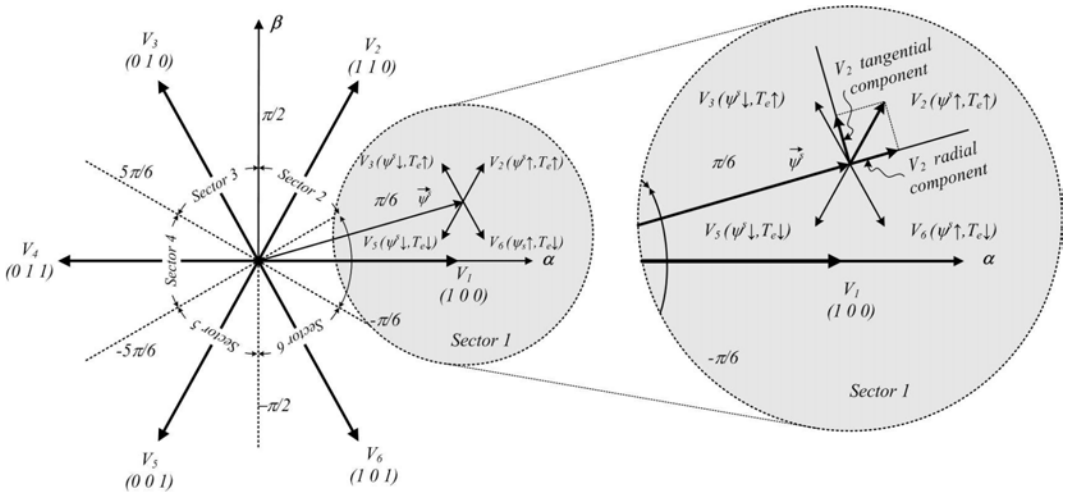

Figure 4.2: Voltage vector influence on stator flux linkage and electromagnetic torque variation.

Figure 4.2 shows the influence of the applied voltage vector on the stator flux linkage and torque variations. The possible flux locus is divided into six different sectors. It also shows the six active vectors of the inverter discussed in section 3.2 of chapter 3, which can be expressed in a general form as

$$V_k = \frac{2}{3} V_{DC} e^{j(k-1)\pi/3} \tag{4.11}$$

where $k = 1, 2, \ldots, 6$. For $k = 0, 7$, the applied vectors are the null vectors V_0 and V_7 respectively.

From Fig. 4.2 and (4.11), table 4.1 can be written. In table 4.1, k corresponds to the sector in which the stator flux linkage is lying. It should be noted that vectors V_k and V_{k+3} are not considered for torque variations because they have opposite effects depending on whether the flux linkage vector is lying in the first portion (*first* 30^o) or in the second portion (*second* 30^o) of the sector.

If a null vector (V_0 *or* V_7) is applied, the machine terminal will be short

Table 4.1: General DTC voltage vector selection table.

	Increase	Decrease
ψ^s	V_k, V_{k+1}, V_{k-1}	V_{k+2}, V_{k-2}, V_{k+3}
T_e	V_{k+1}, V_{k+2}	V_{k-1}, V_{k-2}

circuited almost stoping the stator flux linkage vector rotation[1], hence, keeping the stator flux and electromagnetic torque unaltered.

4.2.1 DTC Scheme and Optimum Voltage Vector Selection for IM

Based on the above considerations, the conventional[2] DTC for IM was developed in [7]. Figure 4.3 shows the block diagram for the conventional DTC for IM using a VSI.

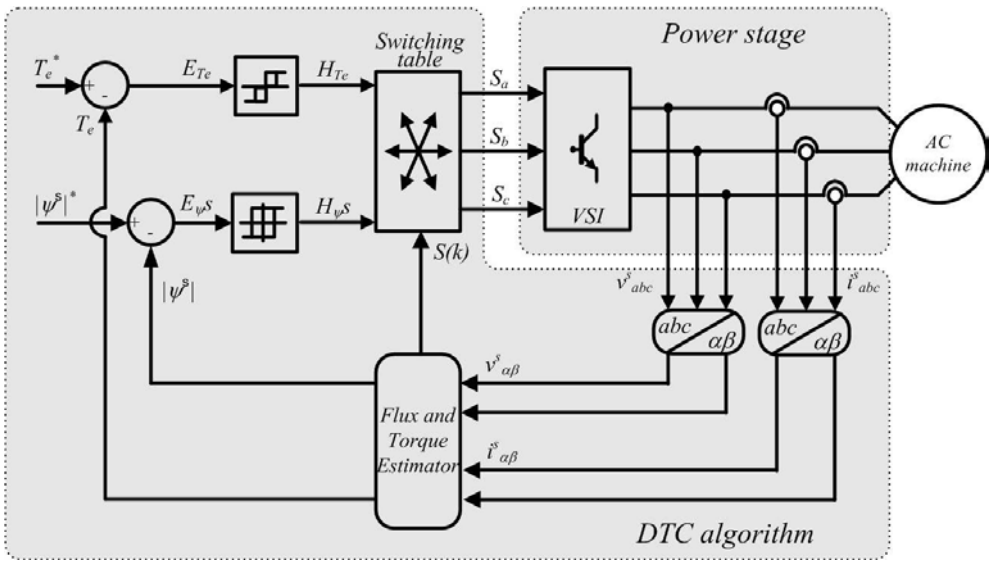

Figure 4.3: Direct Torque Control for IM. Block diagram.

As it can be seen, the stator flux linkage ψ^{s*} and torque T_e^* references

[1]The stator flux will rotate very slowly due to the small resistance voltage drop.

[2]The DTC developed by Takahashi in [7] will be hereinafter refered to as *conventional DTC*.

Table 4.2: DTC optimum voltage vector selection table.

H_{ψ^s}	H_{T_e}	$S(1)$	$S(2)$	$S(3)$	$S(4)$	$S(5)$	$S(6)$
1	1	V_2	V_3	V_4	V_5	V_6	V_1
	0	V_0	V_7	V_0	V_7	V_0	V_7
	-1	V_6	V_1	V_2	V_3	V_4	V_5
-1	1	V_3	V_4	V_5	V_6	V_1	V_2
	0	V_7	V_0	V_7	V_0	V_7	V_0
	-1	V_5	V_6	V_1	V_2	V_3	V_4

are compared with the corresponding estimated values. The corresponding errors, E_ψ and E_{T_e}, are compared by means of hysteresis band comparators. In particular, stator flux is controlled by a two-level hysteresis comparator, whereas the torque is controlled by a three-level comparator as shown in Fig. 4.4. On the basis of the hysteresis comparators and stator flux sector $S(k)$, a proper VSI voltage vector is selected by means of a switching table.

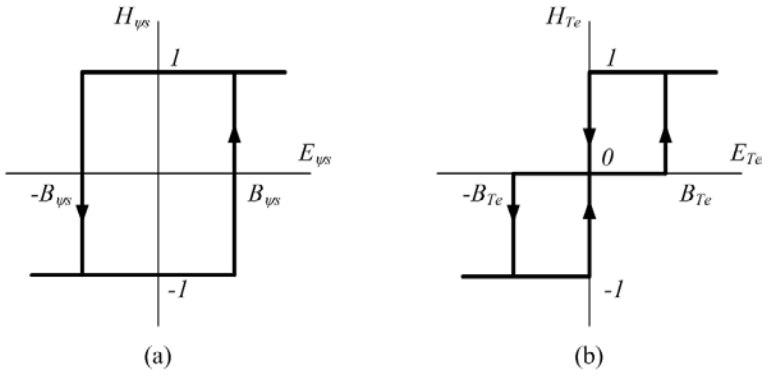

Figure 4.4: Flux and torque hysteresis comparators. (a) Two-level hysteresis comparator. (b) Three-level hysteresis comparator.

Considering the influence of the applied voltage vector explained in the previous section and summarized in table 4.1, the so-called optimum switching vector selection table is derived and shown in table 4.2. This gives the optimum selection of the vectors for all possible stator flux linkage vector positions (*sector in which the stator flux linkage vector lies*) and the desired values of both the stator flux linkage modulus and the electromagnetic torque.

As it can be seen in Fig. 4.5, the stator flux linkage vector reference and the corresponding hysteresis bands tracks a circular trajectory. Thus, the actual stator flux linkage vector follows its reference within the hysteresis bands in a zigzag path.

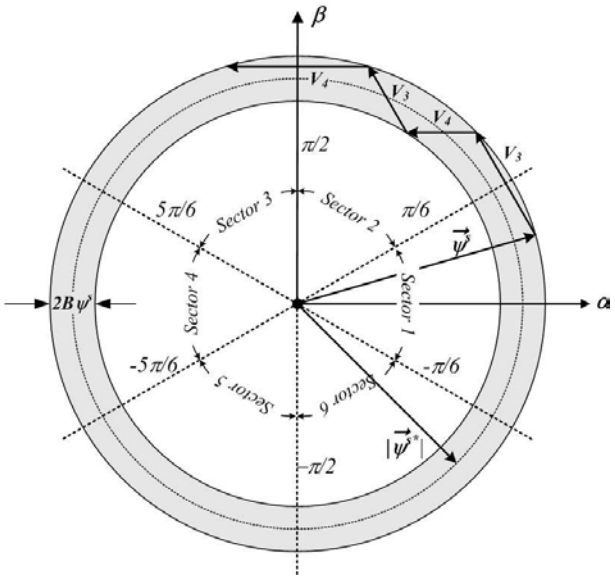

Figure 4.5: Stator flux linkage vector locus.

4.2.2 Stator Flux and electromagnetic Torque estimate

The DTC scheme shown in Fig. 4.3 can achieve decoupled control of both stator flux linkage and electromagnetic torque. Thus, these quantities must be estimated in order to close the corresponding control loops. There are many different methods to estimate the stator flux linkage based on the motor parameters. One of the simplest methods, based on the voltage model of the machine, consist in the integration of the back-emf. From the voltage equations in the $\alpha - \beta$ frame given in (2.11) and (2.12), the $\alpha - \beta$ components of the stator flux linkage can be solved as follows:

$$\psi_\alpha^s = \int (v_\alpha^s - R_s i_\alpha^s) dt \tag{4.12}$$

$$\psi_\beta^s = \int (v_\beta^s - R_s i_\beta^s) dt \tag{4.13}$$

From (4.12) and (4.13), the angle of the stator flux linkage vector γ_s can be easily derived.

$$\gamma_s = \arctan\left(\frac{\psi_\beta^s}{\psi_\alpha^s}\right) \tag{4.14}$$

Although the method does only depend on the stator resistance R_s, the accuracy of the voltage and current measurements and the integration technique is crucial. Pure integrators have infinite gain at zero frequency, hence any offsets present at the input will make the output gradually drift as shown in Fig. 4.6.

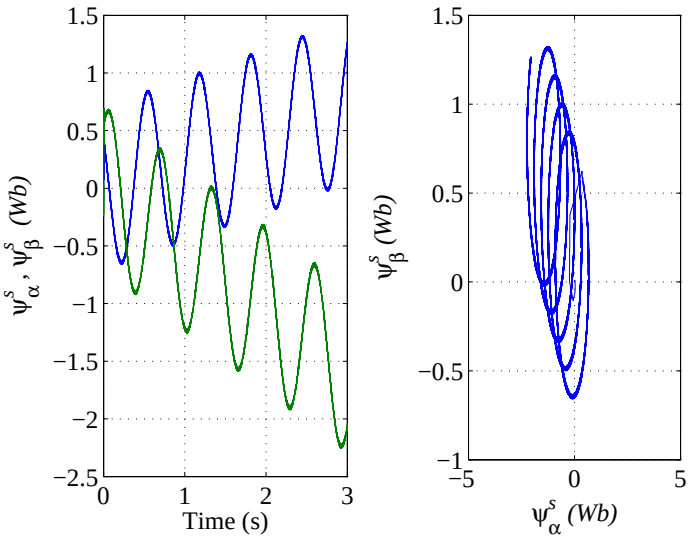

Figure 4.6: Stator flux linkage estimate. Pure integrator drift problem.

Moreover, at very low speed, estimators based on the voltage model can not operate successfully due to the following problems:

- at low frequency, the stator voltage $\alpha - \beta$ components v_α^s and v_β^s, are very low and difficult to measure.

- The variation of the stator resistance R_s, due to temperature variations, reduces the accuracy of the estimated signals. However, at higher voltage, the resistance variation effect can be neglected.

In the low speed region, the $\alpha - \beta$ components of the rotor flux ψ_α^r and ψ_β^r can be easily estimated with the help of the motor speed and current signals [59]. The rotor flux equations given in (2.40), (2.41), (2.43) and (2.44) in chapter 2, can be written in the $\alpha - \beta$ frame as

$$\psi_\alpha^m = \psi_\alpha^s - L_l^s i_\alpha^s = L_m(i_\alpha^s + i_\alpha^r) \tag{4.15}$$

$$\psi_\beta^m = \psi_\beta^s - L_l^s i_\beta^s = L_m(i_\beta^s + i_\beta^r) \tag{4.16}$$

$$\psi_\alpha^r = L_m i_\alpha^s + L_r i_\alpha^r \tag{4.17}$$

$$\psi_\beta^r = L_m i_\beta^s + L_r i_\beta^r \tag{4.18}$$

Eliminating i_α^r and i_β^r from (4.17) and (4.18), the following equations can be derived,

$$\psi_\alpha^r = \frac{L_r}{L_m}\psi_\alpha^m - L_l^r i_\alpha^s \tag{4.19}$$

$$\psi_\beta^r = \frac{L_r}{L_m}\psi_\beta^m - L_l^r i_\beta^s \tag{4.20}$$

which can be written as:

$$\psi_\alpha^r = \frac{L_r}{L_m}\psi_\alpha^s - \frac{L_s'}{L_m} i_\alpha^s \tag{4.21}$$

$$\psi_\beta^r = \frac{L_r}{L_m}\psi_\beta^s - \frac{L_s'}{L_m} i_\beta^s \tag{4.22}$$

Table 4.3: Induction motor parameters.

Output power	2500 W	Current	6.8 A
Voltage	380 V	Stator leakage inductance	9.2516 mH
Pole pairs	2	Rotor leakage inductance	9.2516 mH
Torque	16 Nm	Magnetizing inductance	167.215 mH
Stator resistance	2.1 Ω	Rotor resistance	2.6 Ω

where $L'_s = L_s L_r - L_m^2$.
Finally, the $\alpha - \beta$ components of the stator flux are given by

$$\psi_\alpha^s = i_\alpha^s \frac{L'_s}{L_m} + \psi_\alpha^r \frac{L_m}{L_r} \tag{4.23}$$

$$\psi_\beta^s = i_\beta^s \frac{L'_s}{L_m} + \psi_\beta^r \frac{L_m}{L_r} \tag{4.24}$$

Although the method requires the motor speed and almost all the motor parameters, it has been considered for simulation and experimental tests because it has been shown to be effective achieving very good estimate.

4.2.3 Simulation Results

The performance of the conventional DTC fed by a VSI has been analyzed by means of simulation tests. The simulation models were programmed in MatLab/Simulink operating with a sampling period of $T_s = 70\mu s$ The parameters of the IM used are shown in table 4.3. In the experimental rig, a DC machine dissipating the generated energy in a high power resistor, was coupled to the IM shaft. The high inertia introduced by the coupled DC machine has also been included for simulation purposes.

During the tests, the electromagnetic torque and stator flux linkage hysteresis bands were set to $BT_e = \pm 2.5\%$ and $B\psi^s = \pm 0.5\%$ of their respective rated values. The simulated system correspond to the experimental rig[3] shown in Fig. 4.12.

[3]The experimental rig and results are discussed later in this chapter.

Steady state performance

Firstly, a steady state test was carried out. The torque and stator flux references were set to their rated values $T_e^* = 16Nm$ and $\psi^{s*} = 0.702Wb$. The electromagnetic torque, stator flux linkage modulus and its $\alpha - \beta$ components are shown in Fig. 4.7. As it can be seen, both the stator flux linkage modulus and the electromagnetic torque follow their reference values. However, a high ripple in the electromagnetic torque can be noted, which is one of the main drawbacks of the conventional DTC [10], [60], [61]. The figure also shows the sinusoidal performance of the measured output currents $\alpha - \beta$ components.

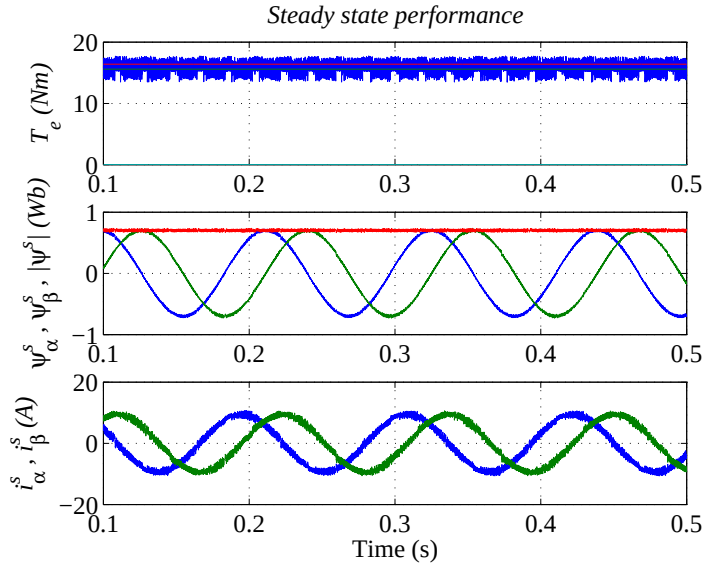

Figure 4.7: Conventional DTC steady state performance.

In order to corroborate the switching strategy explained in section 4.2.1, a zoomed area of the electromagnetic torque, stator flux linkage and the corresponding applied vectors are shown in Fig. 4.8, when the stator flux vector is lying in sector 1. The hysteresis bands corresponding to the torque and stator flux hysteresis comparators are also plotted. It can be seen how the output voltage vectors match with what was expected from column 3 of table 4.2. Moreover, the influence of the applied vectors can be analyzed and

compared to what was explained in section 4.2.1 and shown in Fig. 4.2.

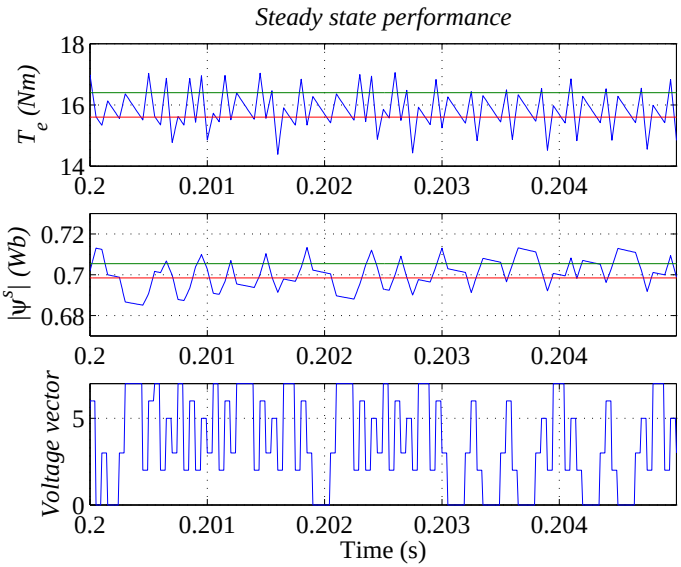

Figure 4.8: Switching strategy. Flux vector lying in sector 1.

The $\alpha - \beta$ components of the stator flux linkage are repeated in Fig. 4.9 showing the stator flux vector path. As expected from section 4.2.1 and Fig. 4.5, the stator flux linkage vector tracks a circular trajectory following its reference, within the hysteresis bands, in a zigzag path.

Transient performance

Here, the transient behavior of the conventional DTC fed by a VSI is analyzed. The start-up transient performance is firstly analyzed, which can be one of the drawbacks of the conventional DTC for IM [10]. As shown in Fig. 4.10, the stator flux can not be controlled while the electromagnetic torque reference is zero.

As it can be noted from table 4.2, when the developed torque is within the corresponding hysteresis bands, the torque comparator takes priority over the stator flux one. Under this condition null vectors (V_0 or V_7) are applied

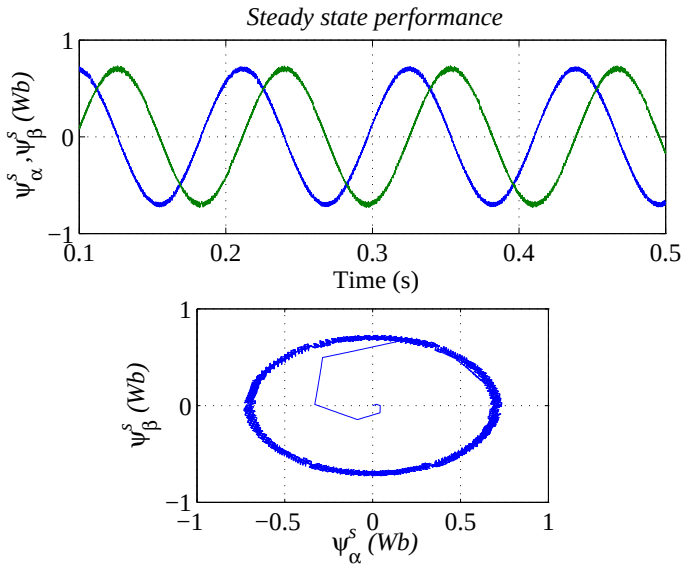

Figure 4.9: Stator flux linkage path.

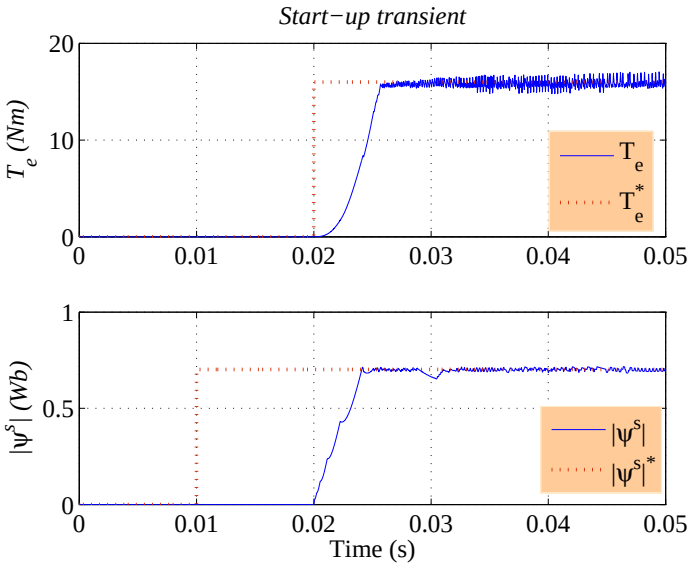

Figure 4.10: Start-up transient.

by the system in order to maintain the electromagnetic torque within the corresponding hysteresis bands, thus not controlling the stator flux any further. At start-up, when both the electromagnetic torque reference and the developed one are zero, the DTC algorithm will apply null vectors being unable

to produce any flux. Since the stator flux is not produced until the torque reference is different from zero, the torque rise time is increased during the start-up due to the dependency of the torque on the stator flux modulus as it follows from 4.7.

In order to analyze the transient performance and the decoupled control capability of the conventional DTC, a transient test has been carried out in which a step in the electromagnetic torque reference, going from positive rated torque T_{eN} to negative rated torque $-T_{eN}$, is introduced at $t = 0.25$ s as shown in Fig. 4.11.

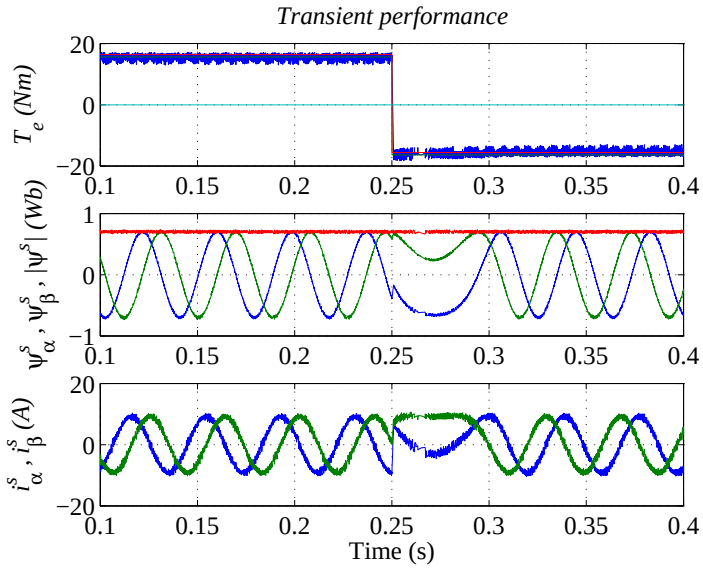

Figure 4.11: Torque step transient.

The fast electromagnetic torque response, which is one of the main advantages of the DTC, is here shown. Furthermore, as it can be seen, there is an effective decoupled control of the electromagnetic torque and the stator flux. Obviously, due to the speed reversal, when the torque step takes place the stator flux vector must rotate in the opposite direction while maintaining its modulus at the reference value. Although the electromagnetic torque response is very fast, the mechanical one is much slower due to the high inertia

introduced by the coupled DC drive. This can be seen from the $\alpha - \beta$ components of the stator flux ψ_α^S and ψ_β^s which rotating speed takes about $50ms$ to be reestablished in the opposite direction. Also the $\alpha - \beta$ components of the measured currents i_α and i_β are shown in Fig. 4.11.

4.2.4 Experimental Results

In order to corroborate the results obtained by simulation tests, experimental tests were also carried out. The machine used is the same as for the simulation tests and its parameters are shown in table 4.3. In order to compare the results, the system setup was the same as for the simulation tests. The sampling period was set to $T_s = 70\mu s$, and the hysteresis bands of both the electromagnetic torque and the stator flux comparators were set to $BT_e = \pm 2.5\% Nm$ and $B\psi^s = \pm 0.5\% Wb$ respectively. The general structure of the experimental rig used to implement and test the conventional DTC is shown in Fig. 4.12. A development system for the TMS320C40 32-bit floating point DSP was used to implement the DTC algorithm. Due to lack of specific peripherals for motor control of this DSP platform, additional logic boards were used for the PWM generation[4], analogue to digital conversion and encoder signals interfacing. As shown in Fig. 4.12, all the interface boards are connected with the DSP through a parallel data bus (DSPLINK). The PWM board directly controls the switches of a 7.5 kW *Eurotherm 620 vector series* IGBT inverter which drives the IM. As a load, a 3kW DC machine, dissipating the generated energy on a high power resistor, was employed throughout the experimental tests.

Steady state performance

As in the case of simulation, the steady state performance is first analyzed by means of the electromagnetic torque, stator flux linkage modulus and its $\alpha - \beta$ components which are shown in Fig. 4.13. The figure also shows the

[4]The PWM board was modified so that a voltage vector could be delivered for the whole sampling period T_s.

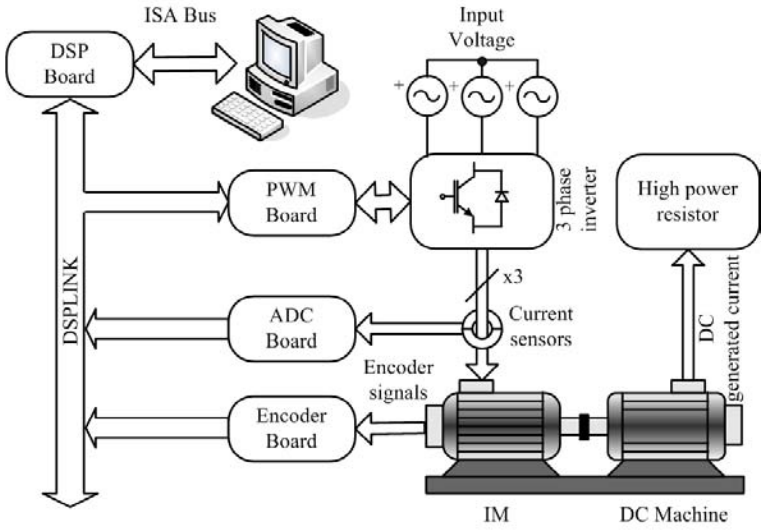

Figure 4.12: General structure of the experimental rig.

sinusoidal performance of the measured output currents $\alpha - \beta$ components. It can be seen how the electromagnetic torque and the stator flux perfectly follow their references. As it was expected from the simulation results, the electromagnetic torque ripple is very high in comparison to other control methods.

Although with higher values of ripple in the electromagnetic torque, the stator flux linkage, and in the measured currents, the experimental results shown in Fig. 4.13 closely match the results expected from the simulation ones shown in Fig. 4.7.

To complete the steady state analysis, the stator flux linkage vector path is shown in Fig. 4.14 in which the circular trajectory of the stator flux vector, following its reference, can be seen.

Transient performance

The transient performance and the decoupled control capability of the conventional DTC for IM is now experimentally analyzed by means of a transient test in which a step in the electromagnetic torque reference, going from posi-

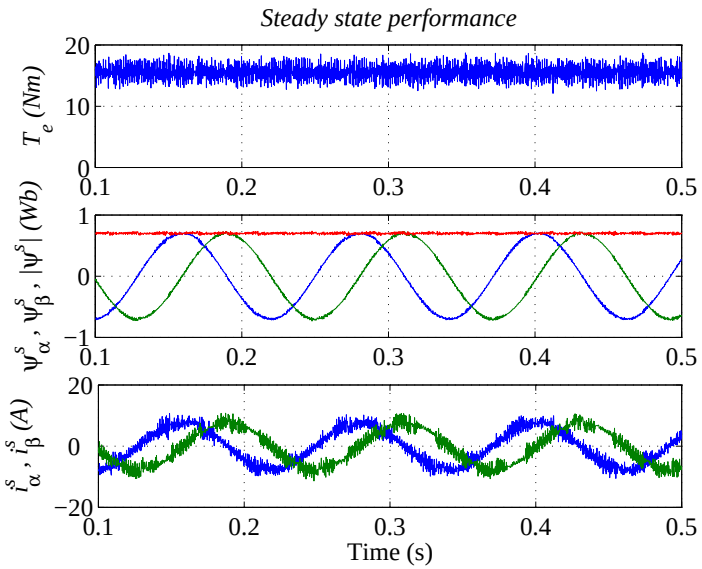

Figure 4.13: Conventional DTC steady state performance.

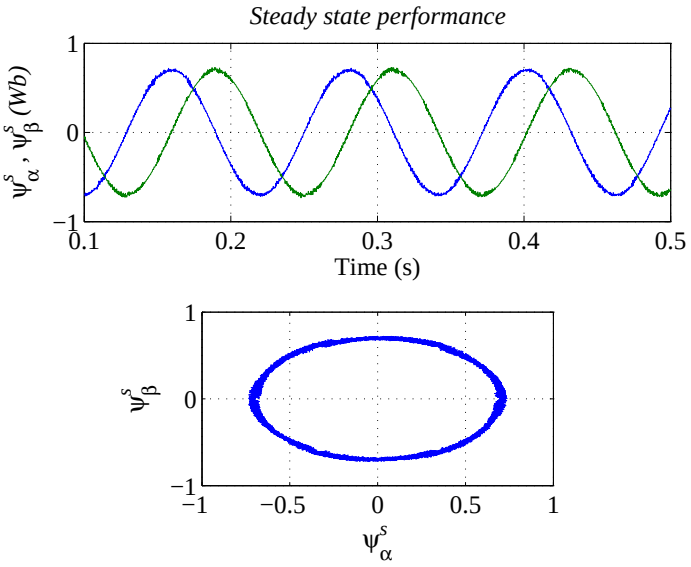

Figure 4.14: Stator flux linkage path.

tive rated torque T_{eN} to negative rated torque $-T_{eN}$, is introduced at $t = 0.25$ s as shown in Fig. 4.15. The fast torque response of the DTC shown in section 4.2.3 is here corroborated.

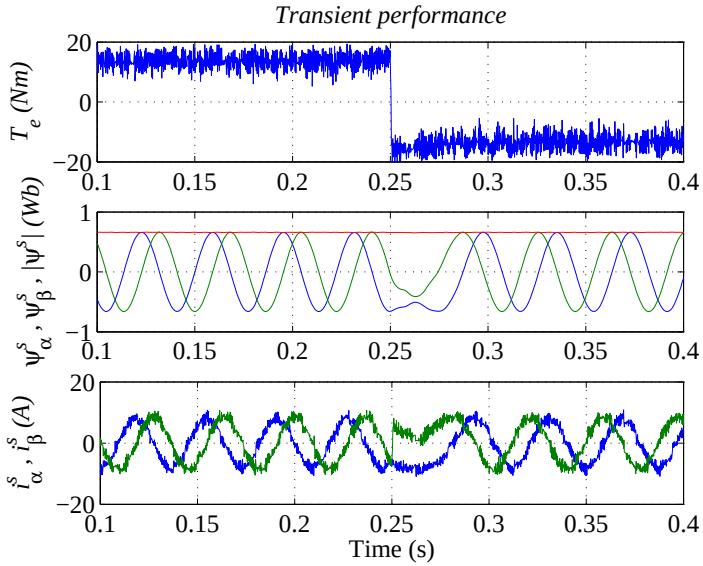

Figure 4.15: Torque step transient.

Moreover, an effective decoupled control of the electromagnetic torque and the stator flux is achieved as it can be seen in Fig. 4.15. As in the simulation results of Fig. 4.11, when the torque step takes place the stator flux vector must rotate in the opposite direction while maintaining its modulus at the reference value. As it can be noted from the $\alpha - \beta$ components of the stator flux ψ^s_α and ψ^s_β, the stator flux vector takes about $50ms$ due to the high inertia and dynamic performance of the DC drive connected as a load.

4.3 Direct Torque Control for Permanent Magnet Synchronous Machines

The DTC for a PMSM is very similar to the solution adopted for an IM. In fact all the above explanation holds for the DTC for the PMSM. Only the stator flux linkage ψ^s, and the electromagnetic torque T_e estimators have to be adapted for the PMSM model. An expression for the electromagnetic torque of a PMSM was introduced in (2.63), and is repeated here for convenience.

$$T_e = \frac{3}{2}p[\psi_{PM} i_q^s + (L_d^s - L_q^s) i_d^s i_q^s] \tag{4.25}$$

Based on the phasor diagram given in Fig. 4.16, the stator flux linkage ψ^s and the torque angle δ can be considered, instead of i_d^s and i_q^s

$$\psi_{PM} + L_d^s i_d = \psi^s \cos\delta \tag{4.26}$$

$$L_q^s i_q = \psi^s \sin\delta \tag{4.27}$$

Hence, (4.25) can be expressed as follows:

$$T_e = \frac{3}{2}p[\psi_{PM} \frac{\psi^s}{L_q^s} \sin\delta + \frac{1}{2}(L_d^s - L_q^s) \frac{(\psi^s)^2}{L_d^s L_q^s} \sin(2\delta)] \tag{4.28}$$

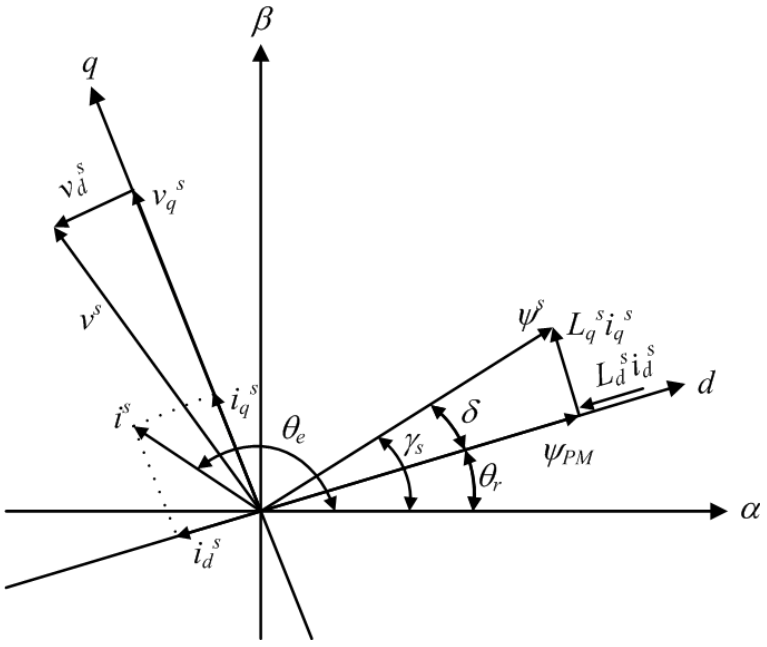

Figure 4.16: Phase diagram in the stationary reference frame.

It is noted that to modify the electromagnetic torque value, either the stator flux linkage amplitude or the angle δ (*torque angle*) has to be changed as in the case of the IM, with the difference that now the coordinates are fixed to the rotor.

4.3.1 DTC Scheme and Optimum Voltage Vector Selection for PMSM

According to (4.28), the electromagnetic torque can be controlled by changing the amplitude and position of the stator flux linkage vector $\vec{\psi}^s$. As in the case of an IM-DTC drive, neglecting the stator resistance, it can be assumed a variation of the stator flux linkage $\Delta\vec{\psi}^s \approx \vec{v}^s\Delta t$ in the same direction of the applied voltage vector $\vec{v}^s$. The stator flux linkage will rotate at a speed proportional to the magnitude of the applied voltage vector. The electromagnetic torque will depend on the tangential component of the applied vector $\vec{v}^s$ while the magnitude of the stator flux linkage will depend on the radial component. The voltage vector influence on the stator flux linkage and the electromagnetic torque variation is similar to that discussed in section 4.2 (*see Fig.* 4.2) and was summarized in table 4.1. Hence the DTC scheme for a PMSM and the optimum switching table (*see table* 4.2) will be identical to the one derived for the IM.

4.3.2 Stator Flux and electromagnetic Torque estimate

The stator flux linkage can be estimated by integrating the back-emf as presented in section 4.2.2. However, when a rotor position sensor is available the stator current components in the rotor reference frame i_d^s and i_q^s can be obtained by using (2.10) [10]. Hence the stator flux linkage components in the rotor reference frame can be estimated as follows:

$$\psi_d^s = L_d^s i_d^s + \psi_{PM} \tag{4.29}$$

$$\psi_q^s = L_q^s i_q^s \tag{4.30}$$

where L_d^s is the direct-axis inductance and L_q^s is the quadrature-axis inductance. The stator flux linkage angle γ_s in the stationary reference frame is equal to the torque angle δ plus the rotor position θ_r, as it follows from Fig. 4.16.

$$\gamma_s = \theta_r + \delta = \theta_r + \arctan\left(\frac{\psi_q^s}{\psi_d^s}\right) \tag{4.31}$$

Finally, the electromagnetic torque can be estimated as follows:

$$T_e = \frac{3}{2}p(\psi_d^s i_q^s - \psi_q^s i_d^s) \tag{4.32}$$

Stator flux linkage reference

Figure 4.17 shows the block diagram for the DTC-PMSM drive which is very similar to the one for IM discussed in section 4.2. However, here the stator flux linkage reference is obtained from the reference value of the electromagnetic torque. The function $\psi^{s*}(Te^*)$ can be obtained, up to the base speed, by ensuring maximum torque per ampere [10].

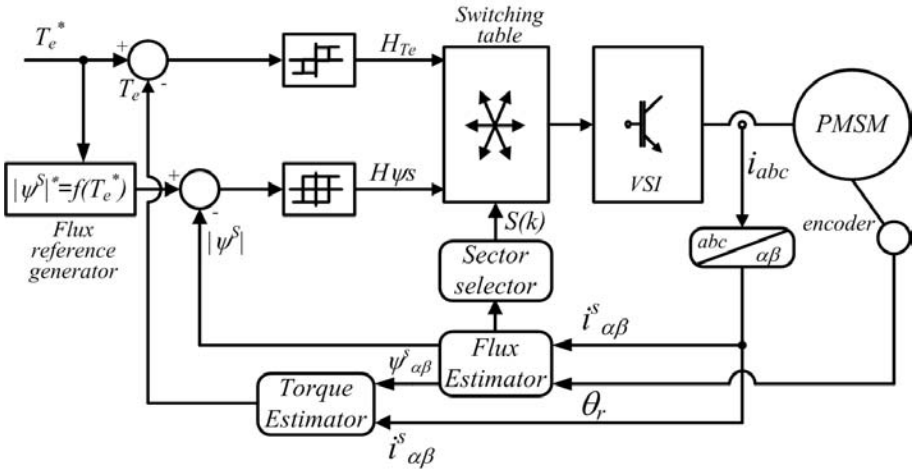

Figure 4.17: Direct Torque Control for PMSM. Block diagram

To achieve the desired electromagnetic torque with minimum stator current, the stator current direct axis component i_d^s is forced to zero. Thus (4.29) becomes

$$\psi_d^s = \psi_{PM} \tag{4.33}$$

and the stator flux modulus

Table 4.4: PMSM parameters.

Output power	200 W	Rated current	2 A
Voltage	100 V	L_d^s per phase	8.3 mH
Pole pairs	4	L_q^s per phase	8.6 mH
Torque	0.64 Nm	Rated speed	3000 rpm
Stator resistance	2.5 Ω	Maximum speed	4500 rpm

$$|\psi^s| = \sqrt{\psi_{PM}^2 + (L_q^s i_q^s)^2} \tag{4.34}$$

For a surface mounted PMSM ($L_d^s = L_q^s$), the electromagnetic torque can be expressed as

$$T_e = \frac{3}{2} p \psi_{PM} i_q^s \tag{4.35}$$

Thus the torque producing current can be written as follows:

$$i_q^s = \frac{2}{3} \frac{T_e}{p\psi_{PM}} \tag{4.36}$$

Substituting (4.36) in (4.34), the relationship between the stator flux linkage and the electromagnetic torque is obtained.

$$|\psi^s| = \sqrt{\left[\psi_{PM}^2 + \left(\frac{2}{3} \frac{T_e L_q^s}{p\psi_{PM}}\right)^2\right]} \tag{4.37}$$

Thus for maximal torque per ampere operation the required value of the stator flux linkage reference is

$$|\psi^{s*}| = \sqrt{\left[\psi_{PM}^2 + \left(\frac{2}{3} \frac{T_e^* L_q^s}{p\psi_{PM}}\right)^2\right]} \tag{4.38}$$

4.3.3 Simulation Results

In order to analyze the performance of the conventional DTC fed by a VSI for a PMSM, simulation tests have been carried out by means of the MatLab/Simulink package. In this case, the sampling period has been set to $T_s = 50\mu s$. The parameters of the PMSM employed throughout the simulation tests are given in table 4.4.

Steady state performance

The analysis of the steady state performance has been carried out with the following settings:

- Torque reference, $T_e = 0.64\ Nm$ (rated torque)
- Flux reference, $|\psi^{s*}| = \sqrt{\left[\psi_{PM}^2 + \left(\frac{2}{3}\frac{T_e^* L_q^s}{p\psi_{PM}}\right)^2\right]}$
- Torque hysteresis bands, $BT_e = \pm 2.5\%$ of rated torque.
- Flux hysteresis bands, $B\psi^s = \pm 2.5\%$ of the permanent magnet flux.

The electromagnetic torque, stator flux linkage modulus, and its $\alpha - \beta$ components are shown in Fig. 4.18. Both the stator flux modulus and the electromagnetic torque follow their references. Due to the lower inductances of a PMSM, the electromagnetic torque ripple is slightly higher compared to a DTC-IM drive.

One of the DTC features is the indirect control of the stator currents (*with approximately sinusoidal waveforms*). The indirect control of the stator currents can be proved by means of the sinusoidal performance of its $\alpha - \beta$ components.

To achieve the desired electromagnetic torque with minimum stator current, the function $\psi^{s*}(Te^*)$ is used to set the correct stator flux reference value. As explained in section 4.3.2, to ensure maximum torque per ampere, the stator current direct axis component i_d^s must be forced to zero.

Figure 4.19 shows both the direct axis i_d^s and the quadrature axis i_q^s currents. It can be seen that the direct axis current i_d^s is zero. This fact proves the maximum torque per ampere operation of the DTC. Varying the torque producing current i_q^s, the torque angle δ can be changed to achieve the desired torque. The stator flux components, in the rotating *d-q* frame, ψ_d^s and ψ_q^s are also shown in Fig. 4.19. As expected, the direct axis flux component ψ_d^s equals the permanent magnet flux $\psi_{PM} = 0.046Wb$. The quadrature axis

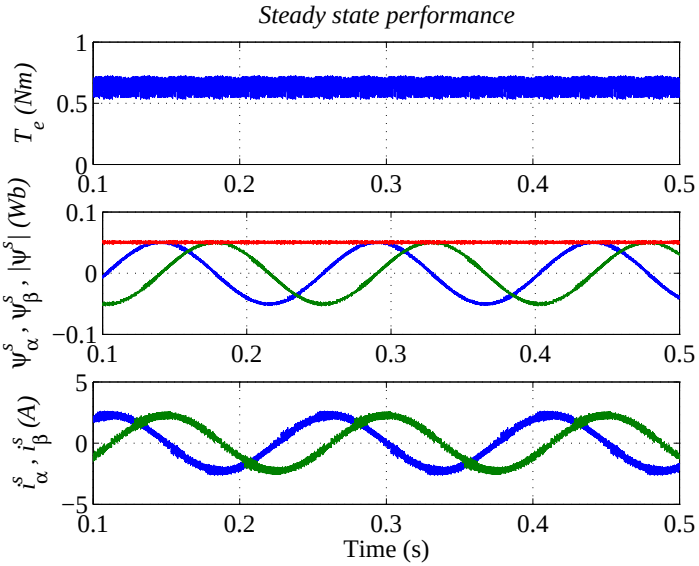

Figure 4.18: DTC for PMSM. Steady state performance.

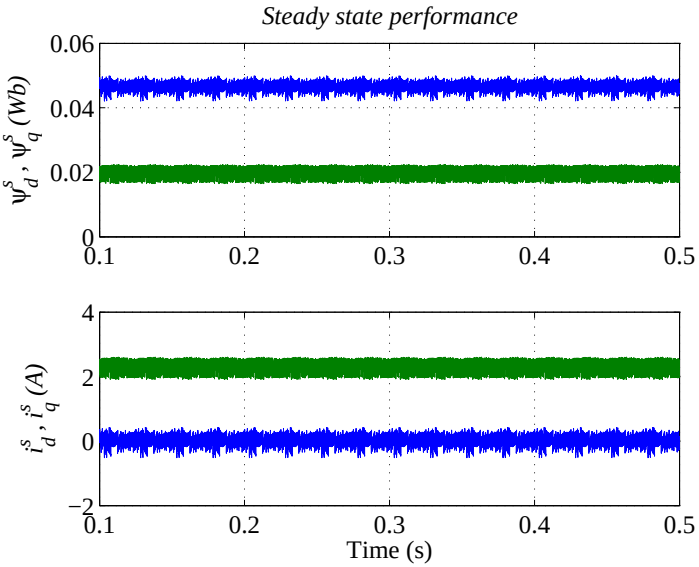

Figure 4.19: DTC for PMSM. Maximum torque per ampere.

flux component makes the stator flux vector to move away from the d-axis (*by a angle* δ), hence, producing the desired torque.

A zoomed area of the electromagnetic torque, the stator flux linkage, and the applied vector is shown in Fig. 4.20 when the stator flux vector is lying in sector 1. The torque and flux hysteresis comparators bands are also depicted. From the figure, the influence of the applied vectors, depending on the hysteresis comparators states, can be analyzed.

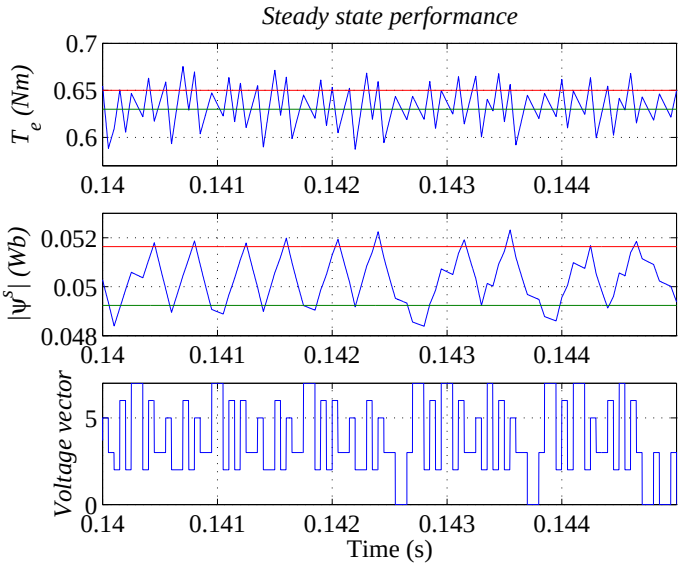

Figure 4.20: DTC for PMSM. Switching strategy for flux vector lying in sector 1.

The sinusoidal performance of the $\alpha - \beta$ components of the stator flux and the circular trajectory of its modulus are shown in Fig. 4.21. Again, the circular trajectory of the stator flux vector, following its reference within the corresponding hysteresis bands, is corroborated.

Transient performance

The transient behavior of the conventional DTC fed by a VSI for a PMSM is analyzed here. The problem of the start-up transient discussed in section 4.2.3 for a DTC-IM drive is solved when using a PMSM. When a IM is employed, the machine cannot be magnetized prior to a non-zero electro-

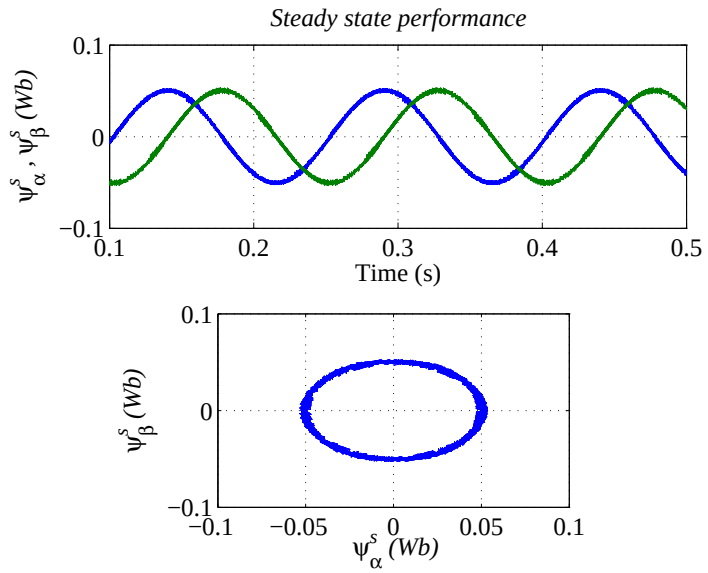

Figure 4.21: DTC for PMSM. Stator flux linkage trajectory.

magnetic torque command. Due to the permanent magnets flux ψ_{PM}, before any excitation, a constant flux is already present in the machine. This value corresponds to the flux reference delivered by the stator flux reference generator shown in Fig. 4.17. When the electromagnetic torque reference is set to zero, from (4.38), derived in section 4.3.2, $|\psi^s|^* = \psi_{PM}$ is obtained. As a Consequence, the electromagnetic torque response of PMSM during the start-up process is much faster compared to that of an IM.

Figure 4.22 shows the performance of both the electromagnetic torque and the stator flux during the start-up process. A step command in the torque reference, going from zero to the rated torque, was imposed at $t = 0.02s$ to carry out the test. The figure shows that prior to the torque step command, the stator flux is the one delivered by the permanent magnets, and the fast response of both the flux and electromagnetic torque when the step command takes place.

A transient test in which a step command in the electromagnetic torque reference, going from positive rated torque T_{eN} to negative rated torque $-T_{eN}$,

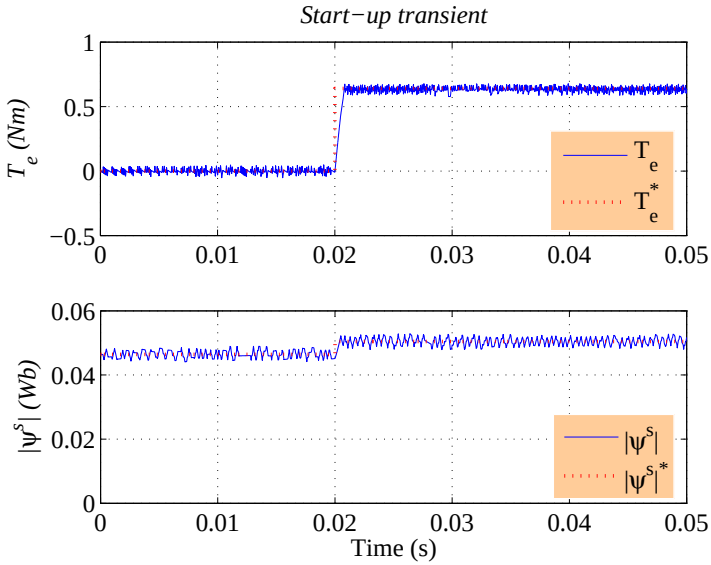

Figure 4.22: DTC for PMSM. Start-up transient.

is introduced at $t = 0.25$ s to analyze the transient performance and the decoupled control capability of the electromagnetic torque and the stator flux.

The electromagnetic torque, the $\alpha - \beta$ components of the stator flux (ψ^s_α and ψ^s_β) and the measured currents (i^s_α and i^s_β) are shown in Fig. 4.23. As it can be noted, the DTC-PMSM drive shows a very fast response in the electromagnetic torque. From flux $\alpha - \beta$ components it is noted that also the speed reversal is very fast due to the very low inertia of the system (PMSM + hysteresis brake). It can be seen how the stator flux modulus remains constant during the electromagnetic torque transient[5], showing an effective decoupled control of both variables.

The decoupled control capability can also be analyzed by means of the direct i^s_d and quadrature i^s_q currents. As shown in Fig. 4.24, the flux producing current i^s_d remains at zero to ensure maximum torque per ampere operation of the drive, whereas the torque producing current i^s_q shows the same tran-

[5]The stator flux reference $|\psi^{s*}|$ remains constant as the modulus of T^*_e is the same for both torque references (see equation (4.38)).

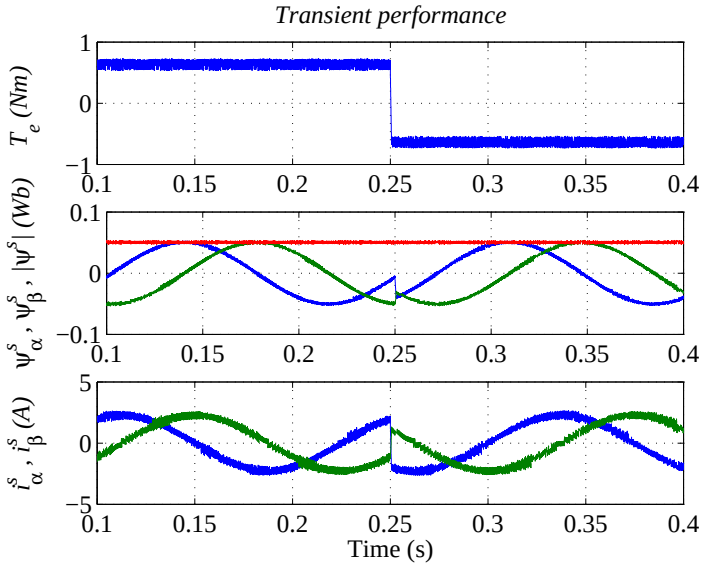

Figure 4.23: DTC for PMSM. Torque step transient.

sient performance as the electromagnetic torque shown in Fig. 4.23.

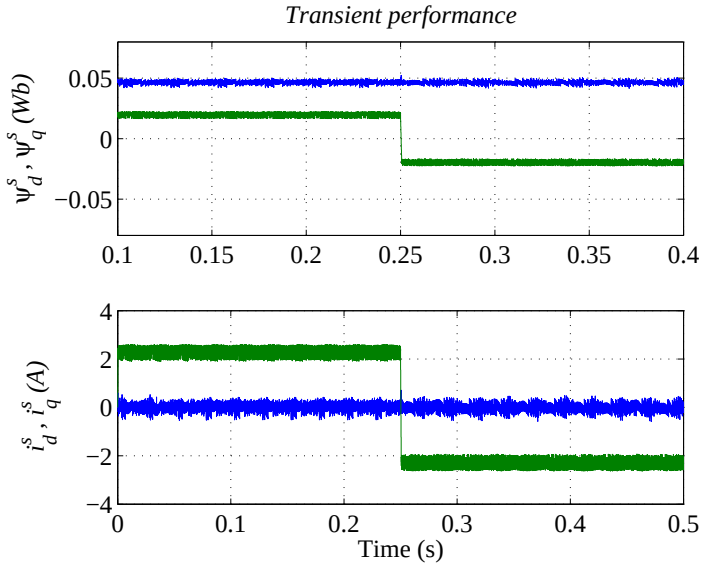

Figure 4.24: DTC for PMSM. Torque step transient.

The stator flux components, in the rotating d-q frame, ψ^s_d and ψ^s_q, are

Table 4.5: DTC advantages and disadvantages.

Advantages	Disadvantages
No coordinate transformation is needed	Possible problems during start up
Absence of separate modulation block	Flux and torque estimators are needed
Current PI controllers are not required	Varying switching frequency
Very fast torque response	High torque ripple

also shown in Fig. 4.24. Due to the maximum torque per ampere operation of the DTC, the direct axis flux component ψ_d^s equals the permanent magnet flux $\psi_{PM} = 0.046Wb$. To produce the desired electromagnetic torque, the quadrature axis flux component ψ_q^s forces the stator flux vector to move away from the d-axis (*by a angle* δ).

4.4 Improvements on Direct Torque Control

The main features of the DTC have been shown in the previous sections. These features can be classified as follows:

- Direct control of both stator flux linkage and electromagnetic torque by selecting the optimum inverter voltage vectors.
- Indirect control of currents (*approximately sinusoidal*) and voltages.
- High dynamic performance.
- The inverter switching frequency depends on the widths of both flux and torque hysteresis bands.

Table 4.5 summarizes the main advantages and disadvantages of the DTC.

Intensive research is being made and different approaches have been proposed to improve the conventional DTC performance. Most of these approaches are devoted to reduce the inherent high torque ripple associated with this control strategy and can be classified, regarding the solution adopted, as follows:

- Modification of the conventional switching table and hysteresis comparators.
- Introduction of Space Vector Modulation.
- DTC with zero vector duty ratio control.
- Use of different converters topologies.

Modification of the conventional switching table and the hysteresis comparators

There are several solutions consisting in the modification of the switching table and the hysteresis comparators. The easiest solution is to divide the stator flux linkage vector path into twelve sectors [59] instead of six as in the conventional switching table. As it has been explained in section 4.2, in the conventional DTC, with the flux vector lying in any sector, there are two voltage vectors presenting torque ambiguity. Hence, these two vectors can not be used. The twelve sectors switching table addresses this problem and a new torque four-level hysteresis comparator is introduced, being able to distinguish between small and large torque errors. However, the results in [59] are not as good as expected and a non remarkable improvement of 9% in the flux integral square error is achieved, while making worse the torque performance.

Other solutions consist in the use of different optimum switching tables [62] depending on the operating point of the machine. It is well known that, due to the back EMF variation, zero vectors have different effect at different speeds. In the high speed region zero vectors produce a large decrease in torque, whereas at low speeds they maintain it almost constant. Several switching tables can be obtained taking into consideration the effects on both stator flux and torque of the applied voltage vector at different operating points.

Discrete Space Vector Modulation (DSVM) [61] consists in dividing the sampling period into three intervals. Applying different vectors in each of

these intervals new voltage vectors can be synthesized. As the number of available vectors is increased, more accurate switching tables can be defined in which the selection of the voltage vectors can be made according to the rotor speed, achieving a considerable torque ripple reduction.

DTC with Space Vector Modulation

As the SVM can synthesize any voltage vector, this technique can be used to synthesize a voltage vector that force the torque and flux errors to zero. In [63] a deadbeat controller is used to calculate the reference voltage vector which will be synthesized by the SVM block. Although very good performance is achieved, the method involves the calculation of a reference voltage vector and more complex computational algorithms. Hence, loosing the simplicity of the conventional DTC. Moreover, an accurate machine model is required.

A method similar to the Stator Field Oriented Control (SFOC) without current control loops is proposed in [64]. This strategy uses torque and stator flux loops with PI controllers to provide the reference voltage vector. Thus, no machine parameters are used to calculate the reference voltage vector as in [63]. However, due to the integral action of the PI controllers, the torque response is slower.

DTC with zero vector duty ratio control

Another alternative to the conventional DTC is the DTC with zero vector duty ratio control. It consists in the amplitude variation of the inverter voltage vectors applying the vector delivered by the conventional switching table during a portion of the sampling period and a zero vector for the remaining time. The duty ratio (δ) determines the duration of the vector selected by the switching table. Varying δ a voltage vector with the desired amplitude can be delivered to the machine terminals achieving a considerable reduction of the torque ripple without increasing the switching frequency as much as in the case of SVM methods. The duty ratio can be calculated by means of

minimizing the torque ripple condition based on a ripple equation derived in [60]. Other approaches to obtain δ, based on fuzzy logic, has been proposed [65], [66].

DTC using different converters topologies

As it has been shown, the conventional DTC fed by a standard two-level VSI has some limitations as the number of available voltage vectors. Techniques based on SVM can increase this number with vectors of different amplitudes and directions. Moreover, an increased number of voltage vectors with different amplitudes is achieved in the DTC with zero vector duty ratio control. However, all the approaches based on these techniques achieve considerable improvements at the cost of increasing the system complexity.

An alternative way to increase the number of available vectors is to use a multilevel topology converter. One of the first works in this field was introduced by Takahashi in 1989 [67], in which a new topology with two sets of VSI using GTO switches is employed to implement a DTC driving an IM. This new topology was able to deliver the same 18 active vectors of a three-level VSI. In recent years intensive research have been done in this field. In order to use all the available vectors of three-level VSI, an extended new switching table is introduced in [13] and [12]. Also the stator flux and torque hysteresis comparators were modified introducing more levels to which compare the corresponding errors.

As it has been mentioned in chapter 3, in the last years, MC has emerged to become a good alternative to the conventional VSI. Following the tendency of using different converter topologies to implement a DTC drive, some authors have investigated the use of MC to improve the DTC performance. The earliest work was presented in 2001 by D. Casadei [2][6]. In addition to the conventional DTC drive, based on a switching table with two entries to select the inverter state, based on the flux and torque errors signals, a new entry was introduced to select the rectification stage vector: the average value of

[6] A detailed explanation of this method is given in chapter5.

the sinus of the displacement angle between the input voltage vector and the corresponding input current vector. The authors claim that this DTC scheme gives good performance in the high speed range, proven with simulations, but no investigation have been made to determine how the limit of the voltage transfer ratio is affected [14].

4.5 Conclusions

In this chapter, the conventional DTC for IM and PMSM has been described and studied. The features of the conventional DTC (*advantages and disadvantages*) have been analyzed. The benefits of the DTC, as the fast torque response and indirect control of the stator currents, have been proved.

It is well known that one of the main drawbacks of this control method is the inherent torque ripple, mainly due to the hysteresis comparators. This issue is more accentuated when a PMSM is driven by the DTC as its stator inductance is around 1/2 of that of an IM of similar ratings. However, as it was mentioned in section 2.2.2 of chapter 2, the PMSM is gaining attention due to its great benefits over the IM and is, nowadays, a very close competitor to IM drives in many industrial applications.

Moreover, different methods, proposed in the literature, to improve the conventional DTC performance have been reviewed. Most of the methods presented involve an increase in the complexity of the control algorithm.

Chapter 5

DTC-PMSM Drives using Matrix Converters: The use of small vectors

5.1 Introduction

Several methods, proposed in the literature, to improve the conventional DTC performance were reviewed in section 4.4 of chapter 4. These methods were classified regarding the solution adopted, the use of an alternative power converter topology being one of them. In chapter 3, the advantages of the MC over the conventional VSI were highlighted.

This chapter starts describing the DTC using a MC proposed in [2][1], driving an IM. The same control method is then implemented using a PMSM. The merits and demerits of the method are analyzed by means of simulation and experimental tests.

[1]This control method will be, hereinafter, referred to as *Classical DTC using MC*, or simply, *Classical method*.

A new DTC using small vectors of MCs[2], which reduces the electromagnetic torque ripple is presented. Finally, both methods are analyzed and compared by means of simulation and experimental tests.

5.2 Classical DTC using Matrix Converters

MCs and VSIs were analyzed in chapter 3 and it was shown that the MCs can generate active voltage vectors with the same direction of those generated by conventional VSIs, but with varying amplitudes (*pulsating vectors*). In fact, as it was shown in table 3.2, at any instant, there are three groups of voltage vectors with different amplitudes and equal direction. The output voltage vectors and the input current vectors of a MC are shown in Fig. 5.1 (a)[3] and (b) respectively.

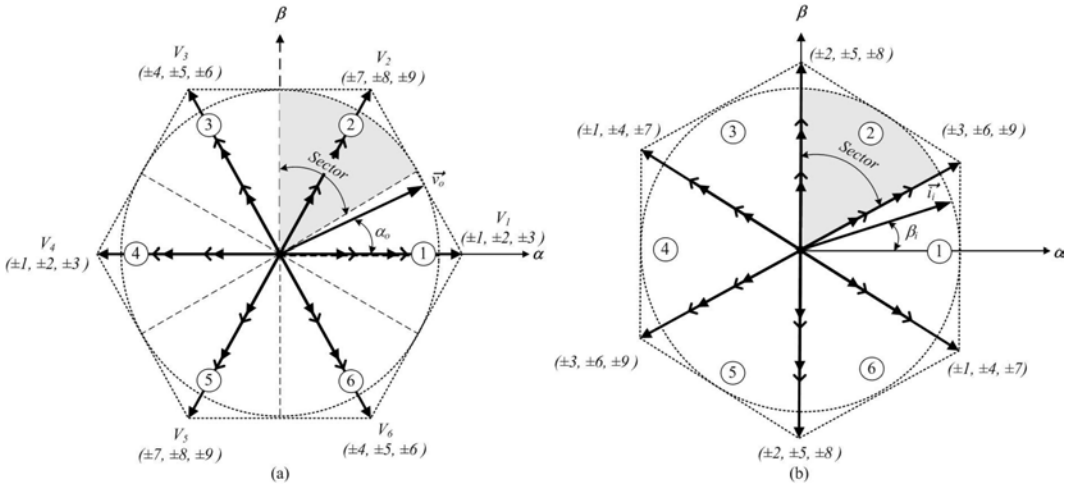

Figure 5.1: MC vectors. (a) Output voltage vectors. (b) Input current vectors.

The magnitude of the output voltage $\vec{v_o}$ and input current $\vec{i_i}$ vectors de-

[2]Hereinafter referred to as *proposed method*.

[3]$V_1 - V_6$ denotes MC vectors having the same direction as vectors $V_1 - V_6$ delivered by a VSI.

pend on the instantaneous input line-to-neutral voltages and output line currents respectively, as it was shown in table 3.2 in chapter 3. Dividing the input voltage vector path into six sectors, with sector one starting at $-\pi/6$ as shown in Fig. 5.2, those vectors with larger amplitudes can be used by the DTC algorithm depending on the sector in which the input voltage vector is lying. It is noted that these vectors (*large vectors* V^L) do not change their direction within a given sector. Moreover, it should be noted that for every sector there are four large vectors (*two of them in one direction and the other two in the opposite direction*) and two vectors with smaller amplitudes (*small vectors* V^S). However, as it can be seen in Fig. 5.2, small vectors change their direction in the middle of the sector. Hence, they cannot be used by the DTC algorithm.

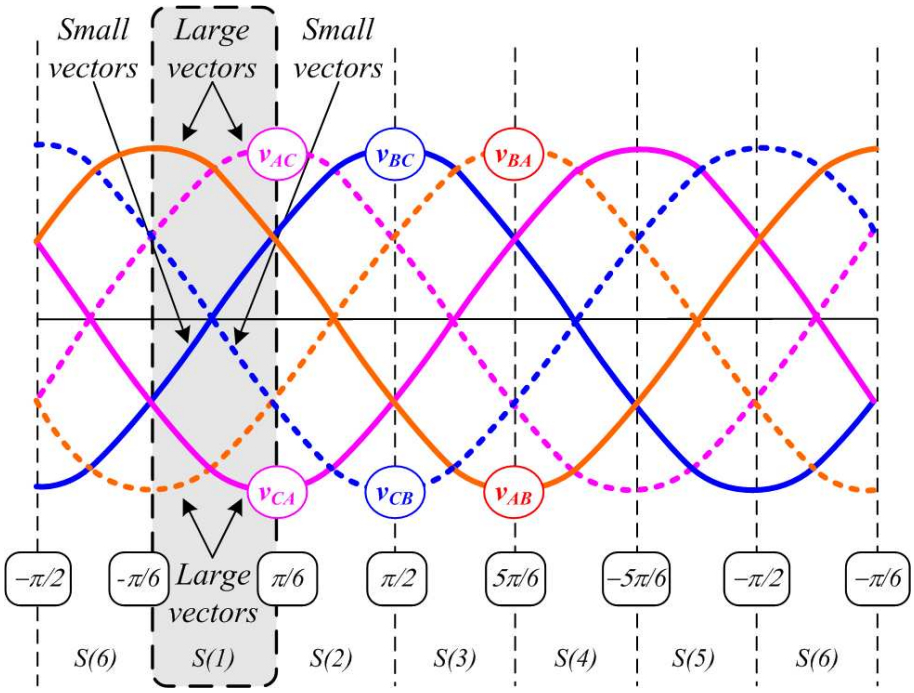

Figure 5.2: Amplitude variation of the input voltages. Six sectors division.

Moreover, for a given sector there are six current vectors. As shown in Fig. 5.1(b), these current vectors have different directions. In table 3.2 of chapter 3, the MC states were classified in groups. The first three groups

correspond to the active vectors (*pulsating vectors*) of the MC. Each of these three groups contain six different states corresponding to the same input line current amplitude; $\pm 2/\sqrt{3}$ of the corresponding output line current.

As it was explained in chapter 4, the DTC principle is based in the control of the stator flux vector (*which can be approximated by* $\Delta\vec{\psi}^s \approx \vec{v}^s \Delta t$), and this depends on the voltage vector direction delivered by the VSI.

The MC can deliver two output voltage vectors V^L fulfilling the DTC demands (*with the same direction of that delivered by a VSI*). These two states of the MC imposes two input current vectors with different direction as shown in Fig. 5.1 (b). One of these vectors will contribute to a leading current, whereas the other will contributed to lag the input current vector.

This extra degree of freedom can be exploited introducing a third control variable, such as the average value of the sine of the displacement angle ϕ between the input line current vector and the input line-to-neutral voltage vector, to keep under control the input power factor (pf). This requirement ($pf = 1$) is accomplished if this third variable is kept close to zero $< \sin\phi > \approx 0$. The average value of $\sin\phi$ can be obtained applying a of a low-pass filter to its instantaneous value. In order to control this new variable, a new hysteresis controller is introduced as shown in Fig. 5.3.

The estimators of the stator flux, electromagnetic torque, and $< \sin\phi >$, require the knowledge of the voltages and currents at the input and output side of the MC. Nevertheless, only the input voltages and output currents are measured. The other quantities are calculated on the basis of (3.16) and (3.17) derived in chapter 3.

The new control algorithm will select the switching state of the MC that generates a voltage vector with the same direction to that selected by the conventional DTC control algorithm[4]. Based on the fact that the magnitude

[4]The conventional DTC is analyzed in chapter 4.

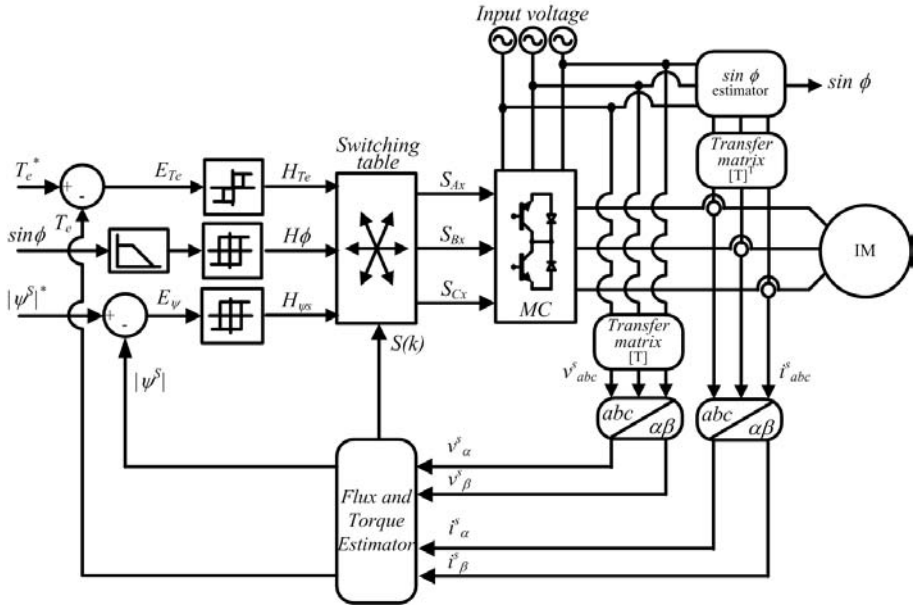

Figure 5.3: DTC fed by MC. Block diagram.

Table 5.1: DTC using MC optimum voltage vector selection table.

$\vec{v_i}$ sector	1		2		3		4		5		6	
H_ϕ	+1	-1	+1	-1	+1	-1	+1	-1	+1	-1	+1	-1
V_1	-3	1	2	-3	-1	2	3	-1	-2	3	1	-2
V_2	9	-7	-8	9	7	-8	-9	7	8	-9	-7	8
V_3	-6	4	5	-6	-4	5	6	-4	-5	6	4	-5
V_4	3	-1	-2	3	1	-2	-3	1	2	-3	-1	2
V_5	-9	7	8	-9	-7	8	9	-7	-8	9	7	-8
V_6	6	-4	-5	6	4	-5	-6	4	5	-6	-4	5

and direction of the output voltage vectors depend on the sector in which the input voltage vector is lying, a new MC switching table can be developed. Table 5.1 shows the switching table for the implementation of the DTC using a MC [2]. The first column contains the VSI voltage vectors selected by the conventional DTC. The top row contains the sector in which the input voltage vector lies. Depending on the pf control needs H_ϕ , one of the two sub-columns $(+1, -1)$ are selected. From Fig. 5.2, table 5.1 and table 3.2, it can be seen that only those vectors having the maximum amplitude are considered for the DTC.

The criteria utilized to select the proper MC state can be clarified by means of an example. Assuming that V_1 is the output voltage vector selected by the conventional DTC control algorithm, from Fig. 5.1 (a) it is noted that one of the switching states ± 1, ± 2 or ± 3 should be selected. Since the magnitude and direction of these voltage vectors depends on the input voltages, only those having the same direction as V_1 will be taken into consideration. If the input line-to-neutral voltage vector lies in sector 1, the switching states $+1$ and -3 can be chosen. From Fig. 5.1 (b), it can be seen that these two switching states corresponds to input current vectors lying on the sector 1 boundary directions. If a power factor increase is needed, that is, the average value of $\sin\phi$ has to be decreased, the switching state -3 has to be selected. On the other hand, if a power factor decrease is needed, that is, $< \sin\phi >$ has to be increased, the switching state $+1$ should be selected. When the torque error is within the hysteresis comparator bands a zero vector which minimizes the number of commutations is selected [2].

5.2.1 Simulation Results

As it has been mentioned in chapter 4, the DTC switching table for a PMSM is identical to the one used for an IM. Thus, the classical DTC using a MC for an IM, developed in [2], can be used to drive a PMSM as well.

Here, the performance of the classical DTC using MC driving a PMSM is analyzed by means of simulation tests. The simulation models were programmed using the MatLab/Simulink package. The PMSM is the same as the one used in section 4.3.3 of chapter 4, where the PMSM parameters are given in table 4.4.

Steady state performance

The DTC settings to analyze the steady state performance are as follows:

- Sampling period, $T_s = 50\mu s$
- Torque reference, $T_e = 0.64\ Nm$ (rated torque)

- Flux reference, $|\psi^{s*}| = \sqrt{\left[\psi_{PM}^2 + \left(\frac{2}{3}\frac{T_e^* L_q^s}{p\psi_{PM}}\right)^2\right]}$
- Torque hysteresis bands, $BT_e = \pm 2.5\%$ of rated torque.
- Flux hysteresis bands, $B\psi^s = \pm 2.5\%$ of the permanent magnet flux.
- Rotor speed, 100 rpm

It should be noted that the DTC settings are the same as those for the simulation tests of the DTC using a VSI to drive a PMSM presented in section 4.3.3 of chapter 4, so that both systems can be compared.

Firstly, the electromagnetic torque T_e and the stator flux linkage modulus $|\psi^s|$ are shown in Fig. 5.4. It can be seen how both variables follow their respective reference values T_e^* and $|\psi^{s*}|$.

The sinusoidal behavior of the stator flux and currents $\alpha - \beta$ components, demonstrates the indirect control capability of the DTC over these variables.

Comparing the results with those obtained in Fig. 4.18, it can be notice the performance similarity of both systems. Also, the electromagnetic torque ripple remains almost the same as in the case of the VSI fed DTC-PMSM analyzed in chapter 4.

The stator flux reference has been set using the function $\psi^{s*}(T_e^*)$ to achieve the desired electromagnetic torque with minimum stator current. In order to prove that the maximum torque per ampere has been achieved, the direct axis i_d^s and quadrature axis i_q^s currents are shown in Fig. 5.5. As it can be seen, the flux producing current i_d^s is zero. The *d-q* components of the stator flux are also depicted, showing that $\psi_d^s = \psi_{PM} = 0.046Wb$.

The influence of the applied vectors (*regarding its direction* $V_0 - V_7$) is analyzed in Fig. 5.6, in which, the electromagnetic torque and stator flux as a function of their respective hysteresis comparators and the applied VSI-vector are shown when the stator flux vector is lying in sector 1. It can be

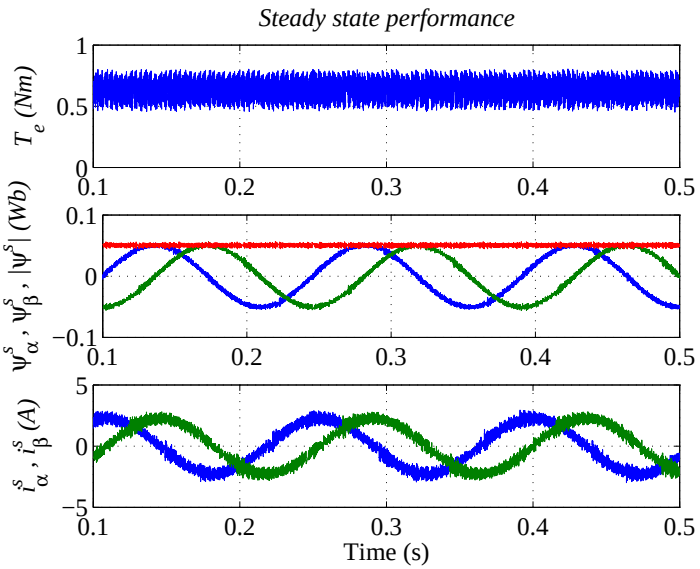

Figure 5.4: DTC-MC for PMSM. Steady state performance.

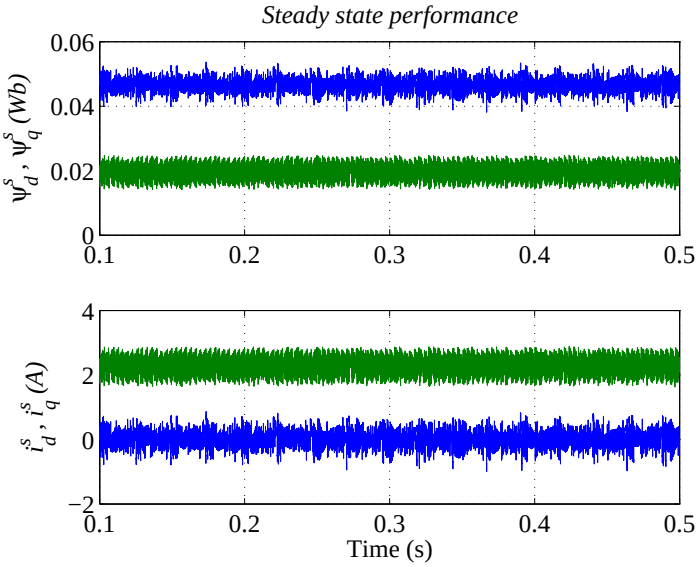

Figure 5.5: DTC-MC for PMSM. Maximum torque per ampere.

noticed that the DTC algorithm obey the conventional VSI fed DTC rules.

As it has been mentioned in section 5.2, the magnitude and direction of the MC states corresponding to active vectors will depend on the input volt-

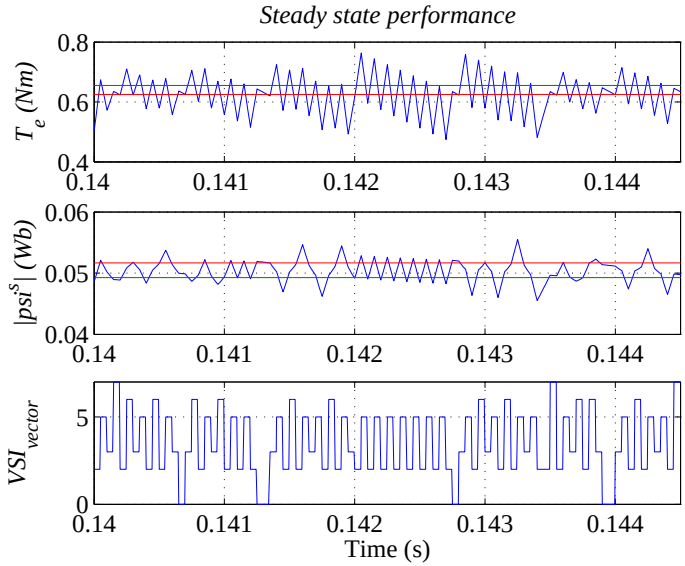

Figure 5.6: DTC-MC for PMSM. VSI switching strategy for flux vector lying in sector 1.

ages. The DTC-MC algorithm will select a MC state according to the VSI vector and the input voltage vector. The behavior of the DTC-MC algorithm is corroborated in Fig. 5.7 which shows the VSI vector, the sector in which the input line-to-neutral voltage vector is lying, and the MC state.

One of the advantages of using MC to implement a DTC-PMSM drive is the possibility to control the input power factor. Due to the action of the MC switches, the current at the input side of the MC is a set of pulses with high di/dt. As it was mentioned in chapter 3, the main purpose of the input power filter is to filter out the high frequency components of the MC input currents generating sinusoidal currents at the mains. Since only the input voltages and output currents are measured, output voltages and input currents are calculated on the basis of the switching states of the MC. With the aid of Kirchhoff's laws and Fig. 3.5 of chapter 3, the input filter can be modeled, for simulation purposes, as follows:

$$v_{si}(t) = v_i(t) + L_f \frac{d}{dt}\left(i_i(t) + C_f \frac{dv_i(t)}{dt} - \frac{v_s(t) - v_i(t)}{R_f}\right) \tag{5.1}$$

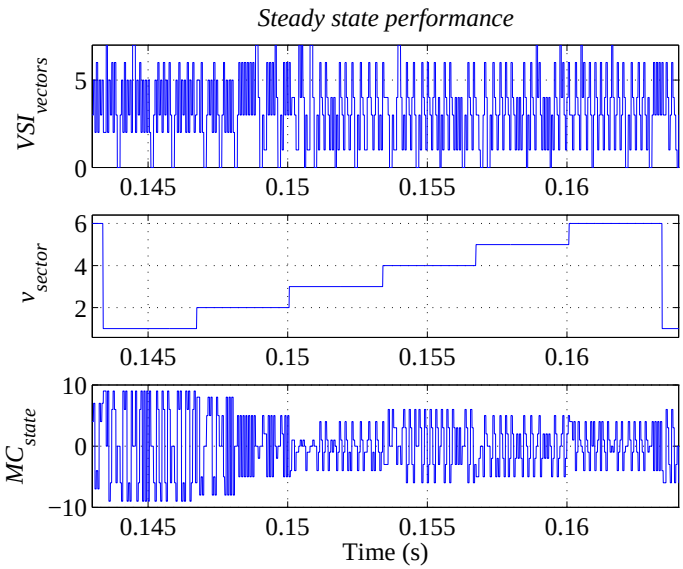

Figure 5.7: DTC-MC for PMSM. MC switching strategy for flux vector lying in sector 1.

Applying the Laplace transform to (5.1),

$$v_i(s) = \frac{v_{si}(s)\,(L_f s + R_f) - i_i(s) R_f L_f s}{R_f L_f C_f s^2 + L_f s + R_f} \tag{5.2}$$

The following expression, in terms of the Laplace transform, for the currents at the mains can be easily found.

$$i_{si}(s) = i_i(s) + C_f s v_i(s) \tag{5.3}$$

Replacing (5.3) in (5.2),

$$i_{si}(s) = \frac{L_f s + R_f}{R_f L_f C_f s^2 + L_f s + R_f} i_i(s) + \frac{L_f C_f s^2 + R_f C_f s}{R_f L_f C_f s^2 + L_f s + R_f} v_{si}(s) \tag{5.4}$$

Equation (5.2) states that if the filter parameters are calculated properly, the MC input voltages (v_A, v_B, and v_C), will be similar to those at the mains (v_{SA}, v_{SB}, and v_{SC}). From (5.4) it can be seen that the currents from the mains (i_{SA}, i_{SB}, and i_{SC}) are a filtered component of the MC input currents (i_A, i_B, and i_C), plus a filtered component of the voltages at the mains. Due

to the low frequency nature of these voltages, it can be assumed that the effects in i_{si} are negligible [68].

For simulation purposes an input filter with the following parameters has been designed:

Table 5.2: Input filter parameters.

Dumping resistor R_f	40 Ω
Inductance L_f	6.5 mH
Capacitor C_f	10 μF

In relation to the input currents waveforms and the power factor correction, Fig. 5.8 shows the input voltage v_{SA} and input current i_{SA}. It can be observed that both variables are in phase showing a good behavior regarding the power factor control. The filter action can be noted comparing the filtered current i_{SA} with the MC input current i_A. The figure also shows the control variable $< sin\phi >$ which, due to the control action of the corresponding hysteresis controller, is kept very close to zero ensuring a power factor very close to unity.

Transient performance

Here, the transient performance of the classical DTC using MC is analyzed by means of a step torque command, going from the positive rated torque to the negative rated torque, at $t = 0.25s$. Firstly, the dynamic performance of the electromagnetic torque is shown in Fig. 5.9. It can be seen a very fast electromagnetic torque response, similar to the VSI fed DTC-PMSM drive analyzed in chapter 4. The $\alpha - \beta$ components of the stator flux ψ^s_α and ψ^s_β, and its modulus is also shown in Fig. 5.9. The stator flux modulus remains constant during the electromagnetic torque step, corroborating the effective decoupled control over these two variables. The sinusoidal waveforms of the stator currents $\alpha - \beta$ components demonstrates the indirect control capabil-

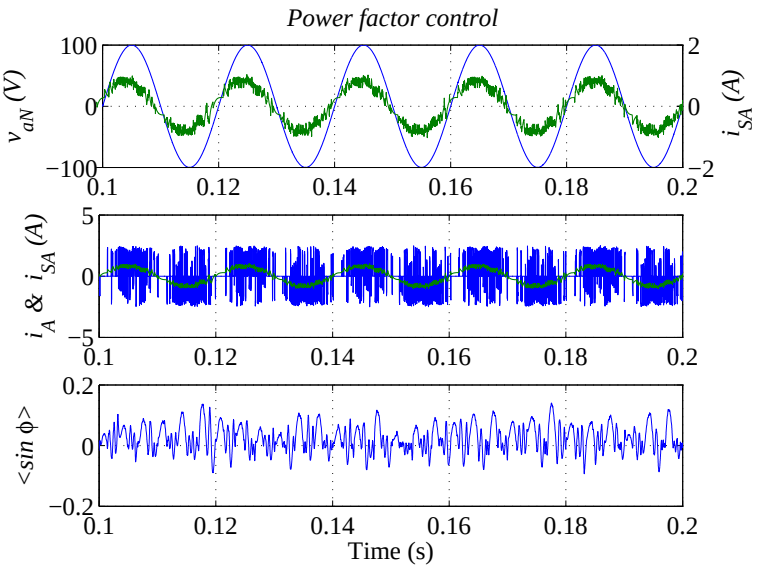

Figure 5.8: DTC-MC for PMSM. Power factor control capability.

ity of the DTC using MC.

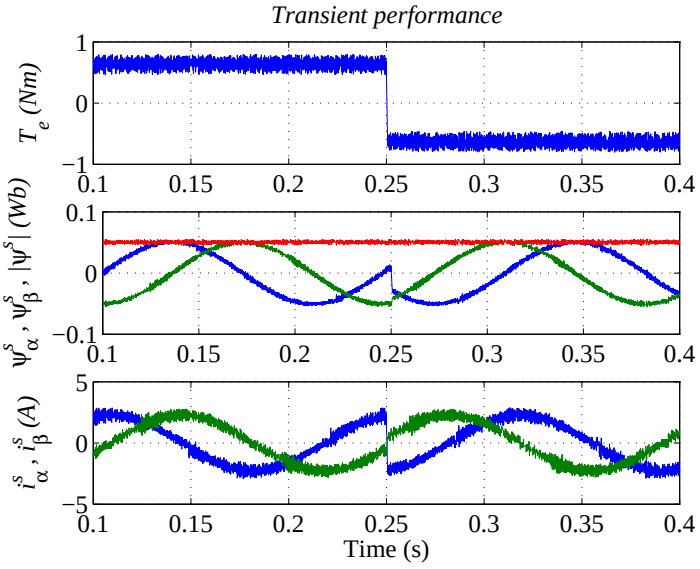

Figure 5.9: DTC-MC for PMSM. Torque step transient.

The decoupled control performance can also be analyzed by means of the

direct and quadrature currents i_d^s and i_q^s. As it can be seen in Fig. 5.10, the flux producing current i_d^s is zero, ensuring maximum torque per ampere operation of the drive. On the other hand, the torque producing current i_q^s shows the same transient behavior as the electromagnetic torque shown in Fig. 5.9.

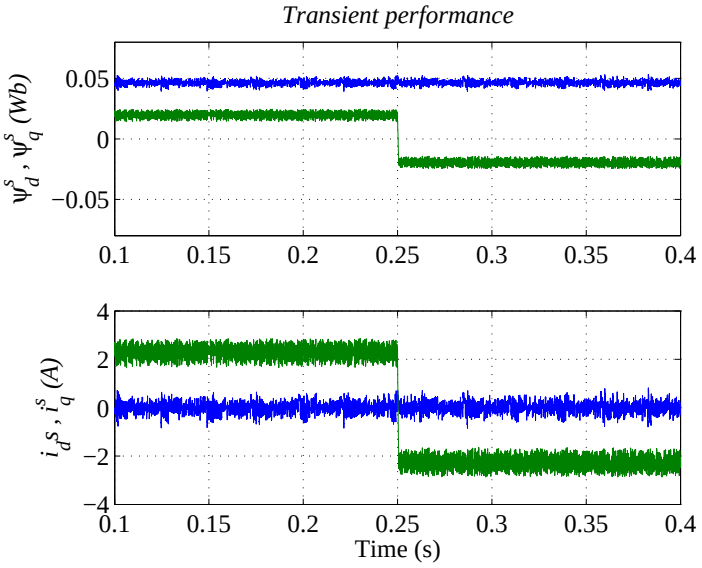

Figure 5.10: DTC-MC for PMSM. Torque step transient.

The stator flux *d-q* components ψ_d^s and ψ_q^s, are also shown in Fig. 5.10. The direct axis stator flux component ψ_d^s equals the permanent magnet flux ($\psi_d^s = \psi_{PM} = 0.046Wb$) due to the maximum torque per ampere operation of the DTC. In contrast, the quadrature stator flux component ψ_q^s, forces a displacement of the stator flux vector (*an angle increment* $\Delta\delta$) producing the desired electromagnetic torque.

5.2.2 Experimental Results

In order to corroborate the results obtained in section 5.2.1, the system is analyzed by means of experimental tests. The rig employed for the experi-

mental tests is shown in Fig. 5.11.

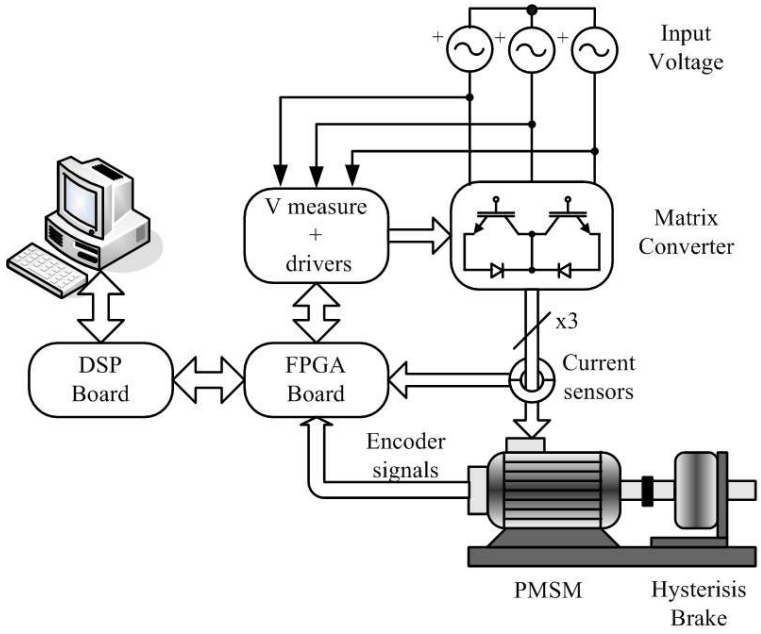

Figure 5.11: DTC-MC for PMSM. Experimental rig.

Steady state performance

The DTC settings to analyze the steady state performance are the same as those employed in the simulation tests.

The electromagnetic torque T_e and the stator flux linkage modulus $|\psi^s|$ are shown in Fig. 5.12. Both variables follow their respective reference values T_e^* and $|\psi^{s*}|$. Moreover, the indirect control capability over the stator flux and currents can be seen from the sinusoidal behavior of these variables.

The function $\psi^{s*}(T_e^*)$ has been employed to set the stator flux reference in order to achieve the desired electromagnetic torque with minimum stator current. The direct axis i_d^s and quadrature axis i_q^s currents are shown in Fig. 5.13 where it can be seen that the flux producing current i_d^s is zero, thus

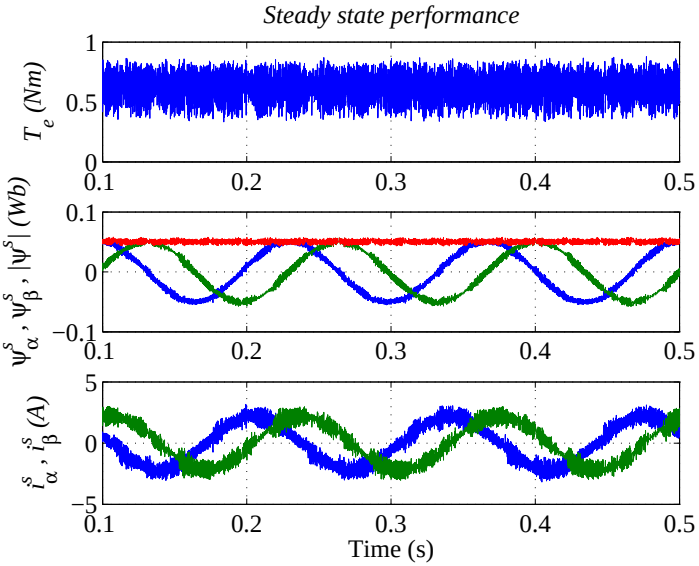

Figure 5.12: DTC-MC for PMSM. Steady state performance.

demonstrating the maximum torque per ampere operation. The *d-q* components of the stator flux are also depicted, showing that $\psi^s_d = \psi_{PM} = 0.046Wb$.

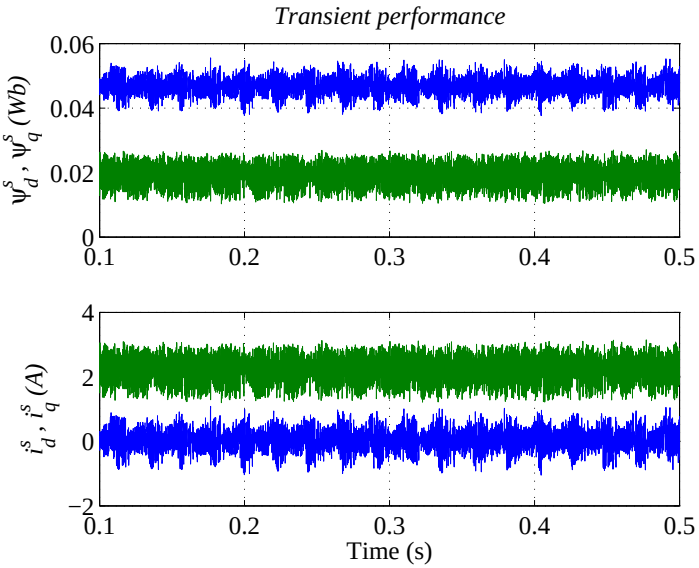

Figure 5.13: DTC-MC for PMSM. Maximum torque per ampere.

Transient performance

The transient performance of the classical DTC using MC is analyzed by means of a step torque command, going from the positive rated torque to the negative rated torque, at $t = 0.25s$. the dynamic performance of the electromagnetic torque can be analyzed in Fig. 5.14.

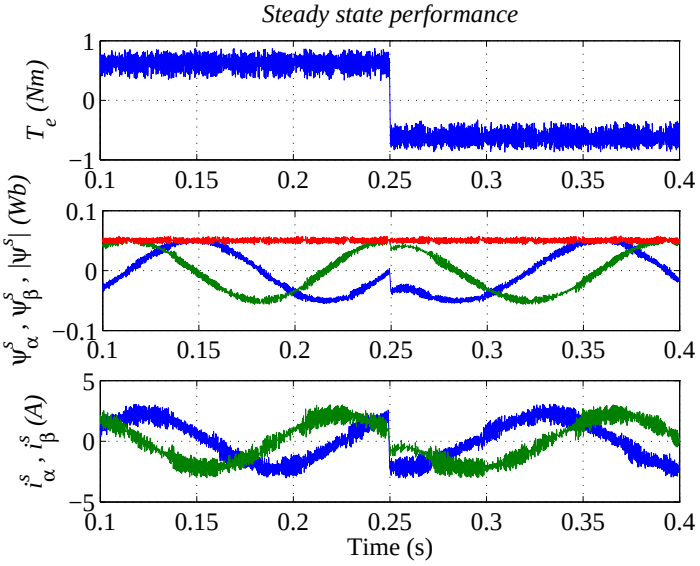

Figure 5.14: DTC-MC for PMSM. Transient performance.

The experimental test has similar performance to that obtained in section 5.2.1, showing a very fast electromagnetic torque response. As shown, during the electromagnetic torque step the stator flux modulus remains constant, corroborating the effective decoupled control over these two variables. Again, the sinusoidal waveforms of the stator currents and flux $\alpha - \beta$ components demonstrates the indirect control capability of the DTC using MC.

As it has been mentioned, the decoupled control capability can also be analyzed by means of the direct and quadrature currents i^s_d and i^s_q. As it can be seen, the flux producing current i^s_d shown in Fig. 5.15 remains at zero during the torque step. This will ensure maximum torque per ampere operation of the drive. The torque producing current i^s_q, on the other hand, shows

the same transient behavior as the electromagnetic torque shown in Fig. 5.14.

The direct axis stator flux component ψ_d^s equals the permanent magnet flux ($\psi_d^s = \psi_{PM} = 0.046Wb$) due to the maximum torque per ampere operation of the DTC drive. The quadrature stator flux component ψ_q^s, shows a similar transient behavior as the quadrature axis current i_q^s, forcing a displacement of the stator flux vector (*an angle increment* $\Delta\delta$) producing the desired electromagnetic torque.

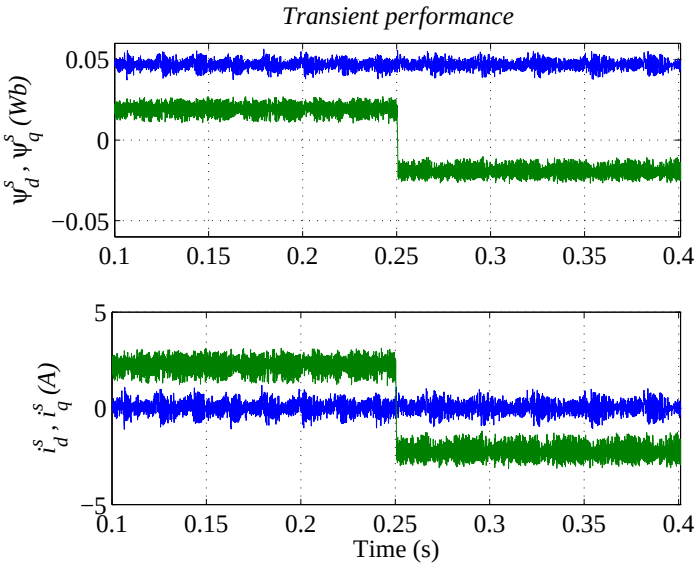

Figure 5.15: DTC-MC for PMSM. Torque step transient.

5.3 The Use of Small Voltage Vectors of Matrix Converters

In the classical DTC using MC discussed in section 5.2, the input voltage vector path was divided into six sectors. With the first sector starting at $-\pi/6$ rad, it was shown in Fig. 5.2 that, for a given sector, those vectors having smaller amplitude (*small vectors* V^S) were useless for DTC due to

their change of direction in the middle of the sector. In order to make them useful for the DTC, it is possible to organize the sector division in such a way that no vector changes its direction in the middle of a sector. This can be done dividing the voltage vector path into twelve sector as shown in Fig. 5.16.

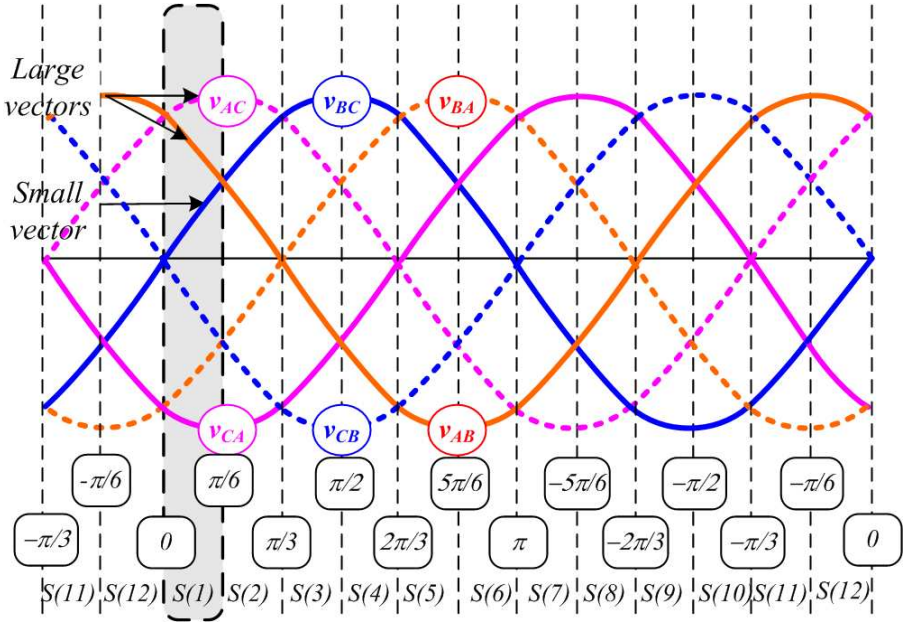

Figure 5.16: Amplitude variation of the input voltages. Twelve sectors division.

Now, there is a vector with smaller amplitude that can be used, allowing the DTC algorithm to distinguish between small and large torque errors. Moreover, this sector division permits to conceive the MC as a three-level converter (*regarding its vectors magnitudes*), however, this approach is out of the scope of this thesis and will not be discussed here.

In steady state, especially at low and medium speeds, low voltage vectors could be sufficient to fulfil DTC torque demands. Since there is only one vector with such properties available in a given sector, the pf could not be controlled.

Another possibility is to divide the input voltage vector path into six sectors making the first sector to start at 0 rad as shown in Fig. 5.17.

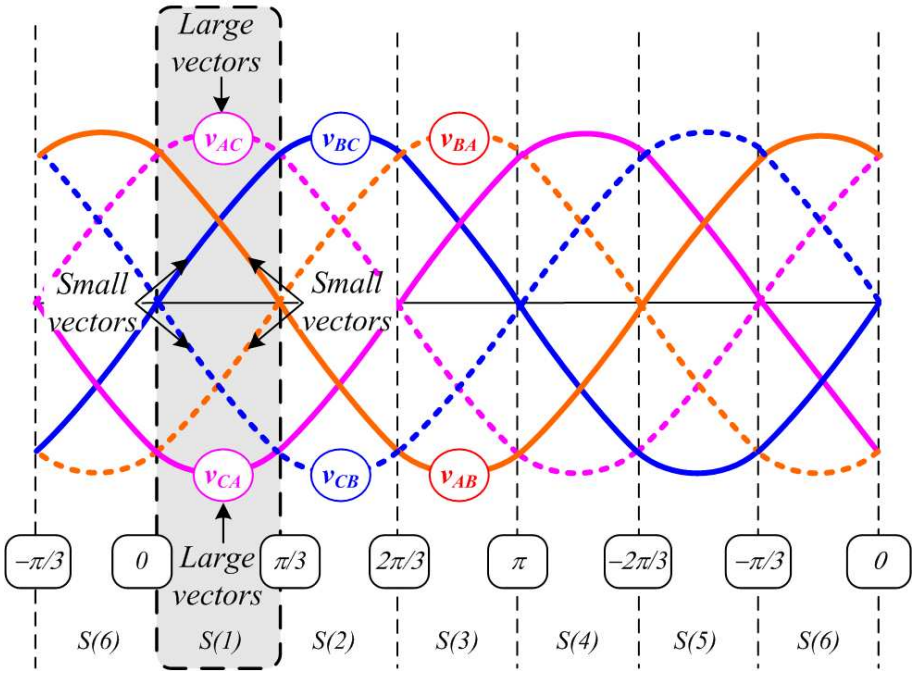

Figure 5.17: Amplitude variation of the input voltages. Six sectors division with sector 1 starting at 0 rad.

Now, for a given sector, there will be two large vectors (V^L) and four small vectors (V^S). Since there is no vectors changing their direction in the middle of the sector, all six vectors can be used to implement the DTC. The DTC algorithm is now able to apply small and large voltage vectors, hence, it will be able to distinguish between small and large torque errors while controlling the pf.

As it was explained in section 5.2, for a given vector direction imposed by the DTC algorithm and a determined sector in which the input voltage vector lies, there will be three vectors that can be selected. In the proposed scheme, these three vectors are divided in a large vector and two small vectors.

It has been mentioned that the proposed DTC algorithm will be able to distinguish between small ($S^{\pm}$) and large ($L^{\pm}$) positive and negative torque errors. This distinction is achieved replacing the electromagnetic torque hysteresis controller by the new four level one shown in Fig. 5.18.

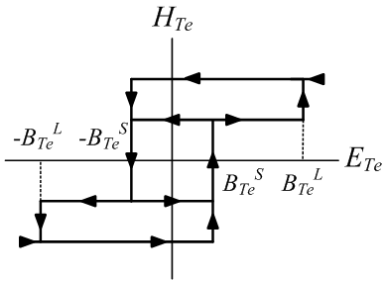

Figure 5.18: Four level hysteresis comparator.

The criteria to select large, small or zero vectors is shown in Fig. 5.19. When a small torque error is detected, the proposed DTC algorithm will impose a small vector to be delivered by the MC. As shown in Fig. 5.19, a small voltage vector will contribute to an electromagnetic torque variation with medium slope. If a large electromagnetic error is detected by the hysteresis comparator, a large voltage vector will be imposed by the DTC algorithm, contributing to a high slope electromagnetic torque variation. Torque errors lying within the small errors bands, will force the MC to deliver a zero vector. Zero vectors will contribute to a small slope electromagnetic torque variation.

The inner torque hysteresis bands in the proposed method can be set to a lower value than the torque hysteresis bands in the classical method. The outer bands in the proposed method can be seen as security limits above which the large vectors are used in order to quickly force the torque towards its reference value.

Based on the above considerations, a new switching table is developed. The new look up table is shown in table 5.3. The first column contains the vectors delivered by the conventional DTC fed by a VSI. However, these vec-

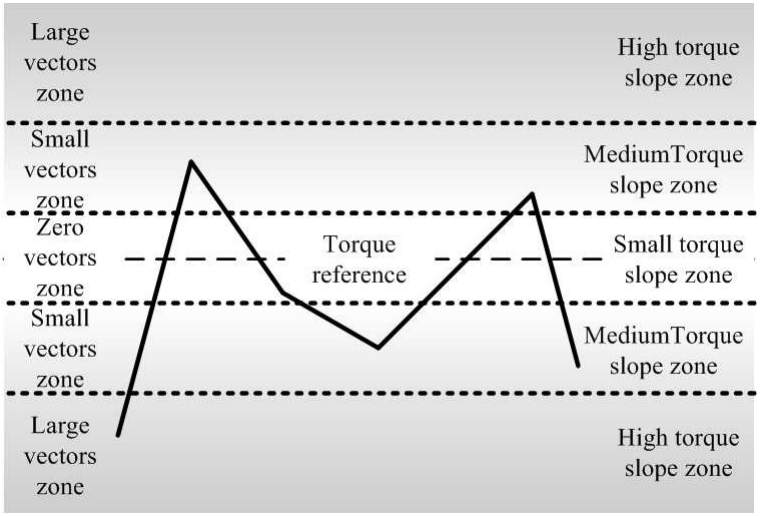

Figure 5.19: Contribution of applied voltages vectors.

tors are divided into small and large vectors V_{VSI}^{S} and V_{VSI}^{L} respectively. The rest of columns corresponds to the sector in which the input line-to-neutral voltage vector lies. Depending on the power factor hysteresis controller H_{ϕ}, each vector is divided into two different MC states (*sub-columns*). Similarly to what was explained in section 5.2, when the torque error is within the inner bands of the four level hysteresis controller, a zero vector which minimizes the number of commutations is selected[5].

In addition to the ability to deliver small and large voltage vectors, the proposed input voltage sector division also improves the voltage transfer ratio compared with the classical DTC using MCs presented in section 5.2.

Figure 5.20 shows a zoomed area of (a) Fig. 5.2 and (b) Fig. 5.17 respectively. In the classical method shown in Fig. 5.20 (a), the large voltage vectors vary their amplitude from 50% of the peak value, up to the peak value. On the other hand, the proposed method shown in Fig. 5.20 (b) employ large voltage vectors with an amplitude variation going from 86.6% of the

[5]This criteria to select zero vectors is discussed in chapter 6 and an alternative criteria is also proposed.

Table 5.3: DTC voltage vector selection table using small vectors of MC.

	Input voltage sector											
	1		2		3		4		5		6	
H_ϕ	+1	-1	+1	-1	+1	-1	+1	-1	+1	-1	+1	-1
V_1^L	-3	-3	+2	+2	-1	-1	+3	+3	-2	-2	+1	+1
V_1^S	+2	+1	-1	-3	+3	+2	-2	-1	+1	+3	-3	-2
V_2^L	+9	+9	-8	-8	+7	+7	-9	-9	+8	+8	-7	-7
V_2^S	-8	-7	+9	+7	-9	-8	+8	+7	-7	-9	+9	+8
V_3^L	-6	-6	+5	+5	-4	-4	+6	+6	-5	-5	+4	+4
V_3^S	+5	+4	-4	-6	+6	+5	-5	-4	+4	+6	-6	-5
V_4^L	+3	+3	-2	-2	+1	+1	-3	-3	+2	+2	-1	-1
V_4^S	-2	-1	+1	+3	-3	-2	+2	+1	-1	-3	+3	+2
V_5^L	-9	-9	+8	+8	-7	-7	+9	+9	-8	-8	+7	+7
V_5^S	+8	+7	-7	-9	+9	+8	-8	-7	+7	+9	-0	-8
V_6^L	+6	+6	-5	-5	+4	+4	-6	-6	+5	+5	-4	-4
V_6^S	-5	-4	+4	+6	-6	-5	+5	+4	-4	-6	+6	+5

peak value, up to the peak value.

The large voltage drop, present in the classical method, can be undesirable when the drive runs at the rated conditions. Under such conditions, the DTC needs to deliver "*true*" large voltage vectors, otherwise the drive could not reach its rated conditions.

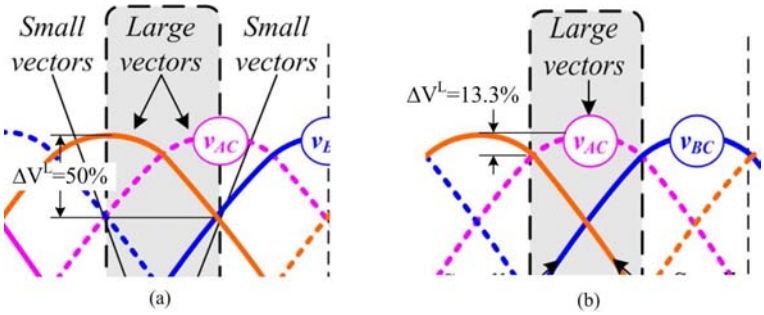

Figure 5.20: Voltage transfer ratio. (a) Classical method. (b) Proposed method

5.3.1 Simulation Results

Here, the performance of the proposed DTC driving a PMSM is analyzed by meas of simulation tests. The simulation models were programmed using the MatLab/Simulink package. The PMSM is the same as the one used in section 4.3.3 of chapter 4, where the PMSM parameters are given in table 4.4.

Steady state performance

The DTC settings to analyze the steady state performance are as follows:

- Sampling period, $T_s = 50\mu s$
- Torque reference, $T_e = 0.64\ Nm$ (rated torque)
- Flux reference, $|\psi^{s*}| = \sqrt{\left[\psi_{PM}^2 + \left(\frac{2}{3}\frac{T_e^* L_q^s}{p\psi_{PM}}\right)^2\right]}$
- Torque hysteresis outer bands, $BT_e^L = \pm 2.5\%$ of rated torque.
- Torque hysteresis inner bands, $BT_e^S = \pm 1.8\%$ of rated torque.
- Flux hysteresis bands, $B\psi^s = \pm 2.5\%$ of the permanent magnet flux.
- Rotor speed, 100 rpm

It should be noted that the DTC settings are the same as those for the simulation tests of section 5.2.1. The only difference between the settings of both methods is the hysteresis bands. However, as it has been mentioned, the hysteresis inner bands are set to a lower value than the hysteresis bands of the classical method and the outer bands can be seen as security limits above which the large vectors are used in order to quickly force the torque towards its reference value.

The electromagnetic torque T_e and the stator flux modulus $|\psi^s|$ are shown in Fig. 5.21. Comparing the results with those obtained in Fig. 5.4, it can be noted that both variables follow their respective reference values, T_e^* and $|\psi^{s*}|$, with less ripple than in the classical method. The sinusoidal behavior

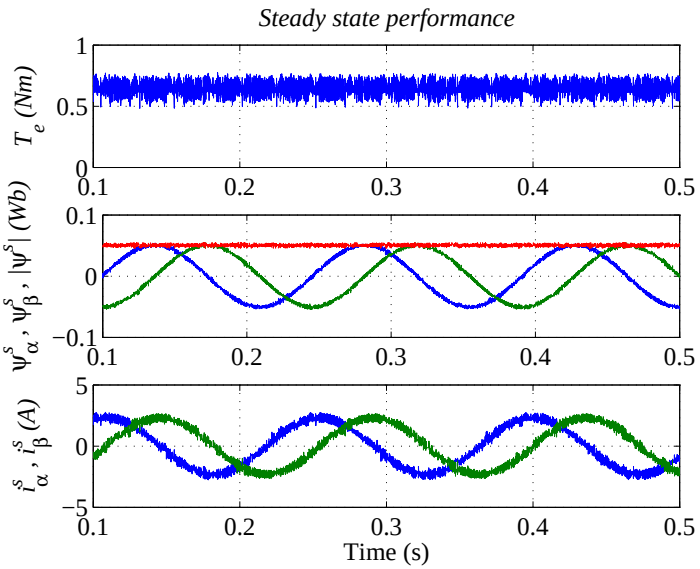

Figure 5.21: DTC-MC using small vectors. Steady state performance.

of the $\alpha - \beta$ components of the stator flux and currents demonstrates the indirect control of these variables. Moreover, the ripples of these variables are smaller than in the classical method.

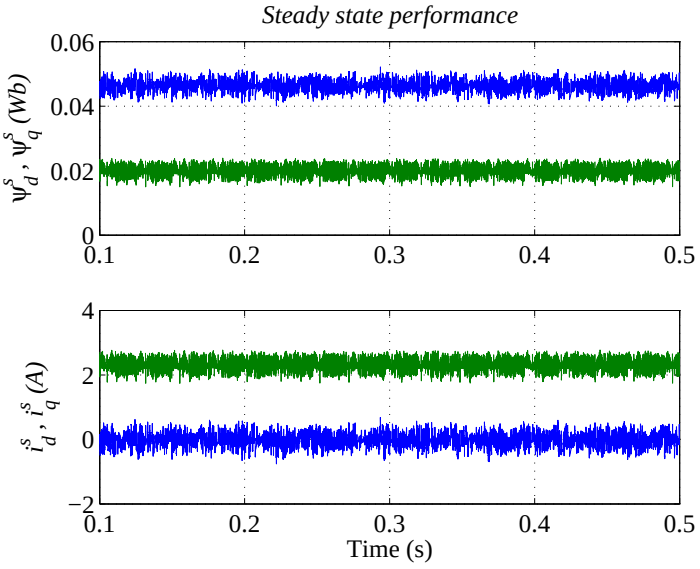

Figure 5.22: DTC-MC using small vectors. Maximum torque per ampere.

Figure 5.22 shows the *d-q* components of the stator currents i_d^s and i_q^s. The flux producing current is zero ($i_d^s = 0$) demonstrating the effectiveness of the maximum torque per ampere operation. The direct and quadrature axis components of the stator flux, ψ_d^s and ψ_q^s, are also shown in Fig. 5.22. As expected, $\psi_d^s = \psi_{PM} = 0.046Wb$. The *d-q* components of the stator flux and currents shown in Fig. 5.22 can be also compared with the ones shown in Fig. 5.5. The ripple of these quantities is again smaller in the proposed method.

The switching strategy for the proposed method is shown in Fig. 5.23. The electromagnetic torque, stator flux and their respective hysteresis bands are shown when the flux vector lies in sector one. As dictated by the rules of the conventional DTC, the corresponding VSI voltage vector are then shown. Finally, the figure shows whether the applied vector correspond to small or large vectors.

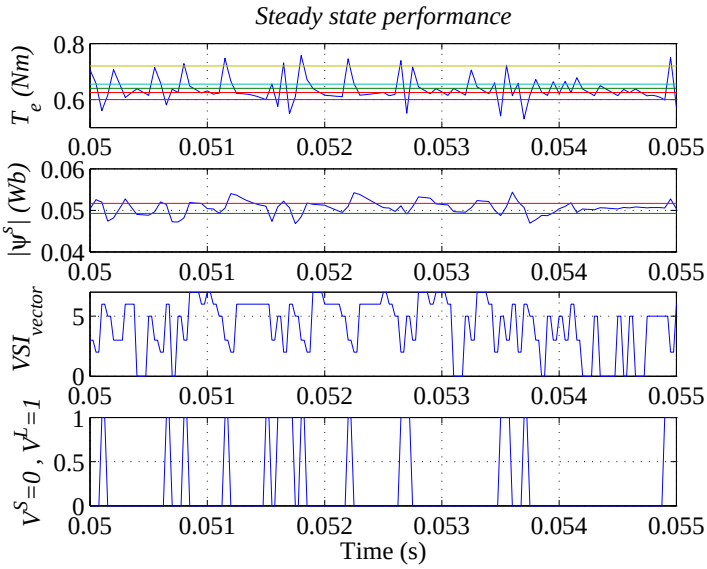

Figure 5.23: DTC-MC using small vectors. Switching strategy for flux vector lying in sector one.

The input voltage v_{SA} and input current i_{SA} are shown in Fig. 5.24. Since both variables are in phase, the power factor control capability of the proposed method is corroborated. However, since the proposed method will apply zero vectors more often than the classical method, the average switching frequency will be reduced and, hence, closer to the the filter cut-off frequency. Moreover, since the proposed method will not be able to control the input power factor when applying large vectors, higher distortion in the input currents will be introduced. This can be noted from the difficulty to keep the power factor control variable $< sin\phi >$ close to zero shown in 5.24.

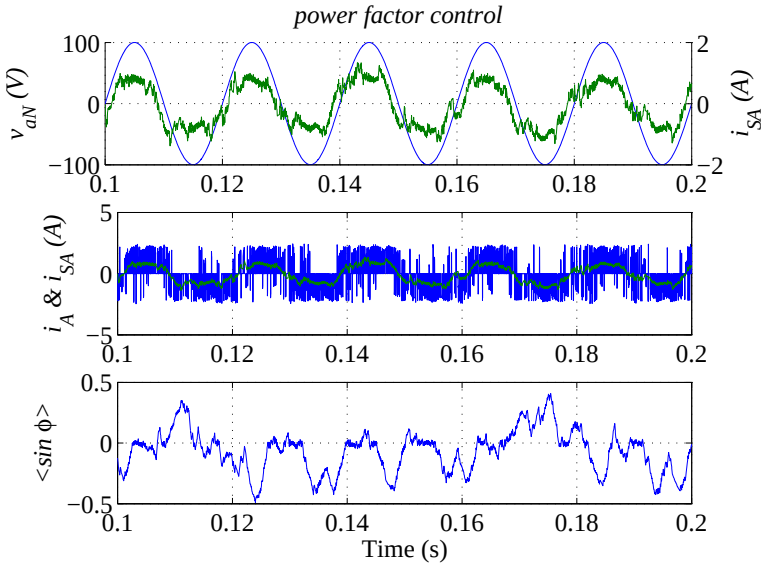

Figure 5.24: DTC-MC using small vectors. Power factor control capability.

Transient performance

The transient performance of the DTC using small vectors of the MC is analyzed by means of a step torque command, going from the positive rated torque to the negative rated torque, at $t = 0.25s$. The dynamic performance of the electromagnetic torque is shown in Fig. 5.25. It can be seen a very fast electromagnetic torque response, similar to the classical DTC using MC drive analyzed in section 5.2.1. The $\alpha - \beta$ components of the stator flux ψ^s_α and

ψ^s_β, and its modulus are also shown in Fig. 5.25. As it can be seen, the stator flux modulus remains unaltered during the electromagnetic torque step, corroborating the effective decoupled control of both variables. The indirect control capability of the DTC using MC is demonstrated by the sinusoidal waveforms of the stator currents $\alpha - \beta$ components.

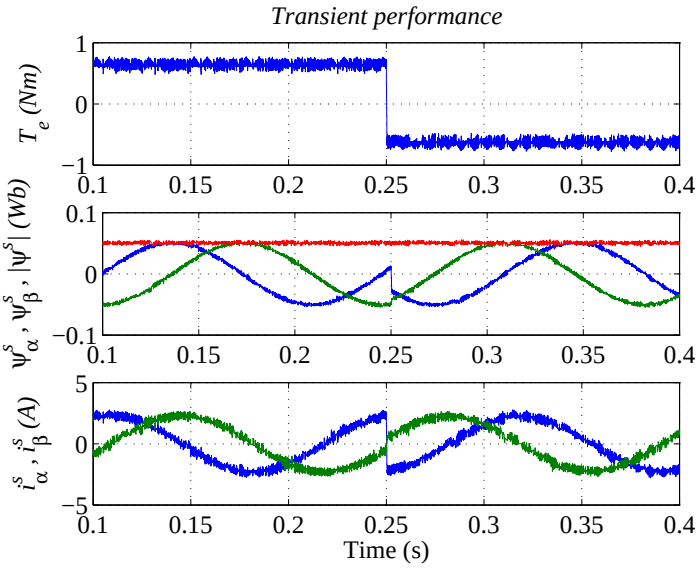

Figure 5.25: DTC-MC using small vectors. Transient performance.

Another way to analyze the decoupled control performance is by means of the direct and quadrature currents i^s_d and i^s_q. The flux producing current i^s_d is zero as shown in Fig. 5.26. This ensures maximum torque per ampere operation of the drive. Moreover, this current remains constant during the torque step demonstrating the decoupled control capability of the system. The torque producing current i^s_q shows the same transient behavior as the electromagnetic torque shown in Fig. 5.25.

5.3.2 Experimental Results

The proposed DTC driving a PMSM is analyzed by means of experimental tests using the rig shown in Fig. 5.11 (*see section 5.2.2*). The DTC settings

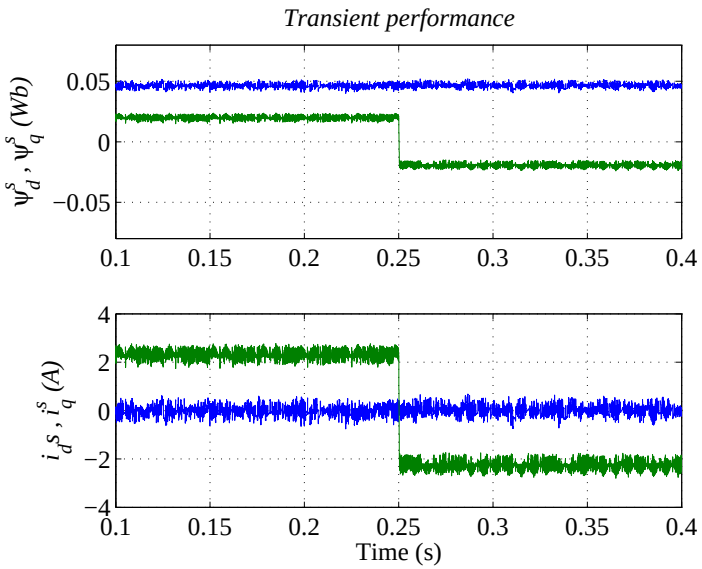

Figure 5.26: DTC-MC using small vectors. Decoupled control capability.

are the same as those for the simulation tests of section 5.3.1.

Steady state performance

Firstly, the electromagnetic torque T_e and the stator flux modulus $|\psi^s|$ are analyzed. These two variables are shown in Fig. 5.27. Comparing these results with those obtained with the classical method in Fig. 5.12 of section 5.2.2, it should be noted the ripple reduction obtained with the proposed method.

The sinusoidal behavior of the $\alpha - \beta$ components of the stator flux and currents demonstrates the indirect control of these variables. Moreover, the ripples of these variables are shown to be smaller than in the classical method.

The d-q components of the stator currents i_d^s and i_q^s are shown in Fig. 5.28. The effectiveness of the maximum torque per ampere operation is achieved since the flux producing current is zero ($i_d^s = 0$). The direct and quadrature axis components of the stator flux, ψ_d^s and ψ_q^s, are also shown in Fig. 5.28 in which, as expected, it can be seen that $\psi_d^s = \psi_{PM} = 0.046Wb$.

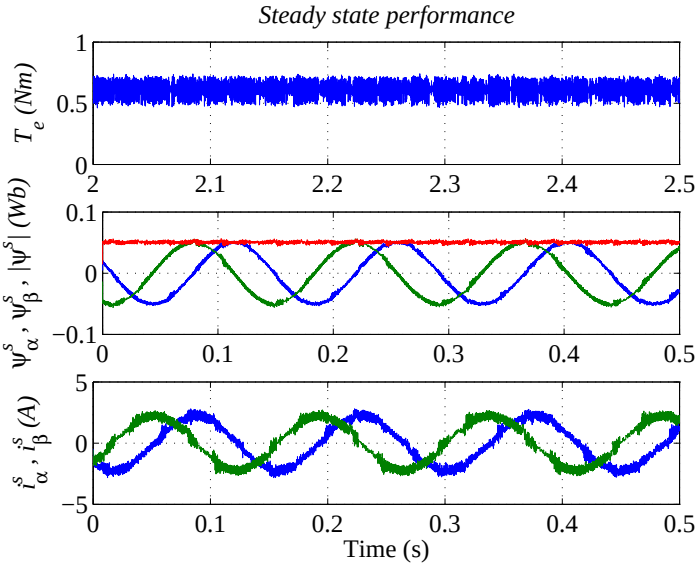

Figure 5.27: DTC-MC using small vectors. Steady state performance.

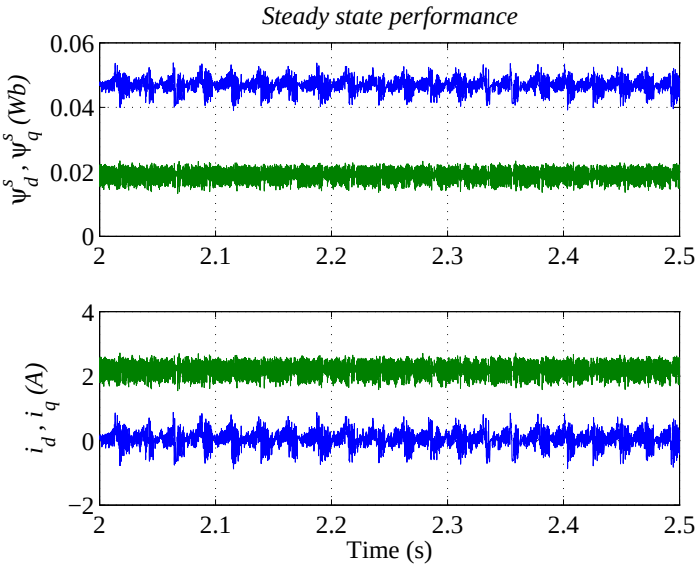

Figure 5.28: DTC-MC using small vectors. Maximum torque per ampere.

Comparing the *d-q* components of the stator flux and currents shown in Fig. 5.28 with the results obtained employing the classical method, and

shown in Fig. 5.22, it can be noted that the ripple of these quantities is again smaller in the proposed method.

Transient performance

The transient performance of the DTC using small vectors of the MC is analyzed by means of a step torque command, going from the positive rated torque to the negative rated torque, at $t = 0.25s$. The dynamic performance of the electromagnetic torque is shown in Fig. 5.29. It should be noted that, due to the use of large vector during the transient, the electromagnetic torque response is similar to the classical DTC using MC drive analyzed in section 5.2.2. The $\alpha - \beta$ components of the stator flux ψ^s_α and ψ^s_β, and its modulus are also shown in Fig. 5.29. As it can be seen, the stator flux modulus remains unaltered during the electromagnetic torque step, corroborating the effective decoupled control of both variables. The indirect control capability of the DTC using MC is demonstrated by the sinusoidal waveforms of the stator currents $\alpha - \beta$ components.

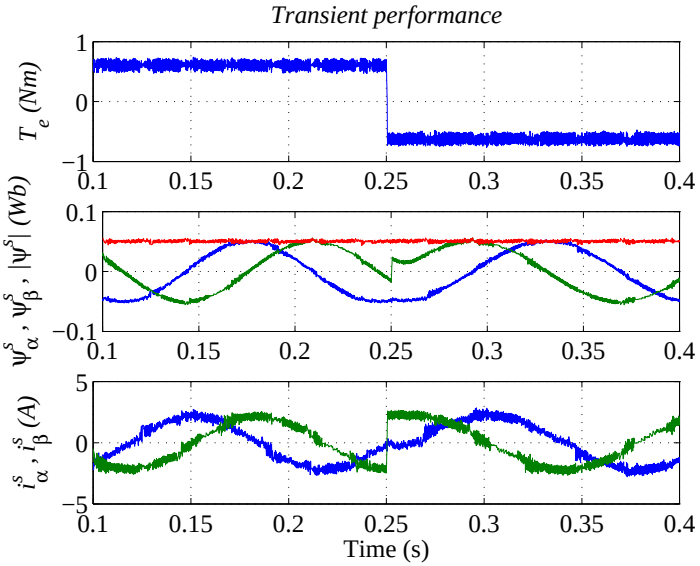

Figure 5.29: DTC-MC using small vectors. Transient performance.

The decoupled control performance is also analyzed by means of the direct and quadrature currents i_d^s and i_q^s. The flux producing current i_d^s is zero as it can be seen in Fig. 5.30, ensuring maximum torque per ampere operation of the drive. This current remains constant during the torque step demonstrating the decoupled control capability of the system. The torque producing current i_q^s shows the same transient behavior as the electromagnetic torque shown in Fig. 5.29.

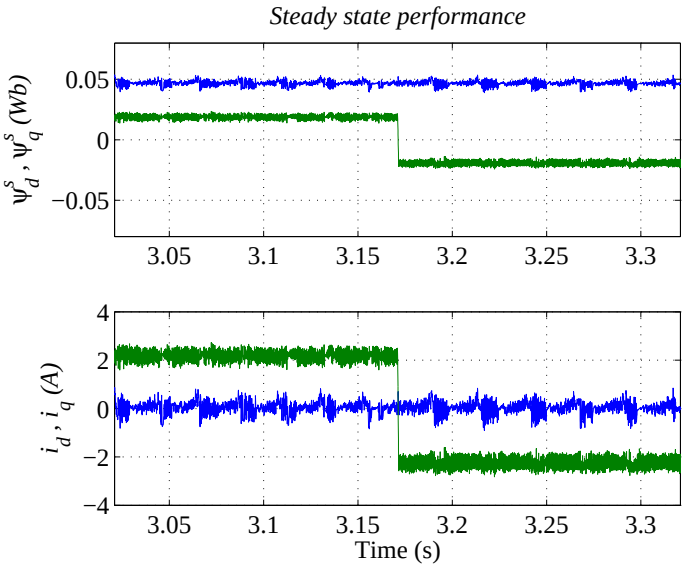

Figure 5.30: DTC-MC using small vectors. Decoupled control capability.

5.4 Comparison between the Classical and the Proposed Method

Experimental tests have been carried out at several operating points of the machine to compare the performance of both systems. The speed is varied from 100 rpm up to 3000 rpm (*rated speed*), whereas the torque reference is varied from 0.1 Nm up to 0.64 Nm (*rated torque*).

5.4.1 Torque and Flux Performance

In order to assess the performance of both systems, the electromagnetic torque and stator flux ripples are evaluated by means of their respective standard deviation values. The expression used for the standard deviation of a generic variable is the following:

$$\sigma = \sqrt{\frac{1}{n-1}\sum_{i=1}^{n}(x_i - \hat{x})^2} \qquad \hat{x} = \frac{1}{n}\sum_{i=1}^{n} x_i \tag{5.5}$$

where n is the number of samples and x_i is the actual sample.

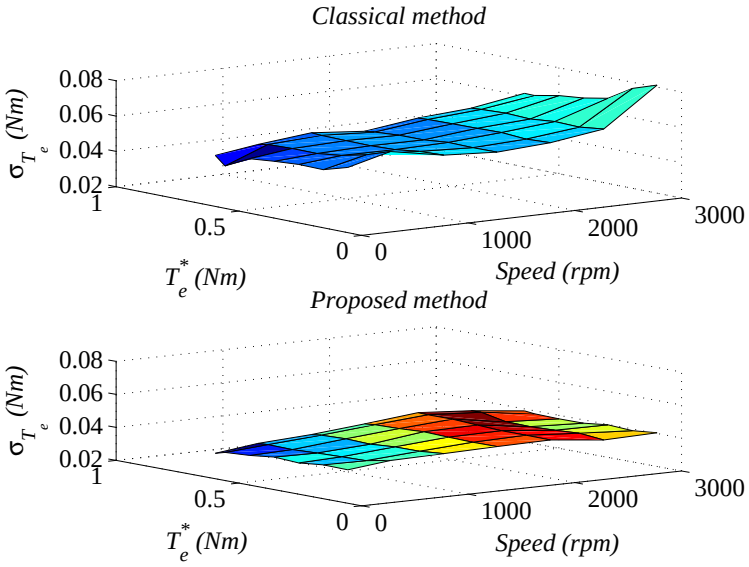

Figure 5.31: Comparison between the classical and the proposed method. Torque performance.

Torque Performance

The torque performance over all the machine operating points can be evaluated from Fig. 5.31. It is noted that the proposed method has better performance at any operating point. However, it should be emphasized the higher difference between both methods as the nominal speed is approached.

As it has been mentioned in section 5.3, this is due to lower voltage transfer ratio the classical method suffers from. Figure 5.32 shows the torque performance of both methods working under nominal conditions ($T_e = 0.64$ Nm and $\omega = 3000$ rpm).

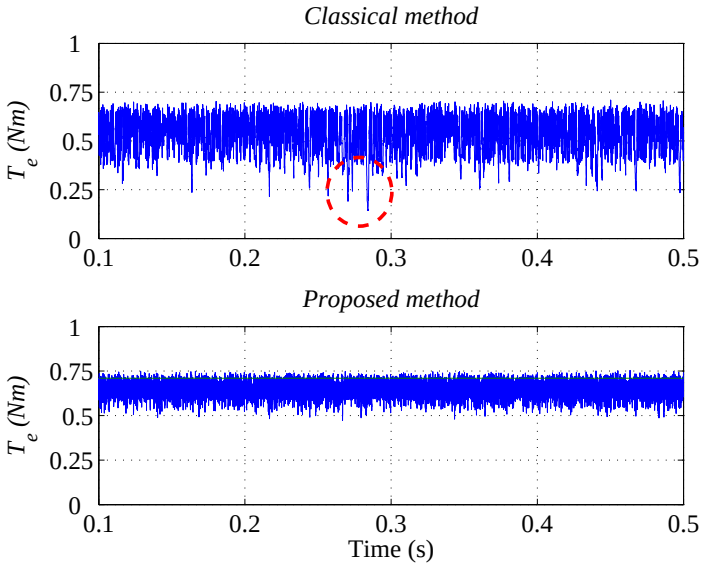

Figure 5.32: Comparison between the classical and the proposed method. Torque performance under nominal conditions.

As the back EMF increases with the speed, the use of large vectors contributing to a torque in the same direction of that imposed by the back EMF, will lead to large errors in the actual torque. In the classical method only large vectors are taken into consideration. When these vectors are applied even when the back EMF is favorable to reach the torque reference value, the total effect regarding the torque variation will be the sum of the back EMF effects and those of the applied vector. This will contribute to a torque variation with a large slope which eventually will contribute to large torque errors. The worse case, shown inside a red circle in Fig. 5.32, will be when large voltage vectors coinciding with the peak value of the input voltage are selected at instant k and a vector coinciding with 50% of the input voltage peak value is applied at instant $k + 1$. Due to the large error introduced by

the vector applied at instant k, the voltage vector applied at instant $k+1$ will not be enough to reach the torque reference value. This fact makes the classical method not only to have larger torque ripple at high speed but also to have a large steady state error.

In order to evaluate the dependence of this phenomena with speed and torque, the relative error of the torque mean value is calculated as follows:

$$\hat{T}_e^{error}(\%) = 100\frac{\left(T_e^* - \hat{T}_e\right)}{T_e^*} \tag{5.6}$$

The ability of both methods to reach the reference torque value can be analyzed from Fig. 5.33, which shows the relative error of the torque mean value over all the machine operating points.

As in the case of the torque ripple, the relative error of the torque mean value shows better performance in the proposed method at any operating point. Low values of torque references T_e^* makes the torque mean error $\hat{T}_e^{error}$ to increase (*see (5.6)*) especially at high speeds due to the high back *emf*. It should be noted the lack of "*true*" large vectors of the classical method as it can not compensate for high values of back *emf*. On the other hand it can be seen that the proposed method is less sensitive to this phenomena.

The increased voltage transfer ratio achieved with the proposed method will also improve the torque transient performance. Since the torque error will exceed the outer bands of the hysteresis comparator during a torque transient in the proposed method, the system will impose large vectors during the transient. As it has been explained in section 5.3, the minimum amplitude of these vectors will be 36.6% greater than those imposed by the classical DTC using MCs. This fact will make the torque response faster employing the proposed algorithm.
The torque transient performance for a torque step of ±0.64 Nm (± rated torque), comparing both methods, is shown in Fig. 5.34.

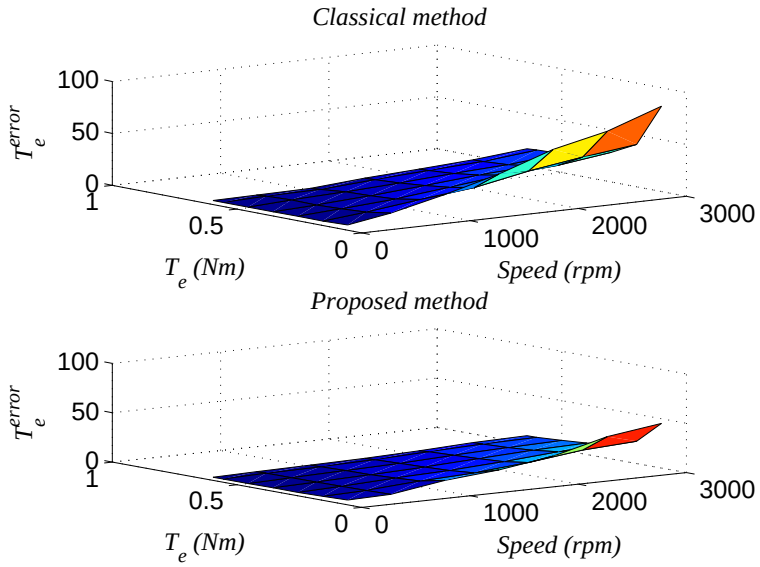

Figure 5.33: Comparison between the classical and the proposed method. Torque steady state error.

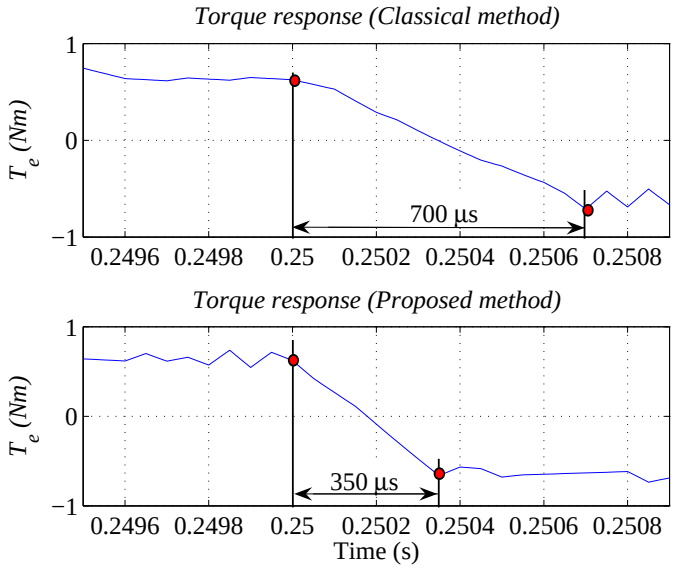

Figure 5.34: Comparison between the classical and the proposed method. Torque transient response.

As it can be seen, the torque transient response is twice faster with the proposed method.

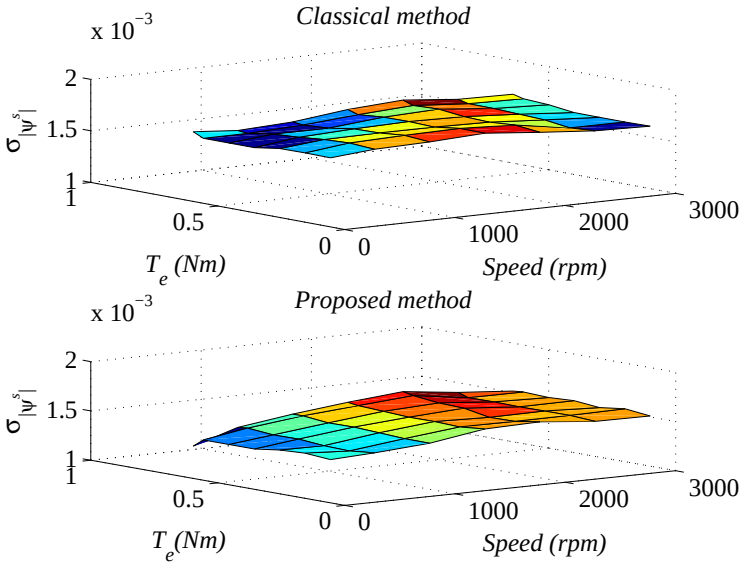

Figure 5.35: Comparison between the classical and the proposed method. Flux performance.

Flux Performance

The stator flux performance (*in terms of its ripple (5.5)*) of both methods over all the machine operating points is shown in Fig. 5.35. Although both systems are very similar, the proposed method shows better performance. Moreover, the difference between both systems is more relevant at low speed when high torque is demanded. However, it should be noted that in both systems the flux ripple is almost constant over all the machine operating points. Hence, it can be said that the stator flux ripple does not depend neither on speed nor torque.

5.4.2 Stator Current Performance

The performance of the stator current have been assessed by means of the Total Harmonic Distortion (THD). The THD is defined as follows:

$$THD = \frac{I_h}{I_f} \qquad I_h = \sqrt{I_2^2 + I_3^2 + \ldots + I_n^2} \tag{5.7}$$

where I_n is the RMS value of the n^{th} harmonic and I_f is the RMS value of the fundamental current.

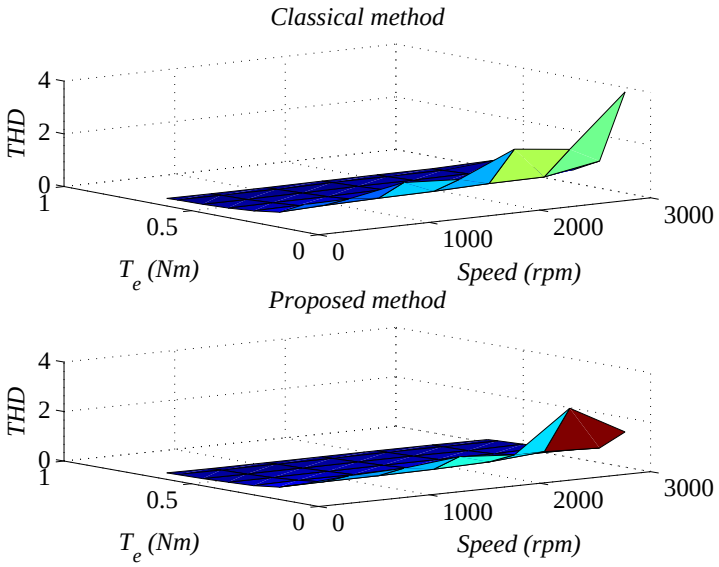

Figure 5.36: Comparison between the classical and the proposed method. Stator current performance.

The stator current performance over all the machine operating points is analyzed in Fig. 5.36. It is noted that the proposed method shows better performance at any operating point. As in the case of the stator flux ripple, it should be emphasize the difference between both systems at low torque values as the rated speed is approached.

Table 5.4 summarizes the improvements achieved by the proposed method in terms of stator flux and electromagnetic torque ripples, relative error of the

torque mean value and the stator current THD. The maximum, minimum, and the average improvement in % is calculated for every improvement variable.

Table 5.4: Improvements of the proposed method.

Improvement	σ_{T_e} (%)	T_e^{error} (%)	$\sigma_{\lvert\psi^s\rvert}$ (%)	THD (%)
max	50.27	37.13	21.22	62.92
min	16.62	0.14	4.12	7.33
average	28.28	7.21	9.64	21.09

It can be seen that higher improvements are achieved in terms of electromagnetic torque ripple. However, it should be noted from Figs. 5.31, 5.33, 5.35 and 5.36 that higher improvements can be achieved by other variables depending on the machine operating point.

Table 5.5 shows the improvements achieved by every variable at different values of speed and torque.

Table 5.5: Improvements dependency of speed and torque.

Speed/Torque	σ_{T_e}	T_e^{error}	$\sigma_{\lvert\psi^s\rvert}$	THD
Low/Low	Medium	Small	High	Medium
Low/High	Medium	Small	Medium	Small
High/Low	High	High	Medium	High
High/High	High	Medium	Small	High

5.5 Conclusions

The use of MC implementing a DTC to drive a PMSM has been investigated in this chapter. A new DTC scheme has been developed and compared with the classical DTC using MC pointing out the benefits of the former. The proposed method employs not only the large voltage vectors of the MC but also the small ones. This fact makes possible the inclusion of a four-level

hysteresis comparator allowing the DTC to distinguish between small and large electromagnetic torque errors and, hence, reducing the electromagnetic torque and stator flux ripples.

The proposed scheme also improves the voltage transfer ratio of the MC by 36% (50% for the classical method and 86% for the proposed method) in the worst case. This fact allows the proposed method to reach the rated operating point of the machine with much less steady state error than the classical DTC using MC. Moreover, the improvement in the voltage transfer ratio will make the system to response faster to a torque transient.

Chapter 6

Reducing the Common Mode Voltage using Matrix Converters

It is well known that one of the main sources of early motor winding failure and bearing deterioration is the Common Mode Voltage (CMV) produced by modern power converters. Moreover, high frequency components and large amplitudes of the CMV at the motor neutral point have been shown to generate high frequency currents to the ground path and induced shaft voltage [69]. Several methods to reduce the CMV have been proposed in the literature [70], [71], however, these methods are designed for three-phase Pulse Width Modulation (PWM) VSI systems. In [50], a new modulation strategy of the converter which reduces the CMV at the output of the MC is presented. Based on the Indirect Space Vector Modulation (ISVM) technique, the method selects a medium value phase voltage as a zero vector and places it in the center or on the both sides of the sampling period without changing the active voltage vectors. The harmonic content of the input current is also reduced. However, these advantages are achieved at the expense of deterio-

rating the output harmonic content.

An approach to reduce the CMV in a DTC-PMSM drive using Matrix Converters is presented in this chapter. Firstly, the CMV in MC is mathematically analyzed. Based on this analysis, a very simple algorithm to reduce the CMV is proposed and investigated.

6.1 Common Mode Voltage in Matrix Converters

Fig. 6.1 shows a MC connected to a PMSM where the impedance Z_{cm} represents the leakage current (i_{cm}) path between the machine's neutral point (n) and ground (N). The CMV v_{cm} is defined as the voltage between these two points:

$$v_{cm} = v_{nN} \tag{6.1}$$

Taking into consideration the CMV v_{cm}, the voltage expressions of the PMSM can be written as:

$$v_{aN} - v_{cm} = R_s i_a + L_s \frac{di_a}{dt} + \frac{d}{dt}\psi_{PM} cos\theta_r \tag{6.2}$$

$$v_{bN} - v_{cm} = R_s i_b + L_s \frac{di_b}{dt} + \frac{d}{dt}\psi_{PM} cos(\theta_r - \frac{2\pi}{3}) \tag{6.3}$$

$$v_{cN} - v_{cm} = R_s i_c + L_s \frac{di_c}{dt} + \frac{d}{dt}\psi_{PM} cos(\theta_r - \frac{4\pi}{3}) \tag{6.4}$$

where v_{aN}, v_{bN}, and v_{cN} are the MC output voltages with respect to ground. R_s and L_s are the resistance and inductance at each phase of the PMSM and ψ_{PM} is the flux produced by the permanent magnets. Since $i_{cm} \approx 0$, it can be assumed that $i_a + i_b + i_c \approx 0$. Assuming a balanced

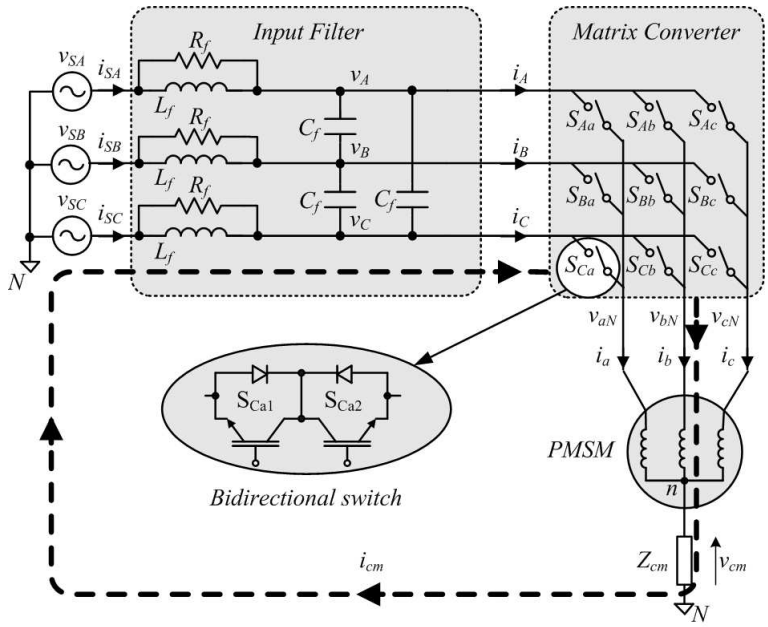

Figure 6.1: 3×3 Matrix Converter.

induced voltage system $\psi_{PM}cos\theta_r + \psi_{PM}cos(\theta_r - \frac{2\pi}{3}) + \psi_{PM}cos(\theta_r - \frac{4\pi}{3}) = 0$, the CMV can be found adding (6.2), (6.3) and (6.4):

$$v_{cm} = \frac{v_{aN} + v_{bN} + v_{cN}}{3} \tag{6.5}$$

As it can be seen in table 3.2 from chapter 3, when active vectors are selected in a MC, there are two output phases connected to the same input phase. Thus, the CMV when active vectors are delivered by a MC v_{cm}^a can be written as:

$$v_{cm}^a = \frac{v_i + 2v_j}{3} \tag{6.6}$$

where i and j represents the two input phases involved when an active vector is present at the output of the MC.

In MCs, the input filter is designed in such a way that the phase voltages v_A, v_B, and v_C can be considered equal to the phase voltages of the mains

v_{SA}, v_{SB}, and v_{SC} respectively [41]. Assuming a balanced voltage system at the mains and, hence, at the input side of the MC,

$$v_{_{SA}} = v_A = V_p \sin(\omega t) \tag{6.7}$$

$$v_{_{SB}} = v_B = V_p \sin(\omega t - \frac{2\pi}{3}) \tag{6.8}$$

$$v_{_{SC}} = v_C = V_p \sin(\omega t + \frac{2\pi}{3}) \tag{6.9}$$

where V_p is the voltage peak value per phase, (6.6) can be written as:

$$v^a_{cm} = \frac{1}{3} V_p \sin(\omega t) + \frac{2}{3} V_p \sin(\omega t \pm \frac{2\pi}{3}) \tag{6.10}$$

Rearranging (6.10), a simpler form of v^a_{cm} can be obtained:

$$v^a_{cm} = \frac{1}{\sqrt{3}} V_p \sin(\omega t \pm \frac{\pi}{2}) \tag{6.11}$$

Equation (6.11) states that the instantaneous value of the CMV when any active vector is delivered by the MC v^a_{cm}, depends on the instantaneous value of the input voltages selected to deliver such vector. Hence, the maximum instantaneous value of the CMV when active vectors are delivered by the MC v^a_{cm} will be:

$$v^a_{cm_{max}} = \pm \frac{1}{\sqrt{3}} V_p \tag{6.12}$$

The contribution to the CMV of each active vector is shown in Fig. 6.2. The frequency of voltages v_{SA}, v_{SB}, and v_{SC} is $50Hz$. In every input voltage period ($T = 0.02s$), a different output vector is delivered by the MC ($+1 \ldots +9$; $-1 \ldots -9$). It can be noted that, for every active vector, the CMV is at its maximum value, $\pm\frac{1}{\sqrt{3}}V_p$, every $k\pi$ radians ($k = 0, 1, 2 \ldots n$).

When a zero vector is selected in a MC, the three output phases are connected to the same input phase. Thus, when a zero vector is delivered by a MC, the CMV v^z_{cm} will follow the selected input voltage:

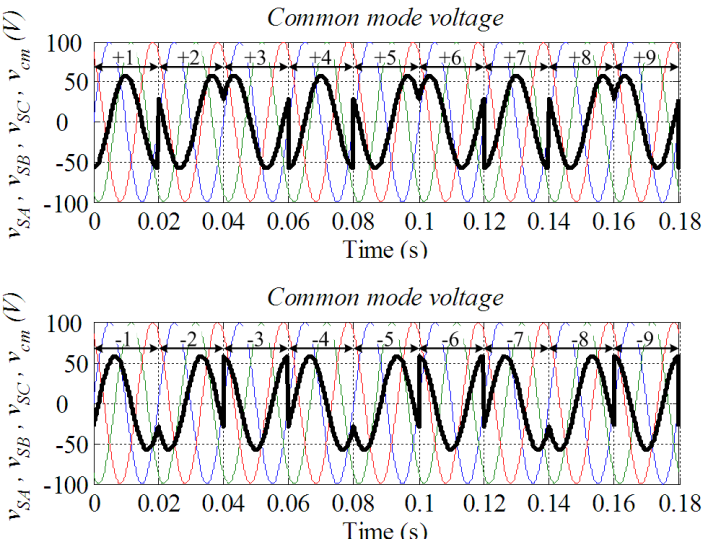

Figure 6.2: Common mode voltage when active vectors are delivered by a MC.

$$v_{cm}^{z} = v_i \tag{6.13}$$

where i represents the selected input phase.

Since $v_i = V_p \sin(wt \pm \phi)$, the maximum CMV v_{cm}^{z} when a zero is selected will be:

$$v_{cm_{max}}^{z} = \pm V_p \tag{6.14}$$

Fig. 6.3 shows the contribution to the CMV of each zero vector (*a different zero vector is selected in every input voltage period* $T = 0.02s$). As it can be seen, the CMV follows the selected phase to deliver the zero vector, being the maximum CMV equal to the peak value of that phase.

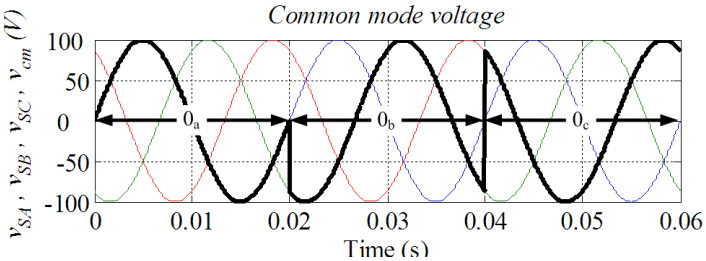

Figure 6.3: Contribution of zero vectors to the common mode voltage.

6.2 Reduction of the Common Mode Voltage

In a DTC scheme, when the actual electromagnetic torque is within the corresponding comparator hysteresis bands, a zero vector is usually selected. Since the MC can deliver three different zero vectors, in [2], the zero vector which minimizes the number of commutations is selected. However, this criteria to select zero vectors will not ensure the minimization of the converter switching during the operation of the drive. In fact, since the next active vector (*after the zero vector*) is not known at the moment of selecting the zero vector, this criteria could also contribute to increase the number of commutations over time.

As it has been shown in section 6.1, the maximum CMV is achieved when the input phase v_i, selected to deliver a zero vector, coincides with its peak value $\pm V_p$. Since the MC can deliver three different zero vectors 0_a, 0_b and 0_c (*see table 3.2* in 3), a reduction of the CMV can be achieved by proper selection of the zero vector. When any input phase voltage is at its positive or negative peak value $\pm V_p$, the other two will be at $\pm\frac{1}{2}V_p$. Hence, the maximum CMV can be reduced to $\pm\frac{1}{2}V_p$ if the input phase voltage with minimum absolute value is selected to deliver a zero vector. In Fig. 6.4, the contribution to the CMV of zero vectors, when the input phase with minimum absolute value is selected to deliver a zero vector, is shown.

Fig. 6.5 shows the simplicity of the zero vector selector method to reduce

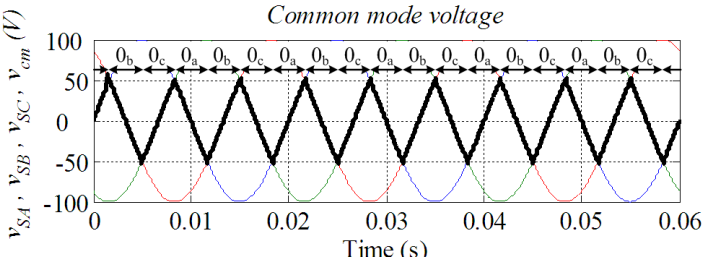

Figure 6.4: Contribution to the common mode voltage of zero vectors selecting the phase voltage with minimum absolute value.

the CMV. When a zero vector has to be selected by the DTC algorithm, the system computes the absolute value of every input phase and selects the one with the minimum value. The selected phase will be the one connected to all the output phases to deliver the zero vector.

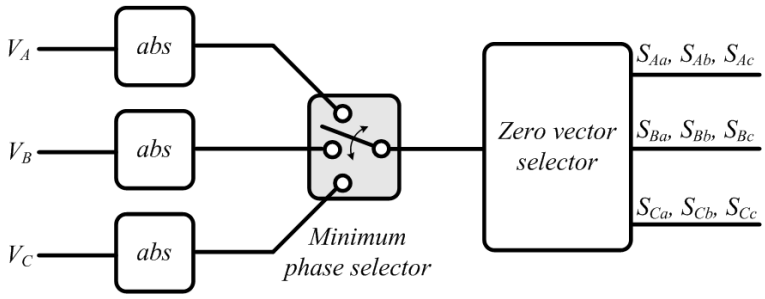

Figure 6.5: Zero vector selector.

As it has been mentioned, in section 5.3, the use of small vectors of the MC are used in order to reduce the torque ripple. At low and medium speeds, small vectors are selected very often. Since the CMV depends on the input phases involved in the selected vector, as stated in (6.10), these vectors will also contribute to reduce the CMV RMS value.

6.2.1 Simulation Results

The proposed method to reduce the CMV is analyzed and compared with the classical DTC using MC proposed in [2] in which the reduction of the number of switching events is used as the criteria to select zero vectors.
The simulation analysis has been carried out by means of the MatLab/Simulink package with the DTC having the same settings as in sections 5.2 and 5.3 for the classical and the proposed method respectively.

Fig. 6.6 shows the v_{cm} when the classical DTC using MC is used to drive the PMSM. The maximum CMV value $v_{cm_{max}}$ reaches $\pm 100V$, corresponding to the input phase negative and positive peak values. This happens when an input phase crossing its peak value is selected to deliver a zero vector.

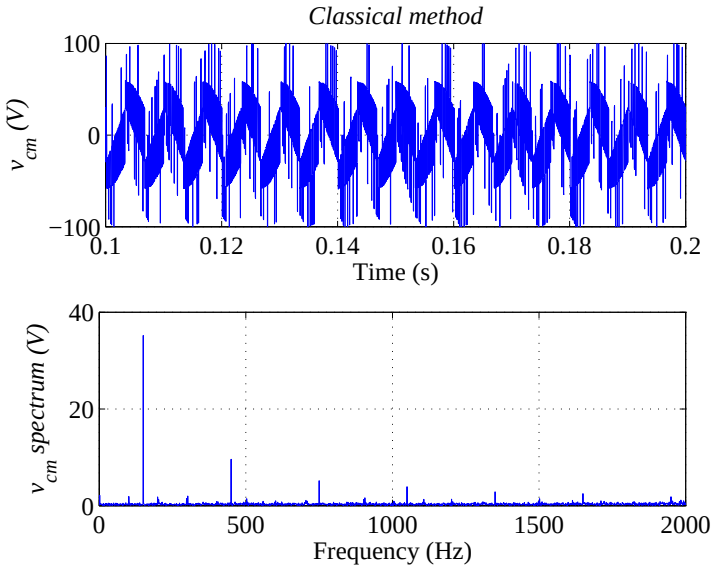

Figure 6.6: Common mode voltage and its spectrum. Classical method.

When the proposed method is used under the same conditions, the maximum CMV value is reduced to $\pm 57.7V$, as shown in Fig. 6.7, corresponding to $\pm 1/\sqrt{3}$ of the input phase peak value when active vectors are selected.

Comparing Fig. 6.6 and Fig. 6.7, it is noted that the proposed method

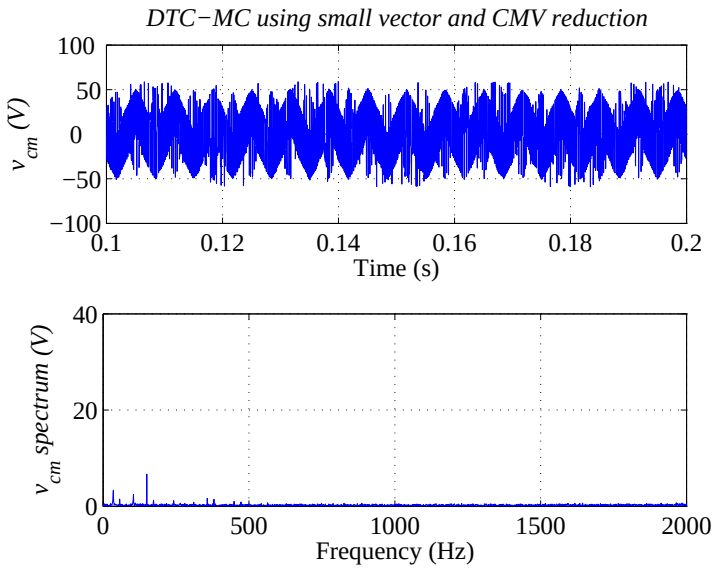

Figure 6.7: Common mode voltage and its spectrum. Proposed method.

shows a better harmonic spectrum of v_{cm}, not only by decreasing the amplitude of the CMV but also the number of harmonics.

Table 6.1: Common mode voltage comparison.

	$v_{cm_{max}}$	$v_{cm_{RMS}}$
Classical method	100 V	42.61 V
Proposed method	57.7 V	31.8 V

Table 6.1 shows the maximum CMV value and its RMS value, summarizing the performance of both methods. The proposed method shows a better performance regarding the maximum CMV and its RMS value, reducing them by 42.3% and 25.4% respectively.

6.2.2 Experimental Results

In order to validate the theoretical and simulation analysis, experimental tests has been carried out employing the rig shown in Fig. 5.11.

The v_{cm} when the classical DTC using MC is employed to drive the PMSM is shown in Fig. 6.8. It can bee seen that the maximum CMV $v_{cm_{max}}$ reaches

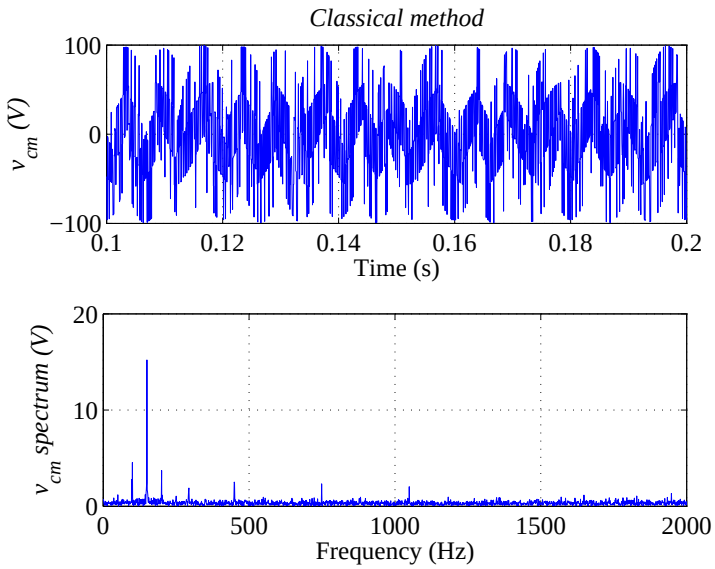

Figure 6.8: Common mode voltage and its spectrum. Classical method.

$\pm 100V$ corroborating the results shown in the simulation analysis. As in the classical method the criteria to select zero vectors is to minimize the number of the converter switching events, the CMV $v_{cm_{max}}$ will coincide with the peak value V_p of the input phase selected to deliver a zero vector.

Fig. 6.9 shows the CMV v_{cm} when the proposed method is used. Now, the maximum value of the CMV $v_{cm_{max}}$ coincides with the CMV maximum value when active vectors are delivered by the MC $v^a_{cm_{max}}$. Thus, $v_{cm_{max}} = v^a_{cm_{max}} = \pm\frac{1}{\sqrt{3}}V_p = \pm 57.7V$ as stated in (6.12).

The comparison of both methods, under the same conditions, is summarized in table 6.2. As it can bee seen, a reduction of 42.3% and 19.3% in the $v_{cm_{max}}$ and $v_{cm_{RMS}}$ respectively is achieved when the proposed method is used.

Table 6.2: Common mode voltage comparison.

	$v_{cm_{max}}$	$v_{cm_{RMS}}$
Classical method	100 V	46.42 V
Proposed method	57.7 V	37.47 V

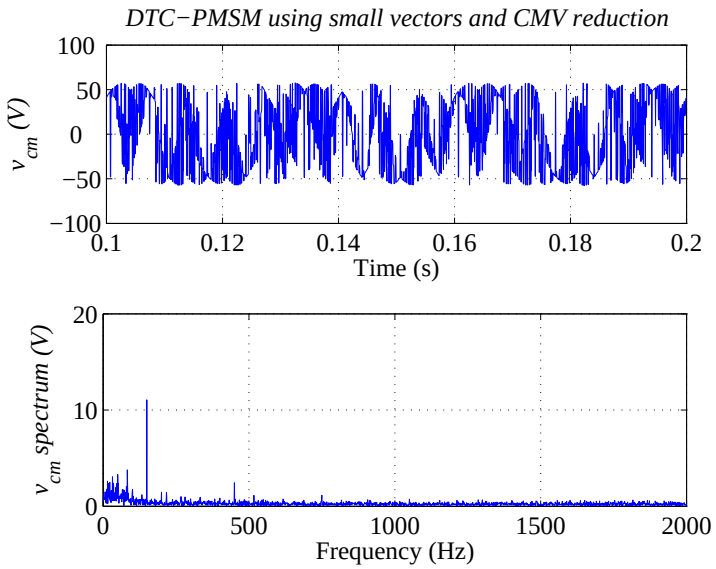

Figure 6.9: Common mode voltage and its spectrum. Proposed method.

In addition to a reduction of the motor winding failure and degradation of its bearings due to the reduction in the CMV [70], comparing the harmonic spectrum of the v_{cm} shown in Fig. 6.8 and Fig. 6.9, it can be said that the better performance shown by the proposed method will reduce the motor shaft induced voltage. Hence, it can be concluded that all these effects will, eventually, contribute to extend the motor's operational life.

Several experimental tests, covering all the machine operating points, have been carried out in order to deeply compare both methods. Both the common mode voltage and switching characteristics are investigated. As in the experiments carried out in chapter 5, the speed has been varied from 100 rpm up to 3000 rpm (*rated speed*), whereas the torque reference was varied from 0.1 Nm up to 0.64 Nm (*rated torque*). In order to assess the performance of both systems, only the RMS value of the CMV $v_{cm_{RMS}}$ has been considered since its peak value is expected to remain constant irrespective of the operating conditions.

The results, comparing the classical and the proposed method, are shown

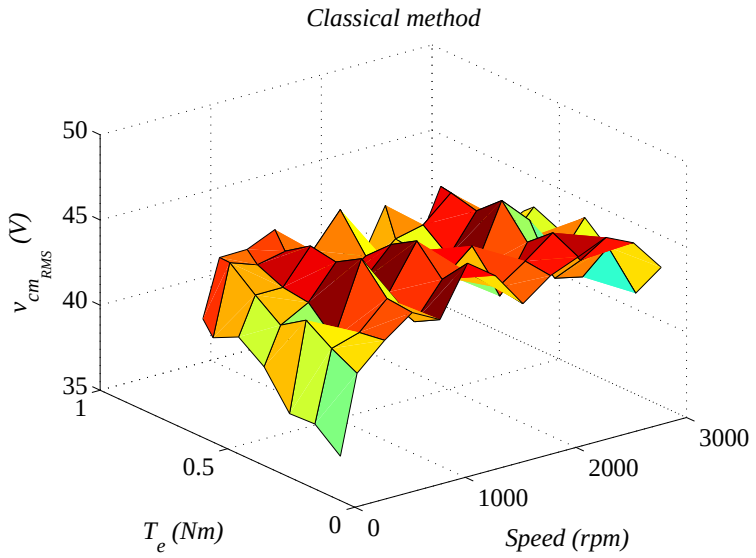

Figure 6.10: Common mode voltage. Classical method.

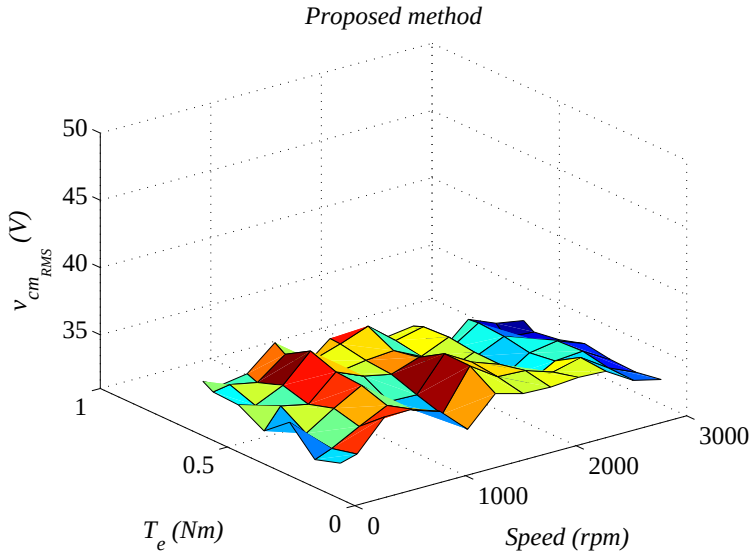

Figure 6.11: Common mode voltage. Proposed method.

in Fig. 6.10 and Fig. 6.11 respectively. It is noted the better performance of the proposed method over all the machine operating points. Moreover, considering the flatness of both figures, it can be conclude that the RMS value of the CMV $v_{cm_{RMS}}$ does not depend neither on torque nor speed.

In order to compare both systems in terms of switching events, the average number of switching events due to zero vectors selection has been calculated as follows:

$$\hat{sw} = \frac{sw_{event}}{zv_{event}} \tag{6.15}$$

where, sw_{event} is the number of switching events per second and zv_{event} is the number of zero vectors events per second[1].

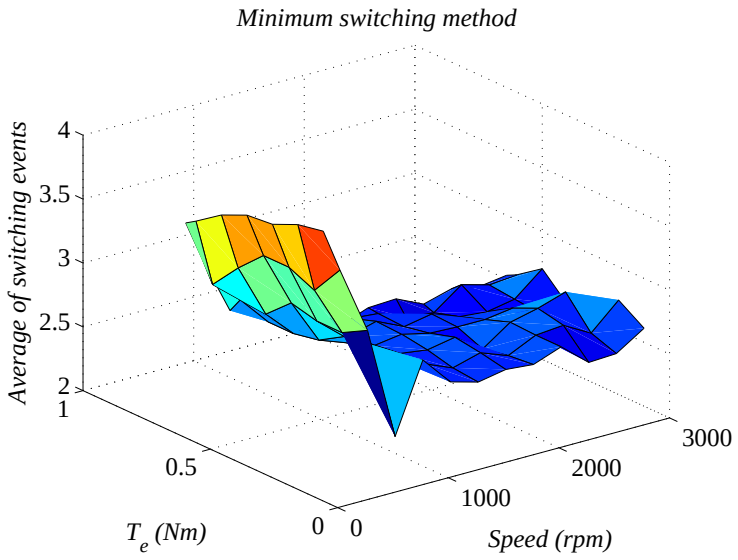

Figure 6.12: Switching events. Classical method.

It can be noted in Fig. 6.12 and Fig. 6.13 the better performance of the proposed method at low speed. At low speed, and especially at low torque, the proposed method employ small voltage vectors contributing to a medium slope torque variation. This allows the torque to easily reach the inner bands of the hysteresis controller and consequently apply zero voltage vectors more often than the classical method. Due to the low value of the back emf at low speed, the same zero voltage vector will be applied during several sampling

[1]a zero vector event is defined as any state transition form or to a zero vector.

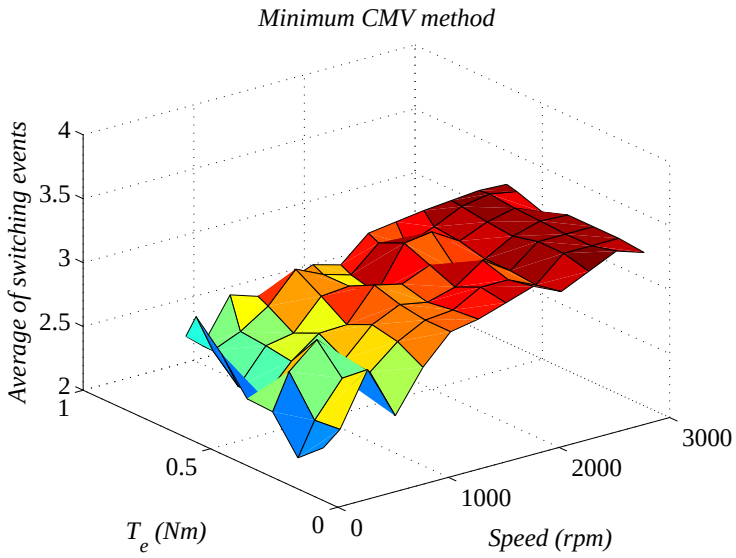

Figure 6.13: Switching events. Proposed method.

periods T_s and therefore, free of switching events. At high speed, however, the proposed method tends to increase the number of commutations when zero vector events are involved. This is mainly due to the increase of the back emf at high speeds that eventually reduces the number of sampling periods during which the same zero vector is delivered by the MC.

6.3 Conclusions

The common mode voltage produced by MCs has been analyzed focusing on the DTC driving PMSMs. The contribution of zero vectors in the CMV has been shown to be greater than that of active vectors. The advantages of the MCs, such as the availability to deliver three different zero vectors, have been exploited to reduce the CMV in DTC drives. A very simple and effective zero vector selector has been developed allowing a reduction of the maximum CMV in 42.3% while not deteriorating the output harmonic content. Moreover, the better harmonic spectrum of the CMV, specially at high frequencies, indicates that there will be a lower level of common mode current contributing to extend the machine's operational life.

Chapter 7

Rotor Position Estimate

7.1 Introduction

The introduction of vector controlled drives on the market meant that AC machines could be employed in industrial applications requiring high dynamic performance. However, this comes at the cost of housing a speed or position sensor on the end of the machine shaft. The most widely used sensor is an incremental encoder which requires a power supply, cabling and decoding hardware. Since the incremental encoder is an optical device, it is fragile and therefore compromises the robustness of the whole system.

It has been mentioned in section 2.3.4 of chapter 2 that, in recent years, there has been considerable interest in the development of sensorless[1] AC drives.

The basic idea behind all the sensorless approaches is to estimate the rotor or flux position from the terminal quantities of the machine. It was mentioned in the same section that one of the simplest model-based method

[1]generic term covering AC drives operating without a position or speed sensor.

consist in the estimate of the rotor flux position through integration of the stator voltages.

The DTC lends itself easily to sensorless control through the flux model estimator [10], but as other sensorless control schemes based on conventional fundamental-frequency models or observer based methods, fulfill the demand in the higher speed range but have been shown to give poor and asymptotically failing performance as zero speed is approached due to the loss of information as the induced back EMF becomes very small [10]. Moreover, such methods are strongly dependent on the machine parameters, which can vary during its operation. The desirability to operate continuously at low or zero speed has led to another sensorless approach where the saliency of the machine is tracked through some form of signal injection to obtain flux or position information. Although successful position and speed control at low and zero speed region has been reported in the literature, even for low saliency machines using *hf* carrier injection techniques, the approaches seem to be limited to FOC drives.

This chapter starts examining the nature of the saliencies in a SM-PMSM. The mathematical model and the corresponding demodulation scheme of the $\alpha - \beta$ frame persistent *hf* rotating carrier injection is described.

A new technique (*developed in this thesis*) to inject the rotating carrier in DTC drives is described.

7.2 Saliency Tracking

Saliency is the term usually employed to define an asymmetry in the machine. Although geometric asymmetries are the easiest to identify, specially in salient-pole machines, saliencies might arise from different sources. All machines will exhibit some kind of saliency. However, the magnitude of saliency varies between different machines.

The objective is to identify some kind of saliency that is fixed to the rotor or flux position. The response of the machine, using a signal injection technique, can then be used to obtain the saliency position. The position of the identified saliency will eventually give the rotor or flux position which will be independent of machine parameters.

7.2.1 Saliency in a Surface Mounted Permanent Magnet Synchronous Machine

The saliency in SM-PMSM is manifested by means of variations in the stator inductance. The SM-PMSM is known as a non-salient machine, thus the inductance in the direct axis (L_d^s) and in the quadrature axis (L_q^s) are usually assumed equal. In practice, a small amount of magnetic saliency can be detected. Usually, L_d^s differs from L_q^s about 25% [72]. Although this percentage is a small difference when compared with 60% of a I-PMSM, is enough to extract position information by means of some form of signal injection.

Geometric Saliency

Variations of the basic SM-PMSM design with partially inset magnets, as shown in Fig. 7.1(a), introduces a small amount of geometric saliency. As it is shown in Fig. 7.1(a), the effective airgap length at a fixed point θ will depend on the rotor position θ_r. When the rotor is aligned with the test position ($\theta_r = \theta$), the effective airgap length will coincide with its maximum (g_{max}), whereas, if the rotor is in quadrature with the test position ($\theta_r = \theta \pm \frac{\pi}{2}$), the effective airgap length will be at its minimum (g_{min}). This airgap asymmetry will lead into magnetizing inductance variation as the rotor rotates. The dependency of the magnetizing inductance with the rotor position is shown in Fig. 7.1(b). The magnetizing inductance variation will interact with the current or voltage waveforms which eventually will contain information about the saliency position. Since the asymmetry is located in the rotor, the saliency will identify the rotor position.

Similarly to a I-PMSM, on the rotor quadrature axis there is only iron,

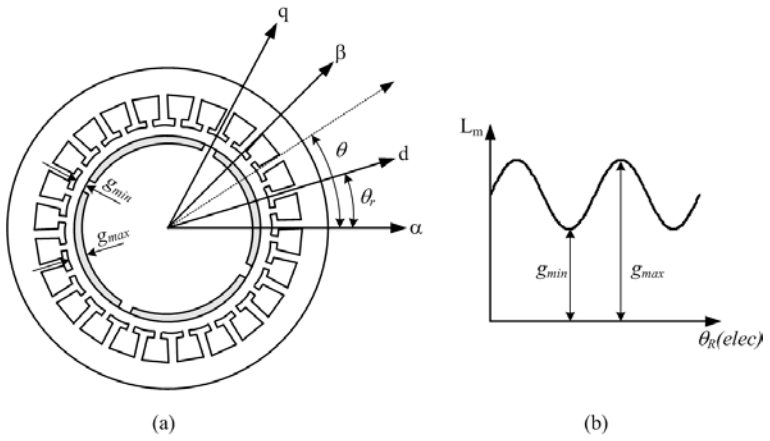

Figure 7.1: Asymmetric airgap of an inset PMSM. (a) Cross section. (b) Variation of the magnetizing inductance.

whereas, in the direct axis consist of the magnets whose permeability is close to that of air. Hence, the reluctance in the quadrature axis is smaller than in the direct axis, being $L_d^s < L_q^s$.

Saturation Saliency

In a SM-PMSM, due to the saturation effects, the stator inductances are a function of the rotor position. This magnetic saturation arises from the high airgap flux density produced by the permanent magnets. Any coil with its flux path in the direction of the saturated sections will present a reduction of its inductance value. Since the saturation will affect the flux path, the inductance will be modulated as the rotor rotates.

Assuming a sinusoidal distribution of the flux density with its maximum oriented towards the d-axis, the saturated section will be in the proximity of the d-axis. An increase of the effective airgap, due to the saturation in the d-axis, will result in a reduction of the direct axis inductance L_d^s while L_q^s will remain unaltered, $L_d^s < L_q^s$.

The explanation above holds only when the machine runs under no load.

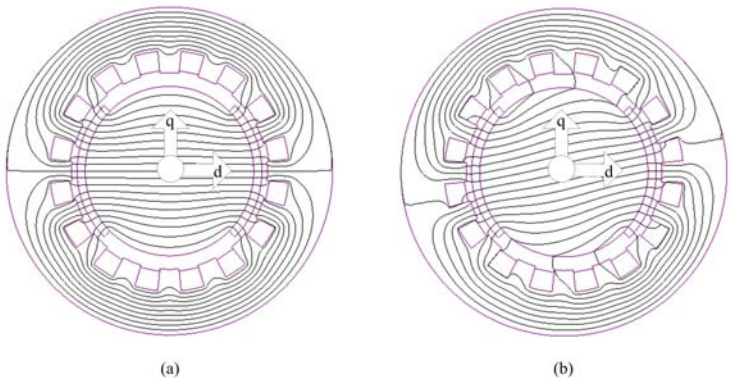

Figure 7.2: Flux displacement. (a) No Load. (b) Full load.

When a torque producing current i_q^s is needed, the term $\psi_q^s = L_q^s i_q^s$ appears, producing a shift of the flux towards the quadrature axis direction. This effect is depicted in Fig. 7.2(b), where a simplified PMSM has been analyzed by means of a finite element method simulation software. As it is shown in Fig. 7.2, the position of the saturated section, and hence the saliency position, will be misaligned under load conditions. Moreover, the misalignment angle will depend on the operating point of the machine.

7.3 High Frequency Rotating Carrier Injection in the $\alpha - \beta$ Frame

The most common way to inject in the $\alpha - \beta$ stationary frame is to superimpose a *hf* voltage carrier on the fundamental excitation. The resulting *hf* current components will contain rotor position information. The frequency of the injected voltage carrier, ω_i , should be high enough to ensure sufficient spectral separation between itself and the fundamental excitation to reduce the requirements of the band-pass filters. One possible form of *hf* voltage carrier injection, with amplitude V_i and frequency ω_i , is as follows:

$$\begin{bmatrix} v^s_{i\alpha} \\ v^s_{i\beta} \end{bmatrix} = V_i \begin{bmatrix} -\sin(\omega_i t) \\ \cos(\omega_i t) \end{bmatrix} \tag{7.1}$$

Assuming a saliency in the machine d-q rotating reference frame, i.e $L^s_d \neq L^s_q$, the PMSM voltage model can be written, in the $\alpha - \beta$ stationary reference frame as follows [15], [72]:

$$\begin{bmatrix} v^s_\alpha \\ v^s_\beta \end{bmatrix} = R_s \begin{bmatrix} i^s_\alpha \\ i^s_\beta \end{bmatrix} + \psi_{PM} \frac{d}{dt} \begin{bmatrix} \cos(\theta_r) \\ \cos\left(\theta_r - \frac{\pi}{2}\right) \end{bmatrix} + \frac{d}{dt} \begin{bmatrix} L_s - \Delta L_s \cos(2\theta_r) & -\Delta L_s \sin(2\theta_r) \\ -\Delta L_s \sin(2\theta_r) & L_s + \Delta L_s \cos(2\theta_r) \end{bmatrix} \begin{bmatrix} i^s_\alpha \\ i^s_\beta \end{bmatrix} \tag{7.2}$$

where $L_s = (L^s_d + L^s_q)/2$, $\Delta L_s = (L^s_d - L^s_q)/2$, R_s is the stator resistance, ψ_{PM} is the machine permanent magnet flux and θ_r is the rotor position in electrical degrees. When a sufficiently high frequency carrier is used, normally between 600Hz and 1KHz, the stator impedance in (7.2) is dominated by the stator inductance. Since $\omega_i L_s \gg R_s$, the first two terms in (7.2) can be neglected and approximated to:

$$\begin{bmatrix} v^s_{i\alpha} \\ v^s_{i\beta} \end{bmatrix} \approx \frac{d}{dt} \begin{bmatrix} L_s - \Delta L_s \cos(2\theta_r) & -\Delta L_s \sin(2\theta_r) \\ -\Delta L_s \sin(2\theta_r) & L_s + \Delta L_s \cos(2\theta_r) \end{bmatrix} \begin{bmatrix} i^s_{i\alpha} \\ i^s_{i\beta} \end{bmatrix} \tag{7.3}$$

From (7.1) and (7.3) the *hf* currents can be resolved and given by [15], [72]:

$$\begin{bmatrix} i^s_{i\alpha} \\ i^s_{i\beta} \end{bmatrix} = \frac{V_i}{\omega_i L^s_d L_{qs}} \begin{bmatrix} L_s \cos(\omega_i t) + \Delta L_s \cos(2\theta_r - \omega_i t) \\ L_s \sin(\omega_i t) + \Delta L_s \sin(2\theta_r - \omega_i t) \end{bmatrix} \tag{7.4}$$

The resulting *hf* currents in (7.4), where θ_r is the rotor position, contain both positive and negative sequences components. However, only the negative sequence contains position information.

7.3.1 Demodulation

The steps to carry out the demodulation of the *hf* currents are shown in Fig. 7.3. Firstly the *hf* currents components must be separated from the fundamental component by means of a band-pass filter. Synchronous filter are then used to demodulate the rotor position signal θ_r.

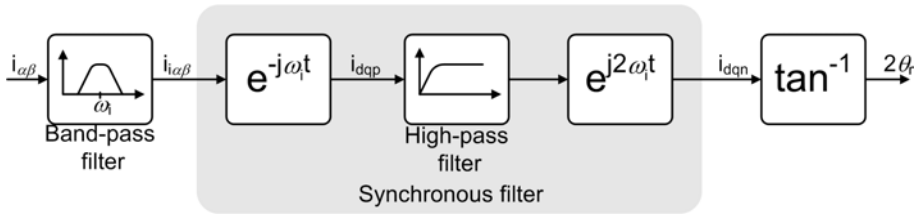

Figure 7.3: Demodulation process scheme.

Once the fundamental component has been filtered out, the *hf* currents $i_{i\alpha}$ and $i_{i\beta}$ are transformed to a reference frame rotating in the same direction as the injected signal (*positive direction*), thus the carrier component becomes DC and the negative sequence is located at $\approx 2\omega_i$, as it can be seen in (7.5) [15], [72].

$$\begin{bmatrix} i_{dp} \\ i_{qp} \end{bmatrix} = \left[T_{(-\theta_i)}\right] \begin{bmatrix} i^s_{i\alpha} \\ i^s_{i\beta} \end{bmatrix} = \frac{V_i}{\omega_i L^s_d L^s_q} \begin{bmatrix} L_s + \Delta L_s \cos(2\theta_r - 2\omega_i t) \\ L_s + \Delta L_s \sin(2\theta_r - 2\omega_i t) \end{bmatrix} \tag{7.5}$$

Note that $T_{(-\theta_i)}$ is the Park transformation matrix with $(-\theta_i)$ as the rotating angle. High-pass filtering in this frame will remove the DC component (*carrier component*). The resulting signal is then transformed to a frame rotating synchronously with the negative sequence to obtain the position signal as follows:

$$\begin{bmatrix} i_{dn} \\ i_{qn} \end{bmatrix} = [T_{2\theta_i}] \begin{bmatrix} i_{dpf} \\ i_{qpf} \end{bmatrix} = \frac{V_i}{\omega_i L^s_d L^s_q} \begin{bmatrix} \Delta L_s \cos(2\theta_r) \\ \Delta L_s \sin(2\theta_r) \end{bmatrix} \tag{7.6}$$

In (7.6) $T_{2\theta_i}$ is the Park transformation matrix with $2\theta_i$ as the rotating angle. Finally, the angle information is obtained by simply applying the atan function:

$$\theta_r = \frac{1}{2} tan^{-1}\left(\frac{i_{qn}}{i_{dn}}\right) \tag{7.7}$$

7.4 $\alpha - \beta$ High Frequency Injection in a DTC Drive

Injecting a *hf* voltage carrier of the form given in (7.1) is relatively straightforward when vector control is used to control a PMSM. Since the vector control algorithm provides a voltage reference $v^*_{\alpha\beta}$, the carrier voltage $v_{i\alpha\beta}$ can be superimposed as shown in Fig. 7.4.

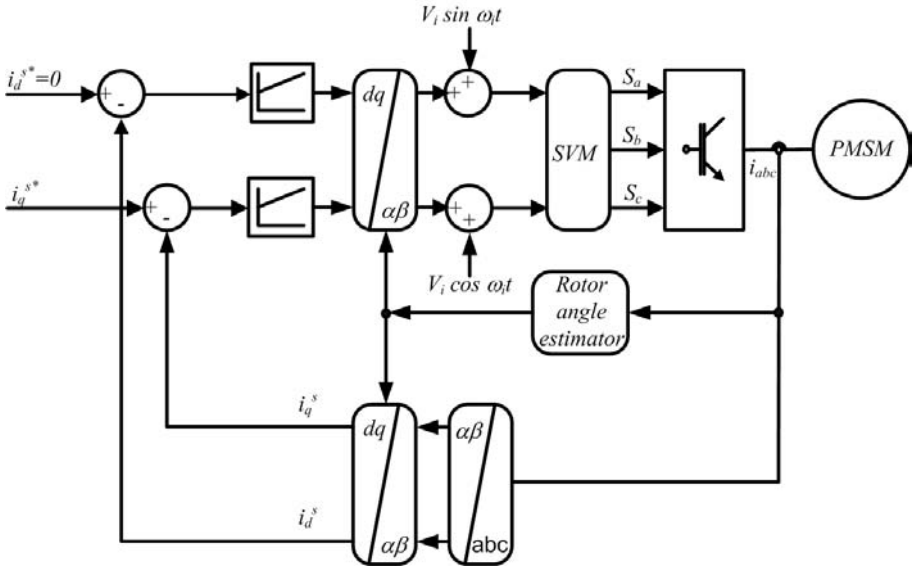

Figure 7.4: $\alpha - \beta$ rotating carrier injection in a FOC drive.

In contrast, as it can be seen in Fig. 4.3 of chapter 4, injecting a *hf* rotating vector in a DTC drive is somewhat difficult. There is no voltage reference provided by the control algorithm. Instead, the flux and torque processed errors, H_ψ and H_{T_e}, are converted directly into switching signals by the DTC

switching table. DTC based on Space Vector Modulation (SVM), and hence, with voltage reference terms, has been proposed in the literature [61], [64], however, these approaches seems to compromise the simplicity of the original DTC drive.

The introduction of a rotating *hf* voltage carrier by directly modifying the vector pattern imposed by the DTC algorithm, using a MC, is proposed in this thesis. The DTC algorithm, based on the approach presented in chapter 5 , will impose a voltage vector from the MC every sample period T_s. An amount of time t_i, from this sample period, will be employed to inject the *hf* rotating carrier as shown in Fig. 7.5. Note that $t_i \ll T_s$ to have minimum distortion effect in the DTC performance.

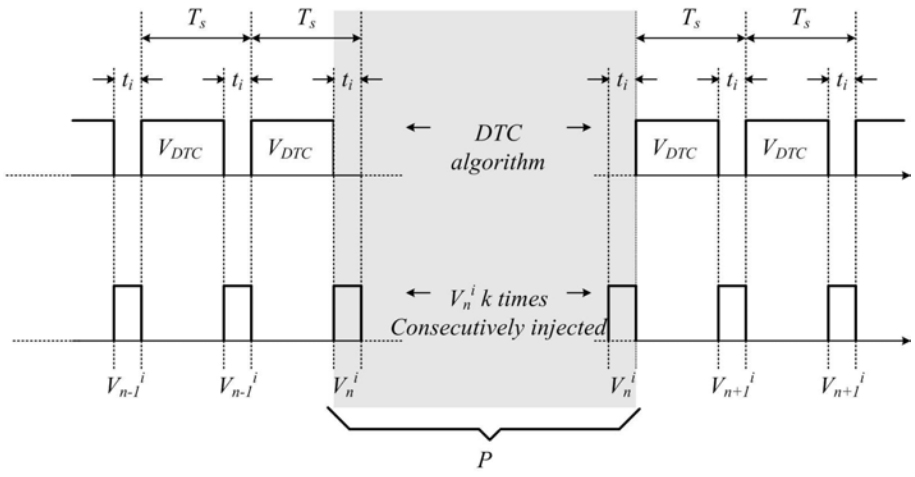

Figure 7.5: *hf* injection algorithm.

The injected vectors in Fig. 7.5 V_n^i, where $n = 1 \ldots 6$, corresponds to the active vectors that would have been applied using a VSI. When a MC is used, an active vector with the same direction as the one imposed by the algorithm using a VSI will be selected as it has been explained in section 5.2 of chapter 5.

The injection algorithm described in Fig. 7.5 will inject vectors $(V_1 - V_6)$, consecutively, at the end of every sample period T_s to superimpose the *hf*

Table 7.1: *hf* injection algorithm summary

P	$1 \ldots \infty$
V_n^i	$P - int(P/6)$
V_{DTC}	$0 \ldots 7$

rotating carrier on the fundamental excitation. Table 7.1, where P is the group of sample periods in which the same vector, V_n^i, is injected, $int(P/6)$ is the integer part of $P/6$, and V_{DTC} is the vector imposed by the DTC scheme, summarizes the *hf* injection algorithm. Depending on the carrier frequency required, the injection of a vector can be done for every sample period or in alternate periods. The carrier frequency can be controlled by means of the repetition rate k of every injected vector:

$$f_i = \frac{1}{6T_s k} \tag{7.8}$$

where $k \geq 1$ and 6 is the number, in terms of direction, of vectors available for injection. From (7.8) it can be seen that the carrier frequency will be a sub-multiple of the DTC algorithm sampling frequency T_s, however this must not be considered a constraint as the sampling frequency must be necessary high.

On the other hand, the amount of time t_i assigned for the injection will determine the magnitude of the injected vector, which can be expressed as follows:

$$V^i = \frac{t_i}{T_s} V_o \tag{7.9}$$

where V_o is the magnitude of the voltage vector at the output side of the MC.

As for the FOC drives, the rotor position is obtained from demodulating the resulting *hf* currents as explained in section 7.3.1. The complete schematic of the implemented $\alpha - \beta$ frame *hf* carrier injection in the DTC drive is shown in Fig. 7.6.

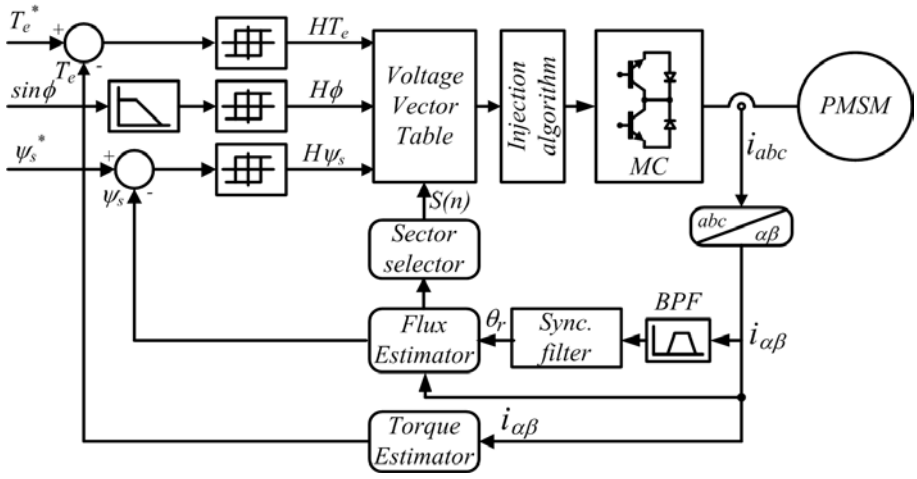

Figure 7.6: $\alpha - \beta$ injection in a DTC drive using MC. Block diagram.

7.5 Experimental Results

The proposed algorithm has been tested in the experimental rig shown in Fig. 5.11 of chapter 5.

The hysteresis brake provides a load torque which is independent of the speed. The hysteresis brake is set to give a constant torque while the PMSM is torque controlled by means of the DTC algorithm. The constant torque developed by the hysteresis brake will determine the rotating speed.

The DTC sampling period has been set to $T_z = 50\mu s$. The time assigned for injection is $t_i = 10\mu s$, giving a relation of $t_i/T_z = 0.2$, thus the magnitude of the injected vector will be 20% of the output vector magnitude. Regarding the injection frequency f_i, a repetition rate of $k = 4$ has been selected, thus obtaining $f_i = 833.33Hz$. The torque command has been set to $T_e^* = 0.4Nm$ (62.5% of the rated torque).

7.5.1 Measured signals

The measured $\alpha - \beta$ currents are depicted in Fig.7.7(a) and the spectrum of i_α can be seen in Fig.7.7(b). Figure 7.7(c) shows the zoomed area of the most important parts of the i_α current spectrum.

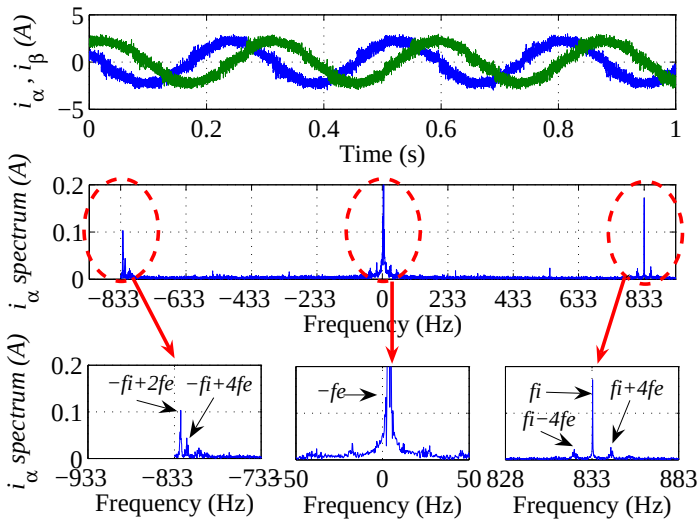

Figure 7.7: Measured currents. (a) i_α and i_β. (b) i_α spectrum. (c) i_α spectrum zoomed area.

The position information is contained in the negative sequence located at $-f_i + 2f_e$. However, as it can be seen in Fig. 7.7, there are other harmonics around this signal. In general, a machine will exhibit more than one type of saliency. The interaction of different fluxes in the machine will lead to other saturation space harmonics [73]. The position signals may also contain other harmonics as a result of the non-linear characteristics of the MC [74]. Moreover, the eccentricity of the machine, more common in small machines, can introduce further corrupting harmonics to the position signal. However, the most relevant corrupting harmonic in Fig. 7.7(c1) is located at $-f_i + 4f_e$ and can be attributed to the non-sinusoidal pattern of the saliency [73]. Comparing the spectrum of Fig. 7.7 with those obtained in [74], it can be conclude that other space harmonics arise from the DTC algorithm and the different technique employed for injecting the *hf* carrier.

The corrupting harmonics will introduce a considerable error in the position angle estimate as it can be seen in Fig.7.12(c) and consequently in the stator flux position estimate. However, the DTC algorithm does not need an accurate stator flux position estimate but just the sector in which is lying.

7.5.2 Permissible error

Considering an error in the sector in which the flux vector lies, the DTC algorithm will impose voltage vectors having similar torque effects to those imposed when no error in the sector is present. This is true, if the angle error γ_s^{error} (angle between the estimated flux vector $\hat{\psi}^s$ and the actual one ψ^s) is within $\pi/3$ radians. For larger errors $\gamma_s^{error} > \pi/3$, the applied vectors will start presenting opposite torque effects to those desired. Figure 7.8(a) shows the permissible error band ($\pi/3$ radians), and those vectors having opposite torque effects considering sectors 1 and 2 are depicted in red. Regarding the stator flux, however, the incorrect applied vector will present opposite effects to those desired. However, as the actual stator flux vector ψ^s approaches the next sector boundary, the undesirable effects of the stator flux are asymptotically mitigated. Let us consider that an increase in both torque and flux is needed in the example shown in Fig. 7.8(b). Since the actual flux vector ψ^s is lying in sector 1, vector V_2 (blue) should be applied by the DTC algorithm. However, since the estimated flux vector $\hat{\psi}^s$ lies in sector 2, vector V_3 (red) will be applied instead and, hence, decreasing the stator flux. The undesirable effects of applying the incorrect vector V_3 (red), will be especially accentuated when the actual flux vector lies in the boundary at the beginning of sector 1 as shown in Fig. 7.8(b). As the actual stator flux ψ^s moves towards the next sector boundary (sector 2), the decreasing flux effects are mitigated.

In order to corroborate the above explanation, an increasing error in the flux angle γ_s^{error}, going from zero up to $\pi/3$ radians, has been deliberately introduced in the control system. The standard deviation σ_{ψ_s} and σ_{T_e} has been computed for both the stator flux and electromagnetic torque values

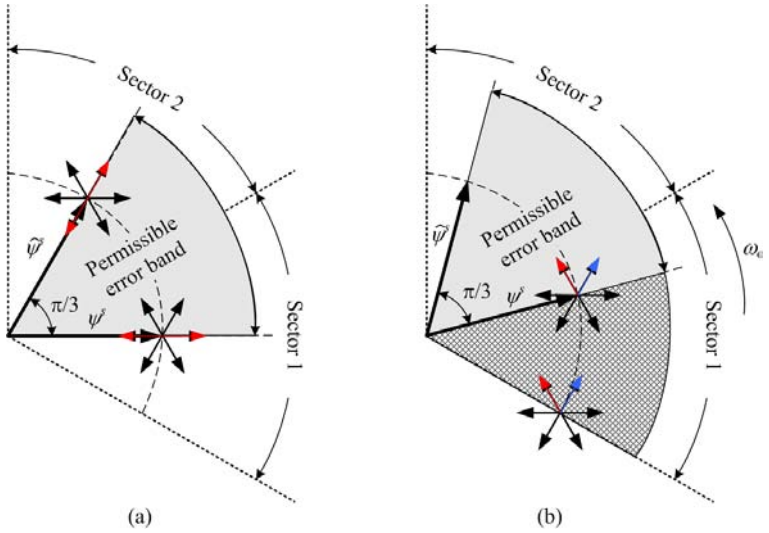

Figure 7.8: Permissible error band.

respectively. The results are shown in Fig. 7.9.

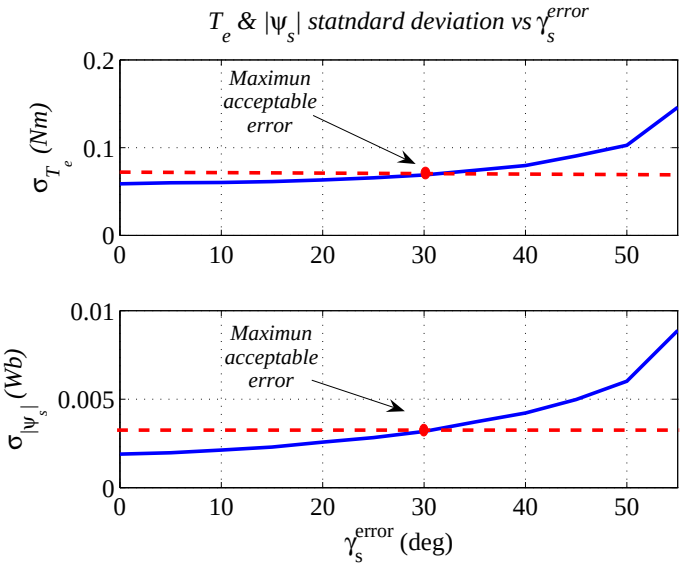

Figure 7.9: Standard deviation and maximum acceptable error.

The experimental results showed that for a flux angle error of $\gamma_s^{error} = \pi/3$ rad (60 deg), the DTC becomes unstable as expected. Moreover, based on the experimental results, a maximum acceptable angle error has been shown

to be at $\gamma_s^{error} = \pi/6$ rad (30 deg) as shown in Fig. 7.9.

The electromagnetic torque and stator flux performance with $\gamma_s^{error} = \pi/6$ rad is shown in Fig. 7.10 and can be compared to Fig. 7.11 in which $\gamma_s^{error} = 0$.

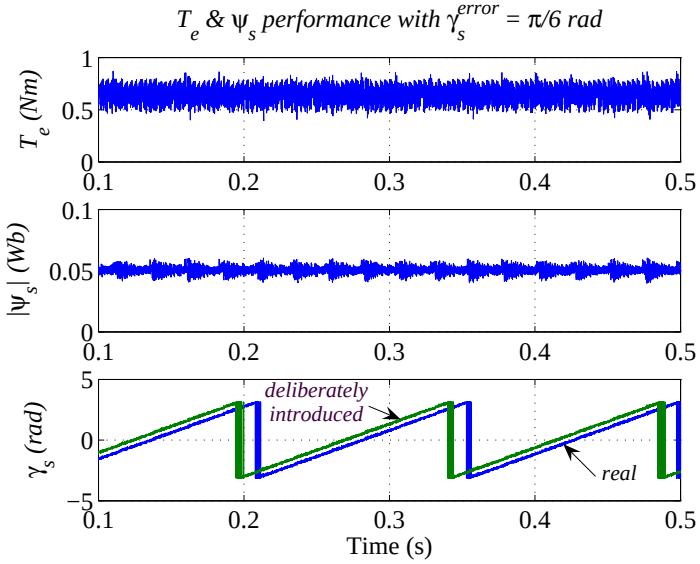

Figure 7.10: Torque and flux performance with maximum acceptable flux angle error $\gamma_s^{error} = \pi/6$.

It can be seen in Fig. 7.10 how the stator flux error abruptly increases when the actual stator flux vector ψ^s crosses a sector boundary and softly decreases as it approaches the next sector.

7.5.3 Sensorless operation

The position signals, after the demodulation process explained in section 7.3.1, i_{dn} and i_{pn}, with the PMSM running at $38rpm$, are shown in Fig.7.12(a). In Fig.7.12(b) the estimated rotor position is compared with the actual (measured) rotor position.

As it can be seen in Fig.7.12(c), the error in the estimated rotor position is within ±20 degrees being inside the permissible error band shown in Fig.

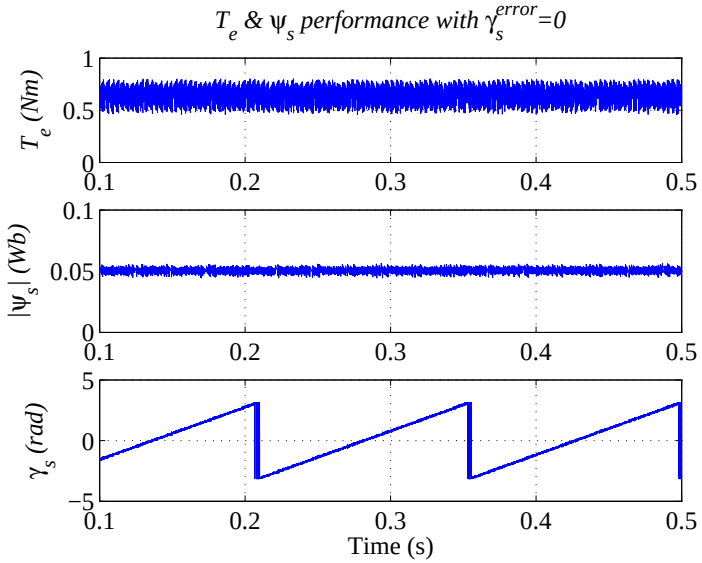

Figure 7.11: Torque and flux performance with no flux angle error $\gamma_s^{error} = 0$.

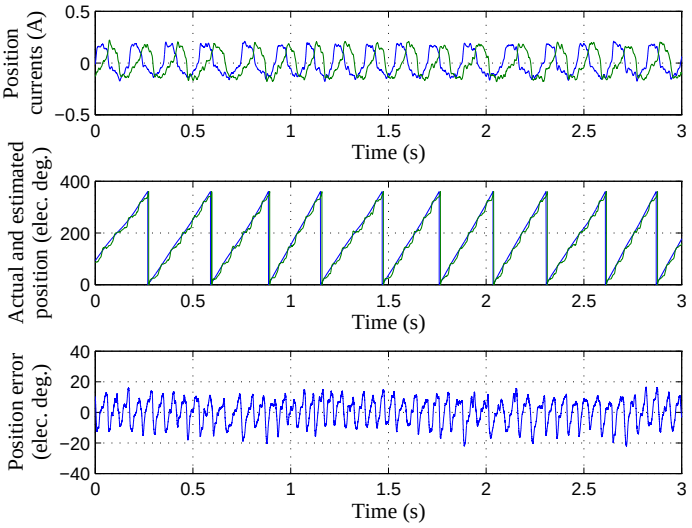

Figure 7.12: Position estimate. (a)i_{dqn} currents. (b) Actual and estimated position. (c) position error.

7.8. Compering the results with those obtained in [75], it can noted that the use of a MC clearly improves the characteristics of the position signals and hence the estimated rotor flux position.

7.6 Conclusions

The extension of the $\alpha - \beta$ frame *hf* carrier injection method to a PMSM DTC drive using a MC has been presented in this paper. The new *hf* injection algorithm does not compromise the original DTC simplicity while has the potential to extend the operation of the sensorless DTC drive to the low speed region. Initial experimental results which demonstrates the effectiveness of the proposed method are shown. Despite MCs have been shown to provide better switching characteristics than VSIs, the remaining non-linearities of the former introduces a significant error in the position angle estimate. Although the error in the position estimate will not make the system fail, further investigation in order to reduce it has to be carried out.

Chapter 8

Conclusion and Further Work

The main objective of this thesis was to investigate the characteristics of the MC that can be exploited to improve the conventional DTC performance.

The conventional DTC, reviewed in chapter 4, can be improved by replacing the standard VSI by a MC. In addition to power factor control capabilities, the advantages of the MC can be further exploited using not only the commonly employed large voltage vector but also those having smaller amplitude. It has been demonstrated that the use of small voltage vectors allow the system to distinguish between small and large torque errors. Based of this fact, a new DTC-PMSM drive using MCs which reduces the electromagnetic torque ripple has been developed in this thesis. The improvement is also noted in the output current THD.

Moreover, as it has been stated in chapter 5, the re-organization of the sectors in which the input voltage vector can lie, contributes to improve the voltage transfer ratio of the MC. This will not only allow the system to reach the machine rated conditions with less steady state error, but also contributes to make the drive torque response faster.

Furthermore, it has been shown that the availability of three different null vectors in MCs can be considered to reduce the undesirable common mode voltage at the output of the converter. A new criteria to select zero vectors which significantly reduces the common mode voltage has been proposed.

In order to overcome the limitations of model based sensorless techniques, a high frequency signal can be injected in a DTC drive by directly modifying the vector pattern. The better switching characteristics of the MC can improve the position signals waveforms.

8.1 Contributions

The main contributions of this thesis can be summarized in the following points:

- **A new DTC using MC has been developed.**
  The use of small voltage vectors of the MC has been investigated in order to reduce the inherent electromagnetic torque and stator flux ripples present in DTC drives. The maximum ripple reduction achieved has been 50.27% and 21.22% for the torque standard deviation σT_e and the flux standard deviation $\sigma \psi^s$ respectively. Moreover, these improvements also contributes to a better output current THD, achieving a maximum improvement of 62.92%.
  Regarding transient performance, the increased voltage transfer ratio allows the system to response twice faster to a torque step transient.

- **A very simple algorithm to reduce the common mode voltage has been implemented.**
  The common mode voltage of a MC has been mathematically analyzed. The maximum common mode voltage arises when zero voltage vectors are selected by the DTC algorithm. By selecting the proper zero vector,

the new algorithm can considerably reduce the common mode voltage. The maximum reduction achieved has been 42.43%.

- **A novel *hf* injection technique for DTC drives has been proposed.**
  The extension of the $\alpha - \beta$ frame *hf* carrier injection method to a PMSM DTC drive using a MC has been proposed by directly modifying the vector pattern.

8.2 Further work

To follow up the work presented in this thesis it is recommended some further work. This can be summarized in the following ideas:

- **Investigate new techniques for *hf* signal injection in a DTC drive.**
  The modification of the vector pattern might not be the only way to superimpose a *hf* signal onto the fundamental excitation. At least two other techniques could be suggested for further investigation:
  - Superimposing the *hf* signal onto the electromagnetic torque and stator flux hysteresis bands.
  - Superimposition of the *hf* signal onto the electromagnetic torque and stator flux references.
- **Further investigation to implement a sensorless DTC drive.**
  After analyzing different techniques for *hf* signal injection in a DTC drive, further work could be done to select the one with better performance.

8.3 Publications

The presented work has resulted in the following conference papers:

8.3.1 Papers directly related with the presented work

- C. Ortega, A. Arias, C. Caruana, M. Apap and J. Balcells, "Torque ripple reduction in PMSM DTC drives using matrix converters," Proceedings of EPE '07, vol. 1, pp. 1 - 10, September, 2007.
- C. Ortega, A. Arias, J. Balcells and C. Caruana, "High frequency injection in a matrix converter dtc drive for sensorless operation of a PMSM," Proceedings of ISIE '07, vol. 1, pp. 2278-2283, July, 2007.
- C. Ortega, A. Arias, J. Balcells, C. Caruana, C. Spiteri and J. Cilia, "The use of small voltage vectors of matrix converters in direct torque control of induction machines," Proceedings of EPE-PEMC '06, vol. 1, pp. 1-4, July, 2006.
- C. Ortega, A. Arias, J. Balcells, C. Caruana, C. Spiteri and J. Cilia, "Sensorless direct torque control of a surface mounted pmsm using high frequency injection," Proceedings of EPE-PEMC '06, vol. 1, pp. 1-4, July, 2006.
- C. Ortega, A. Arias, X. del Toro, E. Aldabas, and J. Balcells, "Novel direct torque control for induction motors using short voltage vectors of matrix converters," Proceedings of IECON '05, vol. 1, pp. 1353-1358, July, 2005.
- C. Ortega, A. Arias, L. Romeral, L. and E. Aldabas, "Power factor correction, using matrix converters, in direct torque control for induction motors," Proceedings of SAAEI '05, vol. 1, pp. 342-348, September, 2005.

Accepted papers. (Not yet published.)

- C. Ortega, A. Arias, C. Caruana and M. Apap, "Reducing the common mode voltage in a dtc-pmsm drive using matrix converters," Presented at ISIE '08.
- C. Ortega, A. Arias, C. Caruana and M. Apap, "Common mode voltage in dtc drives using matrix converters," Presented at ICECS '08.

8.3.2 Papers not directly related with the presented work in which the author of this thesis has collaborated.

- E. Aldabas, L. Romeral, A. Arias and C. Ortega, "Current controller with low total harmonic distortion," Proceedings of EPE '05, vol. 1, pp. 1-8, July, 2005.

- A. Arias, C. Ortega, J. Pou, D. Gonzalez and J. Balcells, "Sensorless Field Oriented Control with Matrix Converters and Surface Mount Permanent Magnet Synchronous Machines," Presented at ICECS '08.

- A. Arias, E. Aldabas, C. Ortega and M. Corbalan, "Current Regulated Matrix Converter for Field Oriented Control of Permanent Magnet Synchronous Machines," Presented at ICECS '08.

- J. Pou, R. Pindado, C. Jaen, A. Arias, J. Zaragoza, C. Hervada, P. Buenestado, C. Ortega and E. Jarauta, "Model, design, analysis and state-of-the-art control from the blowing wind to the sinusoidal voltages and currents," Presented at WREC '08.

- A. Arias, C. Ortega, J. Pou, D. Gonzalez and J. Balcells, "Angle estimation for Sensorless Field Oriented Control with Matrix Converters and Surface Mount Permanent Magnet Synchronous Machines," Presented at PESC '08.

The most relevant of the above listed publications can be found in the appendix.

Bibliography

[1] B. K. Bose, *Modern Power Electronics and AC Drives*, P. Hall, Ed. Prentice Hall, 2002.

[2] D. Casadei, G. Serra, and A. Tani, "The use of matrix converters in direct torque control of induction machines," *IEEE Transactions on Industrial Electronics*, vol. 48, pp. 1057–1064, December, 2001.

[3] D. Casadei, G. Serra, A. Tani, and L. Zarri, "Matrix converter modulation strategies: A new general approach on space-vector representation of the switch state," *IEEE Transactions on Industrial Electronics*, vol. 49, pp. 370–381, April, 2002.

[4] S. Bouchiker, G. Capolino, and M. Paloujadoff, "Vector control of a permanent-magnet synchronous motor using ac-ac matrix converter," *IEEE Transactions on Power Electronics*, vol. 13, pp. 1089–1099, November, 1998.

[5] F. Blaschke, "The principle of field-orientation as applied to the transvector closed-loop control system for rotating-field machines," *Siemens Review*, vol. 34, pp. 217–220, 1972.

[6] K. Hasse, "Drehzahlregel füer schnelle umkehrantriebe mit stromrichtergespeisten asynchron-kurzschlusslaufer-motoren," *Reglungstechnik*, vol. 20, pp. 60–66, 1972.

[7] I. Takahashi and T. Nogushi, "A new quick-response and high-efficiency control strategy of an induction motor," *IEEE Transactions on Industry Applications*, pp. 820–827, October, 1986.

[8] M. E. El-Hawary, *Principles of Electric Machines with Power Electronic Applications*. Reston Pub.CO, 1986.

[9] I. Bolea and S. A. Nasar, *The induction motor machine handbook.*, C. Press, Ed. CRC Press, 2002.

[10] P. Vas, *Sensorless Vector and Direct Torque Control*, O. university press Inc., Ed. Oxford university press Inc., 1998.

[11] Y. Honda and Y. Takeda, "Technical evolution of permanent magnet synchronous motors for home appliances," *IEEE Transactions on Electric and Electronic Engineering*, vol. 2, pp. 118–124, 2007.

[12] K. B. Lee, J. H. Song, I. Choy, and J. Y. Yoo, "Improvement of low-speed operation performance of dtc for three-level inverter-fed induction motors," *IEEE Transactions on Industrial Electronics*, vol. 48, pp. 1006–1014, October, 2001.

[13] V. Perelmuter, "Three-level inverters with direct torque control," *Proceedings of IEEE Industry Apllication Conference '00*, vol. 3, pp. 1368–1374, October, 2000.

[14] M. P. Kazmierkowski, R. Krishman, and F. Blaabjerg, *Control in Power Electronics. Selected Problems*, A. Press, Ed. Academic Press, 2002.

[15] C. Silva, "Sensorless vector control of surface mounted permanent magnet machines without restriction of zero frequency," Ph.D. dissertation, University of Nottingham, 2003.

[16] M. Depenbrock, "Direct self-control (dsc) of inverter-fed induction machine," *IEEE Transactions on Power Electronics*, vol. 3, pp. 420–429, October, 1988.

[17] G. M. A. K. Ohyama and M. Sumner, "Comparative analysis of experimental performance and stability of sensorless induction motor drives," *IEEE Transactions on Industrial Electronics*, vol. 53, pp. 178– 186, Frebruary, 2006.

[18] J. Campbell, "A sensorless induction motor drive employing an artificial neural network for on-line parameter adption," Ph.D. dissertation, University of Nottingham, 2001.

[19] R. Dhauodi, N. Mohan, and L. Norum, "Design and implementation of an extended kalmam filter for the state estimation of a permanent magnet synchronous motor," *IEEE Transactions on Power Electronics*, vol. 6, pp. 491–497, May, 1991.

[20] J. S. Kim and S. K.Sul, "New approach for high performance pmsm drives without rotational position sensors," *IEEE Transactions on Power Electronics*, vol. 12, pp. 904–911, Setember, 1997.

[21] R. B. Sepe and J. H. Lang, "Real-time observer (adaptive) control of a permanent magnet synchronous motor without mechanical sensors," *IEEE Transactions on Industry Applications*, vol. 28, pp. 1345–1352, November./December, 1992.

[22] J. Hu, D. Zhu, and B. Wu, "Permanent magnet synchronous motor drive without mechanical sensors," *Proceedings of CCECE '96*, vol. 2, pp. 603–606, May, 1996.

[23] M. Corley and R. D. Lorenz, "Rotor position and velocity estimation for a salient-pole permanent magnet synchronous machine at standstill and high speeds," *IEEE Transactions on Industry Applications*, vol. 34, pp. 784–789, July/August, 1998.

[24] S. Bolognani, R. Oboe, and M. Zigliotto, "Sensorless full-digital pmsm drive with ekf estimation od speed and rotor position," *IEEE Transactions on Industrial Electronics*, vol. 46, pp. 184–191, February, 1999.

[25] G. F. Franklin, J. Powell, and A. Emami-Naeini, *Feedback Control of Dynamic Systems*, A.-W. P. Company, Ed. Addison-Wesley Publishing Company, 1994.

[26] J. L. Ha, S. J. Kang, and S. K. Sul, "Position-controlled synchronous reluctance motor without rotational transducer," *IEEE Transactions*

on Industry Applications, vol. 35, pp. 1393–1398, November/December, 1999.

[27] S. Kondo, A. Takahashi, and T. Nishida, "Armature current locus based estimation method of rotor position of permanent magnet synchronous motor without mechanical sensor," *Proceedings of IAS '95*, vol. 1, pp. 55–56, 1995.

[28] S. Ogasawara and H. Akagi, "Implementation and position control performance of a position-sensorless ipm motor drive system based on magnetic saliency," *IEEE Transactions on Industry Applications*, vol. 34, pp. 806–812, July/August, 1998.

[29] A. Consoli, F. Russo, G. Scarcella, and A. Testa, "Low and zero-speed sensorless control of synchronous reluctance motors," *IEEE Transactions on Industry Applications*, vol. 35, pp. 1050–1057, September/October, 1999.

[30] P. L. Jansen and R. D. Lorenz, "Transducerless position and velocity estimation in induction and salient ac machines," *IEEE Transactions on Industry Applications*, vol. 31, pp. 240–247, March/April, 1995.

[31] F. Blaschke., J. Burgt, and A. Vandenput, "Sensorless direct field orientation at zero flux frequency," *Proceedings of IAS '96, Annual Meeting*, vol. 1, pp. 189–191, 1996.

[32] J. I. Ha and S. K. Sul, "Sensorless field orientation control of an induction machine by high frequency signal injection," *Proceedings of IAS '97, Annual Meeting*, vol. 1, pp. 426–432, October, 1997.

[33] N.teske, G. Asher, M. Sumner, and K. J. Bradley, "Encoderless position control of induction machines," *Proceedings of EPE '01*, 2001.

[34] J. Holtz, "Sensorless position control of induction motors. an emerging technology," *IEEE Transactions on Industry Applications*, vol. 45, pp. 840–852, December, 1998.

[35] N. Matsui and M. Shigyo, "Brushless dc motor control without position and speed sensors," *IEEE Transactions on Industry Applications*, vol. 28, pp. 120–127, January/February, 1992.

[36] M. Schrodl, "Sensorless control of ac machines at low speed and standstill based on the 'inform' method," *Proceedings of IAS '96, Annual Meeting*, vol. 1, pp. 270–277, October, 1996.

[37] J. Cilia, G. M. Asher, K. J. Bradley, and M. S. 1997., "Sensorless position detection for vector-controlled induction motor drives using an asymmetric outer-section cage," *IEEE Transactions on Industry Applications*, vol. 33, pp. 1162–1169, September/October, 1997.

[38] J.-H. J. N. Bianchi, S. Bolognani and S.-K. Sul, "Comparison of pm motor structures and sensorless control techniques for zero-speed rotor position detection," *IEEE Transactions on Power Electronics*, vol. 22, pp. 2466–2475, November, 2007.

[39] N. Mohan, T. M. Undeland, and W. P. Robbins, *Power Electronics. Converters, applications and Design*, I. John Wiley & sons, Ed. John Wiley & sons, Inc., 1995.

[40] L. Huber and D. Borojevic, "Space vector modulated three-phase to three-phase matrix converter with input power factor correction," *IEEE Transactions on Industry Applications*, vol. 31, pp. 1234–1246, November/December, 1995.

[41] L. Empringham, P. Wheeler, and J. L. Clare, "Intelligent commutation of matrix converter bi-directional switch cells using novel gate drive techniques," *Proceedings of PESC '98*, vol. 1, pp. 707–713, June/July, 1998.

[42] M. Venturini, "A new sine wave in, sine wave out conversion technique eliminates reactive elements," *Proceedings of Powercon '80*, pp. E3–1 E–15, 1980.

[43] M. Venturini and A. Alsina, "The generalized transformer: a new bidirectional sinusoidal waveform frequency converter with continuously adjustable input power factor," *Proceedings of PESC '80*, vol. 1, pp. 242–252, 1980.

[44] ——, "Analysis and design of optimum-amplitude nine-switch direct ac-ac converters," *IEEE Transactions on Power Electronics*, vol. 4, pp. 101–112, January, 1989.

[45] J. H. Youm and B. H. Kwon, "Switching technique for current-controlled ac-to-ac converters," *IEEE Transactions on Industrial Electronics*, vol. 46, pp. 309–318, April, 1999.

[46] C. L. Neft, "Ac power supply static switching apparatus having energy recovery capability," *U.S. Patent No. 4,697,230*, 1987.

[47] C. D. Shauder, "Matrix converter circuit and commutation method," *U.S. Patent No. 5,594,636*, 1997.

[48] M. Venturini and A. Alsina, "Solid-state power conversion: A fourier analysis approach to generalized transformer synthesis," *IEEE Transactions on Circuits and Systems*, vol. 28, pp. 319–330, April, 1981.

[49] C. D. C. L. Neft and Shauder, "Theory and design of a 30-hp matrix converter," *IEEE Transactions on Industry Applications*, vol. 28, pp. 546–551, May/June, 1992.

[50] H. J. Cha and P. N. Enjeti, "An approach to reduce common-mode voltaje in matrix converter," *IEEE Transactions on Industry Applications*, vol. 39, pp. 1151–1159, July/August 2003.

[51] P. Nielsen, F. Blaabjerg, and J. K. Pedersen, "Space vector modulated matrix converter with minimized number of switching and a feedforward compensation of input voltage unbalance," *Proceedings of PEDES '96*, vol. 2, pp. 833–839, 1996.

[52] P. Ziogas, S. Khan, and M. Rashid, "Some improved forced commutated cycloconverters structures," *IEEE Transactions on Industry Applications*, vol. 1A-21, pp. 1242–1253, September/October, 1985.

[53] N. Burany, "Safe control of 4-quadrant switches," *Proceedings of IAS '89, Annual Meeting*, vol. 2, pp. 1190–1194, December, 1989.

[54] J. Oyama, T. Higuchi, T. Yamada, and T. Lipo, "New control strategy for matrix converter," *Proceedings of PESC '89*, vol. 1, pp. 360–367, June, 1989.

[55] P. Wheeler and D. Grant, "Optimized input filter design and low loss switching techniques for a practical matrix converter," *Proceedings of IEE Electric Power Applications*, vol. 114, pp. 53–60, January, 1997.

[56] P. Nielsen, F. Blaabjerb, and J. Pedersen, "Novel solutions for protection of matrix converter to three phase induction machine," *Proceedings of IAS '97*, vol. 2, pp. 1447–1454, 1997.

[57] J. Mahlein and M. Brain, "A matrix converter without diode clamped over-voltage protection," *Proceedings of IPE Matrix Converter '00*, vol. 1, pp. 817–822, October, 2000.

[58] A. Shuster, "A matrix converter without reactive clamp elements for an induction motor drive system," *Proceedings of PESC '98*, vol. 1, pp. 714–720, May, 1998.

[59] A. Arias, "Improvements in direct torque control of induction motors," Ph.D. dissertation, Universitat Politècnica de Catalunya. Campus Terrassa., 2001.

[60] J.-K. Kang and S.-K. Sul, "New direct torque control of induction motors for minimum torque ripple and constant switching frequency," *IEEE Transactions on Industry Applications*, vol. 35, pp. 1076–1082, September/October, 1999.

[61] D. Casadei, G. Serra, and A. Tani., "Implementation of a direct torque control algorithm for induction motors based on discrete space vector

modulation," *IEEE Transactions on Power Electronics*, vol. 15, pp. 769–777, July, 2000.

[62] I. Ludtke and M. G. Jayne, "Direct torque control of induction motors," *IEE Colloquium on Vector Control and Direct Torque Control of Induction Motors*, vol. 1, pp. 1–6, October 1995.

[63] G. Habetler, F. Profuno, M. Pastorelli, and L. Tolbert., "Direct torque control of induction machines using space vector modulation," *IEEE Transactions on Industry Applications*, vol. 28, pp. 1045–1053, September/October, 1992.

[64] G. S. Buja and M. P. Kazmierkowski, "Direct torque control of pwm inverter-fed ac motors: A survey," *IEEE Transactions on Industrial Electronics*, vol. 51, pp. 744–758, August, 2004.

[65] I. G. Bird and H. Zelaya, "Fuzzy logic torque ripple reduction for dtc based ac drives," *IEE Electronics Letters*, vol. 33, pp. 1501–1502, August, 1997.

[66] A. Arias, L. Romeral, E. Aldabas, and M. G. Jayne, "Improving direct torque control by means of fuzzy logic," *IEE Electronics Letters*, vol. 37, pp. 69–71, January, 2001.

[67] I. Takahashi and Y. Ohmori, "High-performance direct torque control of an induction motor," *IEEE Transactions on Industry Applications*, vol. 25, pp. 257–264, March/April 1989.

[68] P. Wheeler, J. Rodriguez, J. C. Clare, L. Empringham, and A. Weinstein, "Matrix converters: a technology review," *IEEE Transactions on Industrial Electronics*, vol. 49, pp. 276–288, April, 2002.

[69] D. A. Rendusara and P. N. Enjet, "An improved inverter output filter configuration reduces common and differential modes dv/dt at the motor terminals in pwm drive systems," *IEEE Transactions on Power Electronics*, vol. 13, pp. 1135–1143, November, 1998.

[70] A. L. Julian, G. Oriti, and T. A. Lipo, "Elimination of common-mode voltage in three-phase sinusoidal power converters," *IEEE Transactions on Power Electronics*, vol. 14, pp. 982–989, September, 1999.

[71] G. V. M. Cirrincione, M. Pucci and G. Cirrincione, "A new direct torque control strategy for the minimization of common-mode emissions," *IEEE Transactions on Industry Applications*, vol. 42, pp. 504–517, March/April, 2006.

[72] C. Spiteri, J. Cilia, B. Michallef, and M. Apap, "Sensorless vector control of surface mount pmsm using high frequency injection," *Proceedings of Power Electronics Machines and Drives '02*, vol. 1, pp. 44–48, June, 2002.

[73] C. Caruana, G. Asher, and M. Summer, "Performance of hf injection techniques for zero-low-frequency vector control of induction machines under sensorless conditions," *IEEE Transactions on Industrial Electronics*, vol. 53, pp. 225–238, February, 2006.

[74] A. Arias, C. A, Silva, G. M. Asher, J. C. Clare, and P. W. Wheeler, "Use of a matrix converter to enhance the sensorless control of a surface-mount permanent-magnet ac motor at zero and low frequency," *IEEE Transactions on Industrial Electronics*, vol. 53, pp. 100–109, April, 2006.

[75] C. Ortega, A. Arias, C. Caruana, C. Staines, J. Balcells, and J. Cilia, "Sensorless direct torque control of a surface mounted pmsm using high frequency injection," *Proceedings of ISIE '06*, vol. 3, pp. 2332–2337, July, 2006.

Appendix

The most relevant publications directly related with the research presented in this thesis are included.

Novel Direct Torque Control for Induction Motors using short voltage vectors of Matrix Converters

Authors: C. Ortega, A. Arias, X. del Toro, E. Aldabas, and J. Balcells.
Proceedings of IECON '05, vol. 1, pp. 1353-1358, July, 2005.

Abstract - This paper investigates the use of short voltage vectors of Matrix Converters to reduce the electromagnetic torque ripple which appears when Direct Torque Control technique is used in Induction Motors. Direct Torque Control for Induction Motors using Matrix Converters is reviewed and it is pointed out the problem of the electromagnetic torque ripple which is one of the most important drawbacks of the Direct Torque Control. The standard look up table for Direct Torque Control, when using Matrix Converters, is improved in order to include the uncommonly used short voltage vectors. This novel Direct Torque Control approach can differentiate between small and large torque errors and consequently the electromagnetic torque ripple is reduced. Finally, some results, which prove the improvement of the novel Direct Torque Control when using small Matrix Converter voltage vectors, are shown.

Novel Direct Torque Control for Induction Motors using short voltage vectors of Matrix Converters

Carlos Ortega[1], Antoni Arias[2] MIEEE, Xavier del Toro[3], Emiliano Aldabas[4] MIEEE, Josep Balcells[5] MIEEE

[1,2,3,4,5] Technical University of Catalonia. Electronics Engineering Dept. Colom 1, Terrassa 08222, Catalonia, Spain.
cortega@euss.es, arias@eel.upc.edu, xdeltoro@glam.ac.uk, aldabas@eel.upc.edu, balcells@eel.upc.edu

Abstract — **This paper investigates the use of short voltage vectors of Matrix Converters to reduce the electromagnetic torque ripple which appears when Direct Torque Control technique is used in Induction Motors.**

Direct Torque Control for Induction Motors using Matrix Converters is reviewed and it is pointed out the problem of the electromagnetic torque ripple which is one of the most important drawbacks of the Direct Torque Control.

The standard look up table for Direct Torque Control, when using Matrix Converters, is improved in order to include the uncommonly used short voltage vectors. This novel Direct Torque Control approach can differentiate between small and large torque errors and consequently the electromagnetic torque ripple is reduced.

Finally, some results, which prove the improvement of the novel Direct Torque Control when using small Matrix Converter voltage vectors, are shown.

I. INTRODUCTION

A new advanced control technique, named as Direct Torque Control (DTC) [1] or Direct Self Control [2] was introduced for Voltage Source Inverters (VSI) drives in 1986 and 1988 respectively. Since then, DTC has gained popularity and nowadays several commercial drives are based on such control technique. However, some research is still being done to adapt DTC to new electrical motors and power converters and also to reduce the electromagnetic torque ripple, which is one of its main drawback [3].

DTC, as the name indicates, is the direct control of torque and flux of an electrical motor by the selection, through a look-up table, of the power converter voltage space vectors. The main advantage of DTC is its structure simplicity, since no coordinate transformations, current controllers and modulations are needed. Moreover the controller does not depend on motor parameters. DTC is considered to be a simple and robust control scheme which achieves quick and precise torque control response. However, torque and flux modulus values and the sector of the flux are needed and more importantly, short sampling period time for the torque and flux control loops are needed in order to keep electromagnetic torque ripple within an acceptable value [3]. In fact, the use of voltage modulation has been employed in order to reduce such ripple. In the literature Space Vector Modulation is also shown to maintain a small torque ripple whilst holding the switching frequency constant [3] [4] [5]. Different methods of determining the voltage space vector reference value using Fuzzy Logic controllers [6] and Neuro Fuzzy Logic controllers [3] have also been presented. However, the simplicity of the DTC is reduced since a Voltage reference value must be calculated.

Other modulation strategies can be used to reduce the torque ripple whilst maintaining the switching frequency constant [7]. The most common of these techniques is the two states modulation method, which consists of an active state, given by the conventional DTC look up table, and a null state. An analytic approach to the calculation of the duty ratio between both states has also been proposed [7].

The literature available [8] [9] implies that the undesirable torque and flux ripple can be considerably reduced by replacing the two level VSI with a multilevel VSI. The more voltage levels used in the inverter the greater becomes the resulting reduction in the ripple.

Recently Matrix Converters (MC) have emerged to become a good alternative to the VSI [10]. Among different advantages the unity input power factor and the lack of bulky capacitors are the most relevant advantages of such converters [10].

It has been already implemented an integrated Induction Motor (IM) drive with a MC [11]. Also in [12] the use of MC in DTC of IM was introduced and a look up table for MC is designed. This DTC approach not only implements the DTC but also keeps the input power factor equals to 1.

In this paper, the use of MC for DTC and IM is reviewed and the use of not only the standard MC voltage vectors but also the uncommonly used lower voltage space vectors is analyzed. Depending on the IM operating point such vectors might be applied and consequently the electromagnetic torque ripple is reduced. Simulation results, which demonstrate the effectiveness of the proposed scheme, are presented.

II. MATRIX CONVERTER MODEL

A MC is an AC-AC converter, with m x n bi-directional switches, which connects an m-phase voltage source to an n-phase load and the most widely used configuration is the three-phase, 3x3 switches, MC shown in Fig. 1. It connects a three-phase voltage source to a three-phase load. In the MC shown in Fig. 1, V_{si}, $i=\{A,B,C\}$ are the source voltages, I_{si}, $i=\{A,B,C\}$ are the source currents, V_{jN}, $j=\{a,b,c\}$ are the load voltages, I_j, $j=\{a,b,c\}$ are the load currents, V_i, $i=\{A,B,C\}$ are the MC input voltages and I_i ,$i=\{A,B,C\}$are the input currents. A switch, S_{ij}, $i=\{A,B,C\}$, $j=\{a,b,c\}$ can connect input phase i to the output phase j of the load. With a suitable switching strategy, arbitrary voltages v_{jN} at arbitrary frequency can be synthesized. Switches are characterized by the following equation:

$$S_{ij} = \begin{cases} 0 & \text{if switch } S_{ij} \text{ is open} \\ 1 & \text{if switch } S_{ij} \text{ is closed} \end{cases} \quad (1)$$

A mathematical model of the MC shown in Fig. 1 can be derived applying Kirchhoff's voltage law and Kirchhoff's current law and equations (2) and (3) are respectively obtained [10].

$$\begin{bmatrix} V_{aN}(t) \\ V_{bN}(t) \\ V_{cN}(t) \end{bmatrix} = \begin{bmatrix} S_{Aa}(t) & S_{Ba}(t) & S_{Ca}(t) \\ S_{Ab}(t) & S_{Bb}(t) & S_{Cb}(t) \\ S_{Ac}(t) & S_{Bc}(t) & S_{Cc}(t) \end{bmatrix} \cdot \begin{bmatrix} V_A(t) \\ V_B(t) \\ V_C(t) \end{bmatrix} \quad (2)$$

$$\begin{bmatrix} I_A(t) \\ I_B(t) \\ I_C(t) \end{bmatrix} = \begin{bmatrix} S_{Aa}(t) & S_{Ab}(t) & S_{Ac}(t) \\ S_{Ba}(t) & S_{Bb}(t) & S_{Bc}(t) \\ S_{Ca}(t) & S_{Cb}(t) & S_{Cc}(t) \end{bmatrix} \cdot \begin{bmatrix} I_a(t) \\ I_b(t) \\ I_c(t) \end{bmatrix} \quad (3)$$

Equations (2) and (3) are the basis of all modulation methods.

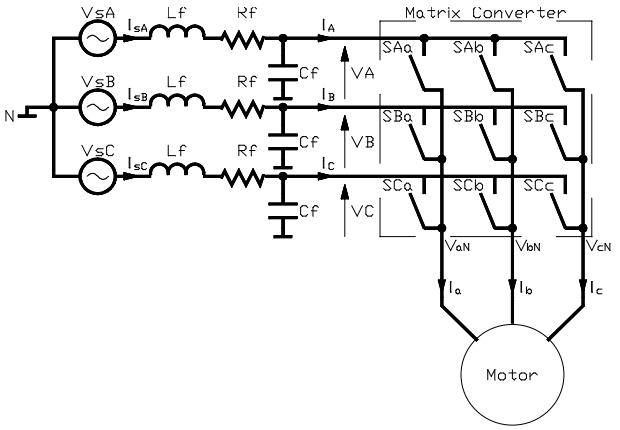

Fig. 1. 3x3 Matrix Converter scheme.

A. Matrix Converter Space Vectors

From Fig. 1, it can be noted that the three phase MC allows any output phase to be connected to any input phase. Obviously, the only restriction to consider is that the input phases should never be short circuited. Therefore, just 27 switching configurations from all nine switches are possible. Applying Clark's transformation to the space voltage and current vectors, given in equations (4) and (5) respectively, all 27 voltage and current space vectors are found.

$$\overrightarrow{Vo} = \tfrac{2}{3}(V_A + e^{j2\pi/3}V_B + e^{j4\pi/3}V_C) \quad (4)$$

$$\overrightarrow{Ii} = \tfrac{2}{\sqrt{3}}(I_a + e^{j2\pi/3}I_b + e^{j4\pi/3}I_c) \quad (5)$$

Table 1 shows the 27 switching states of the three-phase MC. The first 18 states (±1, ±2, ±3, ±4, ±5, ±6, ±7, ±8, ±9) correspond to the active vectors. 0_a, 0_b and 0_c are the corresponding zero vectors states and the last six states (±10, ±11, ±12) are the rotating vectors.

The representation of the output voltages and input current space active vectors is shown in Fig. 2 [10].

Table I shows all different vectors for output voltages and input currents [10]. The first eighteen space vectors are constant in direction but the magnitude depends on the input voltages and the output currents for the voltage and currents space vectors respectively. On the contrary, the magnitude of the six rotating vectors remains constant and corresponds to the maximum value of the input line-to-neutral voltage vector and the output line current vector, while its direction depends on the angles of the line-to-neutral input voltage vector α_i and the input line current vector β_i.

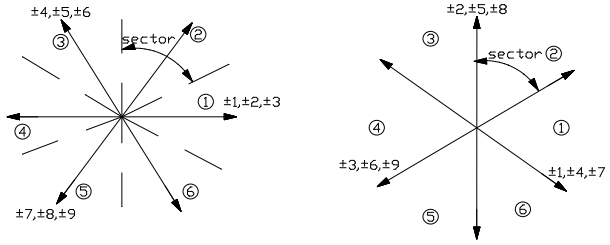

(a) *(b)*

Fig. 2. Locus of the active Matrix Converter vectors. a) voltage space vectors. b) current space vectors.

TABLE I
MATRIX CONVERTER SPACE VECTORS

State	a b c	V_o	α_o	I_i	β_i
+1	*A B B*	$2/3\ V_{AB}$	0	$\frac{2}{\sqrt{3}} I_a$	-π/6
-1	*B A A*	$-2/3V_{AB}$	0	$-\frac{2}{\sqrt{3}} I_a$	-π/6
+2	*B C C*	$2/3V_{BC}$	0	$\frac{2}{\sqrt{3}} I_a$	π/2
-2	*C B B*	$-2/3V_{BC}$	0	$-\frac{2}{\sqrt{3}} I_a$	π/2
+3	*C A A*	$2/3V_{CA}$	0	$\frac{2}{\sqrt{3}} I_a$	7π/6
-3	*A C C*	$-2/3V_{CA}$	0	$-\frac{2}{\sqrt{3}} I_a$	7π/6
+4	*B A B*	$2/3V_{AB}$	2π/3	$\frac{2}{\sqrt{3}} I_b$	-π/6
-4	*A B A*	$-2/3V_{AB}$	2π/3	$-\frac{2}{\sqrt{3}} I_b$	-π/6
+5	*C B C*	$2/3V_{BC}$	2π/3	$\frac{2}{\sqrt{3}} I_b$	π/2
-5	*B C B*	$-2/3V_{BC}$	2π/3	$-\frac{2}{\sqrt{3}} I_b$	π/2
+6	*A C A*	$2/3V_{CA}$	2π/3	$\frac{2}{\sqrt{3}} I_b$	7π/6
-6	*C A C*	$-2/3V_{CA}$	2π/3	$-\frac{2}{\sqrt{3}} I_b$	7π/6
+7	*B B A*	$2/3V_{AB}$	4π/3	$\frac{2}{\sqrt{3}} I_c$	-π/6
-7	*A A B*	$-2/3V_{AB}$	4π/3	$-\frac{2}{\sqrt{3}} I_c$	-π/6
+8	*C C B*	$2/3V_{BC}$	4π/3	$\frac{2}{\sqrt{3}} I_c$	π/2
-8	*B B C*	$-2/3V_{BC}$	4π/3	$-\frac{2}{\sqrt{3}} I_c$	π/2
+9	*A A C*	$2/3V_{CA}$	4π/3	$\frac{2}{\sqrt{3}} I_c$	7π/6
-9	*C C A*	$-2/3V_{CA}$	4π/3	$-\frac{2}{\sqrt{3}} I_c$	7π/6
0_a	*A A A*	0	-	0	-
0_b	*B B B*	0	-	0	-
0_c	*C C C*	0	-	0	-
+10	*A B C*	V_{imax}	α_i+0	I_{omax}	β_i+0
-10	*A C B*	V_{imax}	$-\alpha_i$–0	I_{omax}	$-\beta_i$–0
+11	*C A B*	V_{imax}	α_i+2π/3	I_{omax}	β_i+2π/3
-11	*B A C*	V_{imax}	$-\alpha_i$–2π/3	I_{omax}	$-\beta_i$–2π/3
+12	*B C A*	V_{imax}	α_i+4π/3	I_{omax}	β_i+4π/3
-12	*C B A*	V_{imax}	$-\alpha_i$–4π/3	I_{omax}	$-\beta_i$–4π/3

III. DIRECT TORQUE CONTROL USING MATRIX CONVERTERS

A. Conventional DTC scheme for VSI

The basic principle in conventional DTC for induction motors is to directly select stator voltage vectors according to the stator flux and torque errors and the stator flux sector [3]. As it is shown in Fig. 3, stator flux ψ^*_s and torque T^*_e references are compared with the corresponding estimated values. Both stator flux and torque errors, E_ψ and E_{Te}, are

discretised by means of a hysteresis band comparators. In particular, stator flux is controlled by a two-level hysteresis comparator, whereas the torque is controlled by a three-level comparator. On the basis of the hysteresis comparators and stator flux sector a proper VSI voltage vector is selected by means of the switching table given in Table II.

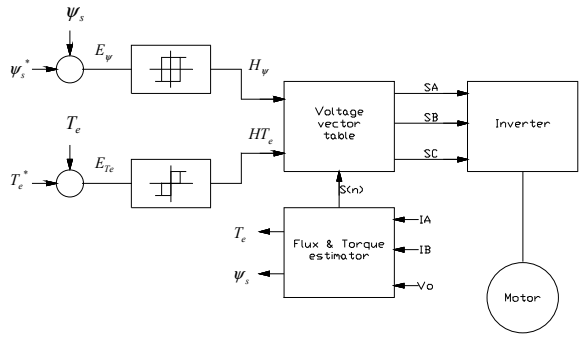

Fig. 3. Conventional DTC with VSI.

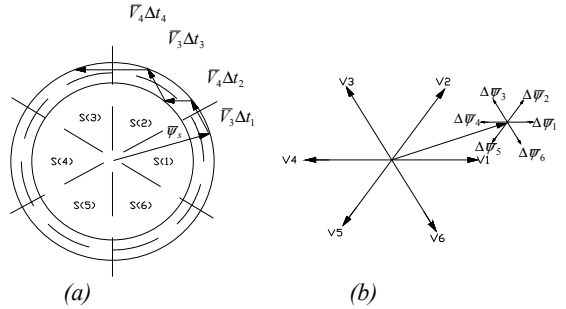

Fig. 4. (a) Flux trajectory. (b) VSI voltage vectors and the corresponding flux increment.

TABLE II
CONVENTIONAL DTC SWITCHING TABLE

$H\psi$	H_{Te}	S(1)	S(2)	S(3)	S(4)	S(5)	S(6)
1	1	V2	V3	V4	V5	V6	V1
	0	V0	V7	V0	V7	V0	V7
	-1	V6	V1	V2	V3	V4	V5
-1	1	V3	V4	V5	V6	V1	V2
	0	V7	V0	V7	V0	V7	V0
	-1	V5	V6	V1	V2	V3	V4

The flux vector reference and the hysteresis band tracks a circular trajectory as shown in Fig. 4 (a). Thus, the actual flux follows its reference within the hysteresis band in a zigzag path. Fig. 4 (b) shows the VSI voltages vectors and the corresponding flux variation per sampling period.

B. DTC look up table for Matrix Converters

Since MC generates a higher number of output voltage vectors with respect to a VSI [4], the introduction of a third variable, such as the average value of the sine of the displacement angle Ψ between the input line current vector and the input line-to-neutral voltage vector, can be used to keep under control the input power factor. This requirement is accomplished if this third variable is kept close to zero. Therefore, a new hysteresis controller, shown in Fig. 5, is introduced, which controls this variable [4].

The flux, torque estimations and the sin Ψ value require the knowledge of voltages and currents at the input and output side of the MC. Nevertheless, only input voltages and output currents are measured. The other quantities are calculated on the basis of equations (2) and (3), that is to say, the switching states of the matrix converter.

The new control algorithm will select the switching state of the matrix converter that generates a voltage vector similar to that selected by the basic DTC control algorithm [4].

Assuming that V_1 is the output voltage vector selected by the basic DTC control algorithm, from Fig. 2 it is obvious that one of the switching states ±1, ±2 or ±3 must be selected. Since the magnitude and direction of these voltage vectors depends on the input line-to-neutral voltage vector, only those having the same direction of V_1 and the maximum magnitude will be taken into consideration. If the input line-to-neutral voltage vectors lies in sector 1, the switching states +1 and –3 are chosen. From Fig. 2, it can be seen that these two switching states correspond to input current vectors lying on sector 1. If a power factor increase is needed, that is to say, the average value of sin Ψ has to be decreased; the switching state –3 has to be selected. On the other hand, if a power factor decrease is needed, in other words, the average value of sin Ψ has to be increased; the switching state +1 has to be selected.

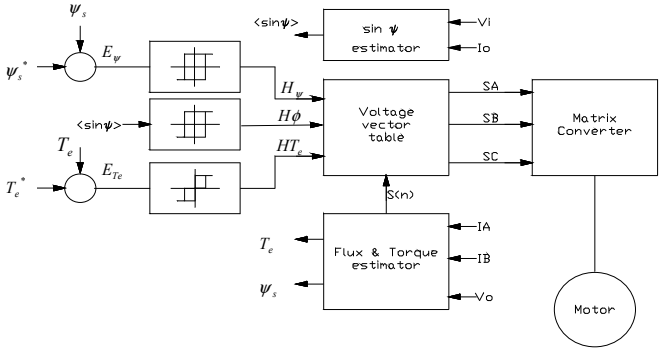

Fig. 5. DTC scheme using MC

Table III shows the switching table for the implementation of the DTC using a MC [4]. In the first column, the voltage vectors selected by the basic DTC are present. The top row contains the sector in which the input line-to-neutral voltage vector lies. Depending on the power factor control needs, that is to say, the output value of the hysteresis comparator H_ϕ, one of the two sub-columns (+1,-1) are selected.

TABLE III
DTC LOOK UP TABLE USING MC

	Input voltage sector											
	S(1)		S(2)		S(3)		S(4)		S(5)		S(6)	
H_ϕ	+1	-1	+1	-1	+1	-1	+1	-1	+1	-1	+1	-1
V1	-3	1	2	-3	-1	2	3	-1	-2	3	1	-2
V2	9	-7	-8	9	7	-8	-9	7	8	-9	-7	8
V3	-6	4	5	-6	-4	5	6	-4	-5	6	4	-5
V4	3	-1	-2	3	1	-2	-3	1	2	-3	-1	2
V5	-9	7	8	-9	-7	8	9	-7	-8	9	7	-8
V6	6	-4	-5	6	4	-5	-6	4	5	-6	-4	5

IV. NOVEL DTC USING MATRIX CONVERTERS SHORT VECTORS

In order to use not only large vectors of the MC but also the small ones, the DTC scheme will be modified. Therefore, the new torque hystersis comparator will provide four dif-

ferent levels instead of three to distinguish between small and large positive and negative torque errors and consequently a new Look up table has to be used.
Fig. 6 shows the new structure of the new torque hystersis comparator with four output levels.

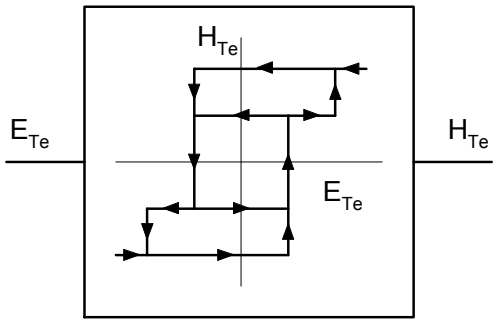

Fig. 6. New torque hysterisis comparator with four output levels.

The second modification is the Look up table because the classical Look up table introduced in [4] uses just the large vectors. Fig. 7 shows how just the largest voltages are used to synthesise the MC voltage vectors and consequently Table III is obtained.

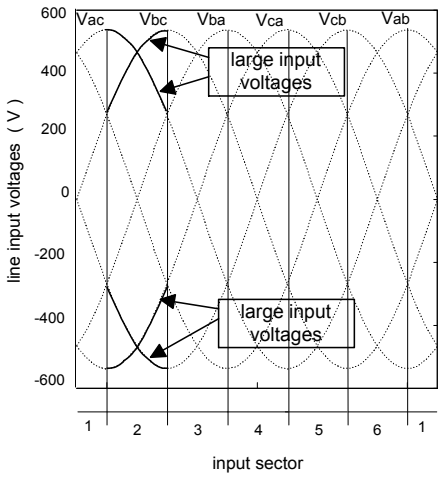

Fig. 7. Input voltages used to synthesize MC large voltage vectors according to the input voltage sectors

The contribution of this novel DTC is based on using not only the largest input voltages but also the small ones. Hence, Fig. 8 shows the small input voltages which will also be used to synthesise small voltage vectors.
The novel Look up table will have the same contents for the large vectors as Table III proposed in [4], but new small MC voltage space vectors will be used as well. Another difference is that the input voltage sector is divided into twelve different sectors instead of six. However, since there are just two small voltages instead of four per sector, just two small vectors can be chosen. Therefore, when a small vector is not found, the large vectors will be used instead.
Zero vectors will be used when the small torque error is selected and the IM back Electro Magnetic Force (EMF) imposes a reduction in torque.

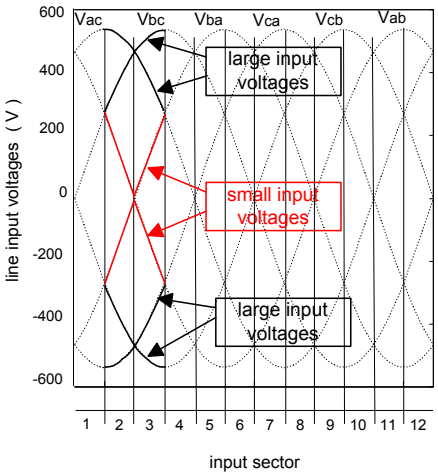

Fig. 8. Large and small input voltages used to synthesize large and small MC voltage vectors. Note that there are twelve input sectors.

TABLE VI
NOVEL DTC LOOK UP TABLE FOR THE USE OF LARGE AND SHORT MC VOLTAGE VECTORS.

	Input voltage sector											
	1	2	3	4	5	6	7	8	9	10	11	12
H_ϕ	+	+	+	+	+	+	+	+	+	+	+	+
	-	-	-	-	-	-	-	-	-	-	-	-
$V1_{large}$	-3	2	2	-1	-1	3	3	-2	-2	1	1	-3
	1	-3	-3	2	2	-1	-1	3	3	-2	-2	1
$V1_{small}$	2		-1		3		-2		1		-3	
		1		-3		2		-1		3		-2
$V2_{large}$	9	-8	-8	7	7	-9	-9	8	8	-7	-7	9
	-7	9	9	-8	-8	7	7	-9	-9	8	8	-7
$V2_{small}$	-8		7		-9		8		-7		9	
		-7		9		-8		7		-9		8
$V3_{large}$	-6	5	5	-4	-4	6	6	-5	-5	4	4	-6
	4	-6	-6	5	5	-4	-4	6	6	-5	-5	4
$V3_{small}$	5		-4		6		-5		4		-6	
		4		-6		5		-4		6		-5
$V4_{large}$	3	-2	-2	1	1	-3	-3	2	2	-1	-1	3
	-1	3	3	-2	-2	1	1	-3	-3	2	2	-1
$V4_{small}$	-2		1		-3		2		-1		3	
		-1		3		-2		1		-3		-2
$V5_{large}$	-9	8	8	-7	-7	9	9	-8	-8	7	7	-9
	7	-9	-9	8	8	-7	-7	9	9	-8	-8	7
$V5_{small}$	8		-7		9		-8		7		-9	
		7		-9		8		-7		9		-8
$V6_{large}$	6	-5	-5	4	4	-6	-6	5	5	-4	-4	6
	-4	6	6	-5	-5	4	4	-6	-6	5	5	-4
$V6_{small}$	-5		4		-6		5		-4		6	
		-4		6		-5		4		-6		5

V. RESULTS

In order to verify both, steady state and transient behavior of the novel DTC scheme, some simulations have been carried out.

The sampling period used is 35 μs and the IM has the following parameters:

V=380 / 50 Hz. R_s=4.3 Ω. R_r=5.05 Ω.
L_s=320 mH. L_r=320 mH. P=2.

A. Steady state

The steady-state behavior has been tested at 1000 r.p.m. motor speed. The references for stator flux and torque are ψ_s^*=0.8 Wb (rated flux) and T_e^* =6.7 Nm (rated torque) respectively.

Fig. 9 and 10 show the proper control of the stator flux which is kept within the reference value. Fig. 11 shows the torque response of the IM. It can be observed how the amplitude of the torque ripple is kept under 0.5 Nm.

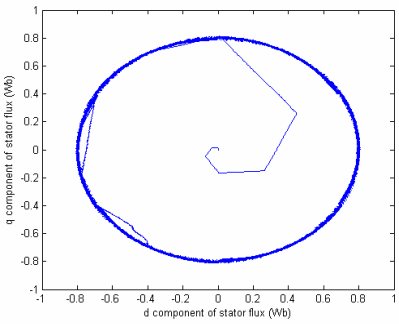

Fig. 9. Stator flux trajectory at 1000 r.p.m., 6.7 Nm.

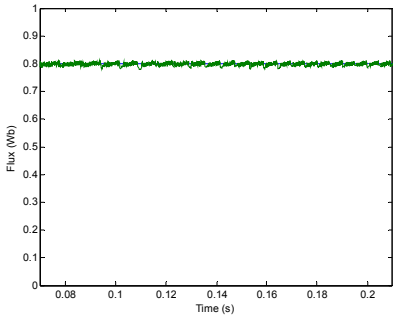

Fig. 10. Stator flux magnitude at 1000 r.p.m. and 6.7 Nm.

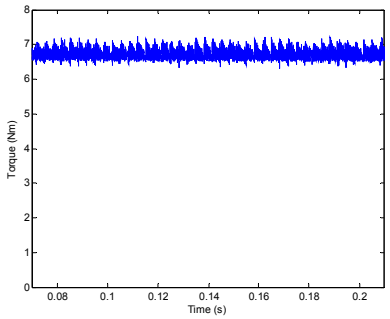

Fig. 11. Electromagnetic torque at 1000 r.p.m. and 6.7 Nm.

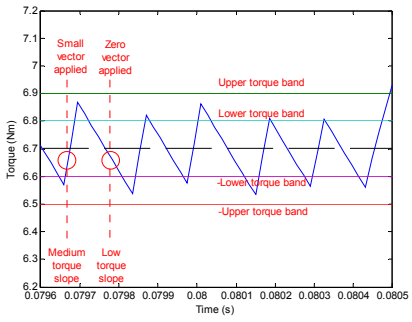

Fig. 12. Torque response when small voltage vectors are applied. The torque ripple is kept under the lower torque hysterisis bands

Fig. 12 is a zoom of Fig.11 which shows how the torque ripple is reduced whenever a small vector is applied and consequently the torque ripple is kept under the lower torque hystersis band. It can also be observed the use of zero vectors and how the back EMF makes the torque slope negative.

Fig. 12 proves the great contribution of using small voltage vectors to reduce the torque ripple. On the contrary, Fig. 13 shows the torque response when large voltage vectors are chosen. Under these circumstances the torque slope is higher and the torque ripple increases up to the upper torque hysterisis bands.

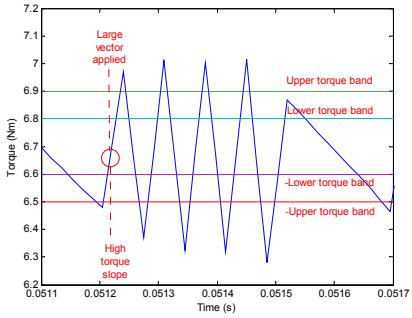

Fig. 13. Torque response when large voltage vectors are applied. The torque ripple increases up to the upper torque hysterisis bands

B.Transient state

The transient behavior has been tested at 1000 r.p.m. motor speed during a torque step reverse from 6.7 Nm to –6.7 Nm. The reference for stator flux is ψ_s^* =0.8 Wb.

Fig. 14 shows how the stator flux is correctly controlled. In Fig. 15 the torque transient is clearly illustrated. Fig. 16 is a zoom of Fig. 15 which proves how the use of small vectors, even when the IM works as a generator, reduces the torque ripple. Finally, Fig. 17 illustrates the stator current of the IM and how it changes when working as a generator.

Further work is being done in order to study the correct control of the input power factor and experimental results are being carried out as well.

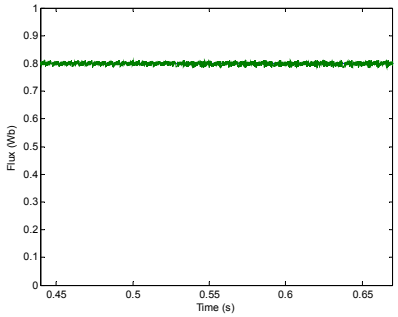

Fig. 14. Stator flux response when a torque step reverse from 6.7 Nm to –6.7 Nm at 1000r.p.m is applied.

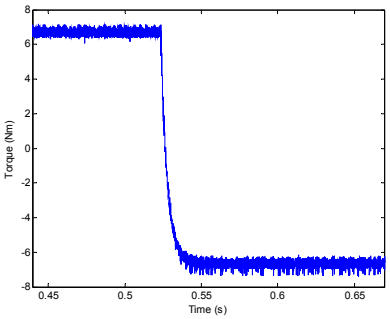

Fig. 15. Electromagnetic torque during the step change from 6.7 Nm to –6.7 Nm at 1000r.p.m.

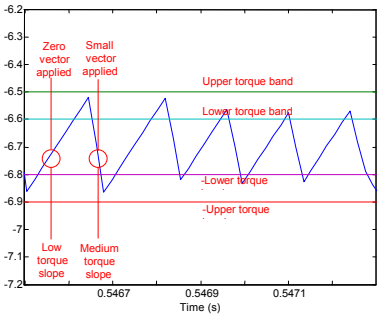

Fig. 16. Torque response when the IM works as a generator. It can be observed how the system uses small vectors and the ripple is constrained within the lower hysterisis bands

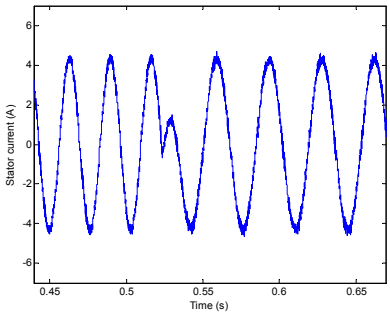

Fig. 17. Stator current during a torque step from 6.7 Nm to –6.7 Nm at a 1000r.p.m.

VI. Conclusions

This paper introduces a novel Direct Torque Control with Matrix Converters which uses not only the largest input voltages but also the small ones to reduce the torque ripple.

The torque error hysteresis comparator is modified in order to distinguish between large and small positive and negative torque errors. The Look up table is also designed for the small and large torque increments. The number of output sectors is increased to 12. As a result the Look up table is improved since it uses much more Matrix Converter voltage space vectors.

Simulation results are presented which shows good torque and flux performance in both steady and transient states. These results show that the torque ripple is clearly reduced when using the short Matrix Converter voltage space vectors.

VII. Acknowledgment

The authors would like to acknowledge the economic support received from the "Ministerio de Ciencia y Tecnología de España" for realising this work under the TEC-2004-0589 Research Project.

VIII. References

[1] TAKAHASHI, I; NOGUSHI, T. "A New Quick-Response and High-Efficiency Control Strategy of an Induction Motor". IEEE Transactions on. Industry Applications, Vol. 1A-22, pp 820-827, October 1986.

[2] DEPENBROCK, M. "Direct Self-Control (DSC) of Inverter-Fed Induction Machine". IEEE Trans. on Power Electronics, Vol. 3, No 4, pp 420-429, October 1988.

[3] G. S. Buja and M. P. Kazmierkowski "Direct Torque Control of PWM Inverter-Fed AC Motors-A Survey". *IEEE Trans. on Industrial Electronics* vol. 51, num. 4 pp. 744-758, August 2004.

[4] CASADEI, D.; SERRA G.; TANI A.; "Implementation of a Direct Torque Control Algorithm for Induction Motors Based on Discrete Space Vector Modulation". IEEE Trans. on Power Electronics, Vol. 15, No. 4; July 2000, pp 769 – 777.

[5] LASCU, C.; BOLDEA, I.; BLAABJERG F.; "A Modified Direct Torque Control for Induction Motor Sensorless Drive". IEEE Trans. on Industry Applications, Vol. 36, No. 1; January/February 2000, pp 122 – 130.

[6] LAI, Y. S.; LIN J. C. "Fuzzy Logic Control for Direct Torque Control Induction Motor Drives with Inverter Controlled using Space Vector Modulation Technique". 9th European Conference on Power Electronics and Applications. EPE 2001. CDROM. EPE Assoc. Belgium.

[7] KANG, J.; SUL S.; "New Direct Torque Control of Induction Motor for Minimum Torque Ripple and Constant Switching Frequency". IEEE Trans. on Industry Applications, Vol. 35, No. 5; September 1999, pp 1076 – 1082.

[8] LEE, K. B.; SONG, J. H.; CHOY, I.; YOO, J. Y. "Torque Ripple Reduction in DTC of Induction Motor Driven by Three-Level Inverter With Low Switching Frequency". IEEE Trans. on Power Electronics, Vol. 17, No 2, pp 255-264, March 2000.

[9] PERELMUTER, V. "Three-Level Inverters with Direct Torque Control". Industry Applications Conference 2000. Conference Record of the IEEE. Vol. 3 pp 1368-1374.

[10] P. WHEELER, J. RODRIGUEZ, J. C. CLARE, L. EMPRINGHAM, A. WEINSTEIN. "Matrix converters: a technology review". IEEE Transactions on Industrial Electronics, page(s): 276-288 Volume: 49, Issue: 2. April 2002.

[11] C. KLUMPNER , P. NIELSEN, I. BOLDEA, F. BLAABJERG. "A New Matrix Converter (MCM) for Industry Applications". IEEE Transactions on Industrial Electronics, page(s): 325-335. Volume: 49, Issue: 2. April 2002.

[12] CASDEI, D; SERRA, G; TANI, A. "The Use of Matrix Converters in Direct Torque Control of Induction Machines". IEEE Transactions on Industrial Electronics, Vol. 48, No. 6, December 2001

High Frequency injection in a Matrix Converter DTC Drive for sensorless operation of a PMSM

Authors: C. Ortega, A. Arias, J. Balcells and Cedric Caruana.
Proceedings of ISIE '07, vol. 1, pp. 2278-2283, July, 2007.

Abstract - A sensorless Direct Torque Control (DTC) of a Permanent Magnet Synchronous Motor (PMSM) drive using a high frequency hf voltage injection technique without compromising the simplicity of the original DTC algorithm, is proposed in this paper. A new hf injection algorithm, in which the hf carrier is introduced by the direct modification of the fundamental voltage vectors of a Matrix Converter (MC), is developed and explained in detail. The position signal is then obtained from the direct demodulation of the resulting hf currents. Experimental results showing the effectiveness of the proposed method are shown.

High Frequency injection in a Matrix Converter DTC Drive for sensorless operation of a PMSM

Carlos Ortega
Electronics Department
Escola Universitaria Salesiana de Sarria
Barcelona, Spain
Email: cortega@euss.es

Antoni Arias, Josep Balcells
Electronics Department
Universitat Politecnica de Catalunya
Terrassa, Spain
Email: arias@eel.upc.edu

Cedric Caruana
Power Electronics Dept.
University of Malta
Msida, Malta
Email: cccaruana@eng.um.edu.mt

***Abstract*— A sensorless Direct Torque Control (DTC) of a Permanent Magnet Synchronous Motor (PMSM) drive using a high frequency *hf* voltage injection technique without compromising the simplicity of the original DTC algorithm, is proposed in this paper. A new *hf* injection algorithm, in which the *hf* carrier is introduced by the direct modification of the fundamental voltage vectors of a Matrix Converter (MC), is developed and explained in detail. The position signal is then obtained from the direct demodulation of the resulting *hf* currents. Experimental results showing the effectiveness of the proposed method are shown.**

I. Introduction

Permanent Magnet Synchronous Motors (PMSM) are becoming a very attractive alternative to Induction Motors (IM). Among other advantages, the PMSM offers a higher efficiency, higher power density and better dynamic performance. The rotor position information is required for an accurate control of the PMSM. Usually, an encoder mounted on the shaft of the machine provides this information, but it also increases system cost, volume and weight. Furthermore, the overall reliability of the drive is reduced, especially in harsh environment. Extensive research has been directed towards sensorless control of PMSM and several approaches are reported in the literature [1], [2], [3].

In the mid 1980's, a new advanced control technique, known as Direct Torque and Flux Control (DTFC or DTC) [4] or Direct Self-Control (DSC) [5], was introduced for voltage-fed PWM inverter drives. Since then, DTC has gained popularity and nowadays is becoming one of the most popular control methods for AC machines and has been shown to be a worthy alternative to the well-known Vector Control. As the name indicates, DTC is the direct control of the torque and flux of an electrical motor by the selection, through a look-up table, of the power converter voltage space vectors. This control technique does not require current controllers. Furthermore, neither coordinate transformations nor PWM generation are needed. Moreover the system does not depend on motor parameters but the stator resistance. It is a very simple and robust scheme and also a very quick and precise torque control response can be achieved [4]. The classical DTC also lends itself easily to sensorless control through the flux model estimator [6], but as other sensorless control schemes based on conventional fundamental-frequency models or observer-based methods, fulfill the demand in the higher speed range but have been shown to give poor and asymptotically failing performance as zero speed is approached due to the loss of information as the induced back emf becomes very small [6]. Moreover, such methods are strongly dependent on the machine parameters, which can vary during operation. The desirability to operate continuously at the low or zero speed has led to another sensorless approach where the saliency of the machine is tracked through some form of signal injection to obtain flux or position information. Saliencies are not restricted to a specific machine type. They are well known in Synchronous Reluctance machines [7] [8] and buried permanent magnet machines [9] [10], but they also exist, even though much smaller, in induction machines, and surface mounted PMSM [2]. Although successful position and speed control at low and zero speed region has been reported in the literature, even for low saliency machines using high frequency *hf* carrier injection techniques, the approaches, seem to be limited to Field Oriented Controlled (FOC) drives. In [11], a new injection algorithm for DTC drives is introduced in order to overcome the lack of performance of the classical DTC drives at the low and zero speed region through the extension of the $\alpha - \beta$ frame *hf* rotating carrier injection technique. However, the accuracy yielded by the *hf* voltage carrier injection techniques has been found to be limited by the non-linearities of the power inverter. The most important effect is due the dead-time. The influence of the inverter dead-time in *hf* signal injection is investigated in [12]. The use of a Matrix Converter, which has different switching characteristics compared with those of a classical Voltage Source Inverter (VSI), is proposed in this paper.

II. $\alpha - \beta$ Frame High Frequency Rotating Carrier Injection

Several *hf* injection methods can be found in the literature. A possible classification of these methods can be: $\alpha - \beta$ frame rotating injection [2], *d-q* frame pulsating injection [13] and *d-q* frame rotating injection [14]. This paper will be concerned with the $\alpha - \beta$ frame persistent *hf* rotating carrier injection. The most common way to inject in the $\alpha - \beta$ stationary frame is to superimpose a *hf* voltage carrier on the fundamental excitation. The resulting *hf* current components will content rotor

1-4244-0755-9/07/$20.00 ©2007 IEEE

position information. The frequency of the injected voltage carrier, ω_i, should be high enough to ensure sufficient spectral separation between itself and the fundamental excitation to reduce the requirements of the band-pass filters. One possible form of *hf* voltage carrier injection, with amplitude V_i and frequency ω_i, is as follows:

$$\begin{bmatrix} v_{i\alpha} \\ v_{i\beta} \end{bmatrix} = V_i \begin{bmatrix} -\sin(\omega_i t) \\ \cos(\omega_i t) \end{bmatrix} \tag{1}$$

Assuming a saliency in the machine *d-q* stationary reference frame, i.e $L_{ds} \neq L_{qs}$, the PMSM voltage model can be written as follows:

$$\begin{bmatrix} v_\alpha \\ v_\beta \end{bmatrix} = R_s \begin{bmatrix} i_\alpha \\ i_\beta \end{bmatrix} + \Psi_{PM} \frac{d}{dt} \begin{bmatrix} \cos(\theta_r) \\ \cos\left(\theta_r - \frac{\pi}{2}\right) \end{bmatrix} + \frac{d}{dt} \begin{bmatrix} L_s - \Delta L_s \cos(2\theta_r) & -\Delta L_s \sin(2\theta_r) \\ -\Delta L_s \sin(2\theta_r) & L_s + \Delta L_s \cos(2\theta_r) \end{bmatrix} \begin{bmatrix} i_\alpha \\ i_\beta \end{bmatrix} \tag{2}$$

where $L_s = (L_{ds} + L_{qs})/2$, $\Delta L_s = (L_{ds} - L_{qs})/2$, R_s is the stator resistance, Ψ_{PM} is the machine permanent magnet flux and θ_r is the rotor position in electrical degrees. When a sufuciently high frequency carrier is used, normally between 600Hz and 1KHz, the stator impedance in (2) is dominated by the stator inductance. Because $\omega_i L_s \gg R_s$, the first two terms in (2) can be neglected and approximated to:

$$\begin{bmatrix} v_{i\alpha} \\ v_{i\beta} \end{bmatrix} \approx \frac{d}{dt} \begin{bmatrix} L_s - \Delta L_s \cos(2\theta_r) & -\Delta L_s \sin(2\theta_r) \\ -\Delta L_s \sin(2\theta_r) & L_s + \Delta L_s \cos(2\theta_r) \end{bmatrix} \begin{bmatrix} i_{i\alpha} \\ i_{i\beta} \end{bmatrix} \tag{3}$$

From (1) and (3) the *hf* currents can be resolved and given by:

$$\begin{bmatrix} i_{i\alpha} \\ i_{i\beta} \end{bmatrix} = \frac{V_i}{\omega_i L_{ds} L_{qs}} \begin{bmatrix} L_s \cos(\omega_i t) + \Delta L_s \cos(2\theta_r - \omega_i t) \\ L_s \sin(\omega_i t) + \Delta L_s \sin(2\theta_r - \omega_i t) \end{bmatrix} \tag{4}$$

The resulting *hf* currents in (4), contains both positive and negative sequences components. However, only the negative sequence contains position information. In Fig. 1 the steps to carry out the demodulation of the *hf* currents are shown. Firstly the *hf* currents components must be separated from the fundamental component by means of a band-pass filter. Synchronous filter are then used to demodulate the rotor position signal θ_r. Once the fundamental component has been filtered out, the *hf* currents $i_{i\alpha\beta}$ are transformed to a reference frame rotating in the same direction as the injected signal (positive direction), thus the carrier component becomes DC and the negative sequence is located at $\approx 2\omega_i$, as it can be seen in (5).

$$\begin{bmatrix} i_{dp} \\ i_{qp} \end{bmatrix} = \left[T_{(-\theta_i)}\right] \begin{bmatrix} i_{i\alpha} \\ i_{i\beta} \end{bmatrix} = = \frac{V_i}{\omega_i L_{ds} L_{qs}} \begin{bmatrix} L_s + \Delta L_s \cos(2\theta_r - 2\omega_i t) \\ L_s + \Delta L_s \sin(2\theta_r - 2\omega_i t) \end{bmatrix} \tag{5}$$

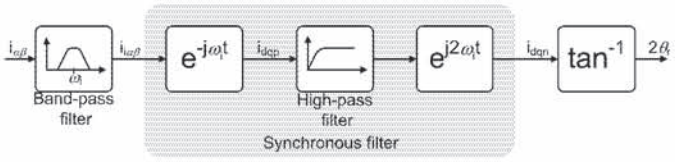

Fig. 1. *hf* currents demodulation. Block diagram

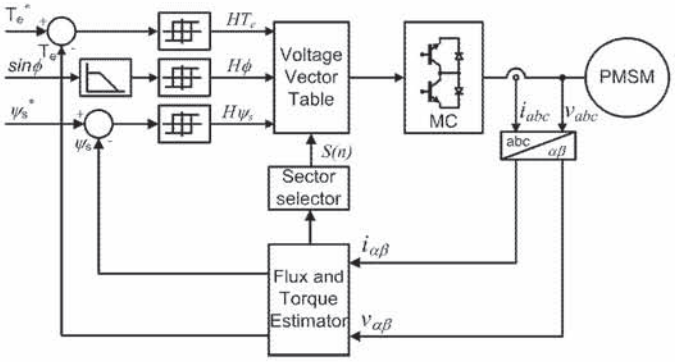

Fig. 2. DTC using MC. Block diagram.

Note that $T_{(-\theta_i)}$ is the Park transformation matrix with $(-\theta_i)$ as the rotating angle. High-pass filtering in this frame will remove the DC component (carrier component). The resulting signal is then transformed to a frame rotating synchronously with the negative sequence to obtain the position signal as follows:

$$\begin{bmatrix} i_{dn} \\ i_{qn} \end{bmatrix} = \left[T_{2\theta_i}\right] \begin{bmatrix} i_{dpf} \\ i_{qpf} \end{bmatrix} = = \frac{V_i}{\omega_i L_{ds} L_{qs}} \begin{bmatrix} \Delta L_s \cos(2\theta_r) \\ \Delta L_s \sin(2\theta_r) \end{bmatrix} \tag{6}$$

In (6) $T_{2\theta_i}$ is the Park transformation matrix with $2\theta_i$ as the rotating angle. Finally, the angle information is obtained by simply applying the atan function:

$$\theta_r = \frac{1}{2} tan^{-1}\left(\frac{i_{qn}}{i_{dn}}\right) \tag{7}$$

III. $\alpha - \beta$ *hf* Injection in a DTC Drive

Injecting a *hf* voltage carrier of the form given in (1) is relatively straightforward when vector control is used to control a PMSM. Since the vector control algorithm provides a voltage reference $v^*_{\alpha\beta}$, the carrier voltage $v_{i\alpha\beta}$ can be superimposed as in [2].

In contrast, as it can be seen in Fig. 2, injecting a *hf* rotating vector in a DTC drive is somewhat difficult. There is no voltage reference provided by the control algorithm. Instead, the flux and torque processed errors, H_Ψ and H_{T_e}, are converted directly into switching signals by the DTC switching table shown in Fig. 2. DTC based on Space Vector Modulation (SVM), and hence, with voltage reference terms, has been proposed in the literature [15] [16], however, this approaches seems to compromise the simplicity of the original DTC drive.

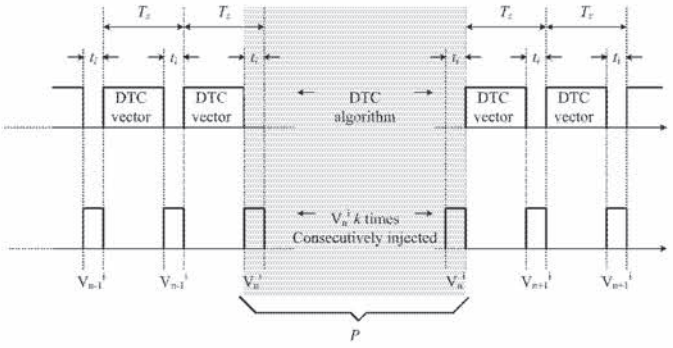

Fig. 3. *hf* injection algorithm.

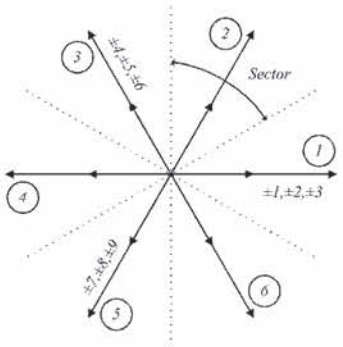

Fig. 4. *hf* MC voltages vectors

The introduction of a rotating *hf* voltage carrier by directly modifying the vector pattern imposed by the DTC algorithm, using a MC, is proposed in this paper. The DTC algorithm, based on the approach presented in [17], will impose a voltage vector from the MC every sample period T_z. An amount of time t_i from this sample period will be used in order to inject the *hf* rotating carrier as shown in Fig. 3. Note that $t_i \ll T_z$, thus not distorting the original DTC performance.

The injected vectors in Fig. 3 V_n^i, where $n = 1 \dots 6$, corresponds to the active vectors that would have been applied using a VSI. When a MC is used, an active vector, from the 18 defined in Fig. 4, with the same direction as the one imposed by the algorithm using a VSI will be selected. Lets assume, for example, that V_1^i is the injection voltage vector imposed by the algorithm using a VSI, from Fig. 4 it can be seen that one of the MC voltage vectors ± 1, ± 2, ± 3 must be selected. Since the magnitude and direction of these voltage vectors depends on the input voltages, only those with the same direction of V_1 and the maximum amplitude will be selected.

The injection algorithm described in Fig. 3 will inject vectors $(V_1 - V_6)$, consecutively, at the end of every sample period

TABLE I

hf INJECTION ALGORITHM SUMMARY

P	$1 \dots \infty$
V_n^i	$P - int(P/6)$
V_{DTC}	$0 \dots 7$

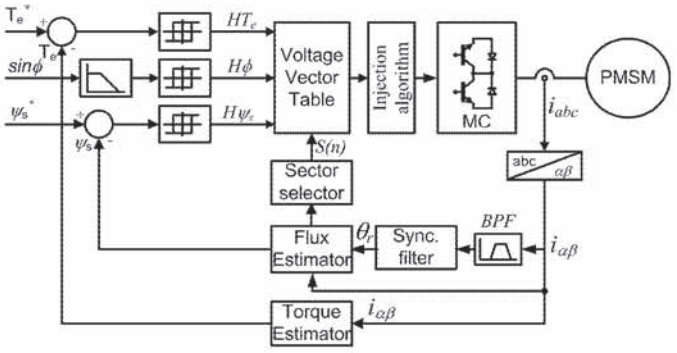

Fig. 5. $\alpha - \beta$ injection in a DTC drive using MC. Block diagram.

T_z to superimpose the *hf* rotating carrier on the fundamental excitation. Table I, where P is the group of sample periods in which the same vector, V_n^i, is injected, $int(P/6)$ is the integer part of $P/6$, and V_{DTC} is the vector imposed by the DTC scheme, summarizes the *hf* injection algorithm. Depending on the carrier frequency required, the injection of a vector can be done for every sample period or in alternate periods. The carrier frequency can be controlled by means of the repetition rate k of every injected vector:

$$f_i = \frac{1}{6T_z k} \tag{8}$$

where $k \geq 1$ and 6 is the number, in terms of direction, of vectors available for injection. From (8) it can be seen that the carrier frequency will be a sub-multiple of the DTC algorithm sampling frequency T_z, however this must not be considered a constraint as the sampling frequency must be necessary high.

On the other hand, the amount of time t_i assigned for the injection will determine the magnitude of the injected vector, which can be expressed as follows:

$$V^i = \frac{t_i}{T_z} V_o \tag{9}$$

where V_o is the magnitude of the voltage vector at the output side of the MC.

As for the FOC drives, the rotor position is obtained from demodulating the resulting *hf* currents as explained in section II. The complete schematic of the implemented $\alpha - \beta$ frame *hf* carrier injection in the DTC drive is shown in Fig. 5.

IV. RESULTS

The proposed algorithm has been tested in an experimental rig using a PMSM with the following parameters:

$V = 100V$	$R_s = 2.1\Omega$	$L_{sd} = 8.6mH$
$L_{sq} = 8.4mH$	$P = 4$	$T_N = 0.64Nm$
$P_N = 200W$	$Nn = 3000rpm.$	

The DTC sampling period is set to $T_z = 50\mu s$. The time assigned for injection is $t_i = 10\mu s$, giving a relation of $t_i/T_z = 0.2$, thus the magnitude of the injected vector will be 20% of the output vector magnitude. Regarding the injection

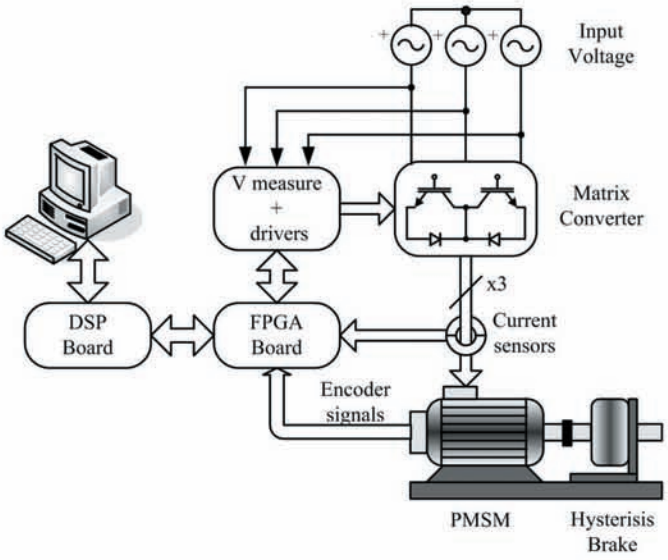

Fig. 6. System setup.

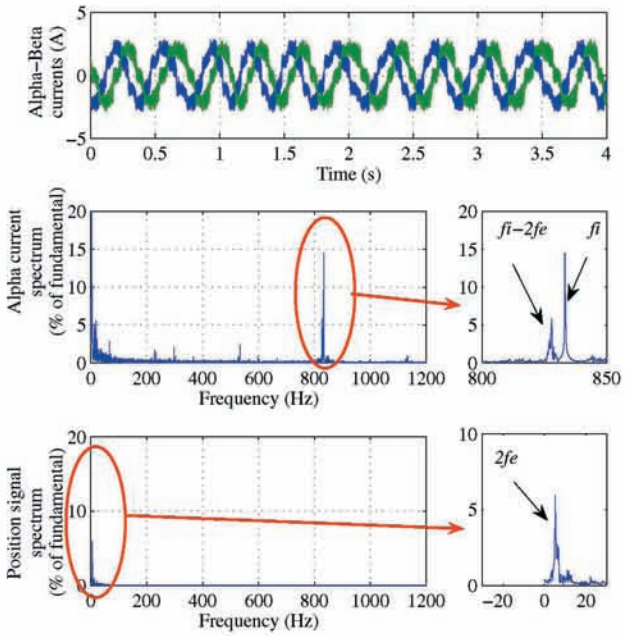

Fig. 7. Demodulation process. (a) $\alpha - \beta$ currents. (b) $\alpha - \beta$ currents spectrum. (c) Position signal spectrum after synchronous filter.

frequency f_i, a repetition rate of $k = 4$ has been selected, thus obtaining $f_i = 833.33Hz$.

The system setup is shown in Fig.6, where the PMSM under test has been coupled to an hysteresis brake. The hysteresis brake provides the load torque which is independent of the speed. The hysteresis brake is set to give a constant torque while the PMSM is torque controlled by means of the DTC algorithm. The constant torque developed by the hysteresis brake will determine the rotating speed.

All the tests has been carried out with a torque command of $T_e^* = 0.4Nm$.

The measured $\alpha - \beta$ currents are depicted in Fig.7(a) and their spectrum can be seen in Fig.7(b). After following the steps for current demodulation explained in section II, the resulting i_{dqn} currents spectrum is shown in Fig.7(c).

It can be seen that other harmonics around $2f_e$ are present after the demodulation process. This will introduce a considerable error in the position angle estimate as it can be seen in Fig.8(c) and consequently in the stator flux position estimate. However, the DTC algorithm does not need an accurate stator flux position estimate but just the sector in which is lying in. This fact will make the DTC algorithm to consider the stator flux position error only around the sectors boundaries as depicted in Fig.9. The errors around the sectors boundaries are also common in the original DTC algorithm due to the noise in the stator flux estimate.

The position signals i_{dn} and i_{pn}, with the PMSM running at $38rpm$, are shown in Fig.8(a). In Fig.8(b) the estimated rotor position is compared with the actual (measured) rotor position. Even a MC has been shown to have zero dead-time, the remaining non-linearities of such converters is one of the error sources in the position estimate process. The use of a MC clearly improve the position signals waveforms compared with those shown in [12]. Another error source comes from the DTC algorithm itself. One of the requirements of *hf* injection methods is to inject the carrier outside of the controllers bandwidth. However, the bandwidth of the hysteresis controllers used in a DTC drive is not known. The bandwidth, however, will depend on the hysteresis bands of the controllers, increasing the bandwidth as the hysteresis bands are decreased. Figure 10 shows the position signals i_{dn} and i_{qn} and their spectrum with two different torque hysteresis bands (BT_e). It can be seen the better signal obtained with a larger torque hysteresis bands.

In order to analyze distortion in torque, introduced by the injection of *hf* signal, Fig.11 shows a comparison of torque performance with and without injection.

As it was expected, the torque performance is slightly affected by the injection algorithm. However, comparing the performance by means of the standard deviation, the difference is negligible. The original DTC using MC gives a standard deviation of $std = 0.227Nm$ while the DTC with the injection algorithm gives $std = 0.2299Nm$.

V. Conclusions

The extension of the $\alpha - \beta$ frame *hf* carrier injection method to a PMSM DTC drive using a MC has been presented in this paper. The new *hf* injection algorithm does not compromise the original DTC simplicity while has the potential to extend the operation of the sensorless DTC drive to the low speed region. Initial experimental results which demonstrates the effectiveness of the proposed method are shown. The better switching characteristics of the MC clearly improve the position signals waveforms. However, the remaining non-

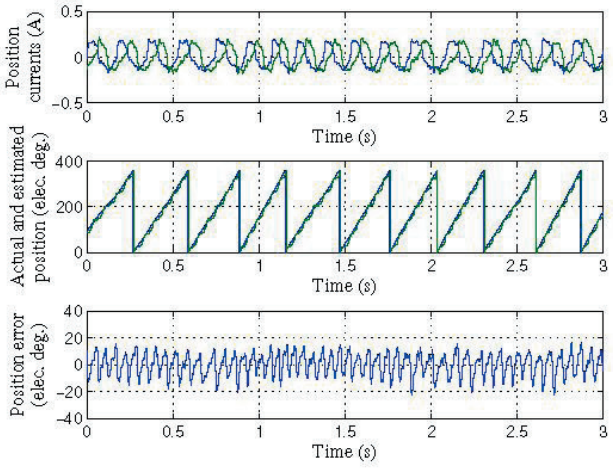

Fig. 8. Position estimate. (a)i_{dqn} currents. (b) Actual and estimated position. (c) position error.

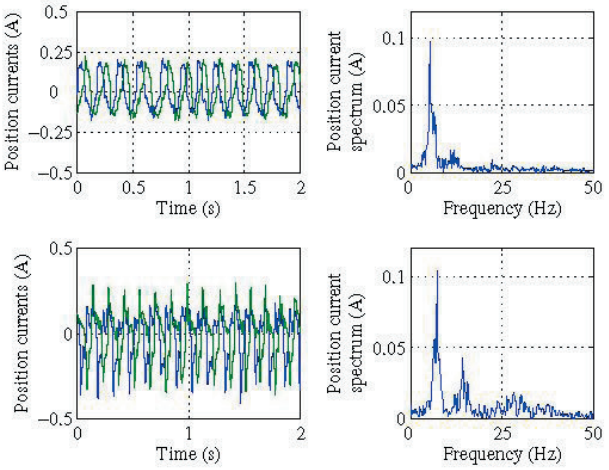

Fig. 10. i_{dqn} position signal. (a) $BT_e = 0.07Nm$. (b) $BT_e = 0.02Nm$

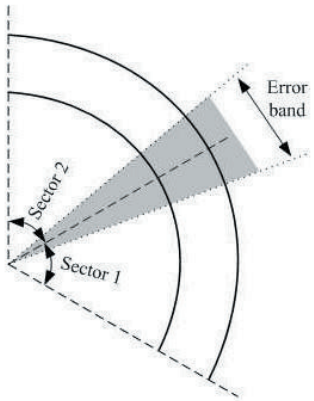

Fig. 9. Boundary error.

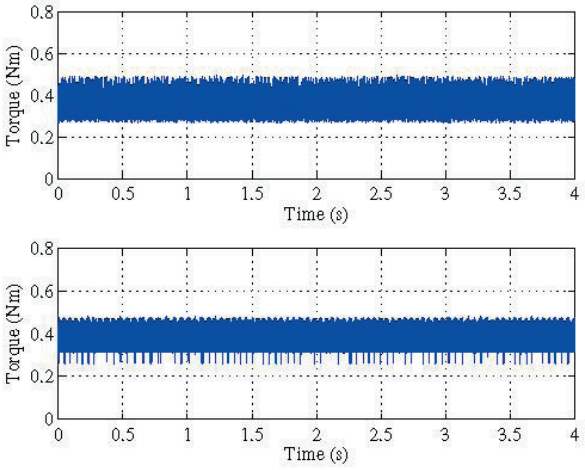

Fig. 11. Torque performance. (a) DTC with *hf* injection. (b) DTC without *hf* injection.

linearities of the converter introduces a significant error in the position angle estimate. Although the error in the position estimate will not make the system to fail, further investigation in order to reduce it has to be carried out.

VI. Acknowledgment

The authors would like to acknowledge the support provided by the European Commission under a Marie Curie Research Training Network for realizing this work under the MEST-CT-2004-504243 Research Project. And also by the "Ministerio de Ciencia y Tecnología de España" under the TEC 2004-00589 Research Project.

References

[1] Ji-Hoon Jang, Seung-Ki Sul, Jung-Ik Ha, Kozo Ide, and Mitsujiro Sawamura. "Sensorless Drive of Surface-Mounted Permanent-Magnet Motor by High-Frequency Signal Injection Based on Magnetic Saliency". IEEE Transactions on Industry Applications, Vol. 39, No. 4, July/August 2003.

[2] Spiteri, C. Cilia, J. Michallef, B. and Apap, M. "Sensorless Vector Control of Surface Mount PMSM using High Frequency Injection", Power Electronics Machines and Drives, 16-18 April 2002, Conference Publication No. 487, IEE2002

[3] Antoni Arias, César A. Silva, Greg M. Asher, Jon C. Clare, and Patrick W. Wheeler. "Use of a Matrix Converter to Enhance the Sensorless Control of a Surface-Mount Permanent-Magnet AC Motor at Zero and Low Frequency", IEEE Transactions on Industrial Electronics, Vol. 53, No. 2, April 2006.

[4] Takahashi, I; Nogushi, T. "A New Quick-Response and High-Efficiency Control Strategy of an Induction Motor", IEEE Trans. Industry Applications, Vol. 1A-22, pp 820-827, October 1986.

[5] Depenbrock, M. "Direct Self-Control (DSC) of Inverter-Fed Induction Machine". IEEE Trans. on Power Electronics, Vol. 3, No 4, pp 420-429, October 1988.

[6] Vas, P. "Sensorless Vector and Direct Torque Control", Oxford University Press, London, 1998

[7] A. Consoli, F. Russo, G. Scarcella, and A. Testa, " Low and Zero-Speed Sensorless Control of Synchronous Reluctance Motors", IEEE Transactions on Industry Applications, vol. 35, pp. 1050-1057, 1999.

[8] J. L. Ha, S. J. Kang, and S. K. Sul, " Position-Controlled Synchronous Reluctance Motor Without Rotational Transducer", IEEE Trans. on Ind. Applications, vol. 35, pp. 1393-1398, 1999.

[9] S. Kondo, A. Takahashi, and T. Nishida, "Armature Current Locus Based Estimation Method of Rotor Position of Permanent Magnet Synchronous

Motor without Mechanical Sensor", presented at IEEE-IAS Annual Meeting, 1995.

[10] P. L. Jansen and R. D. Lorenz, "Transducerless Position and Velocity Estimation in Induction and Salient AC Machines", IEEE Transactions on Industry Applications, vol. 31, pp. 240-247, 1995.

[11] Ortega, C. Arias, A. Caruana, C. Staines, C. Balcells, J. Cilia J. "Sensorless Direct Torque Control of a Surface Mounted PMSM using High Frequency Injection", 2006 IEEE International Symposium on Industrial Electronics, Vol. 3, July 2006 pages: 2332-2337.

[12] J.M. Serrano, M. Leetmaa, F. Briz, A. Zamarron, R.D. Lorenz, "Inverter Nonlinearity Effects in High-Frequency Signal-Injection-Based Sensorless Control Methods", IEEE Trans. on Industry Applications, Vol. 41, No. 2, March/April, 2005

[13] Jung-Ik Ha, and Seung-Ki Sul, "Sensorless Field-Orientation Control of an Induction Machine by High-Frequency Signal Injection", IEEE Transaction on Industry Applications, Vol. 35, No. 1, January/February 1999.

[14] C. Caruana, G.M. Asher, K.J. Bradley and M.S. Woolfson, "Flux Position Estimation in Cage Induction Machines using Synchronous Injection and Kalman Filtering," IEEE Transactions on Industry Applications, Vol.39, No.5, September/October 2003, pp 1372-1378.

[15] G. S. Buja and M. P. Kazmierkowski "Direct Torque Control of PWM Inverter-Fed AC Motors-A Survey". IEEE Trans. on Industrial Electronics vol. 51, num. 4 pp. 744-758, August 2004.

[16] Casadei , D; Serra, G; Tani, "Implementation of a Direct Torque Control Algorithm for Induction Motors Based on Discrete Space Vector Modulation". IEEE Trans. on Power Electronics, Vol. 15, No. 4; July 2000, pp 769 - 777.

[17] Casadei , D; Serra, G; Tani, A. "The Use of Matrix Converters in Direct Torque Control of Induction Machines". IEEE Transactions on Industrial Electronics, Vol. 48, No. 6, December 2001.

Reducing the Common Mode Voltage in DTC-PMSM drives using Matrix Converters

Authors: C. Ortega, A. Arias, C. Caruana and M. Apap
Presented at ISIE '08 (not yet published).

Abstract - The common mode voltage at the output of matrix converters is firstly analyzed in this paper. An approach to reduce it, when a direct torque control scheme is employed to drive a permanent magnet synchronous motor, is then proposed. Simulation results are shown to demonstrate the theoretical background. Experimental results corroborating the effectiveness of the proposed method are also shown.

Reducing the Common Mode Voltage in DTC-PMSM drives using Matrix Converters

Carlos Ortega
Electronic Department
Escola Universitària Salesiana de Sarrià
Barcelona, Spain
Email: cortega@euss.es

Antoni Arias
Electronic Department
Univeristat Politècnica de Catalunya
Terrassa, Spain
Email: arias@eel.upc.edu

Cedric Caruana
and Maurice Apap
Power Electronics Department
University of Malta
Msida, Malta
Email: ccaruana@eng.um.edu.mt

***Abstract*— The common mode voltage at the output of matrix converters is firstly analyzed in this paper. An approach to reduce it, when a direct torque control scheme is employed to drive a permanent magnet synchronous motor, is then proposed. Simulation results are shown to demonstrate the theoretical background. Experimental results corroborating the effectiveness of the proposed method are also shown.**

I. Introduction

Direct Torque Control (DTC) has emerged over the last decade to become an attractive alternative to the well-known Field Oriented Control (FOC). Its main characteristic is a very good performance, obtaining results as good as the classical vector control but with several advantages based on its simpler structure and control diagram. Recently Matrix Converters (MC) have received considerable attention as they are becoming a good alternative to the VSI. Among other advantages, input and output sinusoidal waveforms with controllable input power factor and a very compact design are the most relevant advantages of such converters [1]. In [2] (*hereinafter the classical method*) the use of MC to implement a DTC of an Induction Motor (IM) was introduced, and a look up table for the MC was developed. This DTC approach not only implements the DTC but also keeps the input power factor close to one. In [3] and [4] a novel DTC using not only the large vectors but also the uncommonly used small ones were introduced for induction motors and PMSM respectively, achieving better performance regarding the torque ripple.

It is known that one of the main sources of early motor winding failure and bearing deterioration is the Common Mode Voltage (CMV) produced by modern power converters. Moreover, high frequency components and large amplitudes of the CMV at the motor neutral point have been shown to generate high frequency currents to the ground path and induced shaft voltage [5]. Several methods to reduce the CMV have been proposed in the literature [6], however, these methods seem to be limited to three-phase Pulse Width Modulation (PWM) rectifier-inverter systems. In [7], a new modulation strategy of the converter which reduces the CMV at the output of the MC is presented. Based on the Indirect Space Vector Modulation (ISVM) technique, the method selects a medium value phase voltage as a zero vector and places it in the center or on the both sides of sampling the period without changing the active voltage vectors. The harmonic content of the input current is also reduced. However, these advantages are achieved at the expense of deteriorating the output harmonic content.

This paper presents an approach to reduce the CMV in a DTC-PMSM drive using Matrix Converters without compromising the simplicity of the drive. Simulation and experimental results demonstrating the advantages of the method are shown.

II. Matrix Converters

A MC is an AC-AC converter, with $m \times n$ bidirectional switches, which connects an m-phase voltage source to an n-phase load. The most widely used configuration is the three-phase, 3×3 switches, MC shown in Fig. 1. It connects a three-phase voltage source to a three-phase load. In the MC shown in Fig. 1, v_{Si}, where $i = A, B, C$, are the phase source voltages, i_{Si} are the phase source currents, v_{jN}, where $j = a, b, c$ are the load voltages, i_j are the load currents, v_i are the MC input voltages and i_i are the input currents. A switch, S_{ij} can connect input phase i to the output phase j of the load. With a suitable switching strategy, arbitrary voltages v_{jN} at an arbitrary frequency can be synthesized. Switches are characterized by the following equation:

$$S_{ij} = \begin{cases} 0 & \text{if switch } S_{ij} \text{ is open} \\ 1 & \text{if switch } S_{ij} \text{ is closed} \end{cases} \quad (1)$$

The permitted switching states of a 3×3 MC are shown in table I, and have been classified in groups. The first three groups containing the states (±1, ±2, ±3), (±4, ±5, ±6), and(±7, ±8, ±9), produces active vectors of variable amplitude, depending on the line-to-neutral voltage, but at stationary position (*pulsating vectors*). States 0_a, 0_b and 0_c, corresponding to group 4, connecting all the output lines to the same input line, are the corresponding zero vectors. The last six states (*group 5*), providing a direct connection of each output line to a different input line, are the rotating vectors.

A. Common Mode Voltage in Matrix Converters

Fig. 1 shows a MC connected to a PMSM where the impedance Z_{cm} represents the leakage current (i_{cm}) path

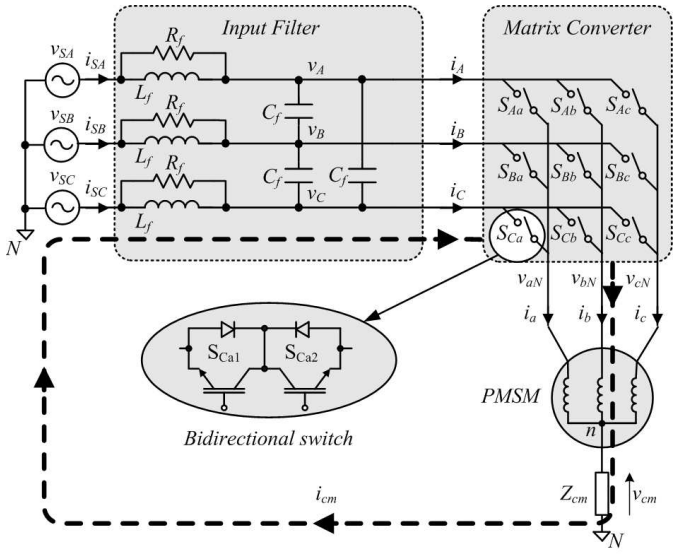

Fig. 1. 3×3 Matrix Converter.

between the machine's neutral point (n) and ground (N). The CMV (v_{cm}) is defined as the voltage between these two points:

$$v_{cm} = v_{nN} \tag{2}$$

Taking into consideration the CMV v_{cm}, the voltage expressions of the PMSM can be written as:

$$v_{aN} - v_{cm} = R_s i_a + L_s \frac{di_a}{dt} + \frac{d}{dt}\psi_a \tag{3}$$

$$v_{bN} - v_{cm} = R_s i_b + L_s \frac{di_b}{dt} + \frac{d}{dt}\psi_b \tag{4}$$

$$v_{cN} - v_{cm} = R_s i_c + L_s \frac{di_c}{dt} + \frac{d}{dt}\psi_c \tag{5}$$

where v_{aN}, v_{bN}, and v_{cN} are the MC output voltages with respect to ground. R_s and L_s are the resistance and inductance at each phase of the PMSM. Since $i_{cm} \approx 0$, it can be assumed that $i_a + i_b + i_c \approx 0$. Assuming a balanced induced voltage system $\psi_a + \psi_b + \psi_c \approx 0$, the CMV can be found adding (3), (4) and (5):

$$v_{cm} = \frac{v_{aN} + v_{bN} + v_{cN}}{3} \tag{6}$$

As it can be seen in table I, when active vectors are selected in a MC, there are two output phases connected to the same input phase. Thus, the CMV when active vectors are delivered by a MC v^a_{cm} can be written as:

$$v^a_{cm} = \frac{v_i + 2v_j}{3} \tag{7}$$

where i and j represents the two input phases involved when an active vector is present at the output of the MC.

In a MC, the input filter is designed in such a way that the phase voltages v_A, v_B, and v_C can be considered equal to the

TABLE I

VOLTAGE AND CURRENT VECTORS OF A 3×3 MC

MC State	On Devices	v_o	α_o	i_i	β_i
$+1$	$S_{Aa}\ S_{Bb}\ S_{Bc}$	$2/3v_{AB}$	0	$2/\sqrt{3}i_a$	$-\pi/6$
-1	$S_{Ba}\ S_{Ab}\ S_{Ac}$	$-2/3v_{AB}$	0	$-2/\sqrt{3}i_a$	$-\pi/6$
$+2$	$S_{Ba}\ S_{Cb}\ S_{Cc}$	$2/3v_{BC}$	0	$2/\sqrt{3}i_a$	$\pi/2$
-2	$S_{Ca}\ S_{Bb}\ S_{Bc}$	$-2/3v_{BC}$	0	$-2/\sqrt{3}i_a$	$\pi/2$
$+3$	$S_{Ca}\ S_{Ab}\ S_{Ac}$	$2/3v_{CA}$	0	$2/\sqrt{3}i_a$	$7\pi/6$
-3	$S_{Aa}\ S_{Cb}\ S_{Cc}$	$-2/3v_{CA}$	0	$-2/\sqrt{3}i_a$	$7\pi/6$
$+4$	$S_{Ba}\ S_{Ab}\ S_{Bc}$	$2/3v_{AB}$	$2\pi/3$	$2/\sqrt{3}i_b$	$-\pi/6$
-4	$S_{Aa}\ S_{Bb}\ S_{Ac}$	$-2/3v_{AB}$	$2\pi/3$	$-2/\sqrt{3}i_b$	$-\pi/6$
$+5$	$S_{Ca}\ S_{Bb}\ S_{Cc}$	$2/3v_{BC}$	$2\pi/3$	$2/\sqrt{3}i_b$	$\pi/2$
-5	$S_{Ba}\ S_{Cb}\ S_{Bc}$	$-2/3v_{BC}$	$2\pi/3$	$-2/\sqrt{3}i_b$	$\pi/2$
$+6$	$S_{Aa}\ S_{Cb}\ S_{Ac}$	$2/3v_{CA}$	$2\pi/3$	$2/\sqrt{3}i_b$	$7\pi/6$
-6	$S_{Ca}\ S_{Ab}\ S_{Cc}$	$-2/3v_{CA}$	$2\pi/3$	$-2/\sqrt{3}i_b$	$7\pi/6$
$+7$	$S_{Ba}\ S_{Bb}\ S_{Ac}$	$2/3v_{AB}$	$4\pi/3$	$2/\sqrt{3}i_c$	$-\pi/6$
-7	$S_{Aa}\ S_{Ab}\ S_{Bc}$	$-2/3v_{AB}$	$4\pi/3$	$-2/\sqrt{3}i_c$	$-\pi/6$
$+8$	$S_{Ca}\ S_{Cb}\ S_{Bc}$	$2/3v_{BC}$	$4\pi/3$	$2/\sqrt{3}i_c$	$\pi/2$
-8	$S_{Ba}\ S_{Bb}\ S_{Cc}$	$-2/3v_{BC}$	$4\pi/3$	$-2/\sqrt{3}i_c$	$\pi/2$
$+9$	$S_{Aa}\ S_{Ab}\ S_{Cc}$	$2/3v_{CA}$	$4\pi/3$	$2/\sqrt{3}i_c$	$7\pi/6$
-9	$S_{Ca}\ S_{Cb}\ S_{Ac}$	$-2/3v_{CA}$	$4\pi/3$	$-2/\sqrt{3}i_c$	$7\pi/6$
0_a	$S_{Aa}\ S_{Ab}\ S_{Ac}$	0	...	0	...
0_b	$S_{Ba}\ S_{Bb}\ S_{Bc}$	0	...	0	...
0_c	$S_{Ca}\ S_{Cb}\ S_{Cc}$	0	...	0	...
$+10$	$S_{Aa}\ S_{Bb}\ S_{Cc}$	v_{imax}	α_i	i_{omax}	β_i
-10	$S_{Aa}\ S_{Cb}\ S_{Bc}$	v_{imax}	$-\alpha_i$	i_{omax}	$-\beta_i$
$+11$	$S_{Ca}\ S_{Ab}\ S_{Bc}$	v_{imax}	$\alpha_i + 2\pi/3$	i_{omax}	$\beta_i + 2\pi/3$
-11	$S_{Ba}\ S_{Ab}\ S_{Cc}$	v_{imax}	$-\alpha_i - 2\pi/3$	i_{omax}	$-\beta_i - 2\pi/3$
$+12$	$S_{Ba}\ S_{Cb}\ S_{Ac}$	v_{imax}	$\alpha_i + 4\pi/3$	i_{omax}	$\beta_i + 4\pi/3$
-12	$S_{Ca}\ S_{Bb}\ S_{Ac}$	v_{imax}	$-\alpha_i - 4\pi/3$	i_{omax}	$-\beta_i - 4\pi/3$

phase voltages of the mains v_{SA}, v_{SB}, and v_{SC} respectively [8]. Assuming a balanced voltage system at the mains and, hence, at the input side of the MC,

$$v_{SA} = v_A = V_p \sin(\omega t) \tag{8}$$

$$v_{SB} = v_B = V_p \sin(\omega t - \frac{2\pi}{3}) \tag{9}$$

$$v_{SC} = v_C = V_p \sin(\omega t + \frac{2\pi}{3}) \tag{10}$$

where V_p is the voltage peak value per phase, (7) can be written as:

$$v^a_{cm} = \frac{1}{3} V_p \sin(\omega t) + \frac{2}{3} V_p \sin(\omega t \pm \frac{2\pi}{3}) \tag{11}$$

Rearranging (11), a simpler form of v^a_{cm} can be obtained:

$$v^a_{cm} = \frac{1}{\sqrt{3}} V_p \sin(\omega t \pm \frac{\pi}{2}) \tag{12}$$

Equation (12) states that the instantaneous value of the CMV when any active vector is delivered by the MC v^a_{cm}, depends on the instantaneous value of the input voltages selected to deliver such vector. The maximum instantaneous value of the CMV when active vectors are delivered by the MC v^a_{cm} will be:

$$v^a_{cm_{max}} = \pm \frac{1}{\sqrt{3}} V_p \tag{13}$$

This value will be reached every $\pm k\pi$ radians.

The contribution to the CMV of each active vector is shown in Fig. 2. The frequency of voltages v_{SA}, v_{SB}, and v_{SC} is $50Hz$. In every input voltage period ($T = 0.02s$), a different output vector is delivered by the MC ($+1 \ldots +9$; $-1 \ldots -9$). It can be noted that, for every active vector, the CMV is at its maximum value, $\pm\frac{1}{\sqrt{3}}V_p$, every $k\pi$ radians.

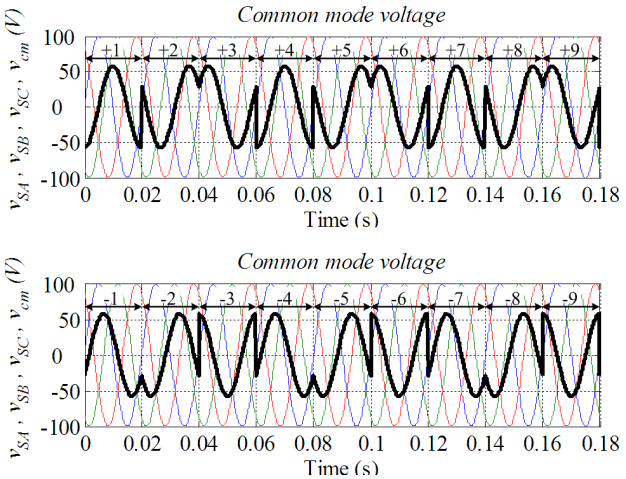

Fig. 2. Common mode voltage when active vectors are delivered by a MC.

When a zero vector is selected in a MC, the three output phases are connected to the same input phase. Thus, when a zero vector is delivered by a MC, the CMV v_{cm}^z will follow the selected input voltage:

$$v_{cm}^z = v_i \tag{14}$$

where i represents the selected input phase.
Since $v_i = V_p \sin(wt \pm \phi)$, the maximum CMV v_{cm}^z when a zero is selected will be:

$$v_{cm_{max}}^z = \pm V_p \tag{15}$$

Fig. 3 shows the contribution to the CMV of each zero vector (*a different zero vector is selected in every input voltage period* $T = 0.02s$). As it can be seen, the CMV follows the selected phase to deliver the zero vector, being the maximum CMV equal to the peak value of that phase.

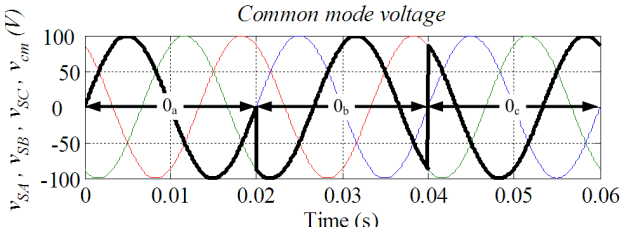

Fig. 3. Contribution of zero vectors to the common mode voltage.

III. Reduction of the Common Mode Voltage

In a DTC scheme, when the actual electromagnetic torque is within the corresponding comparator hysteresis bands, a zero vector is usually selected. Since the MC can deliver three different zero vectors, in [2], the zero vector which minimizes the number of commutations is selected. However, this criteria to select zero vectors will not ensure the minimization of the converter switching during the operation of the drive. In fact, since the next active vector (*after the zero vector*) is not known at the moment of selecting the zero vector, this criteria could also contribute to increase the number of commutations over time.

As it has been shown in the previous section, the maximum CMV is achieved when the input phase v_i, selected to deliver a zero vector, is at its peak value $\pm V_p$. Since the MC can deliver three different zero vectors 0_a, 0_b and 0_c (*see table I*), a reduction of the CMV can be achieved by proper selection of the zero vector. When any input phase voltage is at its positive or negative peak value $\pm V_p$, the other two will be at $\pm\frac{1}{2}V_p$. Hence, the maximum CMV can be reduced to $\pm\frac{1}{2}V_p$ if the input phase voltage with minimum absolute value is selected to deliver a zero vector. In Fig. 4, the contribution to the CMV of zero vectors, when the input phase with minimum absolute value is selected to deliver a zero vector, is shown.

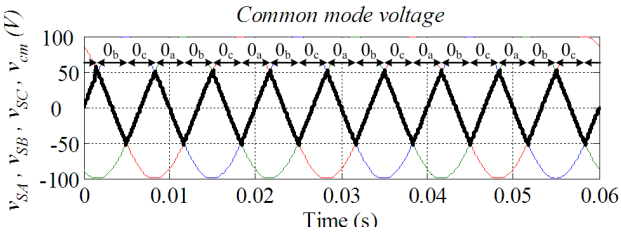

Fig. 4. Contribution to the common mode voltage of zero vectors selecting the phase voltage with minimum absolute value.

Fig. 5 shows the simplicity of the zero vector selector method to reduce the CMV. When a zero vector has to be selected by the DTC algorithm, the system computes the absolute value of every input phase and selects the one with the minimum value. The selected phase will be the one connected to all the output phases to deliver the zero vector.

As it has been mentioned, in [3] and [4], the use of small vectors of the MC are used in order to reduce the torque ripple. At low and medium speeds, small vectors are selected very often. Since the CMV depends on the input phases involved in the selected vector, as stated in (11), these vectors will also contribute to reduce the CMV RMS value.

IV. Simulation Results

The proposed method to reduce the CMV is analyzed and compared with the classical DTC using MC proposed in [2]

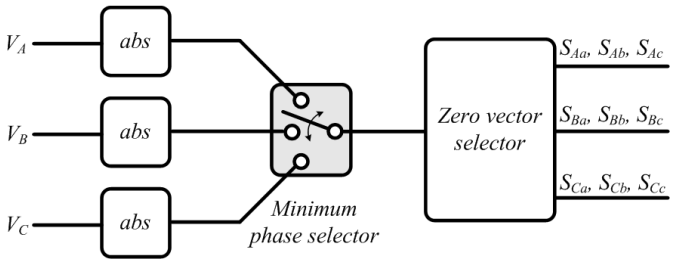

Fig. 5. Zero vector selector.

TABLE II
PMSM PARAMETERS.

Output power	200 W	Rated current	2 A
Voltage	100 V	L_d^s per phase	8.3 mH
Pole pairs	4	L_q^s per phase	8.6 mH
Torque	0.64 Nm	Rated speed	3000 rpm
Stator resistance	2.5 Ω	Maximum speed	4500 rpm

in which the reduction of the number of switching is used as the criteria to select zero vectors.
The parameters of the PMSM employed in the tests are shown in table II.

The simulation analysis has been carried out by means of the MatLab/Simulink package with the DTC having the following settings:

- Torque reference, $T_e^* = 0.64\ Nm$ (rated torque)
- Flux reference, $|\psi^{s*}| = \sqrt{\left[\psi_{PM}^2 + \left(\frac{2}{3}\frac{T_e^* L_q^s}{p\psi_{PM}}\right)^2\right]}$
- Torque hysteresis bands, $BT_e = \pm 0.015\ Nm$
- Flux hysteresis bands, $B\psi^s = \pm 0.0006\ Wb$
- Speed, 500 rpm

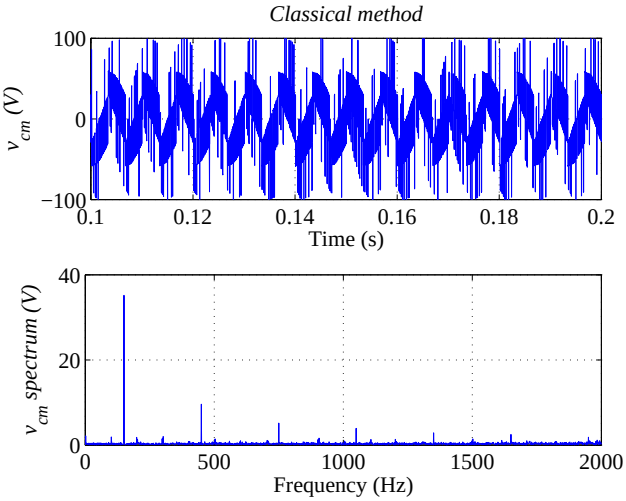

Fig. 6. Common mode voltage and its spectrum. Classical method.

Fig. 6 shows the v_{cm} when the classical DTC using MC is used to drive the PMSM. The maximum CMV value $v_{cm_{max}}$ reaches $\pm 100V$, corresponding to the input phase negative and positive peak values. This happens when an input phase crossing its peak value is selected to deliver a zero vector.

TABLE III
SIMULATION RESULTS.

	$v_{cm_{max}}$	$v_{cm_{RMS}}$
Classical method	100 V	42.61 V
Proposed method	57.7 V	31.8 V

When the proposed method is used under the same conditions, the maximum CMV value is reduced to $\pm 57.7V$, as shown in Fig. 7, corresponding to $\pm 1/\sqrt{3}$ of the input phase peak value when active vectors are selected.

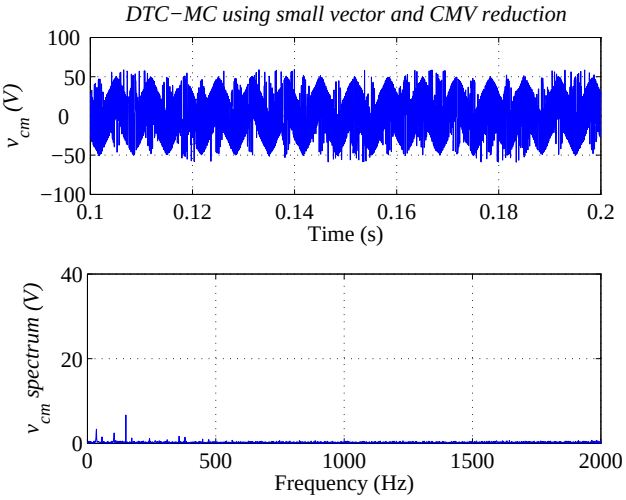

Fig. 7. Common mode voltage and its spectrum. Proposed method.

Comparing Fig. 6 and Fig. 7, it is noted that the proposed method shows a better harmonic spectrum of v_{cm}, not only by decreasing the amplitude of the CMV but also the number of harmonics.

Table III shows the maximum CMV value and its RMS value, summarizing the performance of both methods. The proposed method shows a better performance regarding the maximum CMV and its RMS value, reducing them by 42.3% and 25.4% respectively.

V. EXPERIMENTAL RESULTS

In order to validate the theoretical and simulation analysis, experimental tests has been carried out employing the rig shown in Fig. 8. The PMSM has been coupled to an hysteresis break which has been set to give a constant torque. The PMSM is torque controlled by means of the DTC algorithm, whose settings are the same as those used in the simulation tests.

The v_{cm} when the classical DTC using MC is employed to drive the PMSM is shown in Fig. 9. It can be seen that the maximum CMV $v_{cm_{max}}$ reaches $\pm 100V$ corroborating the results shown in the simulation analysis. As in the classical method, the criteria to select zero vectors is to minimize the number of the converter switching, the CMV $v_{cm_{max}}$ will

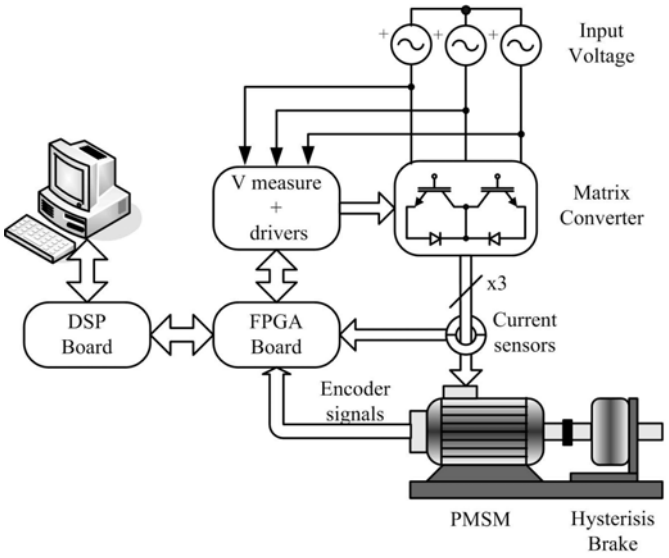

Fig. 8. Experimental rig.

coincide with the peak value V_p of the input phase selected to deliver a zero vector.

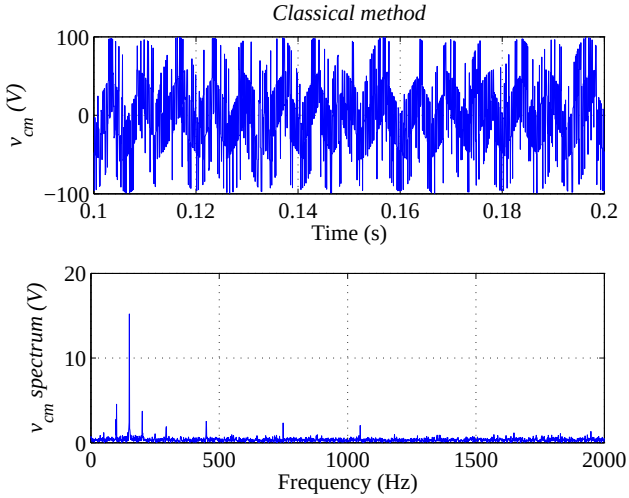

Fig. 9. Common mode voltage and its spectrum. Classical method.

Fig. 10 shows the CMV v_{cm} when the proposed method is used. Now, the maximum value of the CMV $v_{cm_{max}}$ coincides with the CMV maximum value when active vectors are delivered by the MC $v^a_{cm_{max}}$. Thus, $v_{cm_{max}} = v^a_{cm_{max}} = \pm\frac{1}{\sqrt{3}}V_p = \pm 57.7V$ as stated in (13).

The effects of a reduction in the CMV will be reflected in a reduction of the motor winding failure and degradation of its bearings [6]. Moreover, comparing the harmonic spectrum of the v_{cm} shown in Fig. 9 and Fig. 10, it can be said that the better performance shown by the proposed method will reduce the motor shaft induced voltage. Hence, it can be concluded that all these effects will, eventually, contribute to extend the motor's operational life.

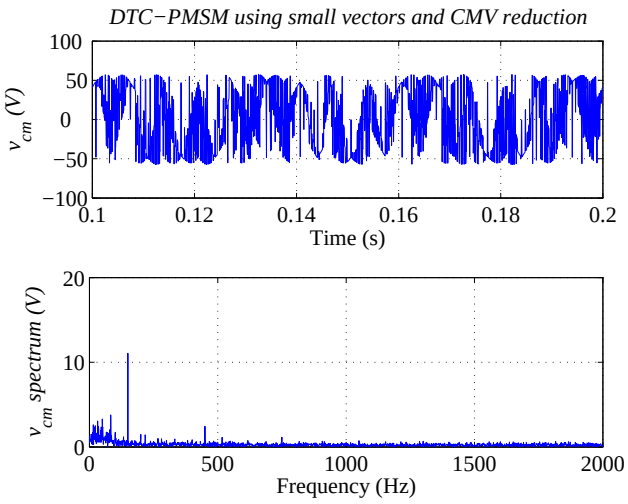

Fig. 10. Common mode voltage and its spectrum. Proposed method.

TABLE IV
EXPERIMENTAL RESULTS.

	$v_{cm_{max}}$	$v_{cm_{RMS}}$
Classical method	100 V	46.42 V
Proposed method	57.7 V	37.47 V

Finally, the comparison of both methods is summarized in table IV. As it can be seen, a reduction of 42.3% and 19.3% in the $v_{cm_{max}}$ and $v_{cm_{RMS}}$ respectively is achieved when the proposed method is used.

VI. CONCLUSION

The CMV in MC has been analyzed in this work. A new strategy to select zero vectors in a DTC-PMSM drive which reduces the CMV has been presented. The proposed method has been shown to suppress the maximum CMV corresponding to the peak value of the input phase selected to deliver a zero vector. This has been achieved by selecting an input phase with medium voltage as a zero vector. The harmonic spectrum of the CMV is also improved with the proposed method.

ACKNOWLEDGMENT

The authors would like to thank the support provided by the European Commission under a Marie Curie Research Training Network for realizing this work under the MEST-CT-2004-504243 Research Project. And also by the "Ministerio de Ciencia y Tecnologa de España" under the TEC 2004-00589 Research Project.

REFERENCES

[1] Alsina, A; Venturini, M. "Analysis and Design of Optimum-Amplitude Nine-Switch Direct AC-AC Converters", IEEE Trans. on Power Electronics. Vol. 4, No. 1, pp. 101-112, January 1989.

[2] Casadei, D; Serra, G; Tani, A. "The Use of Matrix Converters in Direct Torque Control of Induction Machines", IEEE Trans. On Industrial Electronics, Vol. 48, No. 6, pp. 1057-1064, December 2001.

[3] Carlos Ortega, Antoni Arias, Xavier del Toro, Emiliano Aldabas, Josep Balcells, "Novel Direct Torque Control for Induction Motors using short voltage vectors of Matrix Converters" Proc. of IECON05, USA, 2005.

[4] Carlos Ortega; Antoni Arias; Cedric Caruana; Maurice Apap; Josep Balcells "Torque Ripple Reduction in PMSM DTC Drives using Matrix Converters" Proc. of EPE07, Aalbrog, 2007.
[5] D. A. Rendusara and P. N. Enjeti, "An improved inverter output filter configuration reduces common and differential modes dv/dt at the motor terminals in PWM drive systems," IEEE Trans. Power Electron., vol. 13, pp. 11351143, Nov. 1998.
[6] A. L. Julian, G. Oriti, and T. A. Lipo, "Elimination of common-mode voltage in three-phase sinusoidal power converters," IEEE Trans. Power Electron., vol. 14, pp. 982989, Sept. 1999.
[7] Han Ju Cha and Prasad N. Enjeti. "An Approach to Reduce Common-Mode Voltage in Matrix Converters" IEEE Transactions on Industry Applications, Vol. 39, No. 4, pp. 1151-1159, July/August 2003.
[8] Patrick W. Wheeler, Jose Rodriguez, Jon C. Clare, Lee Empringham and Alejandro Weistein, "Matrix Converters: A Technology Review" IEEE Trans. on Industrial Elec., Vol. 49, No. 2, pp. 276-288, April 2002.